



HAL
open science

Identification of the viscoelastic-viscoplastic properties of materials by instrumented nanoindentation

Mohamed Cheikh Barick

► **To cite this version:**

Mohamed Cheikh Barick. Identification of the viscoelastic-viscoplastic properties of materials by instrumented nanoindentation. Mechanics of materials [physics.class-ph]. Université Bourgogne Franche-Comté, 2020. English. NNT : 2020UBFCD004 . tel-02937598

HAL Id: tel-02937598

<https://theses.hal.science/tel-02937598>

Submitted on 14 Sep 2020

HAL is a multi-disciplinary open access archive for the deposit and dissemination of scientific research documents, whether they are published or not. The documents may come from teaching and research institutions in France or abroad, or from public or private research centers.

L'archive ouverte pluridisciplinaire **HAL**, est destinée au dépôt et à la diffusion de documents scientifiques de niveau recherche, publiés ou non, émanant des établissements d'enseignement et de recherche français ou étrangers, des laboratoires publics ou privés.

**THESE DE DOCTORAT DE L'ETABLISSEMENT UNIVERSITE
BOURGOGNE FRANCHE-COMTE
PREPAREE A L'UNIVERSITE DE FRANCHE- COMTE**

Ecole doctorale n°37
Sciences Pour l'Ingénieur et Microtechniques

Doctorat de Mécanique

Par
BARICK Mohamed Cheikh

Identification des propriétés visioélastique-visioplastique des matériaux
par la nanoindentation instrumentée

Thèse présentée et soutenue à Besançon, le 03 juin 2020

Composition du Jury:

M. KERYVIN Vincent	Professeur des Universités, Université de Bretagne Sud	Président
M. LE BOURHIS Eric	Professeur des Universités, Université de Poitiers	Rapporteur
M. KERMOUCHE Guillaume	Professeur, Ecole des Mines de St-Etienne	Rapporteur
M. FRETIGNY Christian	Directeur de Recherche CNRS, ESPCI Paris	Examineur
M. LEJEUNE Arnaud	Ingénieur de Recherche, Université Bourgogne Franche-Comté	Examineur
M. AMIOT Fabien	Chargé de Recherche CNRS HDR, Institut Femto-st	Directeur de thèse
M. RICHARD Fabrice	Maître de Conférences HDR, Université Bourgogne Franche-Comté	Codirecteur de thèse
M. GAILLARD Yves	Maître de Conférences, Université Bourgogne Franche-Comté	Codirecteur de thèse
M. ARNOLD Gilles	Maître de Conférences, Université de Haute-Alsace	Invité

**THESE DE DOCTORAT DE L'ETABLISSEMENT UNIVERSITE
BOURGOGNE FRANCHE-COMTE
PREPAREE A L'UNIVERSITE DE FRANCHE- COMTE**

Ecole doctorale n°37
Sciences Pour l'Ingénieur et Microtechniques

Doctorat de Mécanique

Par
BARICK Mohamed Cheikh

Identification of the viscoelastic-viscoplastic properties of materials by
instrumented nanoindentation

Thèse présentée et soutenue à Besançon, le 03 juin 2020

Composition du Jury:

M. KERYVIN Vincent	Professeur des Universités, Université de Bretagne Sud	Président
M. LE BOURHIS Eric	Professeur des Universités, Université de Poitiers	Rapporteur
M. KERMOUCHE Guillaume	Professeur, Ecole des Mines de St-Etienne	Rapporteur
M. FRETIGNY Christian	Directeur de Recherche CNRS, ESPCI Paris	Examineur
M. LEJEUNE Arnaud	Ingénieur de Recherche, Université Bourgogne Franche-Comté	Examineur
M. AMIOT Fabien	Chargé de Recherche CNRS HDR, Institut Femto-st	Directeur de thèse
M. RICHARD Fabrice	Maître de Conférences HDR, Université Bourgogne Franche-Comté	Codirecteur de thèse
M. GAILLARD Yves	Maître de Conférences, Université Bourgogne Franche-Comté	Codirecteur de thèse
M. ARNOLD Gilles	Maître de Conférences, Université de Haute-Alsace	Invité

To my family...

ACKNOWLEDGEMENTS

This thesis was able to emerge and succeed with the help of people to whom I wish to express my most sincere gratitude. First of all, I would like to extend a big thank you to my supervisors Fabien AMIOT, Fabrice RICHARD, Yves GAILLARD and Arnaud LEJEUNE, for all of their time, guidance and support during my PhD work.

My warmest thanks go to the jury members for the time they dedicated for the evaluation of this work and for the interesting exchanges that ensued during the defense: Vincent KERYVIN president of the jury, Eric LE BOURHIS and Guillaume KERMOUCHE the reviewers and Christian FRETIGNY examiner of the thesis. Moreover, I would like to acknowledge Dr. Gilles ARNOLD for his participation to the defense.

I would also like to thank Xavier GABRION for his help with the tensile and DMA experimental tests.

I would like to thank Emmanuel FOLTÈTE, director of the department, not only for his commitment to the good functioning of the laboratory, but especially for the benevolence and the smile with which he always welcomes us. Thanks also to Isabelle Christine and Delphine, the true pillars of the lab, for the good mood and the availability they show every day. A big thank you, of course, to the people in the IT department, and to Clément in particular, who do a tremendous job, which we do not often recognize the magnitude, and who represent a fundamental brick of all the scientific achievements of the department.

I am thankful for the friendships I developed while at the applied mechanics department with my labmates. Special thanks to my best friends AGNE Aboubakry and AOUALI Kaouthar for the difficult and wonderful moments we shared together during our thesis period. Many thanks for my office colleagues Toky, Reda, Fangnao and Faleh.

Finally and most importantly, I want to acknowledge the support of my family and loved ones. I owe particularly to my parents, my sisters and brother, who have always encouraged me, offered a wonderful environment and providing the propulsive force to achieve my targets. To all the other brothers and sisters that life gave me, you deeply enriched me in many ways through my many adventures that have been part of my academic and personal experiences.

Contents

List of figures	iv
List of tables	xi
Introduction	13
1. Mechanical characterization of materials by nanoindentation	18
1.1. Introduction	19
1.2. Nanoindentation test.....	19
1.3. Identification of mechanical properties based on the contact theory	20
1.3.1. Elasticity and hardness.....	20
1.3.2. Viscoelasticity - plasticity.....	23
1.4. Identification of mechanical properties using contact theory and FE method	28
1.4.1. FEM of the nanoindentation test.....	29
1.4.2. Elasto-plasticity	29
1.4.3. Viscoelasticity - plasticity.....	31
1.5. Identification of the material properties using FEMU.....	33
1.5.1. Elasto-plasticity	34
1.5.2. Viscoelasticity.....	36
1.5.3. Viscoelasticity-viscoplasticity	37
1.6. Uniqueness of material properties from nanoindentation curves	39
1.7. Conclusion.....	43
2. Nanoindentation experiments.....	46
2.1. Introduction	47
2.2. Instrumented nanoindentation	47
2.2.1. Indenter tips	47
2.2.2. Sample	50
2.2.3. Experimental device.....	50
2.3. Experimental tests	52
2.3.1. Single rate	52

2.3.2.	Several rates	54
2.3.3.	Cyclic loading	54
2.4.	Pseudo-experimental tests	55
2.4.1.	Triangular	56
2.4.2.	Trapezoidal	56
2.4.3.	Exponential	57
2.4.4.	Sinusoidal	58
2.5.	Macro tests	58
2.6.	Conclusion.....	59
3.	Identification of materials properties from nanoindentation experiments using FEMU and identifiability analysis	60
3.1.	Introduction	61
3.2.	FEM of the nanoindentation test	61
3.2.1.	Description of the FEM	61
3.2.2.	Convergence study of the FE method for the VE behavior	63
3.2.3.	Friction coefficient effect.....	66
3.3.	FEM updating process.....	67
3.3.1.	Objective function.....	68
3.3.2.	Minimization algorithm	68
3.3.3.	Parameters uncertainties	71
3.4.	Sensitivity analysis	74
3.5.	Identifiability index	79
3.6.	Conclusion.....	83
4.	Estimation of the viscoelastic properties of materials from nanoindentation curves	84
4.1.	Introduction	85
4.2.	Viscoelastic behavior law.....	85
4.3.	Non-uniqueness of the solutions	86
4.3.1.	Updating process from experimental data of single test	87
4.3.2.	Sensitivity analysis	93
4.3.3.	A posteriori identifiability analysis.....	95
4.3.4.	Comparison between 2D and 3D FEM.....	96
4.4.	A priori identifiability analysis using a single nanoindentation test.....	98
4.4.1.	Effect of depth rate	98
4.4.2.	Effect of loading type.....	99
4.4.3.	Effect of the tip angle.....	100
4.4.4.	Effect of measurement noise.....	101
4.4.5.	Link between dissipation and identifiability	106

4.5.	Combination of nanoindentation tests for well-posed the inverse problem	109
4.5.1.	Several nanoindentation triangular tests	109
4.5.2.	Dual nanoindentation	110
4.6.	Estimation of the VE behavior parameters from dual nanoindentation experimental data .	118
4.7.	Assessment of the VE behavior.....	119
4.8.	Conclusion.....	122
5.	Estimation of the viscoelastic-viscoplastic properties of materials from dual nanoindentation	124
5.1.	Introduction	125
5.2.	Viscoelastic-viscoplastic behavior law.....	125
5.2.1.	Results of the updating procedure for the V EVP behavior law	128
5.2.2.	Assessment of the V EVP behavior	131
5.2.3.	Sensitivity analysis	134
5.2.4.	Identifiability analysis.....	138
5.3.	Viscoelastic-plastic behavior law	140
5.3.1.	Results of the updating procedure for the V EP behavior law	140
5.3.2.	Assessment of the V EP behavior	143
5.3.3.	Sensitivity analysis	146
5.3.4.	Identifiability analysis.....	150
5.4.	Conclusion.....	152
	Conclusions and future work	154
	Bibliography	157

List of figures

Figure 1.1. Schematic of a typical $P-h$ curve of an elasto-plastic material. S contact stiffness, P_{max} maximum indentation load, h_f final displacement, h_{max} maximum displacement (Dao et al., 2001).	20
Figure 1.2. Schematic of the indenter and sample surface at full load and full unload showing the parameters of the contact geometry (Oliver and Pharr, 1992, 2004).	22
Figure 1.3. Three-elements Voigt model Standard Linear Solid (SLS) (Cheng et al., 2000).	24
Figure 1.4. Indentation creep and relaxation curves of bulk polystyrene (Cheng et al., 2000).	24
Figure 1.5. (a) Burgers model, (b) Generalized Maxwell model, (c) Generalized Kelvin model (Schiffmann, 2006).	25
Figure 1.6. (a) creep compliance $J(t)$, (b) stress relaxation modulus $G(t)$ for experimental data on PC with Berkovich indenter tip (Schiffmann, 2006).	25
Figure 1.7. Viscoelastic-plastic model (a) loading part, (b) unloading part (Oyen and Cook, 2003).	26
Figure 1.8. Nanoindentation $P-h$ curves for four polymers and the model fits (Oyen and Cook, 2003).	27
Figure 1.9. Viscoelastic-plastic model. C_0, C_1, C_2 compliances, E_0, Y, H_0 , instantaneous modulus, yield strength, hardness, η_V, C_V , viscosity, viscous compliance, τ_1, τ_2 , retardation times. (Menčík et al., 2009).	27
Figure 1.10. (a) experimental procedure, (b) displacement-time experimental and calculated curves for various models (Menčík et al., 2011).	28
Figure 1.11. Typical nanoindentation $P-h$ curve of an elasto-plastic material with associated contact parameters (Dao et al., 2001; Casals and Alcalá, 2005).	31
Figure 1.12. Experimental and numerical $P-h$ curves (Huang et al., 2008).	32
Figure 1.13. Optimized parameter values for the $P-h$ curves using FEMU (Kang et al., 2018).	35
Figure 1.14. Comparison between experimental and simulated curves from optimized results (Kang et al., 2018).	35
Figure 1.15. Load-time experimental and simulated curves of PVC (Resapu et al., 2008).	36
Figure 1.16. Four parameters model (Ovaert et al., 2003).	37

Figure 1.17. V EVP constitutive model (Kermouche et al., 2013).....	38
Figure 1.18. Constitutive models (a) V EVP (b) NVEVP (Chen et al., 2015).....	38
Figure 1.19. (a) Displacement-time experimental and simulated curves using V EVP model, (b) Comparison with tensile test results (Chen et al., 2015).....	39
Figure 1.20. Nanoindentation P - h curves using several combinations of parameters (Cheng and Cheng, 1999).....	40
Figure 1.21. Nanoindentation P - h for three combination of parameters using Berkovich indenter tip 70.3° and a conical indenter tip of equivalent half-angle 60° (Chollacoop et al., 2003).....	41
Figure 2.1. Schema of Berkovich indenter tip.....	48
Figure 2.2. Schema of cube corner indenter tip.....	49
Figure 2.3. Shema of conical indenter tip, $\alpha = 42.28^\circ$ (cube corner), and $\alpha = 70.3^\circ$ (Berkovich).....	49
Figure 2.4. Experimental device: environmental chamber, NHT ² / UNHT nanoindentation and Peltier module (Renner, 2016).....	51
Figure 2.5. Schematic design of (a) NHT and (B) UNHT of Anton Paar (Richard, 2017).....	51
Figure 2.6. Displacement-time and load-displacement experimental curves of PP at rates of 50, 500, 1000 and 5000 nm/min using Berkovich indenter tip.	52
Figure 2.7. Displacement-time and load-displacement experimental curves of PP at rates of 12, 25, 50, 100, 500, 1000, 2000, and 2500 using cube corner indenter tip.....	53
Figure 2.8. Displacement-time and load-displacement of PP for the changed rate curve using Berkovich indenter tip.....	54
Figure 2.9. Load-time and load-displacement curves for PP for the cyclic test using Berkovich indenter tip.....	55
Figure 2.10. Displacement-time and load-displacement curves for PP using Berkovich indenter tip. .	55
Figure 2.11. (a) Normalized time-displacement curve. (b) Normalized time-load curve.	56
Figure 2.12. Normalized time-displacement curve for trapezoidal loading with $t_L = t_U$	57
Figure 2.13. Normalized time-displacement curve for exponential loading.	57
Figure 2.14. (a) Normalized time-displacement using sinusoidal loading. (b) Zoom.	58
Figure 2.15. Repetitive progressive loading test performed at 2 N/s.	59
Figure 3.1. 2D-axisymmetric FEM of the nanoindentation test with Berkovich indenter tip with $d = 5$	62
Figure 3.2. 3D FEM of the conical nanoindentation.	63
Figure 3.3. P_{max}/P_{max} ($d = 16$) ratio for each mesh size using the five indenter tips.....	64
Figure 3.4. VE-Nanoindentation curves performed at 500 nm/min. (a) cube corner indenter tip 42.28° . (b) Indenter tip with half angle 57°	65
Figure 3.5. VE-Nanoindentation curves performed at 500 nm/min. (a) Indenter tip with half angle 60° . (b) Indenter tip with half angle 65°	65

Figure 3.6. VE-Nanoindentation curves performed at 500 nm/min using Berkovich indenter tip 70.3°.	66
Figure 3.7. Factor d versus the indenter tip half angle α .	66
Figure 3.8. Effect of the friction coefficient on the nanoindentation force using cube corner and Berkovich indenter tips.	67
Figure 3.9. Convergence of the objective function $\sqrt{2\omega}$ during the updating process.	73
Figure 3.10. Evolution of the four parameters (E, c_1, ν, η) during the updating process using starting point $\theta^{(01)} = (E = 1.5 \text{ GPa}, c_1 = 12.25 \text{ GPa}, \nu = 0.4, \eta = 65 \text{ GPa.s})$.	73
Figure 3.11. Experimental ($h = 1000 \text{ nm/min}$) and simulated nanoindentation curves for the starting point $\theta^{(01)} = (E = 1.5 \text{ GPa}, c_1 = 12.25 \text{ GPa}, \nu = 0.4, \eta = 65 \text{ GPa.s})$ and the estimated solution $\hat{\theta}^{(1)} = (E = 1.63 \text{ GPa}, c_1 = 1.05 \text{ GPa}, \nu = 0.13, \eta = 18.56 \text{ GPa.s})$.	74
Figure 3.12. Effect of the relative perturbation ε on the sensitivity results using the solution ($E = 1.47 \text{ GPa}, c_1 = 0.94 \text{ GPa}, \nu = 0.4, \eta = 17.08 \text{ GPa.s}$) with cube corner indenter tip.	76
Figure 3.13. Effect of the relative perturbation ε on the sensitivity results using the solution ($E = 1.47 \text{ GPa}, c_1 = 0.94 \text{ GPa}, \nu = 0.4, \eta = 17.08 \text{ GPa.s}$) with Berkovich indenter tip.	77
Figure 3.14. Sensitivity vectors of nanoindentation force to the material parameters θ_j during loading and unloading segments before and after smoothing using nanoindentation test performed at 1000 nm/min with Berkovich indenter tip for the solution ($E = 1.47 \text{ GPa}, c_1 = 0.94 \text{ GPa}, \nu = 0.4, \eta = 17.08 \text{ GPa.s}$).	78
Figure 3.15. Sensitivity vectors of the nanoindentation force to the material parameters θ_j during loading and unloading after and before smoothing using nanoindentation test performed at 500 nm/min for the solution ($E = 1.47 \text{ GPa}, c_1 = 0.94 \text{ GPa}, \nu = 0.4, \eta = 17.08 \text{ GPa.s}$). (a) cube corner indenter tip. (b) Berkovich indenter tip.	78
Figure 3.16. (a) Evolution of the function 2ω as function of $\Delta\theta$. (b) Projection function in the space $(\Delta\theta_1, \Delta\theta_2)$ (Renner, 2016).	80
Figure 3.17. Projection function $2\omega\theta$ in the space $(\Delta\theta_1, \Delta\theta_2)$ for different values of the I -index (Richard, 2017).	81
Figure 3.18. I -index versus the relative perturbation ε using the solution ($E = 1.47 \text{ GPa}, c_1 = 0.94 \text{ GPa}, \nu = 0.4, \eta = 17.08 \text{ GPa.s}$) for three combinations of parameters, (a) Cube corner indenter tip. (b) Berkovich indenter tip.	81
Figure 3.19. Evolution of the I -index for the nanoindentation test performed at 1000 nm/min for the solution ($E = 1.47 \text{ GPa}, c_1 = 0.94 \text{ GPa}, \nu = 0.4, \eta = 17.08 \text{ GPa.s}$) with $\varepsilon = 10^{-3}$.	82
Figure 4.1. VE rheological model.	86
Figure 4.2. Evolution of the four parameters (E, c_1, ν, η) during the updating process using three starting points $\theta^{(01)}, \theta^{(02)}$ and $\theta^{(03)}$.	88

Figure 4.3. Evolution of the parameter $(E(1 - \nu^2))$ during the updating process using three starting points $\theta^{(01)}$, $\theta^{(02)}$ and $\theta^{(03)}$.	88
Figure 4.4. Experimental ($h = 1000$ nm/min) and simulated nanoindentation curves for the three solutions $\hat{\theta}^{(1)} = (E = 1.63$ GPa, $c_1 = 1.05$ GPa, $\nu = 0.13$, $\eta = 18.56$ GPa.s), $\hat{\theta}^{(2)} = (E = 1.63$ GPa, $c_1 = 1.05$ GPa, $\nu = 0.03$, $\eta = 18.48$ GPa.s) and $\hat{\theta}^{(3)} = (E = 1.63$ GPa, $c_1 = 1.06$ GPa, $\nu = 0.03$, $\eta = 18.50$ GPa.s).	89
Figure 4.5. Evolution of the four parameters (E, c_1, ν, η) during the updating process for the two particular cases A and B. Comparison with a case with 4 free parameters for the starting point $(\theta(01) = E = 1.5$ GPa, $c_1 = 12.25$ GPa, $\nu = 0.4$, $\eta = 65$ GPa.s).	90
Figure 4.6. Experimental ($h = 1000$ nm/min) and simulated nanoindentation curves for the three solutions $\hat{\theta}^{(1)} = (E = 1.63$ GPa, $c_1 = 1.05$ GPa, $\nu = 0.13$, $\eta = 18.56$ GPa.s), $\hat{\theta}^{(4)} = (E = 1.50$ GPa, $c_1 = 0.96$ GPa, $\nu = 0.02$, $\eta = 22.87$ GPa.s) and $\hat{\theta}^{(5)} = (E = 1.47$ GPa, $c_1 = 0.94$ GPa, $\nu = 0.4$, $\eta = 17.08$ GPa.s).	91
Figure 4.7. Nanoindentation ($P-h$) curves for the five solutions at nanoindentation depth rate of 50 nm/min.	92
Figure 4.8. Nanoindentation ($P-h$) curves for the five solutions at nanoindentation depth rate of 500 nm/min.	92
Figure 4.9. Nanoindentation ($P-h$) curves for the five solutions at nanoindentation depth rate 5000 nm/min.	93
Figure 4.10. Sensitivity of the nanoindentation force P to θ_j for the five solutions $\hat{\theta}^{(1)}$, $\hat{\theta}^{(2)}$, $\hat{\theta}^{(3)}$, $\hat{\theta}^{(4)}$ and $\hat{\theta}^{(5)}$ (Table 4.3) using triangular test at 1000 nm/min.	94
Figure 4.11. (a) Sensitivity vectors of the nanoindentation force to the material parameters θ_j during loading and unloading after smoothing using triangular test at 1000 nm/min. (b) Collinearity between sensitivity vectors S_{k1} and S_{k3} (sensitivities to E and ν , respectively).	95
Figure 4.12. Comparison of the nanoindentation $P-h$ curves at 1000 nm/min using 2D and 3D FEM.	97
Figure 4.13. Comparison of the I -index for three combinations of parameters using nanoindentation test at 1000 nm/min with 2D, 3D conical and 3D Berkovich indenter tips.	97
Figure 4.14. $P-h$ simulated curves for all depth rates using the solutions $\hat{\theta}^{(5)}$ and Berkovich indenter tip.	98
Figure 4.15. $P-h$ simulated curves for all indenter tips using nanoindentation depth rate of 500 nm/min and the solution $\hat{\theta}^{(5)}$.	101
Figure 4.16. Nanoindentation $P-h$ curves for three levels of measurement noise of nanoindentation triangular test at 1000 nm/min.	102
Figure 4.17. Evolution of the 3 parameters (E, c_1, η) during the updating process for the three starting points of the minimization algorithm $\theta^{(05)}$, $\theta^{(06)}$ and $\theta^{(07)}$ using noisy force values.	104

Figure 4.18. Evolution of the 3 parameters (E, c_1, η) during the updating process for the three starting points of the minimization algorithm $\theta^{(05)}$, $\theta^{(06)}$ and $\theta^{(07)}$ using loading segments of noisy force. 106

Figure 4.19. I -index for the nanoindentation triangular tests and the loss factor using the solution $\hat{\theta}^{(5)}$ with equivalent cube corner indenter tip, (a) displacement-controlled mode. (b) force-controlled mode. 107

Figure 4.20. I -index for the nanoindentation triangular tests and the loss factor using the solution $\hat{\theta}^{(5)}$ with equivalent Berkovich indenter tip, (a) displacement-controlled mode. (b) force-controlled mode. 108

Figure 4.21. I -index versus $\tan(\delta)$ using three loading types with the solution $\hat{\theta}^{(5)}$ for three combinations of parameters, (a) $I(E, \nu)$. (b) $I(E, c_1, \eta)$. (c) $I(E, c_1, \nu, \eta)$ 109

Figure 4.22. Nanoindentation pseudo-experimental ($P-h$) curves for equivalent cube corner and Berkovich indenter tips at 500 nm/min obtained using the solution $\hat{\theta}^{(5)} = (E = 1.47 \text{ GPa}, c_1 = 0.94 \text{ GPa}, \nu = 0.4, \eta = 17.08 \text{ GPa.s})$ 111

Figure 4.23. Sensitivity of the nanoindentation force P to θ_j for the five solutions $\hat{\theta}^{(1)}$, $\hat{\theta}^{(2)}$, $\hat{\theta}^{(3)}$, $\hat{\theta}^{(4)}$ and $\hat{\theta}^{(5)}$ (Table 4.3) using triangular test with cube corner tip at 500 nm/min. 112

Figure 4.24. Sensitivity of the nanoindentation force P to θ_j for the five solutions $\hat{\theta}^{(1)}$, $\hat{\theta}^{(2)}$, $\hat{\theta}^{(3)}$, $\hat{\theta}^{(4)}$ and $\hat{\theta}^{(5)}$ (Table 4.3) using triangular with Berkovich tip at 500 nm/min. 112

Figure 4.25. (a) Sensitivity vectors of the nanoindentation force to the material parameters θ_j during loading and unloading after smoothing using triangular test at 500 nm/min with cube corner indenter tip. (b) collinearity between sensitivity vectors S_{k1} and S_{k3} (sensitivities to E and ν , respectively).. 113

Figure 4.26. (a) Sensitivity vectors of the nanoindentation force to the material parameters θ_j during loading and unloading after smoothing using triangular test at 500 nm/min with Berkovich indenter tip. (b) collinearity between sensitivity vectors S_{k1} and S_{k3} (sensitivities to E and ν , respectively). 113

Figure 4.27. Evolution of the 4 parameters (E, c_1, ν, η) during the updating process using the three starting points $\theta^{(01)}$, $\theta^{(02)}$, $\theta^{(03)}$ and $\theta^{(08)}$ with dual nanoindentation technique. 115

Figure 4.28. Nanoindentation ($P-h$) pseudo-experimental and simulated curves of the obtained solution. 115

Figure 4.29. Disrupted pseudo-experimental nanoindentation $P-h$ curves ($h = 500 \text{ nm/min}$) for three levels of noise with equivalent cube corner and Berkovich indenter tips obtained using $\hat{\theta}^{(5)}$ 116

Figure 4.30. Evolution of the 4 parameters (E, c_1, ν, η) during the updating process for the three starting points of the minimization algorithm $\theta^{(01)}$, $\theta^{(02)}$ and $\theta^{(03)}$ using noisy force values of dual nanoindentation data. 118

Figure 4.31. Nanoindentation ($P-h$) experimental and simulated curves for the viscoelastic behavior from dual nanoindentation with cube corner and Berkovich indenter tips at 500 nm/min. 119

Figure 4.32. Experimental and simulated nanoindentation curves of PP at rates of 12, 25, 50, 100, 500, 1000, 2000, and 2500 nm/min using cube corner tip for the VE behavior with the solution $\hat{\theta}^{(5)}$ 121

Figure 4.33. Experimental and simulated nanoindentation curves of PP at rates of 50, 500, 1000, and 5000 nm/min using Berkovich indenter tip for the VE behavior with the solution $\hat{\theta}^{(5)}$	122
Figure 4.34. Experimental data of the tensile test and simulation response using the VE behavior for the estimated solution $\hat{\theta}^{(5)}$	122
Figure 5.1. Optical images of imprints on PP samples. (a) cube corner indenter tip ($2.48 \times 2.48 \mu\text{m}^2$). (b) Berkovich indenter tip ($6.55 \times 6.55 \mu\text{m}^2$).....	125
Figure 5.2. V EVP rheological model.	126
Figure 5.3. Evolution of the seven parameters ($E, c_1, \nu, \eta, \sigma_y, c_2, K$) of the V EVP behavior during the updating process using the three starting points $\theta^{(09)}$, $\theta^{(10)}$ and $\theta^{(11)}$ with dual nanoindentation technique.	131
Figure 5.4. Experimental ($h = 500 \text{ nm/min}$) and simulated nanoindentation ($P-h$) curves using cube corner and Berkovich indenter tips for the three V EVP solutions (Table 5.1).....	131
Figure 5.5. Experimental and simulated nanoindentation ($P-h$) curves of PP at rates of 12, 25, 50, 100, 500, 1000, 2000, and 2500 nm/min using cube corner indenter tip for the V EVP behavior with the solution $\hat{\theta}^{(9)}$	133
Figure 5.6. Experimental and simulated nanoindentation ($P-h$) curves of PP at rates of 50, 500, 1000, and 5000 nm/min using Berkovich indenter tip for the VE behavior with the solution $\hat{\theta}^{(5)}$ and V EVP behavior with $\hat{\theta}^{(9)}$	134
Figure 5.7. Experimental data of the tensile test and simulation response using the V EVP behavior for the estimated solution $\hat{\theta}^{(9)}$	134
Figure 5.8. Sensitivity of the nanoindentation force P to θ_j for the solution $\hat{\theta}^{(9)}$ using nanoindentation tests performed with cube corner and Berkovich indenter tips for the V EVP behavior.	135
Figure 5.9. (a) Sensitivity vectors of the nanoindentation force to the material parameters θ_j during loading and unloading using cube corner indenter tip for the V EVP behavior. (b) Collinearity between sensitivity vectors S_{k3} and S_{k5} (sensitivities to ν and σ_y , respectively).....	137
Figure 5.10. (a) Sensitivity vectors of the nanoindentation force to the material parameters θ_j during loading and unloading using Berkovich indenter tip for the V EVP behavior. (b) Collinearity between sensitivity vectors S_{k3} and S_{k5} (sensitivities to ν and σ_y , respectively).....	138
Figure 5.11. Evolution of the I -index for five combinations of parameters using nanoindentation experimental tests of cube corner and Berkovich indenter tips at 500 nm/min with the V EVP behavior law.	139
Figure 5.12. V EP rheological model.	140
Figure 5.13. Evolution of the 5 parameters ($E, c_1, \nu, \eta, \sigma_y$) of the V EP behavior during the updating process using the four starting points $\theta^{(12)}$, $\theta^{(13)}$, $\theta^{(14)}$ and $\theta^{(15)}$ with dual nanoindentation technique.	142

Figure 5.14. Experimental ($h = 500$ nm/min) and simulated nanoindentation P - h curves using cube corner and Berkovich indenter tips for the four VEP solutions (Table 5.3). 143

Figure 5.15. Experimental and simulated nanoindentation (P - h) curves of PP at rates of 12, 25, 50, 100, 500, 1000, 2000, and 2500 nm/min using cube corner tip for the VEP behavior with the solution $\hat{\theta}^{(12)}$ 144

Figure 5.16. Experimental and simulated nanoindentation (P - h) curves of PP at rates of 50, 500, 1000, and 5000 nm/min using Berkovich indenter tip for the VEP behavior with the solution $\hat{\theta}^{(12)}$ 145

Figure 5.17. Experimental data of the tensile test and simulation response using the VEP behavior for the estimated solution $\hat{\theta}^{(12)}$ 146

Figure 5.18. Sensitivity of the nanoindentation force P to θ_j for the solution $\hat{\theta}^{(12)}$ using nanoindentation experimental tests performed using cube corner and Berkovich indenter tips for the VEP behavior. 147

Figure 5.19. (a) Sensitivity vectors of the nanoindentation force to the material parameters θ_j during loading and unloading using cube corner indenter tip for the VEP behavior. (b) Collinearity between sensitivity vectors S_{k3} and S_{k5} (sensitivities to ν and σ_y , respectively). 148

Figure 5.20. (a) Sensitivity vectors of the nanoindentation force to the material parameters θ_j during loading and unloading using Berkovich indenter tip for the VEP behavior. (b) Collinearity between sensitivity vectors S_{k3} and S_{k5} (sensitivities to ν and σ_y , respectively). 149

Figure 5.21. Evolution of the I -index for four combinations of parameters using nanoindentation experimental tests of cube corner and Berkovich indenter tips at 500 nm/min with the VEP behavior. 150

List of tables

Table 1.1. Parameters of the Sneddon's solution for three indenter tips. M_r is the contact reduced modulus.	21
Table 2.1. Specifications of the NHT ² /UNHT nanoindenter.....	51
Table 3.1. Elements number and the computation time for the 2D VE behavior using Berkovich indenter tip.....	64
Table 3.2. Estimated parameters set $\hat{\theta}$ (Equation 3.1) and uncertainties (Equation 3.17).	72
Table 4.1. Estimated parameters set $\hat{\theta}$ (Equation 3.1) using three starting points and uncertainties (Equation 3.17).....	87
Table 4.2. Estimated parameters for the two particular cases A and B.	90
Table 4.3. Five solutions of the inverse problem.	91
Table 4.4. I -index for all combinations of parameters using triangular test at 1000 nm/min with the solution $\hat{\theta}^{(5)}$. $I \leq 2$ (green, potentially identifiable), $I < 2 \leq 3$ (difficult to identify), $I > 3$ (red, not identifiable).	96
Table 4.5. I -index for all combinations of parameters for all nanoindentation triangular load-unload tests using the solution $\hat{\theta}^{(5)}$. $I \leq 2$ (green, potentially identifiable), $I < 2 \leq 3$ (difficult to identify), $I > 3$ (red, not identifiable).....	99
Table 4.6. Minima and maxima I -index values ($I_{min}; I_{max}$) for different loading types: triangular, trapezoidal, exponential and a sinusoidal loading with max rate (1000 nm/min), and $f = 4$ Hz for the solution $\hat{\theta}^{(5)}$. $I \leq 2$ (green, potentially identifiable), $I < 2 \leq 3$ (difficult to identify), $I > 3$ (red, not identifiable).	100
Table 4.7. I -index for all combinations of parameters using the nanoindentation load-unload test of 500 nm/min with five indenter tip angles for the solution $\hat{\theta}^{(5)}$. $I \leq 2$ (green, potentially identifiable), $I < 2 \leq 3$ (difficult to identify), $I > 3$ (red, not identifiable).	101
Table 4.8. Estimated solutions for the four levels of measurement noise using load-unload test with the starting point $\theta^{(05)}$	103
Table 4.9. Estimated solutions for the three levels of measurement noise using loading segments with the starting point $\theta^{(05)}$	105

Table 4.10. Minima and maxima I -index values ($I_{min}; I_{max}$) of all combinations of parameters for all subsets of nanoindentation triangular load-unload tests using the solution $\hat{\theta}^{(5)}$. $I \leq 2$ (green, potentially identifiable), $I < 2 \leq 3$ (difficult to identify), $I > 3$ (red, not identifiable). 110

Table 4.11. I -index for all combinations of parameters for all dual nanoindentation data at 500 nm/min with the solution $\hat{\theta}^{(5)}$. $I \leq 2$ (green, potentially identifiable), $I < 2 \leq 3$ (difficult to identify), $I > 3$ (red, not identifiable). 111

Table 4.12. Estimated solutions for the three starting points using dual nanoindentation. 114

Table 4.13. Estimated solutions for the three levels of measurement noise using dual nanoindentation with the starting point $\theta^{(02)}$. Reference $\hat{\theta}^{(5)} = (E = 1.47 \text{ GPa}, c_1 = 0.94 \text{ GPa}, \nu = 0.4, \eta = 17.08 \text{ GPa.s})$ 117

Table 4.14. Estimated parameters of the viscoelastic behavior using the dual nanoindentation (cube corner and Berkovich tips). 119

Table 5.1. Estimated parameters set $\hat{\theta}$ (Equation 3.1) for the V EVP behavior law using three starting points. 129

Table 5.2. Minima and maxima I -index values ($I_{min}; I_{max}$) for different combinations of parameters with the solution $\hat{\theta}^{(9)}$. $I \leq 2$ (green, potentially identifiable), $I < 2 \leq 3$ (difficult to identify), $I > 3$ (red, not identifiable). 140

Table 5.3. Estimated parameters set $\hat{\theta}$ (Equation 3.1) for the VEP behavior law using four starting points. 141

Table 5.4. I -index for all combinations of VEP parameters using nanoindentation experimental tests of cube corner and Berkovich indenter tips at 500 nm/min with the solution $\hat{\theta}^{(12)}$. $I \leq 2$ (green, potentially identifiable), $I < 2 \leq 3$ (difficult to identify), $I > 3$ (red, not identifiable). 151

Introduction

Motivation

Over the last twenty years, thin films and small volume materials have been employed in the development of microsystems. In order to determine sufficient accuracy for these microsystems, the investigation of the link between the microstructure and the mechanical properties is very important. The nanoindentation technique is widely used for the characterization of the mechanical properties of materials at small-scale. Several models have been proposed to retrieve the elastic modulus and the hardness from such experimental data (Doerner and Nix, 1986; Oliver and Pharr, 1992). These methods generally assume that the material features a purely elastic behavior during the unloading part and does not exhibit any loading rate dependence (Oliver and Pharr, 1992). However, most of polymers exhibit a significant time-dependent behavior (Tang and Ngan, 2003). It is therefore important to develop a method to retrieve the intrinsic properties of a material from the temporal data of such nanoindentation test. Three approaches have thus been proposed in the literature (Cheng and Cheng, 1998a; Chen et al., 2013).

The first approach is based on the viscoelastic contact theory (Lee, 1955; Radok, 1957; Lee and Radok, 1960). The Laplace transform method is employed to extend the elastic solution to viscoelastic phenomena. The models yield closed-form solutions, which are used to analyze the nanoindentation test. The parameters are obtained by fitting the experimental load–displacement data (Cheng et al., 2000; Oyen, 2006). These viscous parameters, such as compliance constants and retardation times describe a mechanical system behavior in which the material is involved, but these are not intrinsic to the material. Indeed, these models generally include correction factors, which mix intrinsic material properties with geometrical consideration, to tune the contact conditions. A good example is the β factor which corrects the Sneddon relation of elasticity for non-axisymmetric indentation (Oliver and Pharr, 1992). The vast majority of reported results make use of $\beta = 1.034$ (King, 1987). It is however known that this factor

strongly depends on the tested material (Oliver and Pharr, 2004). This furthermore makes these models often over-parameterized, thus leading to multiple solutions for the fitting procedure (Menčík et al., 2011). Converting the properties estimated by this approach, which should be taken into account for the structural engineering problems based on the finite element (FE) analysis, is therefore a difficult and non-obvious task.

The second approach combines the contact theory and the FE method. It is mostly used for the elasto-plastic and viscoelastic materials (Cheng and Cheng, 1998a; Cao and Lu, 2004a; Cheng and Cheng, 2004) and there are only a few of measurements on viscoplastic properties so far (Bucaille et al., 2002; Kermouche et al., 2008). Dimensional analysis is commonly employed to relate the nanoindentation response and the materials properties. The basic idea of this method is that the physical laws do not depend on the arbitrariness in the choice of the units of the physical quantities. This concept often allows to reduce the number of arguments in functions describing the physical phenomena, thus making them simpler to determine either from the computations or from the experiments. However, the uniqueness of the obtained solution has widely been discussed (Cheng and Cheng, 1999).

The third approach, which is called finite element model updating (FEMU), is carried out by combining FE method and numerical optimization. In this method, the objective function, which is a norm of difference between the numerical nanoindentation force and/or displacement and experimental data, is minimized using optimization techniques (Qasmi et al., 2004; Guessasma et al., 2008). The parameters of the model are determined as the minimizer of the objective function. However, the uniqueness of this minimizer is generally not assessed in the literature, but it remains a fundamental question, particularly in instrumented nanoindentation. In fact, in the case of elasto-plastic behavior, numerous works have shown that a group of materials with distinct elasto-plastic properties may yield almost the same nanoindentation P - h curve (Cheng and Cheng, 1999; Alkorta et al., 2005a). It implies that the material properties cannot be uniquely determined by using a single sharp indenter tip. In order to address this problem in the case of elasto-plastic behavior, dual or multiple indentation techniques have been proposed by several authors (Le, 2008; Heinrich et al., 2009; Le, 2011). However, the existence of “mystical materials” that give almost similar P - h curves for different indenter tips with half angles ranging from 60° to 80° has also been shown (Chen et al., 2007). Recently, this problem of non-uniqueness of the elasto-plastic properties was investigated by Phadikar et al. (Phadikar et al., 2013). They found that non-uniqueness of the solution is caused by a high sensitivity of the solution to the experimental errors. They also demonstrated that dual nanoindentation techniques are reliable when the experimental error is within $\pm 1\%$. This question is poorly addressed in the presence of viscous phenomena (viscoelastic and/or viscoplastic). Constantinescu and Tardieu (Constantinescu and Tardieu, 2001) highlighted this difficulty in the case of Maxwell and Norton–Hoff behaviors.

The objective of this thesis is to extract intrinsic viscoelastic-viscoplastic properties of bulk materials from nanoindentation technique. In this context, series of nanoindentation experimental tests

is performed on polypropylene (PP) polymer at several depth rate. Also, pseudo-experimental tests are simulated using several loading types, namely, triangular, trapezoidal, exponential and sinusoidal loading. A viscoelastic-viscoplastic behavior law (VEVP) is implemented in ANSYS FE software with a particular case (i.e viscoelastic-plastic (VEP)) via a UMAT subroutine. The viscoelastic (VE) behavior is treated using the behavior law available in ANSYS. The mechanical properties of PP are estimated using FEMU method and quantified by an identifiability index. The main idea is to design experimental protocols using this index in order to uniquely determine intrinsic and reliable properties.

Overview

The manuscript is organized as follows:

In chapter 1, we present a general overview of the methods used for the extraction of mechanical properties of materials by nanoindentation for various mechanical behavior such as elastic, elastoplastic, viscoelastic, viscoelastic-plastic and viscoelastic-viscoplastic. The nanoindentation technique is introduced and the different approaches used for the identification of materials properties from nanoindentation data are detailed. The characterization of the mechanical properties of materials using these approaches are reviewed. In this work, the FEMU method has been chosen for the identification procedure. This method allows to estimate the material parameters by minimizing the difference between the results obtained from FE simulation and the experimental data. The uniqueness of the parameters estimated by this method is also discussed.

After this presentation of the state of the art in the identification of material properties from nanoindentation technique, chapter 2 presents the experimental device and experimental tests carried out on PP polymer. Subsequently, the pseudo-experimental tests simulated using triangular, trapezoidal, exponential and sinusoidal loading types and used for the conception of an identification methodology for the intrinsic material properties are detailed. Also, a tensile test performed to examine the identified behavior laws is presented.

Chapter 3 describes the 2D-axisymmetric and 3D FEM used for the modelling of the nanoindentation test. Then, the convergence study of the 2D-axisymmetric FEM for the VE behavior law using five different indenter tips (42.28° , 57° , 60° , 65° , 70.3°) and the study of the friction coefficient effect on the nanoindentation $P-h$ curve are performed. The FEMU method chosen for the identification of the material properties is detailed. The sensitivity of the nanoindentation response to the behavior law parameters is then investigated. An identifiability index (I -index) is used to analyze the reliability of the estimated parameters. This I -index allows to quantify the completeness of the data contained in the nanoindentation $P-h$ curves.

In chapter 4, the stability of the viscoelastic properties of PP extracted by the FEMU method using nanoindentation tests is examined. The VE behavior law is described. The updating process is performed using a nanoindentation triangular experimental test realized at depth rate of 1000 nm/min. The non-uniqueness of the viscoelastic properties of PP estimated from single nanoindentation experimental test is demonstrated. The effect of the nanoindentation rate, apex angle of the indenter tip and the measurement noise on the identifiability results is numerically investigated and the link between these results and the dissipation energy is shown. In order to design an experimental procedure which leads to a unique solution for the inverse problem, combinations of nanoindentation tests and apex angles are considered in view of the I -index. Finally, an updating process using two nanoindentation experimental tests carried out at 500 nm/min with cube corner (42.28°) and Berkovich (70.3°) indenter tips is performed.

Chapter 5 is dedicated to the investigation the mechanical behavior of PP by three behavior laws which are V EVP, and VEP. Firstly, a V EVP behavior law is detailed and updating process is performed using the dual nanoindentation experimental tests carried out at 500 nm/min with cube corner (42.28°) and Berkovich (70.3°) indenter tips with three starting points. The identifiability of the behavior law parameters is also examined. Secondly, a VEP behavior law is chosen and updating process using four starting points is carried out. The identifiability study is conducted to analyze the ill-posed character of the inverse problem.

In conclusion, the identification of a unique set of the VE behavior parameters (E, c_1, ν, η) from single nanoindentation test using FEMU method is impossible ($I = 3.7$). The combination of dual indenter tips from five different indenter tips ($42.28^\circ, 57^\circ, 60^\circ, 65^\circ, 70.3^\circ$) numerically examined shows that the four parameters can be uniquely extracted from the dual nanoindentation tests performed at 500 nm/min with cube corner (42.28°) and Berkovich (70.3°) indenter tips. The updating process using the experimental tests of dual nanoindentation illustrates that the PP does not only exhibit a VE behavior. In order to fully describe the mechanical behavior of this material, the V EVP, and VEP behaviors are investigated. The numerical results shows that the V EVP behavior law ($E, c_1, \nu, \eta, \sigma_y, c_2, K$) generates almost the same $P-h$ curves as those obtained experimentally. The identifiability analysis shows that the identification of the seven V EVP parameters from these nanoindentation data is impossible ($I = 4.9$). For the VEP behavior ($E, c_1, \nu, \eta, \sigma_y$), the comparison model/experience indicates that this behavior law is better than the V EVP one. The I -index of the five VEP parameters is $I = 2.8$ which means that their identification is difficult.

Mechanical characterization of materials by nanoindentation

1.1.	Introduction	19
1.2.	Nanoindentation test.....	19
1.3.	Identification of mechanical properties based on the contact theory	20
1.3.1.	Elasticity and hardness.....	20
1.3.2.	Viscoelasticity - plasticity.....	23
1.4.	Identification of mechanical properties using contact theory and FE method	28
1.4.1.	FEM of the nanoindentation test.....	29
1.4.2.	Elasto-plasticity	29
1.4.3.	Viscoelasticity - plasticity.....	31
1.5.	Identification of the material properties using FEMU.....	33
1.5.1.	Elasto-plasticity	34
1.5.2.	Viscoelasticity.....	36
1.5.3.	Viscoelasticity-viscoplasticity	37
1.6.	Uniqueness of material properties from nanoindentation curves	39
1.7.	Conclusion.....	43

1.1. Introduction

In this chapter, we introduce different approaches used for the determination of mechanical properties of materials from nanoindentation data. From the literature, these approaches can be organized into three characterization methods families:

- Analytical methods based on the contact theory,
- Combination between the contact theory and finite element (FE) method,
- Inverse analysis methods based on the simulation of the indentation test (by FE method for example).

Then a review of the development of the identification methods for different mechanical behaviors of materials is given. Finally, an overview of the published results on the uniqueness of the extracted parameters from nanoindentation is provided.

1.2. Nanoindentation test

Nanoindentation test consists of driving a hard indenter tip of known geometry into a material by applying a prescribed load P or displacement h . Basically, one can distinguish two regimes in this test, the loading phase where the indenter penetrates the material and the unloading where the indenter is removed. In a first approximation, the loading part is generally considered as elasto-plastic and the unloading part as purely elastic (Bulychev et al., 1975; Doerner and Nix, 1986).

Generally, the characterization of the mechanical properties of materials by the indentation technique can be performed from the nanoindentation P - h curves (Figure 1.1) following three approaches. The first one uses analytical methods based on the contact theory, the second uses the contact theory and the FE method and the third method is based on the combination of the FE method and an optimization process. These approaches are described in the next sections.

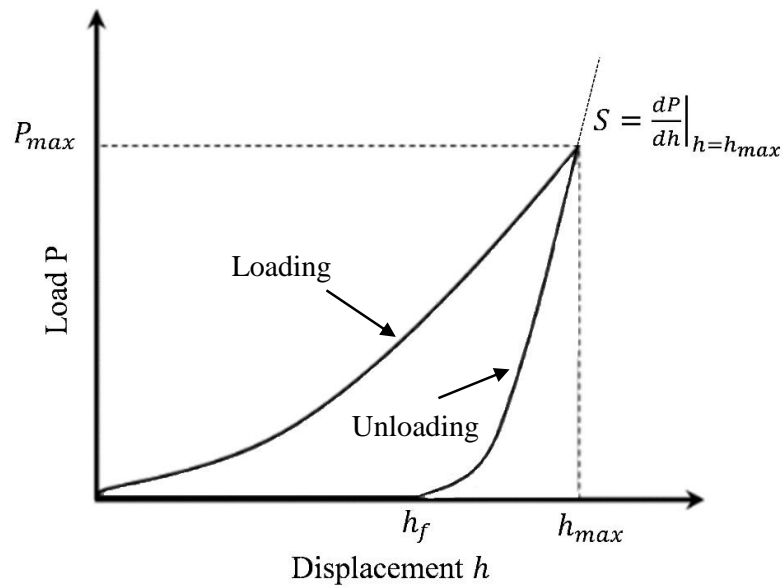


Figure 1.1. Schematic of a typical P - h curve of an elasto-plastic material. S contact stiffness, P_{max} maximum indentation load, h_f final displacement, h_{max} maximum displacement (Dao et al., 2001).

1.3. Identification of mechanical properties based on the contact theory

The contact theory was commonly used to study the deformation of two solids caused by the load generated when they touch each other. Under this load, the solids deform and a contact area is formed. At the end of the 19th century, theoretical and semi empirical models able to describe this method have been developed. It allows to determine the elastic, plastic and viscous properties and the hardness of materials from nanoindentation data. An overview is presented in the following sections.

1.3.1. Elasticity and hardness

The characterization of material properties by indentation technique started ago over a century by the Hertz's contribution on the contact between elastic solids (Hertz, 1881). Boussinesq subsequently developed a method based on the potential theory to solve the contact problem between a linear elastic solid and a rigid axisymmetric indenter (Boussinesq, 1885). Love treated the Boussinesq's problem to derive a solution for cylindrical and conical indenters (Love, 1939, 1929). Sneddon successively used Boussinesq's problem to develop general solutions for different geometries such as spherical, cylindrical and conical indenters (Harding and Sneddon, 1945; Sneddon, 1946). Later, he extended his solution to an arbitrary indenter which is a solid of revolution (Sneddon, 1965). He found the following relation between load P and displacement h for any axisymmetric indenter:

$$P = Ch^m \quad (1.1)$$

where C is a constant depending on the indenter shape and properties of the indented material and m is a constant depending on the indenter type given in Table 1.1.

Table 1.1. Parameters of the Sneddon's solution for three indenter tips. M_r is the contact reduced modulus.

$P = Ch^m$	Conical (half angle α)	Spherical (radius R)	Cylindrical (radius R)
C	$\frac{2}{\pi} M_r \tan \alpha$	$\frac{4}{3} M_r \sqrt{R}$	$2M_r R$
m	2	3/2	1

For an isotropic elastic material, the contact reduced modulus M_r (or equivalent modulus) is defined as function of the reduced modulus of the specimen M and the indenter tip M_i as follows:

$$\frac{1}{M_r} = \frac{1}{M} + \frac{1}{M_i} = \frac{1 - \nu^2}{E} + \frac{1 - \nu_i^2}{E_i} \quad (1.2)$$

where E and ν are Young's modulus and Poisson's ratio for the specimen, and E_i and ν_i are the same parameters for the indenter tip.

Bulychev et al. extended the Sneddon's elastic contact solution to extract elastic properties from elastoplastic material behavior (Bulychev et al., 1975). They introduced an experimental method allowing the calculation of the equivalent modulus. This solution is based on the contact stiffness S which is given by:

$$S = \left. \frac{dP}{dh} \right|_{h=h_{max}} = 2M_r \sqrt{\frac{A_c}{\pi}} \quad (1.3)$$

where S and A_c are the contact stiffness at the beginning of the unloading part and the projected area of the elastic contact, respectively.

Doerner and Nix reused the stiffness equation proposed by Bulychev et al. (Bulychev et al., 1975) to demonstrate that the hardness H and Young's modulus E could be calculated from the indentation load-displacement data (Doerner and Nix, 1986). However, these results were obtained assuming that the contact area remains constant during the initial unloading and similar to those of a flat cylindrical punch. In subsequent years, Oliver and Pharr (Oliver and Pharr, 1992) starting from the Sneddon's solution (Equation 1.1), modified the method introduced by Doerner and Nix (Doerner and Nix, 1986). In their work, they proposed an improved method to determine hardness and Young's modulus using

the indentation P - h curve. They found that the unloading part is usually not linear, but is better described by a simple power law.

$$P = B(h - h_f)^m \quad (1.4)$$

where B and m are constants determined by a fitting procedure, h_f is the final displacement and h is the total displacement calculated as:

$$h = h_c + h_s \quad (1.5)$$

where h_s is the displacement of the surface at the perimeter of the contact. They determine the contact displacement h_c from the Sneddon's expression for the shape of the surface outside the contact area (Figure 1.2).

$$h_c = h_{max} - \varepsilon \frac{P_{max}}{S} \quad (1.6)$$

where ε depends on the indenter tip geometry, and usually about 0.75.

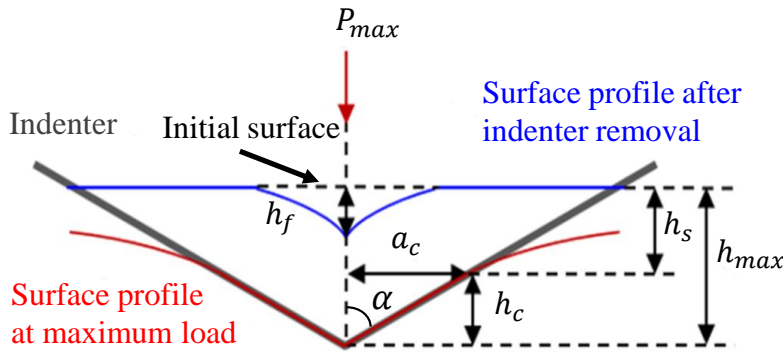


Figure 1.2. Schematic of the indenter and sample surface at full load and full unload showing the parameters of the contact geometry (Oliver and Pharr, 1992, 2004).

Once the contact area A is determined, the hardness H and the indentation modulus M are computed as follows:

$$H = \frac{P_{max}}{A} \quad (1.7)$$

$$M = \left[\frac{1 - \nu_i^2}{E_i} - 2 \frac{\beta}{S} \sqrt{\frac{A}{\pi}} \right]^{-1} \quad (1.8)$$

where β is a geometry correction factor depending on the indenter type and the tested material (Oliver and Pharr, 2004).

This factor has been introduced by King (King, 1987) for elastic indentations formed with rigid flat-ended punches. He found that $\beta = 1.034$ for the Berkovich indenter tip. In the literature, the values of this factor have been intensely debated (Troyon and Huang, 2005; Fischer-Cripps, 2006; Woïrgard, 2006).

Many authors employed the Oliver-Pharr's method to extract the hardness and the elastic properties of isotropic and anisotropic materials from nanoindentation (Vlassak and Nix, 1994; Rho et al., 1997; Marx and Riester, 1999; Oliver and Pharr, 2004). However, one should be careful because the hardness is not a material property, as its value depends on the indenter geometry, and the elastic modulus determined by this method is a combination of at least two elastic constants in the case of isotropic materials and depends on the factors β and ε . In the next section, an overview on the characterization of viscous - plastic properties of materials by nanoindentation using contact theory is presented.

1.3.2. Viscoelasticity - plasticity

The Oliver-Pharr's method presented above, does not consider the time dependent deformation in the mechanical response of the material. Most of viscoelastic solutions derived from the viscoelastic contact theory (Lee, 1955; Radok, 1957; Lee and Radok, 1960). Their method, which is called "the method of functional equations" consists in solving the viscoelastic problem from the elastic solution using the Laplace transform. It remains valid as long as the contact area does not decrease with time (the loading part of the nanoindentation test) (Lee and Radok, 1960; Hunter, 1960; Graham, 1965). This restriction has been studied by Yang who suggested a method to cover more general indentation problems (Yang, 1966). Subsequently, Ting introduced a method to solve the contact problem for the indentation in linear viscoelastic material with axisymmetric rigid indenter (Ting, 1966).

A large number of studies have been conducted to characterize the viscoelastic behavior of materials such as metals, polymers and composites materials using this approach. Cheng et al. derived a closed-form solution of the equations of the flat punch indentation of a linear viscoelastic half-space (Cheng et al., 2000). The solution is obtained from the Laplace transform of the solution of the indentation of a semi-infinite elastic solid by a rigid punch developed by Harding and Sneddon (Harding and Sneddon, 1945). It allows to extract some viscoelastic properties of thin films and coated materials from micro or nanoindentation creep and relaxation tests described by a three-elements standard linear solid (SLS) model with four parameters (E_1, E_2, ν, η) (Figure 1.3). The analytical results were validated by the comparison with experimental creep and relaxation performed on bulk polystyrene (Figure 1.4).

$$P(r) = \frac{P_m}{2\sqrt{1-r^2/R^2}}, \quad 0 < r < R, \quad P_m = \frac{4Gh}{\pi R(1-\nu)} \quad \text{and} \quad G = \frac{E}{2(1+\nu)} \quad (1.9)$$

where $P(r)$, P_m and G are the contact pressure, the mean contact pressure and the shear modulus, respectively. The relation between the load and the displacement in terms of the Laplace variable is given by:

$$\hat{P}(s) = 2R\hat{h} \frac{q_0 + q_1 s}{1 - p_1 s} \quad \text{with} \quad p_1 = \frac{\eta}{G_1 + G_2}, \quad q_0 = \frac{2G_1 G_2}{G_1 + G_2} \quad \text{and} \quad q_1 = \frac{2G_1 \eta}{G_1 + G_2} \quad (1.10)$$

where G_1 and G_2 are the shear moduli of the spring elements (Figure 1.3) and determined by:

$$G_1 = \frac{E_1}{2(1+\nu_1)}, \quad G_2 = \frac{E_2}{2(1+\nu_2)} \quad (1.11)$$

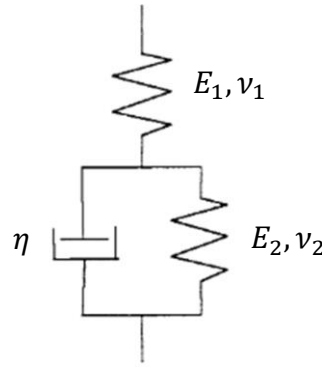


Figure 1.3. Three-elements Voigt model Standard Linear Solid (SLS) (Cheng et al., 2000).

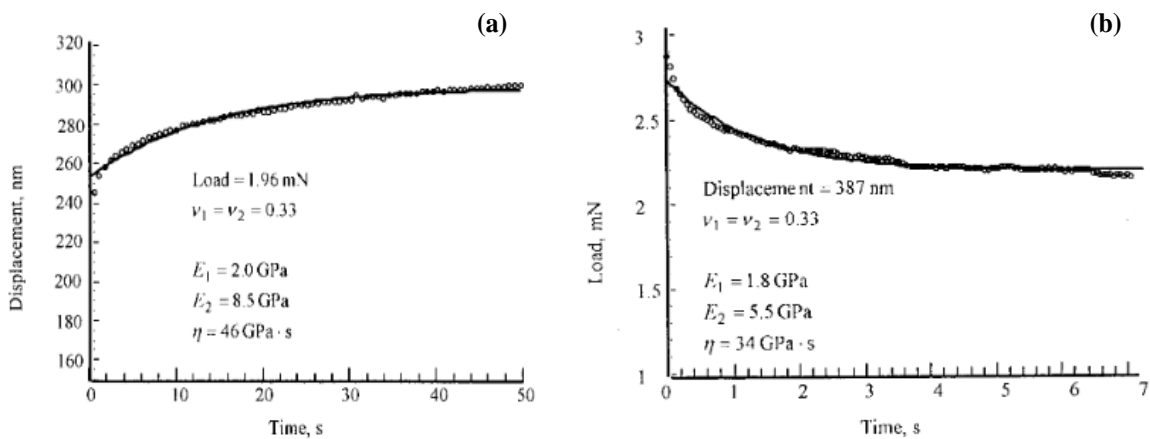


Figure 1.4. Indentation creep and relaxation curves of bulk polystyrene (Cheng et al., 2000).

Later, Schiffmann analyzed the nanoindentation creep and relaxation tests of polycarbonate (PC) (Schiffmann, 2006). For the description of creep and relaxation processes, Burgers model, generalized Maxwell model, generalized Kelvin model (Figure 1.5) were applied with the relationships derived by Shimizu et al. and VanLandingham et al. (Shimizu et al., 1999; VanLandingham et al., 2005). He showed that the models may fit the experimental data in a restricted time interval (Figure 1.6), but do not yield useful material parameters.

$$J(t) = \frac{A(t)}{(1 - \nu)P_0 \tan \alpha} \quad (1.12)$$

$$G(t) = \frac{(1 - \nu)P(t) \tan \alpha}{A_0} \quad (1.13)$$

where P_0 , A_0 and α are the constant force, contact area corresponding to h_0 and the indenter tip half angle, respectively.

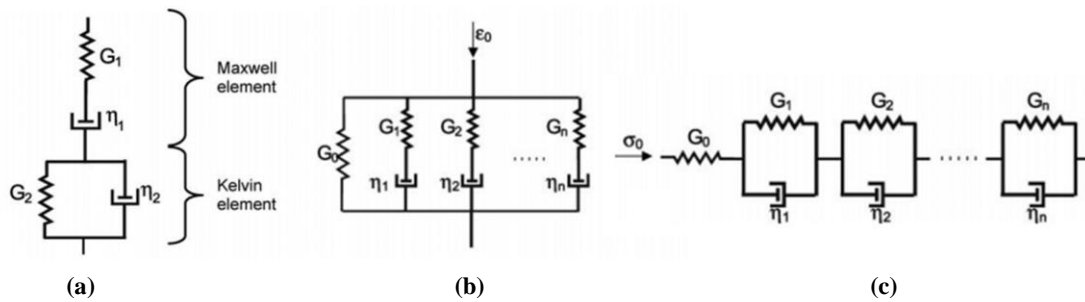


Figure 1.5. (a) Burgers model, (b) Generalized Maxwell model, (c) Generalized Kelvin model (Schiffmann, 2006).

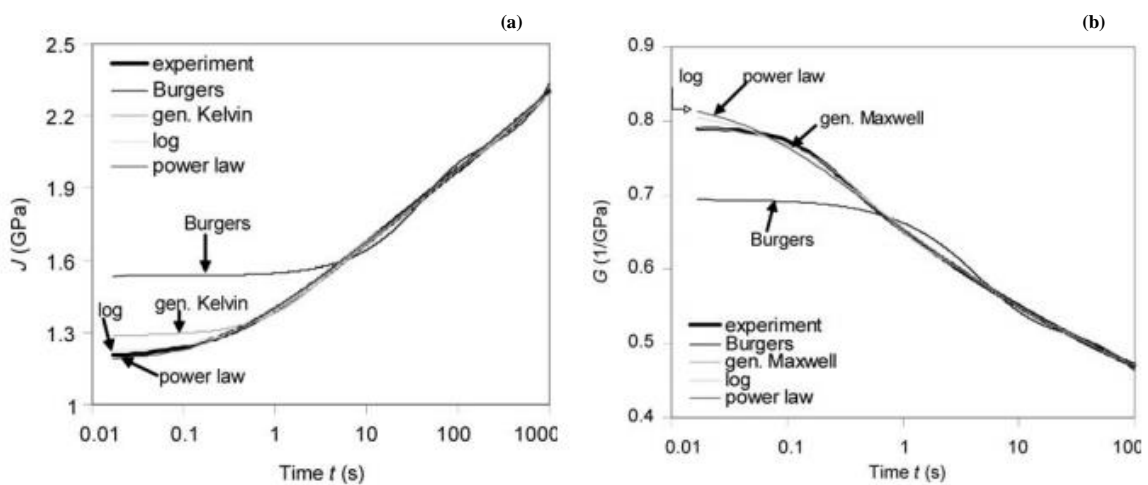


Figure 1.6. (a) creep compliance $J(t)$, (b) stress relaxation modulus $G(t)$ for experimental data on PC with Berkovich indenter tip (Schiffmann, 2006).

Other researches have also been conducted for the combination of viscous and plastic phenomena. Oyen and Cook developed a model to describe the viscoelastic-plastic responses of polymeric materials (Oyen and Cook, 2003). The model is composed of two parts, which describe the loading-unloading cycle (Figure 1.7). They are constructed from a series of the following quadratic mechanical elements:

- Plastic slider with hardness $\alpha_1 H$
- Elastic spring with stiffness $\alpha_2 E'$
- Viscous damper with viscosity coefficient $\alpha_3 \eta_Q$

α_1 , α_2 and α_3 are terms depend on the indenter tip geometry.

Experimental loading-unloading tests were performed on several polymers PMMA, PC, high-density poly-ethylene (HDPE) and polyurethane (PU) (Figure 1.8). The increasing tendency to viscous creep for PC, PMMA, HDPE and the negligible plasticity for PU is obvious in the indentation $P-h$ curves. The model well describes the time dependent behaviors of materials.

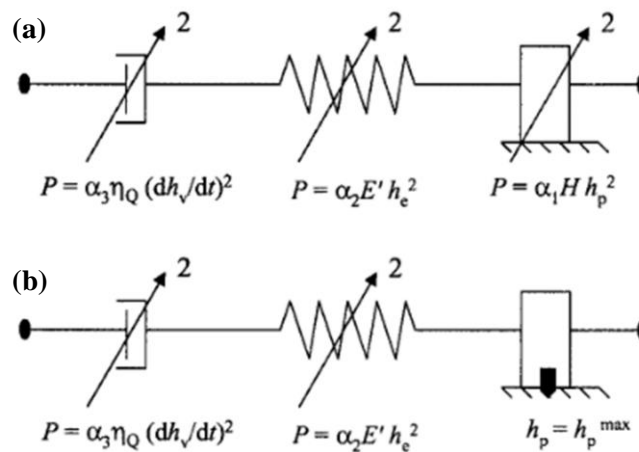


Figure 1.7. Viscoelastic-plastic model (a) loading part, (b) unloading part (Oyen and Cook, 2003).

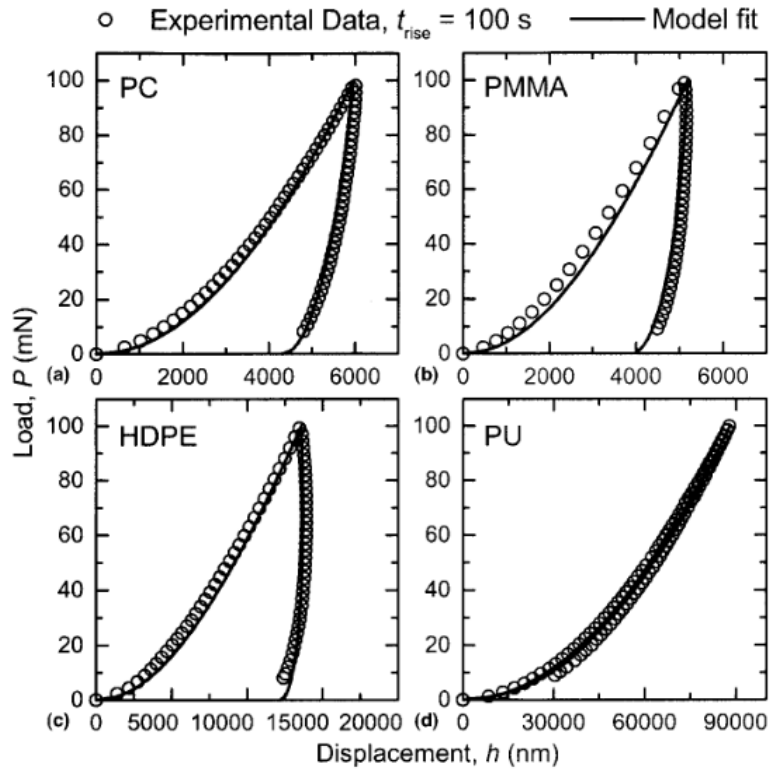


Figure 1.8. Nanoindentation P - h curves for four polymers and the model fits (Oyen and Cook, 2003).

Menčík et al. analyzed the viscoelastic-plastic behavior of PMMA for different indenter shapes (Menčík et al., 2011). They proposed a viscoelastic-plastic model consisted of spring, slider, damper and Kelvin-Voigt model connected in series (Figure 1.9). An experimental five-step procedure was used to determine the parameters in creep compliance function (Figure 1.10a). The creep test (step II) was approximated by seven rheological models, which are a combination of spring, damper and Kelvin-Voigt model connected in series (Figure 1.10b). The obtained parameters in the creep function have no rigorous physical meaning. They should be understood as regression constants, which depend on the material, indenter shape, rheological model and the test time.

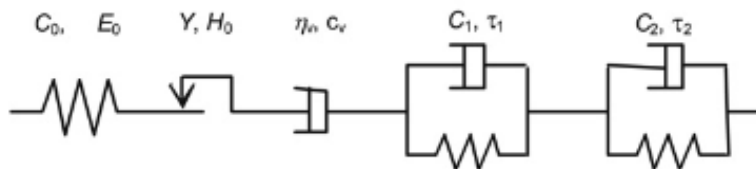


Figure 1.9. Viscoelastic-plastic model. C_0 , C_1 , C_2 compliances, E_0 , Y , H_0 , instantaneous modulus, yield strength, hardness, η_v , c_v , viscosity, viscous compliance, τ_1 , τ_2 , retardation times. (Menčík et al., 2009).

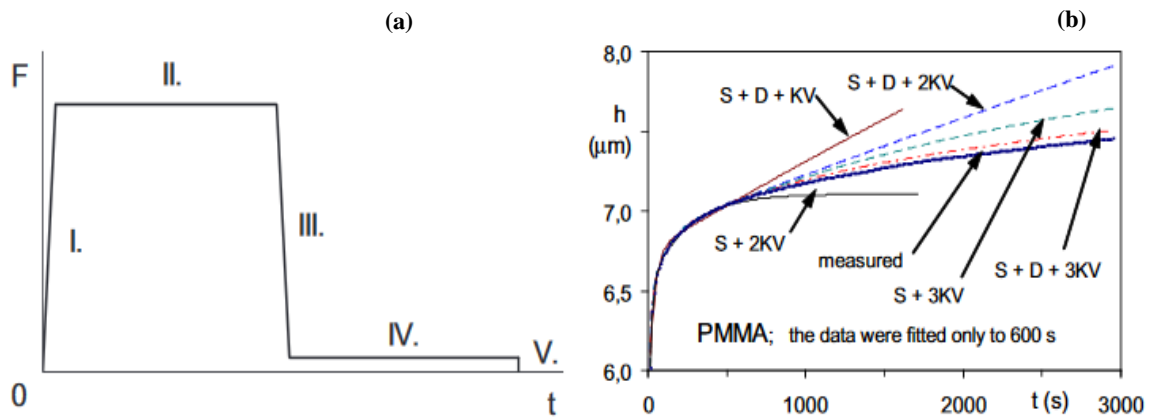


Figure 1.10. (a) experimental procedure, (b) displacement-time experimental and calculated curves for various models (Menčík et al., 2011).

Many studies have been carried out using the approach based on the contact theory to characterize the mechanical behavior of materials by nanoindentation.

- Viscoelastic behavior: (Lu et al., 2003; Fischer-Cripps, 2004; Zhang et al., 2004; VanLandingham et al., 2005; Cheng et al., 2005; Oyen, 2006; Vandamme and Ulm, 2006; Jäger et al., 2007; Huang and Lu, 2007; Martynova, 2016; Samadi-Dooki et al., 2018).
- Viscoelastic-plastic behavior: (Cook and Oyen, 2007; Menčík et al., 2009; Stan et al., 2011; Peng et al., 2012; Cook, 2018).

The approach based on the contact theory allows to determine the elastic, the elasto-plastic and the viscous properties from nanoindentation tests such as the reduced modulus, the storage modulus, the yield strength and the viscosity coefficient. These properties describe a mechanical system behavior in which the material is involved, but these are not intrinsic to the material. Many hypotheses and corrections factors were involved that influence the reliability of the estimated properties. Furthermore, complex material behavior laws are not fully accessible. For that purpose, other inverse methods were proposed to characterize the material properties by combining of the contact theory and the FE method.

1.4. Identification of mechanical properties using contact theory and FE method

Over the past 50 years, the method has been used in the numerical modeling of the indentation test. The improvements of the computational tools allowed to analyze the indentation experiments. In this section, the finite element model (FEM) of the nanoindentation test and the inverse methods, which combine the contact theory and the FE method are reviewed.

1.4.1. FEM of the nanoindentation test

In the indentation field, the FE method was first used by Lee and Kobayashi (Lee and Kobayashi, 1970) to study the elasto-plastic contact problem of a half space surface under a rigid flat punch, and Dumas and Baronet have extended it to a rigid cylindrical indenter (Dumas and Baronet, 1971). Subsequently, Hardy et al. and Lee et al. carried out FE computations in spherical indentation (Hardy et al., 1971; Lee et al., 1972). Since that time, the FEM of the indentation test has been used to numerically explore the elastic and the elasto-plastic behavior of materials:

- 2D-axisymmetric FEM: (Follansbee and Sinclair, 1984; Sinclair et al., 1985; Bhattacharya and Nix, 1988; Laursen and Simo, 1992; Knapp et al., 1999).
- 3D FEM: (Giannakopoulos et al., 1994; Hill et al., 1989; Wang and Bangert, 1993; Olaf and Scheer, 1993; Storåkers and Larsson, 1994; Zeng et al., 1995; Shimamoto et al., 1996; Giannakopoulos and Larsson, 1997).

The FE method has first been used to compare the experimental and numerical results. At the end of the 20th century, the inverse analysis methods based on the combination of the contact theory and the FE method were commonly employed in the characterization of mechanical properties of materials from the indentation data with different behavior laws. These methods are reviewed hereafter.

1.4.2. Elasto-plasticity

The development of the analytical models in the indentation contact problems has consequently allowed for a better understanding and provided tools to characterize the elasto-plastic properties of materials. Cheng and Cheng introduced the dimensional analysis method to identify the material properties by considering the contact between an elastic perfectly plastic solid and a rigid conical indenter (Cheng and Cheng, 1998b). It consists in performing several numerical simulations for various sets of the initial parameters using the FEM of the nanoindentation test. The mechanical properties of materials are extracted by comparing the computed nanoindentation loading-unloading curves with that obtained from experiments. In their study, the loading part of the $P-h$ curve depends on the Young's modulus E , the Poisson's ratio ν and the yield strength σ_y , which are described by a dimensionless function $\Pi_1\left(\frac{\sigma_y}{E}, \nu\right)$. Several FE simulations were performed by varying the three parameters (E, ν, σ_y) . They demonstrated that it is possible to estimate one of the three parameters from the indentation loading curves provided that the two others are known. This result illustrates the three parameters cannot be uniquely determined from the indentation loading curves alone.

They later extended their method to take into account the unloading part of the indentation $P-h$ curves (Cheng and Cheng, 1998a). In this work, using a power-law, they described the stress-strain ($\sigma - \varepsilon$) relationships of elasto-plastic materials by the following functions:

$$\begin{aligned} \sigma &= E\varepsilon & \varepsilon < \frac{\sigma_y}{E} \\ \sigma &= \sigma_y \left(\frac{E}{\sigma_y} \right)^n \varepsilon^n & \varepsilon \geq \frac{\sigma_y}{E} \end{aligned} \quad (1.14)$$

where n is the work-hardening exponent.

The loading part is described by the dimensionless function $\Pi_1 \left(\frac{\sigma_y}{E}, \nu, n \right)$, the unloading part is described by another dimensionless function $\Pi_2 \left(\frac{\sigma_y}{E}, \frac{h}{h_{max}}, \nu, n \right)$. They derived scaling relationships between hardness, contact area, initial unloading slope, and mechanical properties. For a fixed value of ν , several FE simulations were performed by varying the three parameters (E, σ_y, n) . This analysis allows to interpret the information contained in indentation measurements limited by the assumptions of rigid indenter and frictionless contact between material and indenter tip.

As the works progress, four dimensionless functions have been established based on the 2D and 3D FE simulations to characterize the shape of the indentation $P-h$ curve: the loading part (Π_1), the unloading part (Π_2), the ratio between the final depth h_f and the maximum depth h_{max} (Π_3) and the ratio between the total work W_T and the plastic work W_P .

$$\Pi_1 \left(\frac{\sigma_y}{E}, n \right) = \frac{P}{Eh^2} = \frac{P_{max}}{Eh_{max}^2} = \frac{C}{E} \quad (1.15)$$

$$\Pi_2 \left(\frac{\sigma_y}{E}, n \right) = \frac{S}{Eh^2} = \frac{bC}{E} \left(1 - \frac{h_f}{h} \right)^{-1} \quad (1.16)$$

$$\Pi_3 \left(\frac{\sigma_y}{E}, n \right) = \frac{h_f}{h} \quad (1.17)$$

$$\Pi_4 \left(\frac{\sigma_y}{E}, n \right) = \frac{W_p}{W_t} = 1 - \frac{3}{1+b} \left(1 - \frac{h_f}{h} \right) \quad (1.18)$$

where b is the exponent of a power-law fitting to the unloading curve: $P = Ch_{max}^2 \left(\frac{h-h_f}{h_{max}-h_f} \right)^b$, $C = \frac{P}{h^2}$ is the loading curvature. The parameters involved in these dimensionless functions are represented in Figure 1.11.

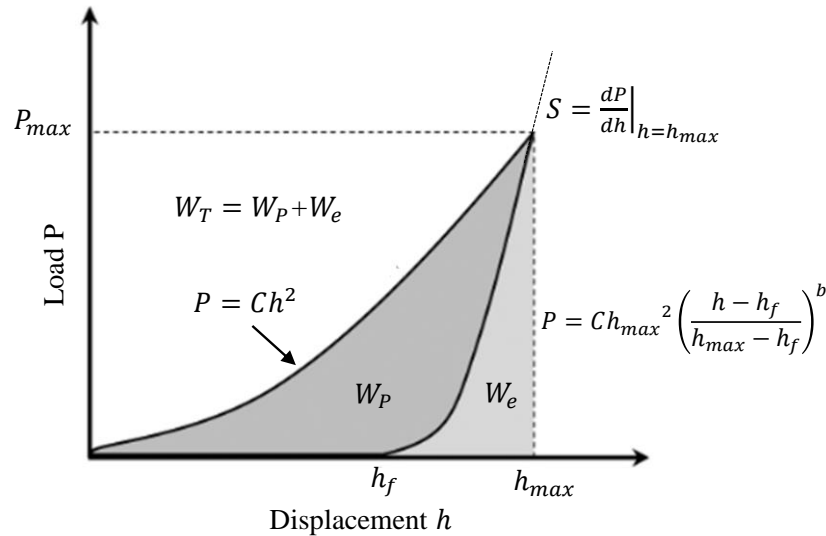


Figure 1.11. Typical nanoindentation P - h curve of an elasto-plastic material with associated contact parameters (Dao et al., 2001; Casals and Alcalá, 2005).

Subsequently, the dimensional analysis has been used in many works using different tips such as conical, Berkovich, Vickers and spherical tips (Cheng and Cheng, 1999; Giannakopoulos and Suresh, 1999; Venkatesh et al., 2000; Dao et al., 2001; Kucharski and Mroz, 2001; Tunvisut et al., 2002; Capehart and Cheng, 2003; Chollacoop et al., 2003; Bucaille et al., 2003; Cheng and Cheng, 2004; Cao et al., 2005; Casals and Alcalá, 2005; Zhao et al., 2006; Collin et al., 2007; Liao et al., 2009; Kang et al., 2011).

1.4.3. Viscoelasticity - plasticity

Most works using this approach in literature have studied the elasto-plastic properties. Cheng and Cheng applied dimensional analysis to provide load-displacement relationship for conical indentation of isotropic linear viscoelastic materials (Cheng and Cheng, 2004). The same viscoelastic model (SLS) proposed by Cheng et al (Cheng et al., 2000) was employed (Figure 1.3). They studied the determination of the model parameters from loading curves under various loading conditions. They also performed FE simulations using the linear viscoelastic model available in ABAQUS to demonstrate the effects of the loading type, such as constant displacement rate, constant loading rate, and constant strain rate on the indentation responses. Later, Huang et al. and Daphalapurkar et al. used spherical nanoindentation to extract viscoelastic properties of a human tympanic membrane (Huang et al., 2008; Daphalapurkar et al., 2009). Using the time dependent displacement relation given by Lu et al. (Lu et al., 2003), an inverse problem coupled with FEM was solved to determine the material relaxation moduli. The measurement results indicate that two exponential terms in the Prony series are sufficient to describe the viscoelastic behavior of the material (Figure 1.12). Subsequently, Peng et al. used dimensional analysis and FE

simulations to establish a method for the characterization of the viscoelastic-plastic properties of the unplasticized polyvinyl chloride (UPVC) from the nanoindentation step-hold-unload loading (Peng et al., 2013). They assumed that the elasto-plastic deformation is dominant and the viscoelastic deformation can be neglected during the fast loading segment, and there is only viscoelastic deformation during the holding segment. Therefore, the viscoelastic and plastic properties can be determined separately from the different segments of the P - h curve. The method showed that the creep compliance, relaxation modulus and the yield strength can be determined from a single nanoindentation test.

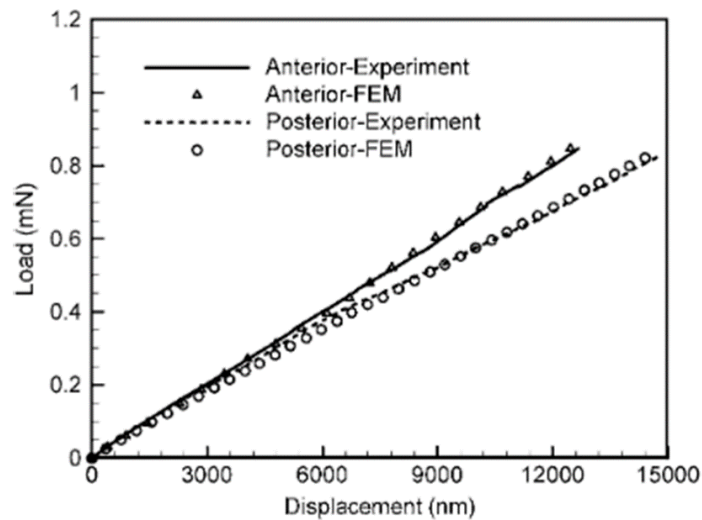


Figure 1.12. Experimental and numerical P - h curves (Huang et al., 2008).

The approach based on the combination of the contact theory and FEM can be employed to characterize the elastic, plastic, and viscous properties of materials with either constitutive laws, like simple power law hardening laws or via the construction of analytical dimensionless functions that relate nanoindentation data to the material properties. They present many limitations such as the required number of nanoindentation tests, the time computation and the non-uniqueness of the identified parameters. In the following section, we present a review of the finite element model updating (FEMU) method, which will be used in this work for the identification of the material properties.

1.5. Identification of the material properties using FEMU

The FEMU method is widely used in the mechanical characterization of materials (Kavanagh and Clough, 1971). In this thesis, the method will be used to identify the polypropylene properties from nanoindentation response. Generally, the researchers explored two types of data: only the $P-h$ curve or by adding the residual imprint. In the first case, the method allows to estimate one or more parameters values $\hat{\boldsymbol{\theta}}$ which minimize the difference between the response $y(t; \boldsymbol{\theta})$ obtained from the FE simulation and from the experimental (or pseudo-experimental) data $y^{exp}(t)$. This response can be the force acting on the indenter or the displacement of the indenter following if the experiment is in force or displacement-controlled mode. The inverse problem is recast as the minimization of an objective function ω , which quantifies the difference between the numerical model and the experiment. The lower the objective function the better estimated is the solution:

$$\hat{\boldsymbol{\theta}} = \underset{\boldsymbol{\theta}}{\operatorname{argmin}} \omega [y(t; \boldsymbol{\theta}), y^{exp}(t)] \quad (1.19)$$

The objective function ω is defined as:

$$\omega(\boldsymbol{\theta}) = \frac{1}{2T} \sum_{k=1}^T \left[\frac{y_k(\boldsymbol{\theta}) - y_k^{exp}}{y_{max}^{exp}} \right]^2 \quad (1.20)$$

where T is the number of data points for the nanoindentation test, i.e. number of the measured force or displacement values $y_k(\boldsymbol{\theta}) = y(t_k; \boldsymbol{\theta})$ and $y_k^{exp} = y^{exp}(t_k)$, and y_{max}^{exp} is the maximum of the experimental response.

In the case where the residual imprint of the sample's surface at the end of the nanoindentation test is taken into account as additional information to complement the $P-h$ curve (Bolzon et al., 2004). This combination provides more information for a reliable identification of the material properties. The objective function (Equation 1.20) becomes:

$$\omega(\boldsymbol{\theta}) = \frac{1}{2T} \sum_{k=1}^T \left[\frac{y_k(\boldsymbol{\theta}) - y_k^{exp}}{y_{max}^{exp}} \right]^2 + \frac{1}{2N} \sum_{n=1}^N \left[\frac{u_n(\boldsymbol{\theta}) - u_n^{exp}}{u_{max}^{exp}} \right]^2 \quad (1.21)$$

where N is the number of data points for the sample surface, i.e. number of the measured imprint values $u_n(\boldsymbol{\theta}) = u(t_n; \boldsymbol{\theta})$ and $u_n^{exp} = u^{exp}(t_n)$, and u_{max}^{exp} is the maximum of the residual imprint.

In this thesis, The FEMU method will be used for the identification of mechanical properties of material from nanoindentation response $y(t)$. An overview will be presented in the following paragraphs

for the identification of mechanical properties from nanoindentation of different material behaviors such as elasto-plastic, viscoelastic, viscoelastic-plastic and viscoelastic-viscoplastic.

1.5.1. Elasto-plasticity

Many studies have been carried out to determine the elasto-plastic properties of different material systems such as bulk, thin film, and coating materials applying the FEMU method to the $P-h$ curves obtained from nanoindentation responses (Nakamura et al., 2000; Gu et al., 2003; Rauchs, 2006; Sun et al., 2014; Fizi, 2015). These may also be complemented with other experimental data such as the mapped imprint and pile-up left after the indentation procedure (Bolzon et al., 2004; Bocciarelli et al., 2005; Bocciarelli and Bolzon, 2007, 2009; Bolzon et al., 2009; Moy et al., 2011; Bolzon et al., 2011; Bolzon and Talassi, 2013). These works suggest that the nanoindentation data ($P-h$ curve and residual imprint) from multiple indenters are required to extract a unique set of material properties. However, Kang et al. proposed a method to determine the elasto-plastic properties of materials from a single nanoindentation $P-h$ test (Kang et al., 2012). They investigated the accuracy of the optimization algorithm results using three different three-dimensional indenter geometries (conical, Berkovich and Vickers indenters). They concluded that the method could be used to extract a unique set of the elasto-plastic properties (Young's modulus, Poisson's ratio, yield strength, work hardening exponent) without the need for multiple indenter tips.

Subsequently, Arizzi and Rizzi developed an inverse analysis method for the identification of elasto-plastic properties of materials through static and dynamic indentation tests (Arizzi and Rizzi, 2014). The use of data from both nanoindentation $P-h$ curve and residual imprint was investigated. They showed that the identification of the parameters remains possible when using the residual imprint only, while it becomes more uncertain when only the nanoindentation curve is taken in account, which proves that the relevant information towards reliable evaluations of the elasto-plastic material parameters (Young's modulus E , yield strength σ_y , work hardening exponent n) comes from the residual imprint. Additionally, for the data affected by random noise, despite a higher number of iterations, the parameters are estimated with lower errors (7%) which encourage the use of these data instead the $P-h$ curve. Recently, Wang et al. developed an inverse method to estimate the elasto-plastic properties of metal materials using the residual imprint of spherical indentation (Wang et al., 2017). The effectiveness of the method is achieved only when the penetration depth or the imposed load is sufficient. The sensitivity investigation showed that the method is very effective and reliable in real engineering application. Also, using the imprint from different nanoindentation loads is able to give more stable and reliable solution. Kang et al. extracted the elasto-plastic properties of P91 steel from nanoindentation $P-h$ curves using FEMU (Kang et al., 2018). They used several starting points for the optimization algorithm (Figure 1.13) and the optimized results were compared with experimental data (Figure 1.14). The comparison of the estimated parameters by this method with the values obtained from uniaxial tensile test indicated

that the extraction of a unique set of the elasto-plastic material properties, especially the yield stress and work hardening exponent required nanoindentation curves from different indenter tip geometries rather than using the same indenter with different loads.

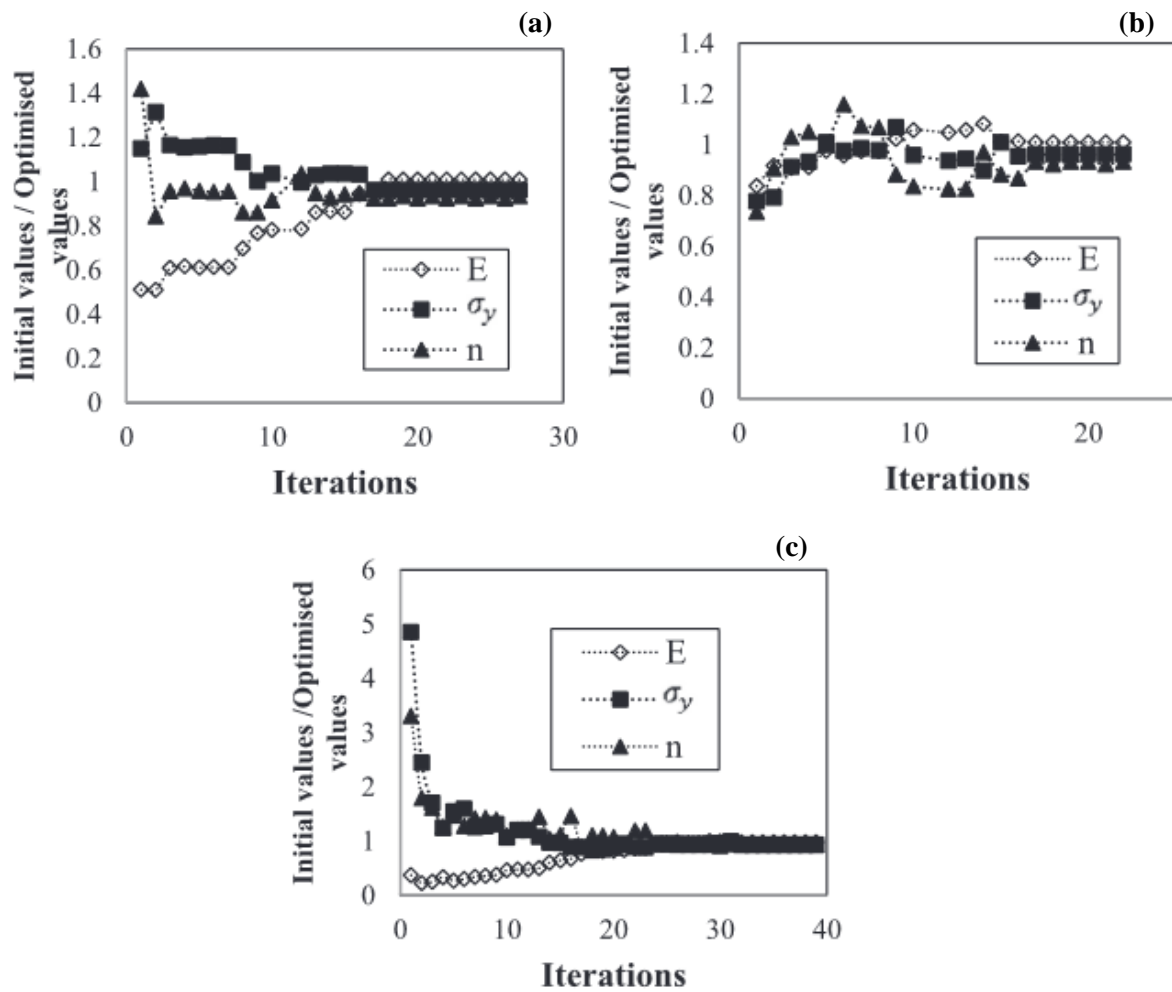


Figure 1.13. Optimized parameter values for the P - h curves using FEMU (Kang et al., 2018).

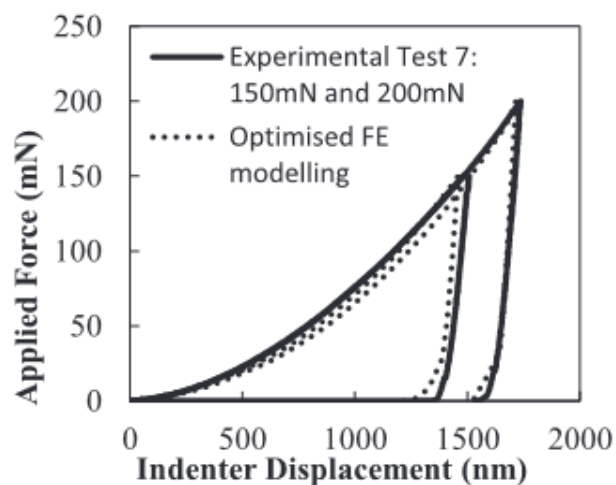


Figure 1.14. Comparison between experimental and simulated curves from optimized results (Kang et al., 2018).

1.5.2. Viscoelasticity

The identification of the viscoelastic properties of materials from indentation P - h curves using FEMU method was started at the beginning of the 21st century (Constantinescu and Tardieu, 2001). They performed several numerical identification examples to illustrate the accuracy and robustness of this method. Qasmi et al. analyzed the viscoelastic properties of polypropylene modified by He⁺ particles and electrons irradiation determined from P - h curves using FEMU (Qasmi et al., 2004). They quantify the variation of the instantaneous and relaxed modulus due to these modifications. Resapu et al. employed FEMU to determine viscoelastic properties of PVC film, polyethylene sheet, and wire with PVC insulation in both pristine and thermally aged conditions from nanoindentation P - h curves (Resapu et al., 2008). A constitutive viscoelastic model available in ANSYS FE software was used. The optimization approach minimized the objective function (RMS) (Figure 1.15) and allowed to characterize the changes in mechanical properties with thermal aging.

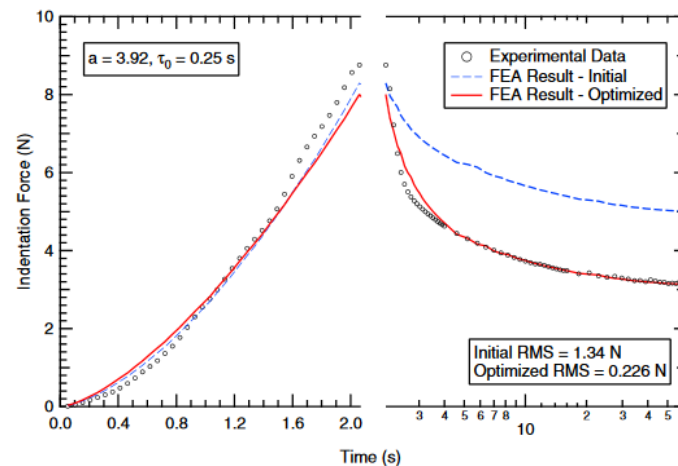


Figure 1.15. Load-time experimental and simulated curves of PVC (Resapu et al., 2008).

Liu et al. developed an inverse FE analysis method to identify the viscoelastic properties of gel from nanoindentation technique using the Kelvin-Voigt two parameters model available in ABAQUS FE software (Liu et al., 2009). Rauchs et al. determined the properties of rubber material by FEMU method, using spherical indentation (Rauchs et al., 2010). Kucuk et al. established a method to describe the nonlinear viscoelastic behavior of polymers under spherical indenter (Kucuk et al., 2013). A nonlinear Burgers model implemented in ABAQUS by introducing a UMAT subroutine was used for the analysis of nanoindentation of PMMA and the parameters were determined using the FEMU method. Chen and Diebels applied the FEMU method to characterize the viscoelastic properties of polymers from nanoindentation (Chen and Diebels, 2013). A linear viscoelastic model for small strain, based on a general Maxwell rheological model was employed to describe the rate dependent material behavior. Richard et al. used FEMU to quantify the effects of osteoarthritis on the viscoelastic behavior of human

articular cartilage (Richard et al., 2013). A viscoelastic behavior law corresponding to the SLS model was employed. They proposed an identifiability analysis to determine the uncertainties of nanoindentation data on the estimated parameters. In this thesis, the same analysis will be performed in order to evaluate the reliability of the behavior laws parameters. Yao et al. used the FEMU method to measure the compressive viscoelastic properties of human cervical tissue from spherical indentation (Yao et al., 2014). The initial parameters of the algorithm were obtained from the analytical solution of Oyen (Oyen, 2006).

In our case, the viscoelastic behavior law is described by a linear elastic spring in series with Kelvin-Voigt model. This rheological model can be decomposed into spherical (volumetric) and deviatoric parts and is presented in Chapter 4.2.

1.5.3. Viscoelasticity-viscoplasticity

Compared with the numerous works related to the identification of elastic, elasto-plastic or viscoelastic properties of materials, a few authors have proposed constitutive models to characterize the viscoelastic-plastic (VEP) or viscoelastic-viscoplastic (VEVP) material parameters from nanoindentation creep and relaxation tests. Ovaert et al. studied the VEP properties of bulk materials by nanoindentation (Ovaert et al., 2003). They used the four parameters model proposed by Kim (Kim, 1999) and Wang (Wang, 2001) based on the stress decomposition (volumetric and deviatoric) to formulate the constitutive equations of the materials. The model consists of a linear damper of viscosity η , in parallel with an elasto-plastic spring of stiffness E , yield stress σ_y and hardening exponent n as shown in Figure 1.16. The Poisson's ratio is an input variable. Wang and Ovaert implemented the four parameters VEP model developed by Ovaert et al. (Ovaert et al., 2003) in the FE software ABAQUS (Wang and Ovaert, 2009). They combined numerical FE/optimization-based and nanoindentation creep tests for the identification of mechanical properties of materials.

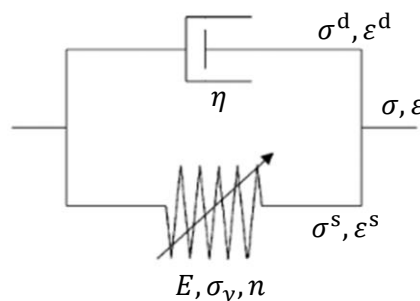


Figure 1.16. Four parameters model (Ovaert et al., 2003).

Later, Kermouche et al. studied the time dependent behavior of PMMA during the scratch loading at constant rate using a viscoelastic-viscoplastic model with constant Poisson's ratio available in the SYSTUS FE software (Kermouche et al., 2013). The model consists of the combination of the Kelvin-Voigt model (Model 1) and the Arruda-Boyce model (Model 2) which is composed of a linear elasticity in series with a Argon's viscosity (Figure 1.17). Then, they used the FEM to examine the potential of the model to reproduce the experimental results.

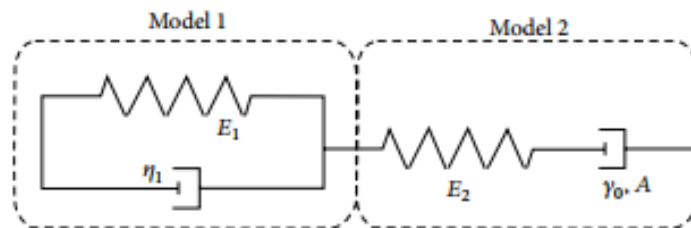


Figure 1.17. VEVP constitutive model (Kermouche et al., 2013).

Chen et al. implemented a VEVP (ten parameters) and nonlinear viscoelastic-viscoplastic (NVEVP) (twelve parameters) constitutive models (Figure 1.18) in ABAQUS to investigate the mechanical behavior of polymers by nanoindentation (Chen et al., 2015). They employed the FEMU method to determine the best-fit model parameters to experimental data and validate the results by the comparison with uniaxial tensile test performed on the ultra-high molecular weight polyethylene (UHMWPE) (Figure 1.19).

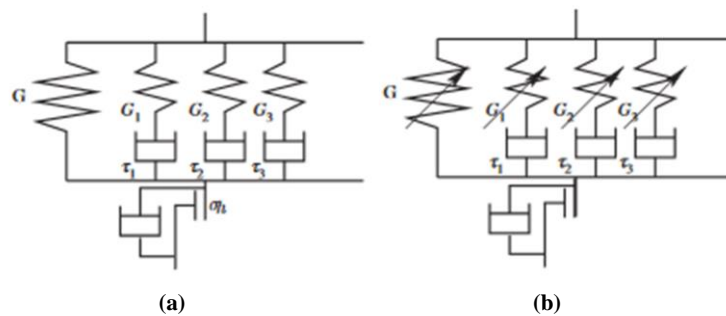


Figure 1.18. Constitutive models (a) VEVP (b) NVEVP (Chen et al., 2015).

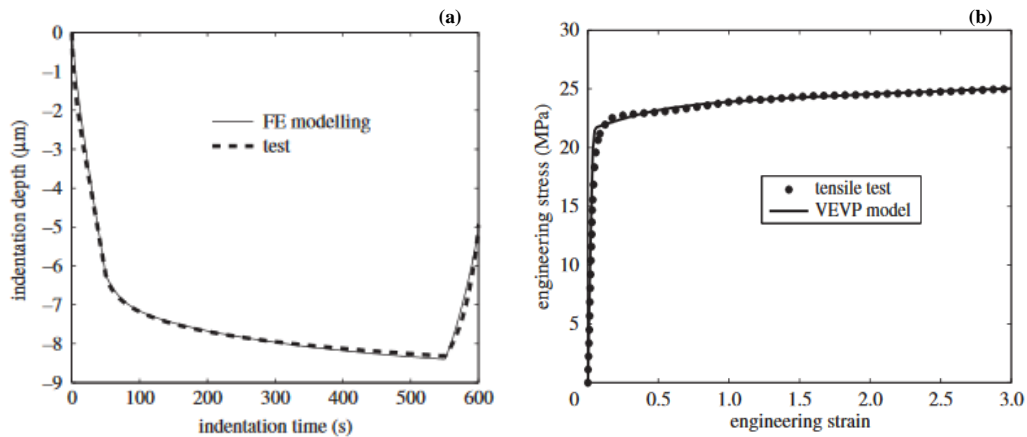


Figure 1.19. (a) Displacement-time experimental and simulated curves using VEP model, (b) Comparison with tensile test results (Chen et al., 2015).

Using material's thermodynamic, Poilâne et al. developed a VEP behavior law which composed of a SLS viscoelastic model and viscoplastic model with nonlinear kinematic hardening to study the mechanical behavior of the flax/epoxy composite using creep and relaxation tests (Poilâne et al., 2014). It was implemented in ANSYS FE software via the UMAT subroutine with a particular case: VEP. In the VE case, the behavior law available in ANSYS is used in this work (Chapter 4.2). The other behavior laws will be described in Chapter 5.2 (VEP without the nonlinear kinematic hardening) and Chapter 5.3 (VEP). Also, the identification of material properties from nanoindentation P - h responses will be approached using FEMU method. The major challenge with the identification procedure using the FEMU method is the uniqueness of the obtained solution. In the next section, the different suggestions proposed to solve this problem will be presented.

1.6. Uniqueness of material properties from nanoindentation curves

The question of uniqueness of the parameters determined from nanoindentation data was studied by several authors for the elasto-plastic materials behavior (Cheng and Cheng, 1999; Capehart and Cheng, 2003; Tho et al., 2004; Alkorta et al., 2005a). They numerically illustrated that is not possible to uniquely determine three unknown elastic-plastic material properties $\langle E, \sigma_y, n \rangle$ from nanoindentation single P - h curve using conical tip (Figure 1.20).

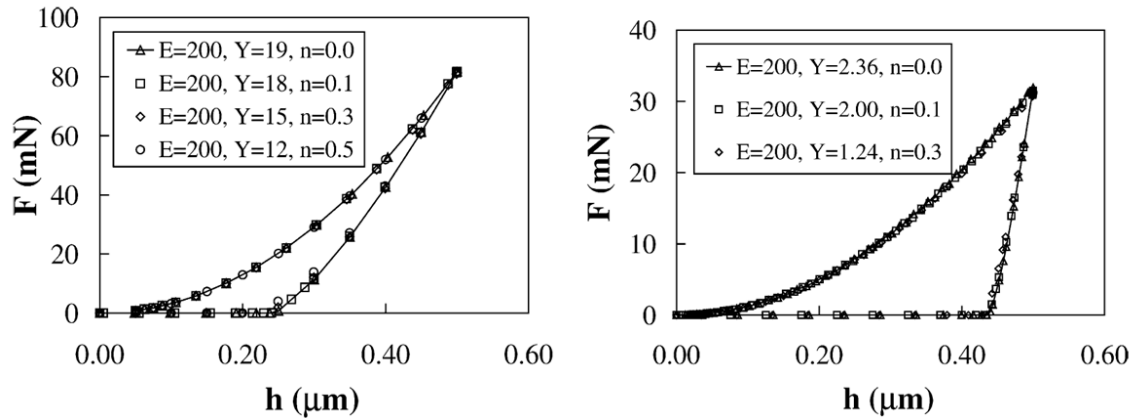


Figure 1.20. Nanoindentation P - h curves using several combinations of parameters (Cheng and Cheng, 1999).

In order to overcome this problem, the authors suggested to enrich the information to be exploited in the FEMU method by the mapped imprint or by combining several nanoindentation P - h tests performed with different indenter tip geometries. In this context, Bolzon et al. and Bocciarelli et al. were the first to study the identification of elasto-plastic material properties from the combination of nanoindentation P - h curves and the residual imprint (Bolzon et al., 2004; Bocciarelli et al., 2005). Subsequently, they used the same methodology for the determination of material properties in film/substrate systems (Bocciarelli and Bolzon, 2007) and the interface properties (Bocciarelli and Bolzon, 2009). Bolzon et al. compared three identification approaches using, only the nanoindentation P - h curve, only the imprint profile, both P - h curve and imprint geometry (Bolzon et al., 2011). In their study, an elasto-plastic material model was employed and the parameters were estimated by the approaches above using FEMU method. They showed that the imprint geometry is more competitive than the other approaches for the identification of the plastic parameters (σ_y, n) . The inverse analysis method returned accurate and robust results also in presence of input data corrupted by some noise when both the P - h curve and the imprint geometry data are employed in the inverse analysis procedure; the same conclusion does not hold true if the P - h curve only is exploited.

Challicoop et al. established a method for interpreting sharp indentation results obtained with dual indenter with different half angles (Challicoop et al., 2003). They also examined the uniqueness of the elasto-plastic properties (E, σ_y, n) of aluminum alloys and found that using a second indenter helps in reducing the non-uniqueness problem and improves the accuracy of the inverse problem (Figure 1.21). The sensitivity analysis performed for the estimated properties showed much improvement of the dual indenter algorithms over the single indenter results.

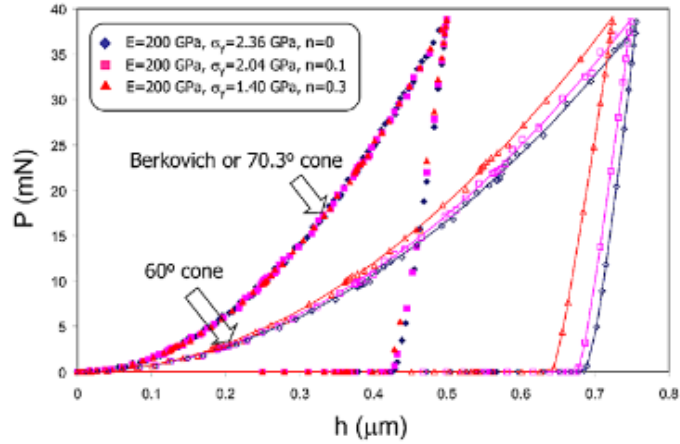


Figure 1.21. Nanoindentation P - h for three combination of parameters using Berkovich indenter tip 70.3° and a conical indenter tip of equivalent half-angle 60° (Chollacoop et al., 2003).

Cao and Lu explored the stability of the reverse dual indenter algorithms proposed by Chollacoop et al. (Chollacoop et al., 2003) to determine the elasto-plastic properties of material using a power law (Cao and Lu, 2004b). They employed the dimensionless function Π_α to identify the representative stress σ_r produced by a conical indenter with a half angle α :

$$y = \Pi_\alpha \left(\frac{M_r}{\sigma_r} \right) \quad (1.22)$$

where $y = \frac{C}{\sigma_r}$, is a scalar and Π_α the dimensionless function describing the loading curvature C , respectively.

A condition number was used to analyze the stability of the inverse problem. It measures the sensitivity of the identified parameters θ to small modification in the input data. This condition number varies with the indenter half angle α and the material properties:

$$Cond_1 = \frac{y \partial \theta}{\theta \partial y} \quad (1.23)$$

They demonstrated that the lower the $Cond_1$, the better conditioned is the inverse problem and if the $Cond$ is large, the inverse problem is considered as ill-conditioned which means it is ill-posed.

Subsequently, this condition number was used to investigate the stability of the inverse problem solution for plastic and elasto-plastic behaviors (Cao and Lu, 2004a; Cao et al., 2005; Cao and Huber,

2006; Seltzer et al., 2011) and hyperplastic behavior of soft materials by spherical indentation (Zhang et al., 2014).

Swaddiwudhipong et al. demonstrated that $P-h$ curves of two conical indenters with different apex angles could lead to unique solution of the three elasto-plastic material properties (M_r, σ_y, n) (Swaddiwudhipong et al., 2005). However, such study is far from being systematic regarding the wide material space and infinite combinations of elasto-plastic properties as well as indenter geometries. Nakamura and Gu used dual nanoindentation method (Berkovich, spherical) to determine the elasto-plastic anisotropic properties of the thermally sprayed NiAl coatings (Nakamura and Gu, 2007). They showed that the additional information improves the convergence of the inverse problem. Chen et al. investigated the elasto-plastic properties of material extracted from dual (or plural) conical indentation (Chen et al., 2007). They found the existence of mystical materials that gives almost similar $P-h$ curves for different indenter tips with half angles ranging from 60° to 80° . Therefore, without knowing other information in advance, many of the mystical materials cannot be distinguished by the dual (or plural) indenter methods unless extreme indenter angles are used. Many works were conducted for extracting of the elasto-plastic material using nanoindentation data. They showed that using the data of multiple indenters with different apex angles delivers better information than using the data from single indenter and removes the non-uniqueness problem (Luo and Lin, 2007; Lan and Venkatesh, 2007; Yan et al., 2007; Heinrich et al., 2009; Le, 2008, 2009).

Later Phadikar et al. studied the problem of non-uniqueness of inverse problem solution (Phadikar et al., 2013). They found that non-uniqueness is caused by a high sensitivity of the solution to the experimental errors. They also demonstrated that dual nanoindentation techniques are reliable when the experimental error is within $\mp 1\%$. They established a condition number to investigate the uniqueness of the elasto-plastic parameters (E, σ_y, n) and quantify the sensitivity of the conical nanoindentation results (Phadikar et al., 2013). In their work, an elasto-plastic power law for strain hardening is chosen:

$$\sigma = \begin{cases} E\varepsilon^n & \text{for } \varepsilon \leq \frac{\sigma_y}{E} \\ \sigma_y \left(\frac{E}{\sigma_y}\right)^n \varepsilon^n & \text{for } \varepsilon \geq \frac{\sigma_y}{E} \end{cases} \quad (1.24)$$

where σ_y , E and n are the yield strength, the Young's modulus and the strain hardening exponent of the material, respectively. They used three shape functions to describe nanoindentation $P-h$ curve:

$$\mathbf{y} = \langle \Psi_{1\alpha}, \Psi_{2\alpha}, \Psi_{3\alpha} \rangle \quad (1.25)$$

where \mathbf{y} is the data vector and $\Psi_{1\alpha}, \Psi_{2\alpha}, \Psi_{3\alpha}$ are the shape functions that describe the $P-h$ curve for a conical indenter with half angle α . The condition number is defined as:

$$Cond_2 = \|\mathbf{J}\|_2 \|\mathbf{J}^{-1}\|_2 = \sqrt{\rho(\mathbf{J}\mathbf{J})} \sqrt{\rho((\mathbf{J}\mathbf{J})^{-1})} \quad (1.26)$$

where \mathbf{J} the jacobian matrix, $\|\cdot\|_2$ the matrix 2-norm and ρ the spectral radius, respectively.

A well-conditioned problem has condition number close to 1. When the condition number tends to $+\infty$, the inverse problem is ill-posed. Between the two cases, the assessment of the conditioning will be ambiguous.

The condition numbers presented above have some limitations, obstructing their applications in this work (Renner, 2016):

- Specific behavior law (power law with three parameters),
- The better conditioning interval is not limited,
- The $P-h$ curve is described by three shape functions.

For that, the identifiability index (Chapter 3.5) proposed by Richard et al. (Richard et al., 2013) which can be used whatever the considered nanoindentation data will be employed. The stability of the parameters of different behaviors namely, viscoelastic (VE), viscoelastic-viscoplastic (VEVP) and viscoelastic-plastic (VEP) estimated from nanoindentation responses will be studied in Chapter 4 and 5 through this identifiability index.

1.7. Conclusion

In this chapter, the methods for analyzing data of nanoindentation load-displacement responses were introduced. The literature review has shown how the use of this technique to extract the materials elastic and elasto-plastic properties has been studied since the late 1800s. Since that time, many efforts have been made to establish advanced theoretical and semi empirical models able to reasonably describe the contact mechanics phenomena occurring during indentation procedure. The development of analytical models in early 1980s and 1990s offers the possibility to extract the elasto-plastic properties of material from nanoindentation test. At the end of the 20th century, more complex models, such as viscoelastic, viscoplastic have been developed and used to characterize mechanical behavior of materials.

Three approaches can be employed to determine mechanical properties of materials from nanoindentation data. The first one uses analytical methods based on the contact theory, the second uses the contact theory and the FE method and the third method is based on the combination of the FE method and an optimization process (the finite element model updating (FEMU)) which will be used in this thesis. After the introduction of the different analysis methods, an overview of different constitutive models developed for the characterization of elastic, elasto-plastic, viscoelastic, viscoelastic-plastic and viscoelastic-viscoplastic material behaviors was presented.

The parameters extracted by the first two approaches describe a mechanical system behavior in which the material is involved, but these are not intrinsic to the material. Many hypotheses and corrections factors were involved that influence the reliability of the estimated properties. Furthermore, complex material behavior laws are not fully accessible. They also present many limitations such as the required number of nanoindentation tests, the time computation and the non-uniqueness of the identified parameters. The problem of non-uniqueness of the properties obtained from nanoindentation data was reviewed and the proposed approaches to solve this problem for elasto-plastic behaviors were discussed.

The literature review presented above, shows that the problem of non-uniqueness of the parameters determined from nanoindentation data is poorly discussed in the presence of viscous phenomena (viscoelastic and/or viscoplastic). In view of different approaches, the FEMU method is chosen for the characterization of the mechanical properties of PP from nanoindentation responses using four behavior laws (VE, VEP and VEP). The uniqueness of the obtained solutions is studied through an identifiability index (*I*-index) in order to determine intrinsic material properties.

For that purpose, the Chapter 2 presents the nanoindentation experimental device and experimental tests performed on PP. Then, the pseudo-experimental tests simulated using several loading types namely, triangular, trapezoidal, exponential and sinusoidal and used for the conception of an identification methodology for the intrinsic material properties are detailed.

In chapter 3, the 2D-axisymmetric and 3D FEM used for the modelling of the nanoindentation test are described. A convergence study of the 2D-axisymmetric FEM for the VE behavior using five different indenter tips (42.28°, 57°, 60°, 65°, 70.3°) and the study of the friction coefficient effect on the *P-h* curve are conducted. The FEMU method is detailed and the sensitivity analysis of the nanoindentation response to the behavior law parameters is then investigated. The *I*-index is employed to analyze the reliability of the extracted parameters.

The chapter 4 is devoted to the determination of the viscoelastic properties from nanoindentation tests. The VE behavior law is described and the updating process is performed using a nanoindentation triangular experimental test realized at 1000 nm/min. The non-uniqueness of the viscoelastic properties of PP estimated from this test is demonstrated. The effect of the nanoindentation rate, apex angle of the indenter tip and the measurement noise on the identifiability results is numerically investigated and the link between these results and the dissipation energy is shown. In order to design an experimental

procedure which leads to a unique solution for the inverse problem, combinations of nanoindentation tests and apex angles are considered in view of the I -index. Finally, an updating process using two nanoindentation experimental tests conducted at 500 nm/min with cube corner (42.28°) and Berkovich (70.3°) indenter tips is performed.

In Chapter 5, the mechanical behavior of PP is studied using three behavior laws, which are V EVP and VEP. Firstly, updating process is carried out using two experimental tests carried out at 500 nm/min with cube corner (42.28°) and Berkovich (70.3°) indenter tips with three starting points for the V EVP behavior law. The identifiability of the V EVP parameters is then examined. Secondly, the VEP behavior law is employed for the updating process using four starting points is performed. The identifiability analysis is conducted to analyze the ill-posed character of the inverse problem.

In the next chapter, the nanoindentation device used for the experimental tests and all experiments performed during this thesis will be presented.

Nanoindentation experiments

2.1.	Introduction	47
2.2.	Instrumented nanoindentation	47
2.2.1.	Indenter tips	47
2.2.2.	Sample	50
2.2.3.	Experimental device	50
2.3.	Experimental tests	52
2.3.1.	Single rate	52
2.3.2.	Several rates	54
2.3.3.	Cyclic loading	54
2.4.	Pseudo-experimental tests	55
2.4.1.	Triangular	56
2.4.2.	Trapezoidal	56
2.4.3.	Exponential	57
2.4.4.	Sinusoidal	58
2.5.	Macro tests	58
2.6.	Conclusion.....	59

2.1. Introduction

This chapter presents the nanoindentation tests used to characterize the mechanical properties of materials. The employed indenter tips as well as the experimental and pseudo-experimental nanoindentation tests conducted during this work are presented. The nanoindentation equipment used for the experimental measurement is also described. We describe the experimental procedure for the experimental tests realized on polypropylene (PP) polymer. The experimental tests are to be used for the extraction of the intrinsic material properties. The pseudo-experimental tests simulated using triangular, trapezoidal, exponential and sinusoidal loading type and employed for the conception of an identification methodology for the extraction of intrinsic material properties are detailed. In addition, conventional tensile tests are also conducted during this work to validate the behavior laws.

2.2. Instrumented nanoindentation

Nanoindentation is very a popular technique used to probe the mechanical properties of a small volume of materials. The nanoindentation test allows probing a material with a solid indenter tip featuring known geometry and mechanical properties. Depending on whether the test is displacement, force or strain controlled, the load and the displacement of the indenter tip are measured/applied continuously generating a nanoindentation load-displacement ($P-h$) curve. This ($P-h$) curve is a function of the intrinsic mechanical properties of the indented material. This technique is now widely used to study the behavior of metallic, ceramic, composites, polymeric and biomaterials.

As presented in the Chapter 1, nanoindentation technique is frequently used to characterize the materials elasto-plastic and viscous properties. In this work, the material properties are measured from experimental nanoindentation triangle tests. Concerning the pseudo-experimental tests, which are simulated using several loading rates, they are used to investigate the influence of the rate, loading type and the indenter tip angle on the parameters identifiability and design a robust experimental identification procedure, which allows to determine reliable intrinsic material properties.

2.2.1. Indenter tips

In experimental nanoindentation tests, the most frequently used indenter tips are conical, spherical (defined by its radius), Vickers (square pyramid), Berkovich (triangular pyramid), Knoop (pyramidal diamond base), flat punch and cube corner indenters. Many aspects should be considered while choosing an indenter tip for a nanoindentation test, the indented material such as a thin film, bulk or composite materials and the information one wishes to extract from the test (elastic and/or plastic parameters). For the experimental tests carried out during this study, diamond cube corner and Berkovich are used.

2.2.1.1. Berkovich

The Berkovich indenter tip is a triangular base pyramid having a three-fold symmetry with a half opening angle of 65.3° (Berkovich, 1950). It has a symmetry of order six and the resulting point from the intersection of the three faces gives a better definition of the point of contact between indenter and specimen during the test. For that, it is the most common tip used for experimental nanoindentation test to measure the mechanical properties of bulk and thin film materials due to its simplified shape that avoids the edge effects during the nanoindentation test (Figure 2.1). In case of anisotropic material, the load-displacement curve is expected to be different according the indented material for each orientation variation of the indenter in the direction of indentation. The information from the test is then much richer on the material behavior than with an axisymmetric indenter.

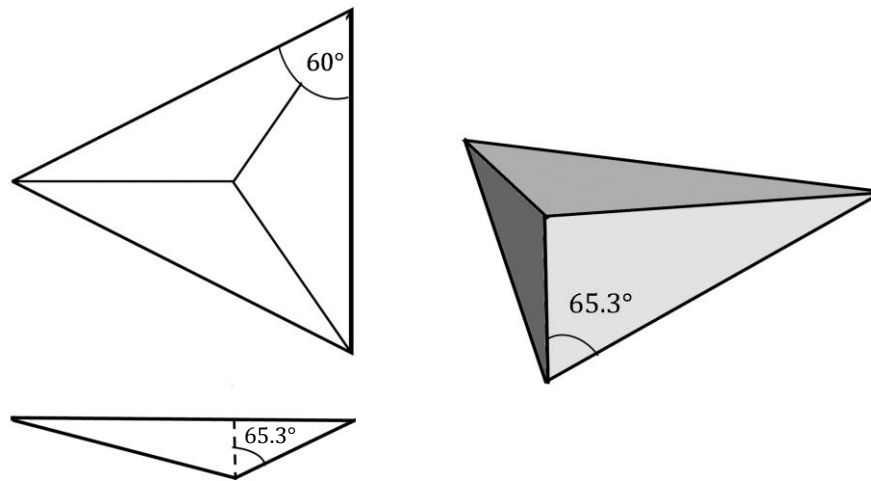


Figure 2.1. Schema of Berkovich indenter tip.

2.2.1.2. Cube corner

The cube corner indenter tip is a three-sided pyramidal tip that is much more sharper than the Berkovich indenter (Figure 2.2). The angle between the axis of symmetry and a face is 35.3° (Fischer, 2002). The sharpness of the indenter generates much higher stresses and strains in the contact area and reduces the cracking threshold. This is useful in producing very small, well-defined cracks around hardness impressions in brittle materials. These cracks can be used to determine fracture toughness at very small scales (Kruzic et al., 2009). During the test, this indenter tip displaces a much larger volume of the material (more than three times that of the Berkovich indenter tip) and thus yields a greater plastic deformation after the unloading part which makes it suitable for plastic materials (Jang et al., 2005).

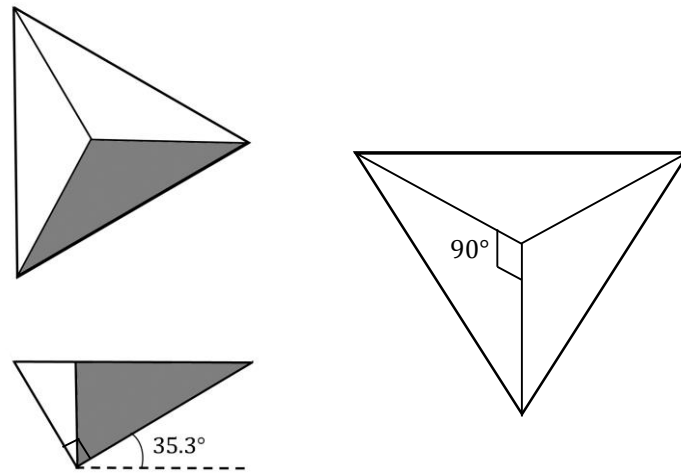


Figure 2.2. Schema of cube corner indenter tip.

2.2.1.3. Conical

The cone indenter tip is widely used, especially in the numerical modeling of the nanoindentation test (Figure 2.3). It is attractive because the complications correlated with the stress concentrations at the sharp edges of the indenter are absent. However, very little experimental nanoindentation tests have been conducted using a conical indenter due to the fabrication difficulties. Two conical indenter tips were numerically used in this work, with equivalent half angles of 42.28° and 70.3° . These indenters are supposed rigid and correspond to the axisymmetric equivalent cone, of displaced volume for a given nanoindentation depth, of the cube corner and Berkovich indenter tips used in the experimental tests (Lichinchi et al., 1998; Fischer, 2002).

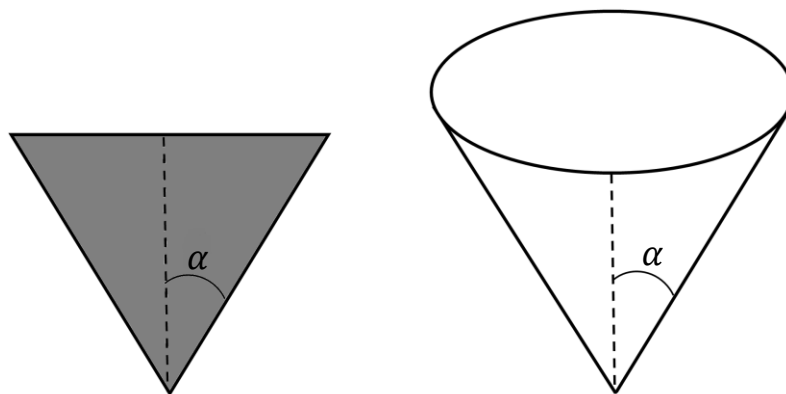


Figure 2.3. Shema of conical indenter tip, $\alpha = 42.28^\circ$ (cube corner), and $\alpha = 70.3^\circ$ (Berkovich).

2.2.2. Sample

In this thesis, the polypropylene (PP301440) produced by the Goodfellow company has been used for the nanoindentation experimental tests. This material is a thermoplastic polyolefin that is produced by polymerizing propylene monomer, which is a gaseous by product of petroleum refining, in the presence of a catalyst under controlled heat and pressure (Maier and Calafut, 1998). It was initially produced in 1954 by G. Natta's group following the work of K. Ziegler regarding to successful development of a suitable stereo-specific catalyst, which conferred polypropylene a kind of structural characteristics useful for rigid items (Vasile, 2000). It is used in a wide range of applications such as medical devices, packaging, labelling, fibers, pipes and automobile industry due to its excellent chemical, physical, mechanical and thermal properties for room temperature uses (Mendenhall et al., 1987; Brun et al., 2001). In this research, PP specimens (PP301440) with dimensions of 15 mm × 15 mm × 0.5 mm have been used for experimental tests.

2.2.3. Experimental device

All experimental nanoindentation tests are performed at room temperature and humidity using Anton Paar nanoindenter (Figure 2.4). This device is capable to apply forces from the micronewton range and measure displacement from nanometer range with controlled environmental conditions (temperature between 20 and 200°C, humidity between 10 and 90%). It is composed of an optical microscope, a Nano Hardness Tester (NHT²) head and a Ultra Nano Hardness Tester (UNHT) head. The UNHT head uses a differential displacement sensor to overcome almost completely the thermal drifts and has a high resolution in load and displacement. Table 2.1 summarizes the specifications of the two nanoindentation heads. A Berkovich indenter is installed on both, NHT² and UNHT. heads In Figure 2.5, the schematic description of the NHT² and UNHT heads provided by Anton Paar is presented.

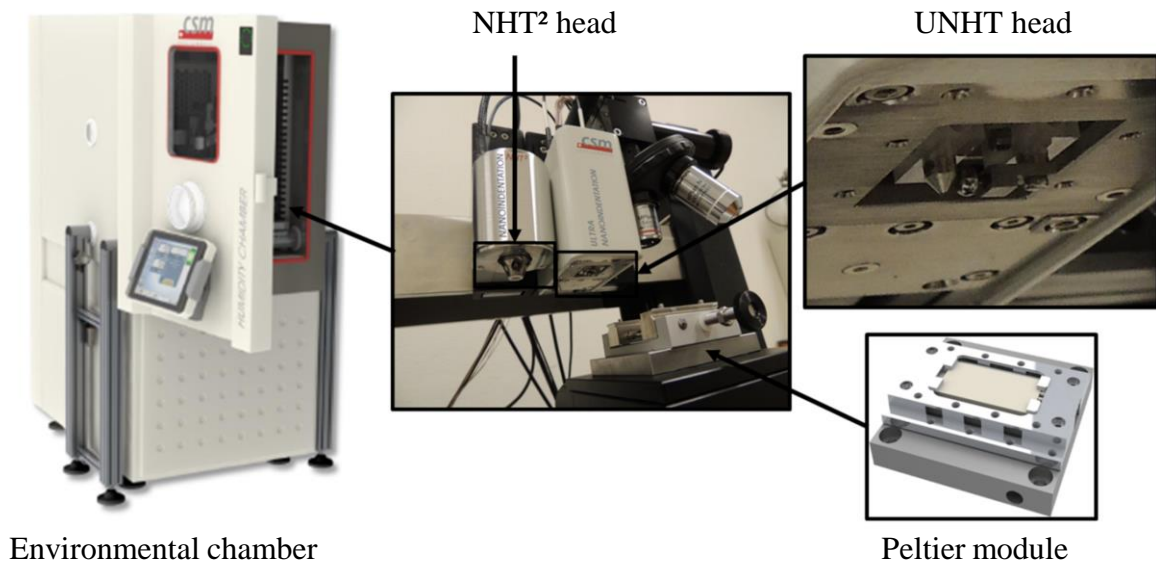


Figure 2.4. Experimental device: environmental chamber, NHT²/ UNHT nanoindentation and Peltier module (Renner, 2016).

Table 2.1. Specifications of the NHT²/UNHT nanoindenter.

Head	Load			Displacement		
	Max	Resolution	Noise level	Max	Resolution	Noise level
UNHT	50 mN	0.003 μ N	< 0.1 μ N	40 μ m	0.003 nm	< 0.03 nm
NHT ²	500 mN	0.02 μ N	< 1 μ N	200 μ m	0.01 nm	< 0.3 nm

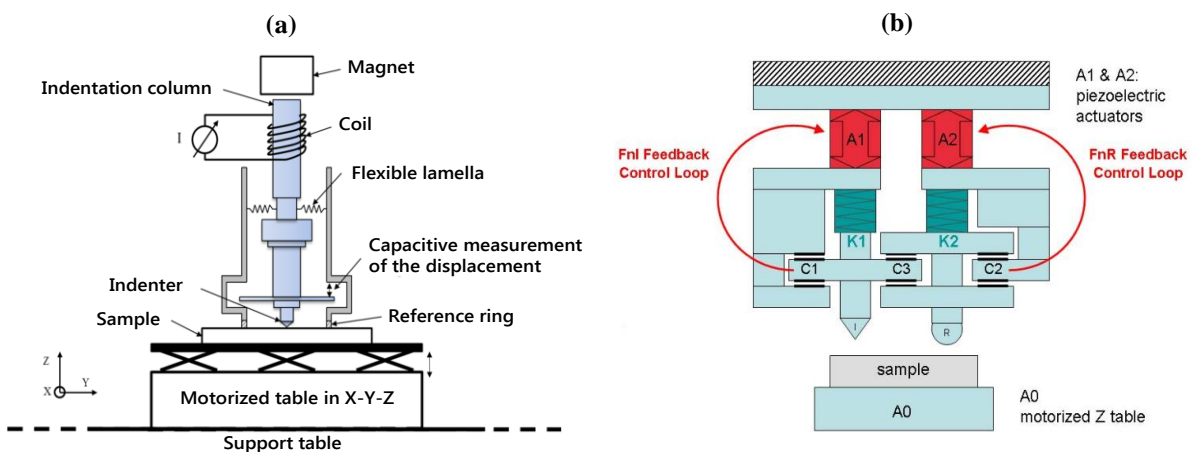


Figure 2.5. Schematic design of (a) NHT and (B) UNHT of Anton Paar (Richard, 2017).

2.3. Experimental tests

In this section, the nanoindentation tests performed in displacement-controlled mode PP specimens are presented. Nanoindentation tests are carried out using Berkovich indenter tip to a maximum depth of $h_{max} \approx 550$ nm at four different nanoindentation depth rates. Also, height tests are conducted using cube corner indenter tip. The indentation experiment consists of approach-load-unload segments. Firstly, the nanoindentation device uses an approach rate, which is not the same for all depth rates to detect the sample. Once the contact is detected, the indenter penetrates the sample at a quasi-constant nanoindentation depth rate until the maximum displacement h_{max} , then during the unloading phase the indenter is lift off the surface with the same rate until a critical force (about $20 \mu\text{N}$). From $20 \mu\text{N}$ to $0 \mu\text{N}$, the approach rate is then used. This explains why there is a setback on the unloading segments (arrow in Figure 2.6 and Figure 2.7). The data points are automatically recorded for the nanoindentation load and displacement during loading and unloading parts. In addition, experimental test at different nanoindentation depth rates, cyclic test, and dynamic tests but also nanoindentation at constant strain rate are conducted on PP material.

2.3.1. Single rate

Herein, experimental nanoindentation tests carried out on PP specimens using Berkovich and cube corner indenter tips at constant depth rate are presented. Series of four nanoindentation loading-unloading tests at depth rates of 50, 100, 500, 1000, 5000 nm/min are performed with a Berkovich tip (Figure 2.6). In addition, eight nanoindentation tests are performed sample using cube corner indenter tip at depth rates of 12, 25, 50, 100, 500, 1000, 2000 and 2500 nm/min (Figure 2.7).

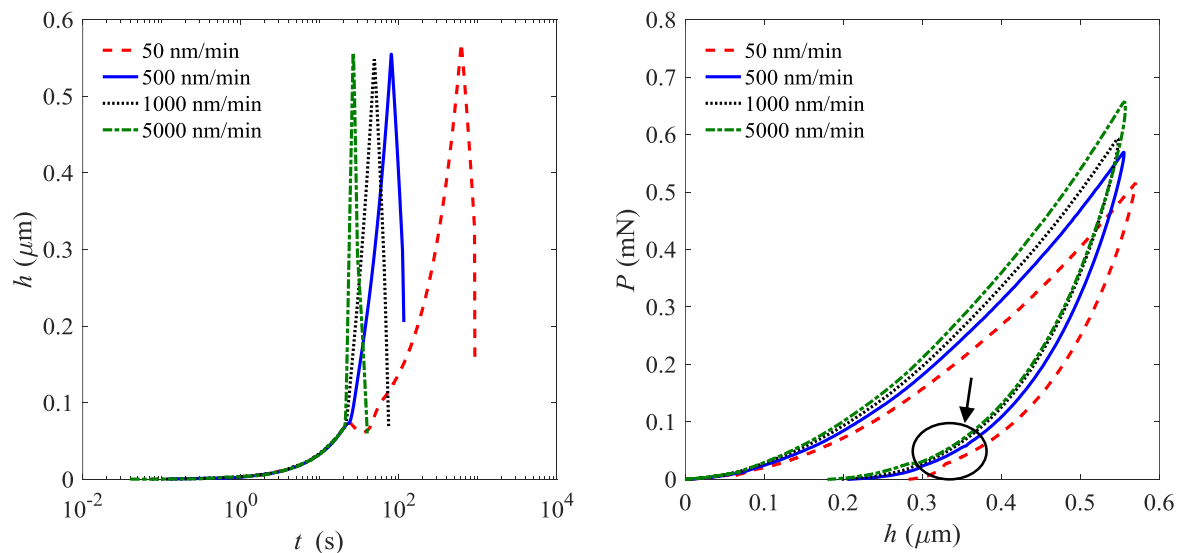


Figure 2.6. Displacement-time and load-displacement experimental curves of PP at rates of 50, 500, 1000 and 5000 nm/min using Berkovich indenter tip.

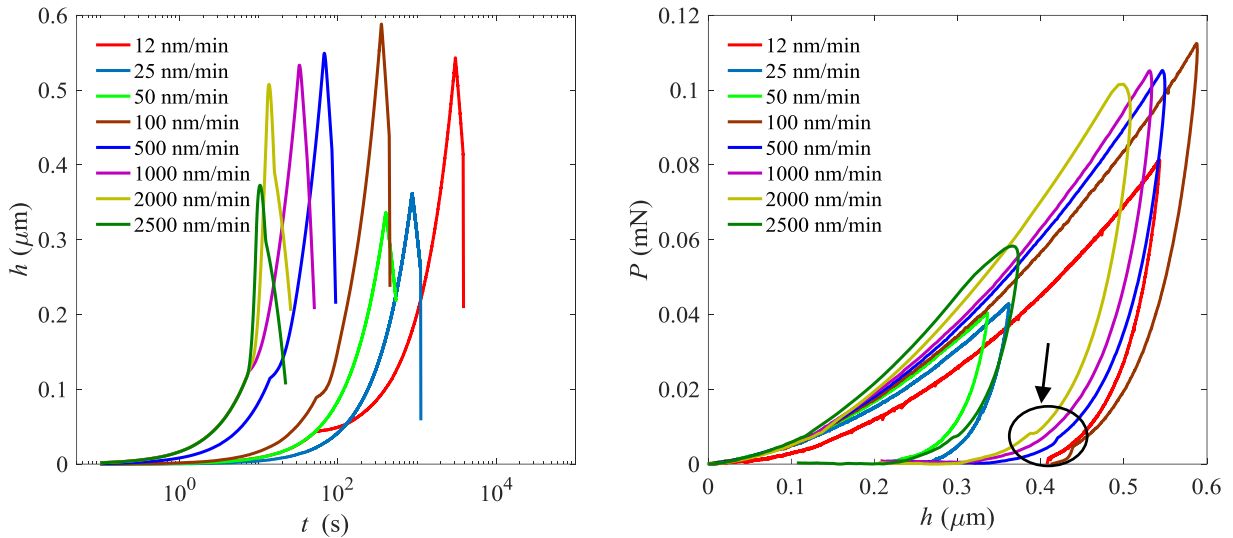


Figure 2.7. Displacement-time and load-displacement experimental curves of PP at rates of 12, 25, 50, 100, 500, 1000, 2000, and 2500 using cube corner indenter tip.

In Figure 2.6 and Figure 2.7, one can make the following observations:

- For the same displacement, the nanoindentation load increases when increasing the loading rate. This indicates that the material could have rate dependent properties.
- For the tests with cube corner indenter tip, from the depth rate of 500 nm/min, the maximum displacement h_{max} does not necessarily occur at maximum load P_{max} . This means that during the unloading segment the deformation and the recovery coexist. The material does not entirely relax during the loading segment.
- For lower nanoindentation rate (12 nm/min) with the cube corner indenter tip, (50 nm/min) with the Berkovich indenter tip, the loading and unloading segments are not superimposed. This suggests that the material may exhibit plastic deformation.

It can be concluded from the above observations that the PP polymer exhibit elastic, elasto-plastic, viscoelastic, and/or viscoplastic properties. These different mechanical behaviors coexist during the loading and unloading segments. This makes difficult to separate one property from the others. Since it is also impossible to determine an analytical solution for this problem, numerical approach must be employed. In this thesis, the FEMU method presented in Chapter 3 is chosen for the estimation of the mechanical properties of PP using several behavior laws, which are viscoelastic (VE) (Chapter 4), viscoelastic-viscoplastic (VEVP) and viscoelastic-plastic (VEP) (Chapter 5).

2.3.2. Several rates

A combined rates nanoindentation experimental test is performed in displacement-controlled mode on PP specimen with Berkovich indenter tip to a maximum value of $h_{max} \approx 720$ nm. This test is composed of seven steps during $t_{max} \approx 655$ s. It is accomplished by implementing multistep load-unload cycles with various loading rates in each cycle. We used nanoindentation depth rates of 200, 250, 500, 10, 2000, 100 nm/min during the loading segment and depth rate of 350 nm/min for the unloading segment. Figure 2.8 illustrates the imposed displacement and the load-displacement curves. Instead, several tests performed at several loading rates, this kind of tests can be useful for the characterization of material properties from nanoindentation.

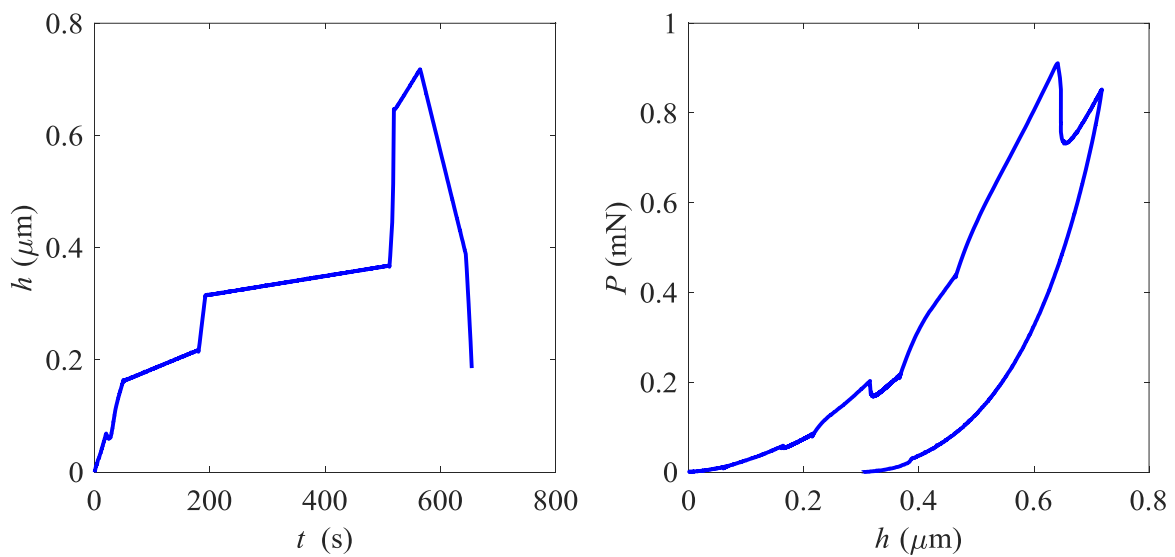


Figure 2.8. Displacement-time and load-displacement of PP for the changed rate curve using Berkovich indenter tip.

2.3.3. Cyclic loading

An experimental test of three cycles of loading and unloading is conducted on PP specimen in load-controlled mode using Berkovich indenter. After the approach step of 25 s, the cyclic indentations are done with a quadratic load increment (from 0.015 mN to 0.514 mN). The total time of the test is 145 s. Figure 2.9 displays the evolutions of the displacement-time and the load-displacement in cyclic indentations test. The comparison between the loops shows that no changes in the shape are visible. However, variations in the width loops can be observed and that due to the indentation under low load. In addition, a nanoindentation test is conducted in strain-controlled mode using strain rate $\dot{h}/h = 0.05$ s^{-1} and adding sinusoidal signal over the loading time 125 s with amplitude of 2.5 nm and

frequency of 5 Hz (Figure 2.10). This test allows to dynamically determine the stiffness and the phase shift during the loading segment.

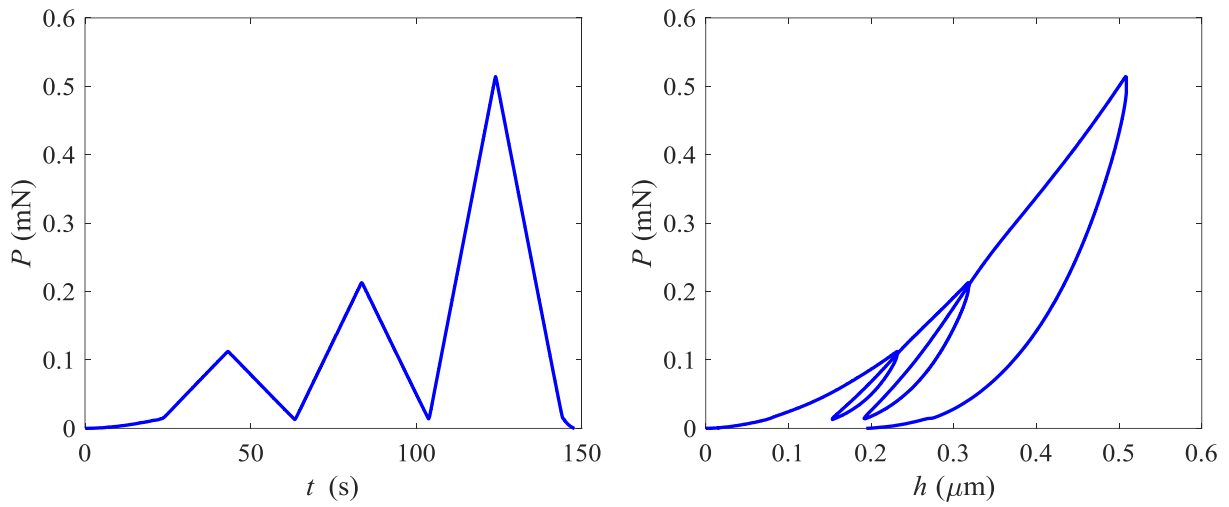


Figure 2.9. Load-time and load-displacement curves for PP for the cyclic test using Berkovich indenter tip.

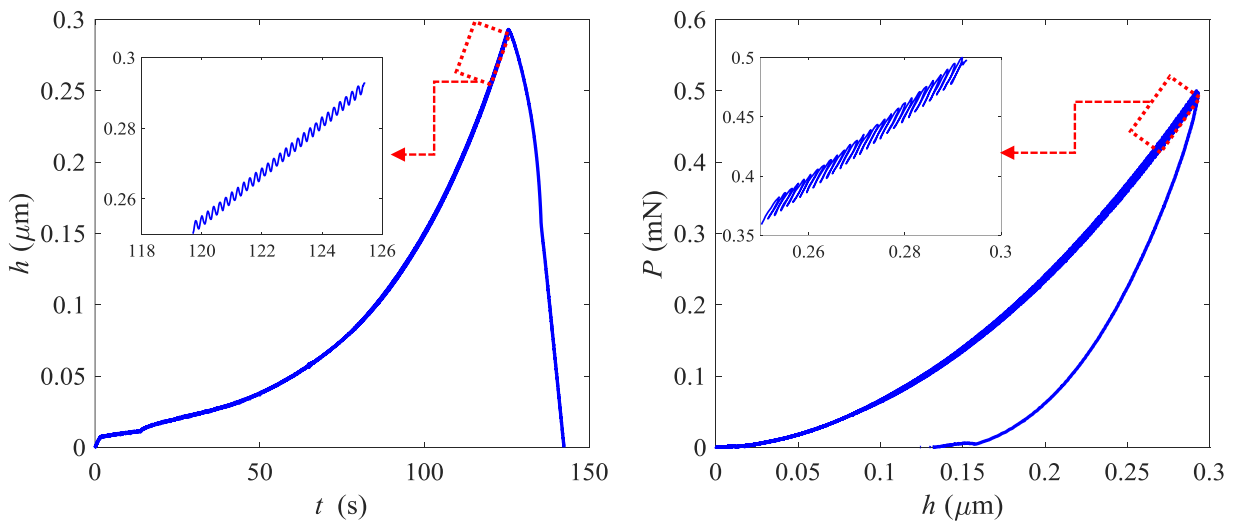


Figure 2.10. Displacement-time and load-displacement curves for PP using Berkovich indenter tip.

2.4. Pseudo-experimental tests

In order to design a methodology for the identification of the intrinsic material properties, several pseudo-experimental nanoindentation tests are numerically generated at maximum depth of $h_{max} = 500$ nm. Four loading types, which are triangular, trapezoidal, exponential and sinusoidal are used. The triangular tests are simulated using 2D-axisymmetric FEM presented in Chapter 3 in displacement and load controlled modes. The following paragraphs describe these tests. These tests will be employed in the a priori identifiability study (Chapter 4).

2.4.1. Triangular

Nanoindentation triangular tests at maximum depth of $h_{max} = 500$ nm and maximum time t_{max} are numerically carried out at eight nanoindentation depth rates $\dot{h} = 50, 100, 500, 1000, 2500, 5000, 10000$ and 20000 nm/min. Other nanoindentation tests at maximum load of $P_{max} = 0.6$ mN are also conducted in force-controlled mode with eight nanoindentation loading rates (60, 120, 600, 1200, 3000, 6000, 12000 and 24000 $\mu\text{N}/\text{min}$). The same time is considered for loading and unloading phases for each nanoindentation depth and load rate (Figure 2.11). The test times are $t_{max} = 1200, 600, 120, 60, 24, 12, 6$ and 3 s, respectively.

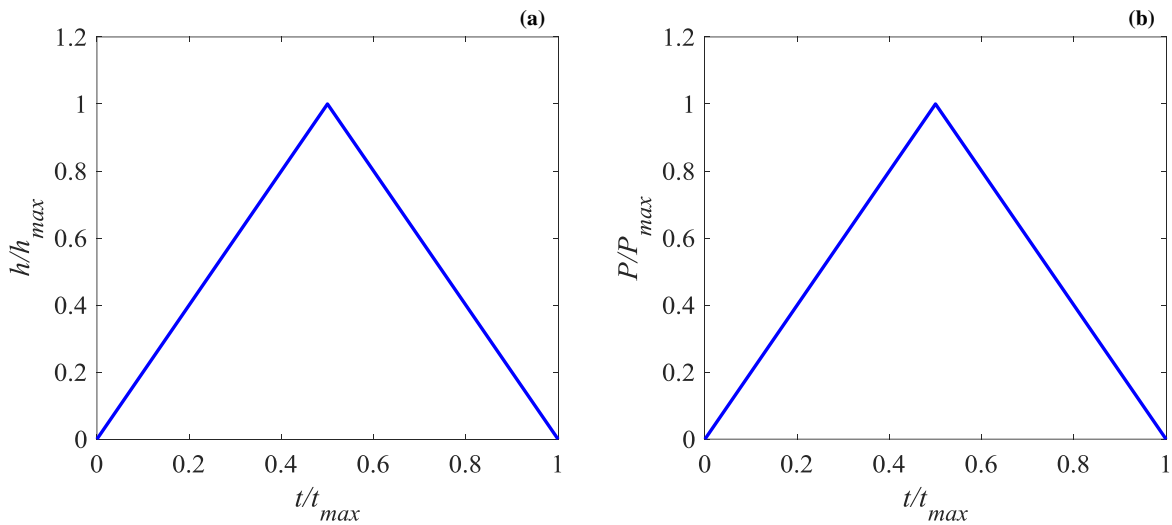


Figure 2.11. (a) Normalized time-displacement curve. (b) Normalized time-load curve.

2.4.2. Trapezoidal

Eight nanoindentation trapezoidal tests are carried out at nanoindentation rates of 50, 100, 500, 1000, 2500, 5000, 10000 and 20000 nm/min. The trapezoidal test consists of three stages, loading, holding and unloading phases: for each depth rate, the indenter penetrates the material until $h_{max} = 500$ nm at time t_L , the depth is then maintained during holding time $t_H = t_L/3$, the indenter is finally removed with the same rate as loading part during unloading time $t_U = t_L$ (Figure 2.12). The holding time allows to evaluate the creep function of the tested material. The test times are $t_{max} = 1400, 700, 140, 70, 28, 14, 7$ and 3.5 s, respectively.

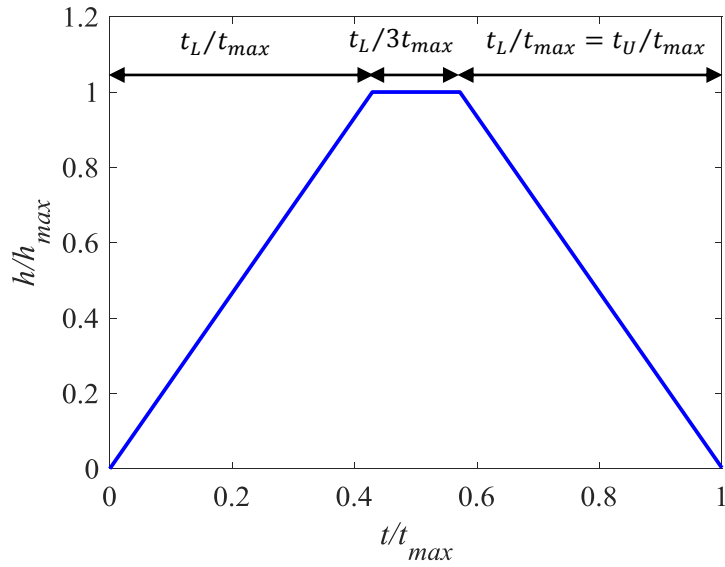


Figure 2.12. Normalized time-displacement curve for trapezoidal loading with $t_L = t_U$.

2.4.3. Exponential

In this section, nanoindentation exponential tests are performed at depth of $h_{max} = 500$ nm using eight strain rates ($\dot{h}/h = 0.0104, 0.0207, 0.1036, 0.2072, 0.5179, 1.0359, 2.0722$ and 4.1458 s^{-1}). The loading and unloading segments have the same time for each strain rate (Figure 2.13). This loading type is widely used for the indentation of viscous materials. Varying the strain rate allows to show the dependence of the material behavior.

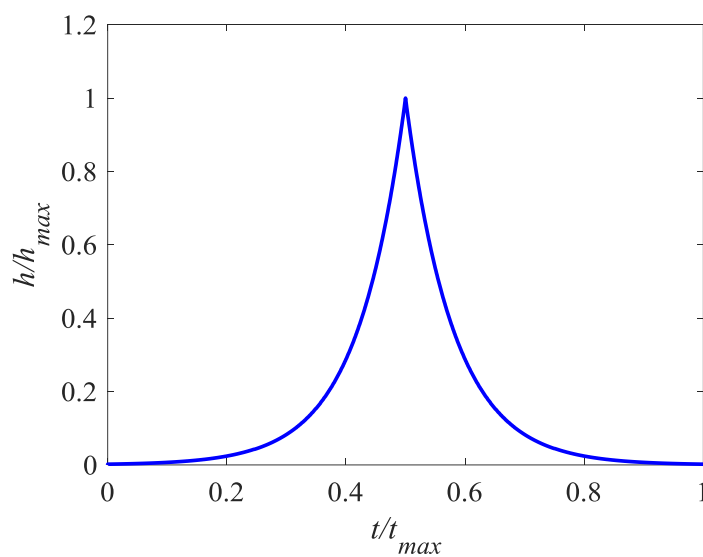


Figure 2.13. Normalized time-displacement curve for exponential loading.

2.4.4. Sinusoidal

A monotonic loading test is conducted to a maximum depth of $h_{max} = 510$ nm over a loading time of 30 s with superimposed sinusoidal loading at an amplitude $0.01 \mu\text{m}$ and a frequency of 4 Hz. In Figure 2.14, the time-displacement curve and a zoom showing the sinusoidal signal are displayed. This test will be used for the identifiability analysis and compared with the triangular loading.

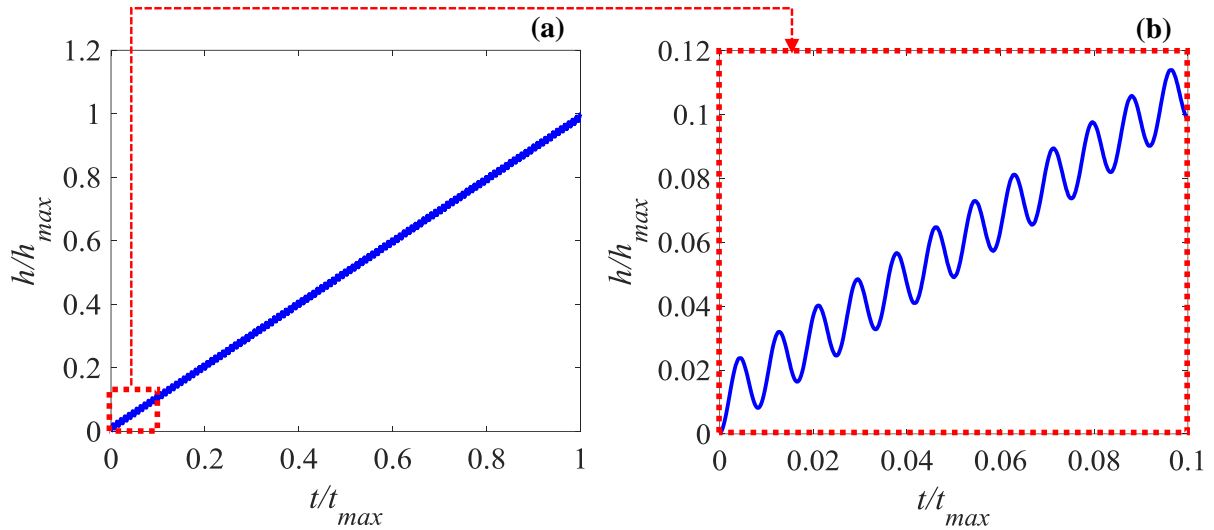


Figure 2.14. (a) Normalized time-displacement using sinusoidal loading. (b) Zoom.

2.5. Macro tests

During this thesis, tensile tests have been performed using PP dumbbell-shaped specimens with useful zone (20 mm x 4 mm x 0.5 mm) in order to validate the identified behavior laws for material properties. Figure 2.15 shows the repetitive progressive loading test carried out at 2 N/s. The full-field strains have been measured by the technique of digital image correlation (DIC). These data are to be compared with the numerical results obtained using the identified behavior laws (Chapter 4.7, Chapter 5.2 and Chapter 5.3).

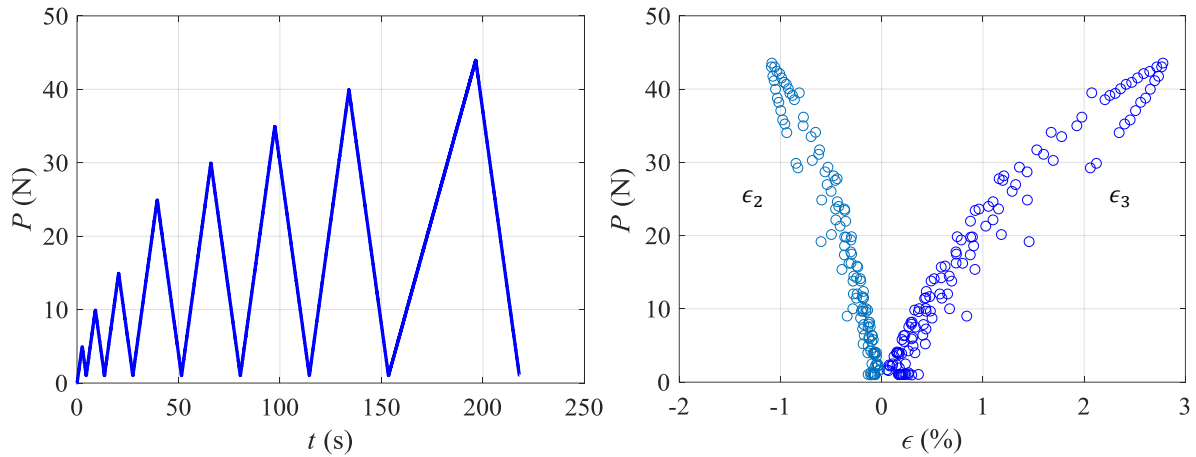


Figure 2.15. Repetitive progressive loading test performed at 2 N/s.

2.6. Conclusion

In this chapter, the nanoindentation was presented as method widely used to characterize the mechanical properties of bulk and thin film materials. The materials, the nanoindentation device and the experimental measurements were introduced. The pseudo-experimental tests allowed to design nanoindentation experiments that ensure the robustness of the intrinsic properties extraction were also detailed.

In this thesis, we examine the mechanical properties of PP and the FEMU method presented in Chapter 3 is chosen. For that, the experimental tests performed on PP samples at 1000 nm/min with Berkovich indenter tip and 500 nm/min with Berkovich and cube corner indenter tips will be employed. Several behavior laws, namely viscoelastic (VE), viscoelastic-viscoplastic (VEVP) and viscoelastic-plastic (VEP) will be investigated in order to extract reliable and intrinsic properties (Chapters 4 and 5). In the next chapter, the FEMU method and identifiability index will be described.

Identification of materials properties from nanoindentation experiments using FEMU and identifiability analysis

3.1.	Introduction	61
3.2.	FEM of the nanoindentation test	61
3.2.1.	Description of the FEM	61
3.2.2.	Convergence study of the FE method for the VE behavior	63
3.2.3.	Friction coefficient effect.....	66
3.3.	FEM updating process	67
3.3.1.	Objective function	68
3.3.2.	Minimization algorithm	68
3.3.3.	Parameters uncertainties	71
3.4.	Sensitivity analysis	74
3.5.	Identifiability index	79
3.6.	Conclusion.....	83

3.1. Introduction

In this chapter, the finite element models (FEM) in two-dimensional and three-dimensional used to simulate the nanoindentation test are presented. The finite element model updating method (FEMU) chosen in this work for the identification of material properties using viscoelastic (VE), viscoelastic-viscoplastic (VEVP) and viscoelastic-plastic (VEP) behaviors laws is described. A sensitivity analysis, which allows to determine the influence of model parameters on the nanoindentation results is detailed. Finally, an a priori identifiability index used to quantify the completeness of the nanoindentation data and design numerical experiments for better identification of materials properties is presented.

3.2. FEM of the nanoindentation test

The finite element method is a numerical approach widely used to analyze and predict the nanoindentation load-displacement curve ($P-h$) of the bulk and thin film materials. We have discussed in the first chapter the performances of this approach in nanoindentation field. In this section, the characteristics of the FEM used in this thesis are detailed. The convergence study of the 2D FE model is performed for five conical indenter tips with equivalent half angles $\alpha = 42.28^\circ, 57^\circ, 60^\circ, 65^\circ$ and 70.3° using the VE behavior law. The effect of the friction coefficient on the ($P-h$) curve is also investigated.

3.2.1. Description of the FEM

In this work, two parametric two-dimensional (2D) axisymmetric and three-dimensional (3D) FEM are constructed using the ANSYS commercial software, (FE software Ansys 16.0, 2016). In Figure 3.1, the 2D-axisymmetric FEM, which allows the simulation of the nanoindentation test using material that exhibit VE, VEVP and VEP behaviors is presented. Five conical indenter tips are used, with half angles of $\alpha = 42.28^\circ, 57^\circ, 60^\circ, 65^\circ$ and 70.3° and are assumed to be rigid. The indenters 42.28° and 70.3° correspond to the axisymmetric equivalent cones of the cube corner and Berkovich indenter tips used experimentally (Fischer, 2002; Chen et al., 2007). The Coulomb's friction law is used to model the contact between the surfaces. Linear quadrangular elements with 4 nodes (Q4 PLANE182) are used. The size of the modeled sample is 60 times greater than the maximum nanoindentation depth h_{max} in order to render realistic boundary conditions. The nodes belonging to the lower surface of the part of the modeled sample are clamped. The mesh size in the area right below the indenter is made finer than in the rest of the sample over a length 8 times greater than the h_{max} , which makes possible to model the contact and to increase the precision of the result of the simulation. The mesh is progressively coarser when moving away from the indented area, making it possible to reduce the number of elements and thus reduce the computation time. The size of the elements m below the indenter and the elements number in the model depend on a factor d ($m = h_{max}/d$). The test is simulated by two subsequent

parts: loading and unloading. During the loading part, the tip penetrates the specimen up to the h_{max} ; during the unloading part, the tip returns to the initial position. The loading and unloading times depends of the nanoindentation depth rate. In each simulation, the Newton-Raphson method requires 1 to 5 iterations at each time step to converge.

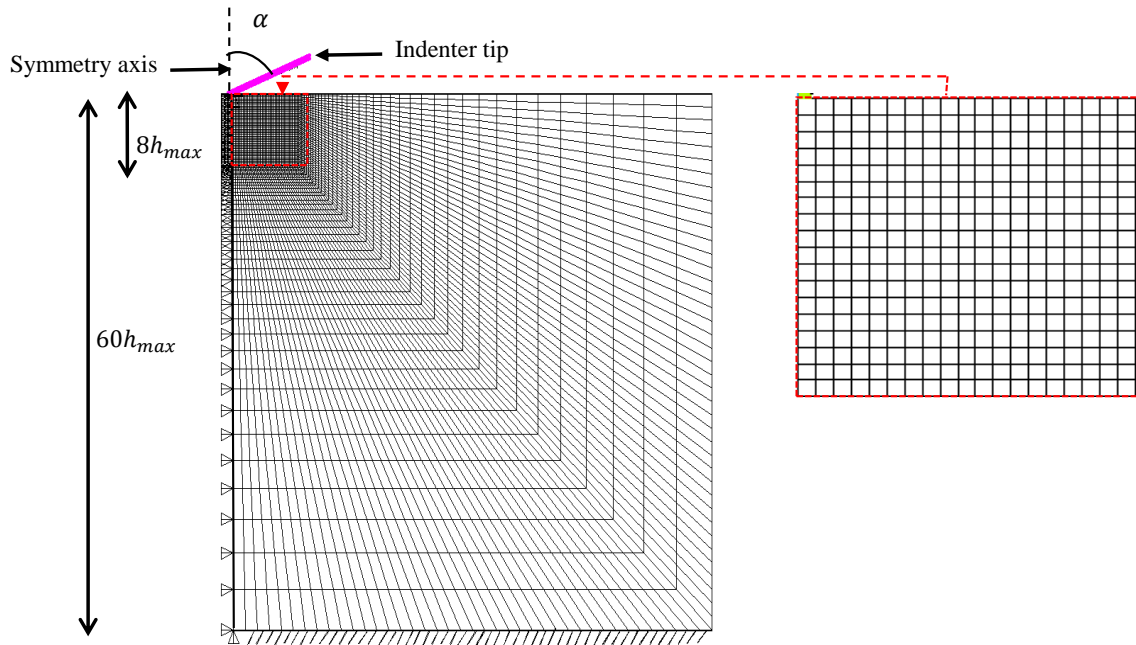


Figure 3.1. 2D-axisymmetric FEM of the nanoindentation test with Berkovich indenter tip with $d = 5$.

The 3D FEM is built in this work to achieve higher accuracy in the simulations of the nanoindentation test (Figure 3.2). In the 3D numerical simulations, FEM with conical and Berkovich indenter tips are considered. These indenter tips are modeled as rigid solids and representing a sixth of their complete geometries. The 3D Berkovich indenter tip corresponds to a three-sided pyramid with inner angle of 65.3° . Reducing the size of the 3D model to a sixth of its real volume allows a substantial reduction in the elements number and thus decreases the computational time. 3D 8-node hexahedral elements (SOLID185) and 3D 10-node tetrahedral elements (SOLID187) are used. The mesh size in the area right below the indenter is made finer than in the rest of the sample over a length 10 times greater than the h_{max} . The model has about 39.000 finite elements. The nodes belonging to the lower surface of the part of the modeled sample are clamped. The benefit of using the 2D-axisymmetric FEM is that it requires less computation time compared to the 3D FEM. The results obtained using both models will be compared in Chapter 4 for the viscoelastic behavior.

The computation time for the updating process depends on the FEM, constitutive behavior law and the equipment used in the calculation. The department of applied mechanics (DMA) possess a cluster

with 12 computation nodes: 7 bi-processors 4 cores (36 Go RAM), 1 bi-processors 6 cores (64 Go RAM), 2 bi-processors 8 cores (64 Go RAM) and 2 bi-processors 10 cores (96 Go RAM). For example, the updating process using the 2D-axisymmetric FEM with Berkovich indenter tip for the VE behavior lasts about 24 hours. In the case of 3D FEM, one numerical simulation takes 8 hours and is very expensive in terms of data storage. The VEVP and VEP behaviors will not be studied using the 3D FEM in this thesis.

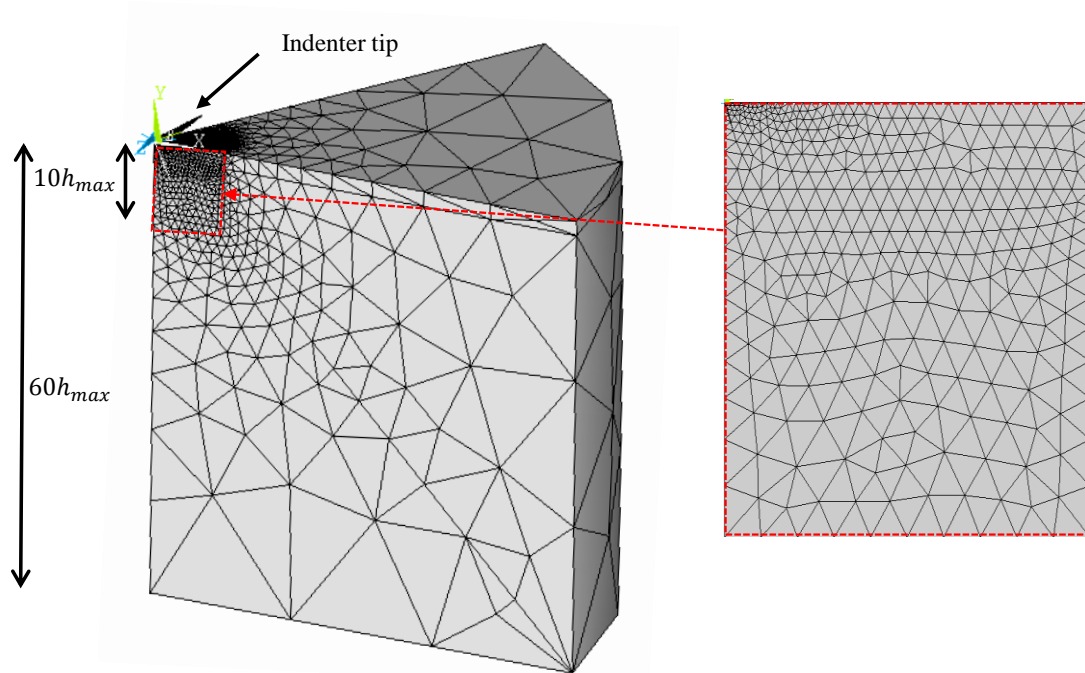


Figure 3.2. 3D FEM of the conical nanoindentation.

3.2.2. Convergence study of the FE method for the VE behavior

The convergence of the FE method is studied for the 2D-axisymmetric VE behavior using the several indenter tips with equivalent half angles of 42.28° (cube corner), 57° , 60° , 65° and 70.3° (Berkovich). In order to assess the influence of the mesh type on the simulated results, several simulations with refined meshes and time increments are performed using nanoindentation pseudo-experimental triangular test with depth rate of 500 nm/min (Chapter 2) for all indenter tips. Figure 3.3 shows the $P_{max}/P_{max}(d = 16)$ ratio for several mesh refinement when using the five equivalent half angles. The number of elements in the FEM and the computation using VE behavior are given in (Table 3.1). The viscoelastic behavior law with four parameters ($E = 1.47$ GPa, $c_1 = 0.94$ GPa, $\nu = 0.4$, $\eta = 17.08$ GPa.s) is used in the simulations. In Figure 3.4, Figure 3.5 and Figure 3.6, the ($P-h$) curves using the five indenter tips and varying the refinement factor are displayed. It can be seen that the ($P-h$) curves are disturbed during loading and unloading segments when the mesh below the indenter is too coarse.

These perturbations disappear when decreasing the size of the elements below the indenter. The small difference between the forces will probably affect the identifiability results. It is found that the force convergence is considered to be achieved from mesh with a factor $d = 10$ for the cube corner indenter, $d = 8$ for the indenter with equivalent half angle 57° , $d = 7$ for the indenter with 60° , $d = 6$ for the indenter 65° and $d = 5$ for Berkovich indenter. This means that increasing the half angle, the factor d decreases (Figure 3.7). The computation time for the simulation increases when the mesh size decreases. For example, a numerical simulation using mesh with $d = 16$ lasts 4h.

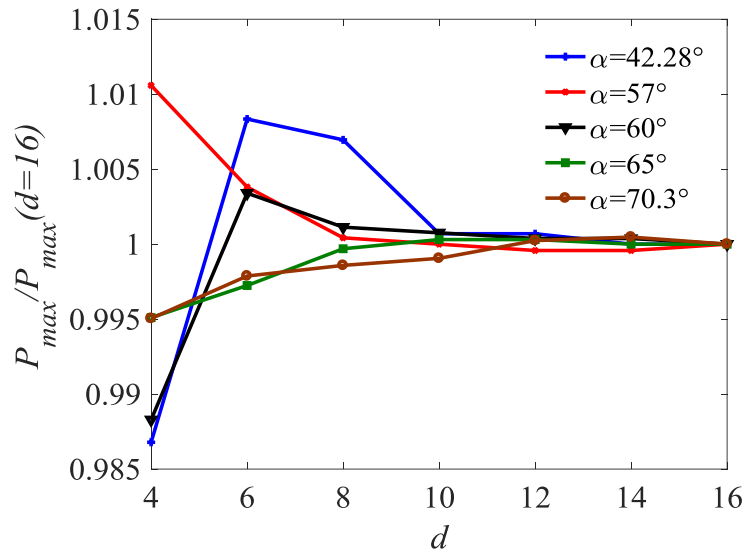


Figure 3.3. $P_{max}/P_{max}(d = 16)$ ratio for each mesh size using the five indenter tips.

Table 3.1. Elements number and the computation time for the 2D VE behavior using Berkovich indenter tip.

Factor d	Mesh						
	4	6	8	10	12	14	16
Elements number	3300	7200	12800	20000	28000	38000	50000
Elements in contact with the indenter tip	8	11	14	18	21	25	28
Computation time (h)	0.3	0.6	1	1.5	3	3.5	4

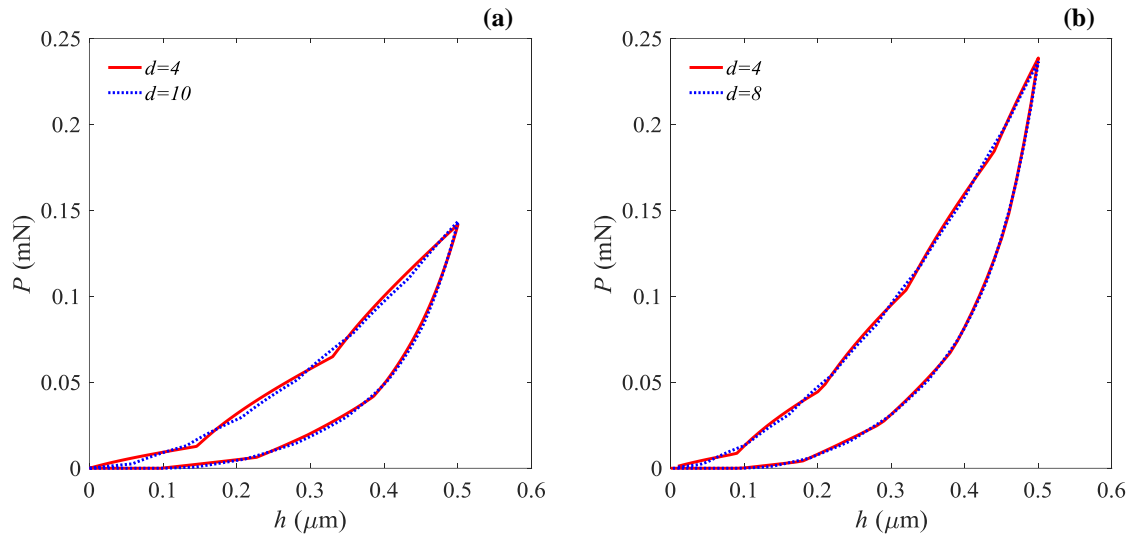


Figure 3.4. VE-Nanoindentation curves performed at 500 nm/min. (a) cube corner indenter tip 42.28° .
(b) Indenter tip with half angle 57° .

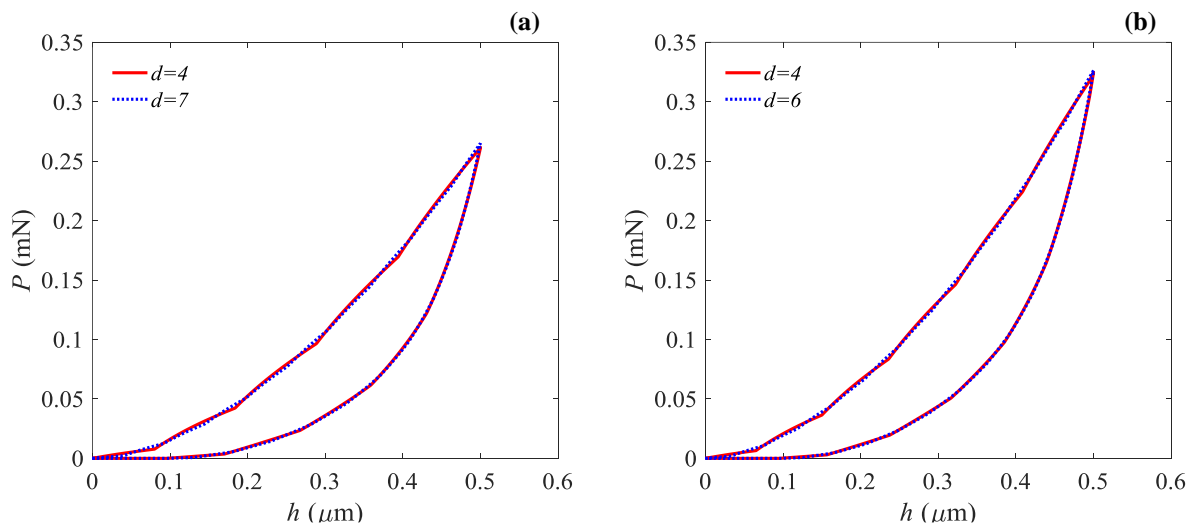


Figure 3.5. VE-Nanoindentation curves performed at 500 nm/min. (a) Indenter tip with half angle 60° .
(b) Indenter tip with half angle 65° .

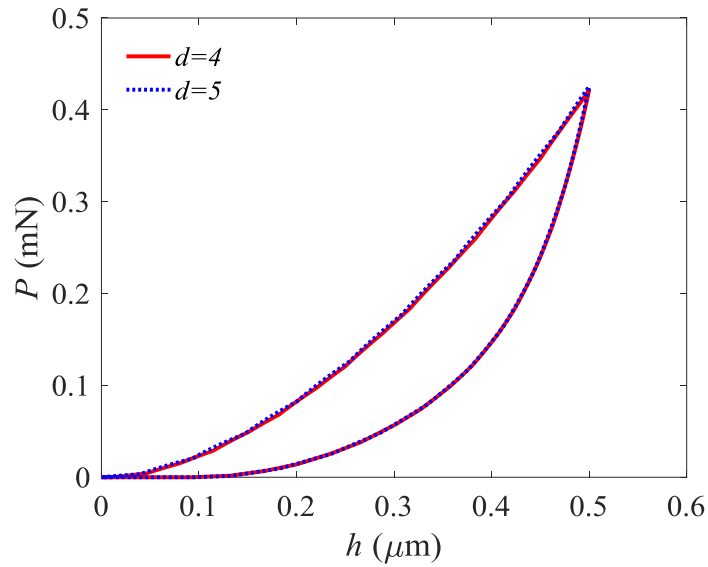


Figure 3.6. VE-Nanoindentation curves performed at 500 nm/min using Berkovich indenter tip 70.3° .

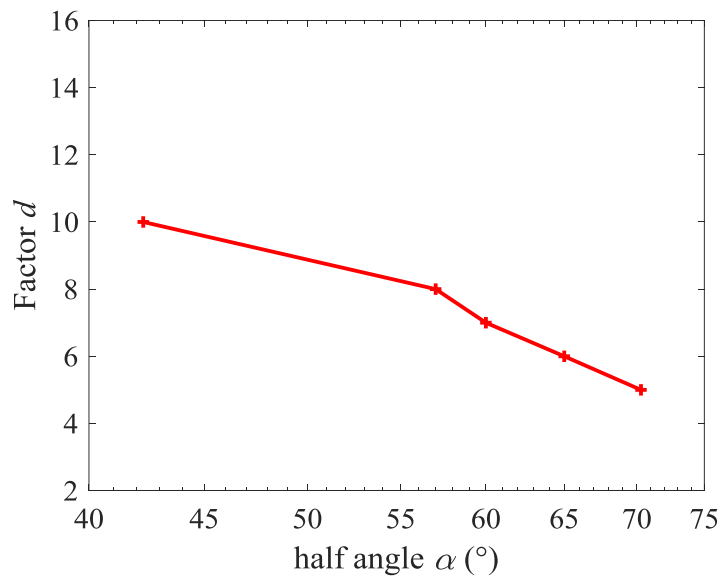


Figure 3.7. Factor d versus the indenter tip half angle α .

3.2.3. Friction coefficient effect

In this section, the influence of friction coefficient μ on the load-displacement curve has been investigated with different indenter geometries such as cube corner, Berkovich, spherical or Vickers indenter tips (Johnson, 1985; Bucaille et al., 2003; Mata and Alcalá, 2004; Huang and Pelegri, 2007). In Figure 3.8, we present the load-displacement curves obtained with friction coefficient values vary from 0.1 to 0.5 using nanoindentation triangular test performed at 500 nm/min with cube corner and

Berkovich indenter tips in the VE case. It is observed that the friction coefficient does not have a significant effect on the nanoindentation results. The influence of this parameter during nanoindentation measurement is considered negligible. In our work, the friction coefficient is set to 0.2.

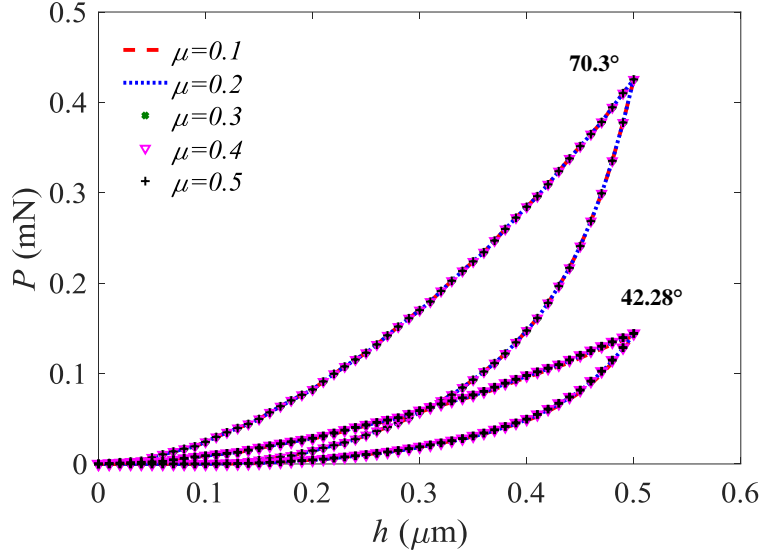


Figure 3.8. Effect of the friction coefficient on the nanoindentation force using cube corner and Berkovich indenter tips.

After presenting the 2D-axisymmetric and 3D FEM of the nanoindentation test, the Finite Element Model Updating method (FEMU) which is employed for the identification of material properties is detailed in the next section.

3.3. FEM updating process

In this section, the FEMU method used for the determination of material properties is presented. From a starting point $\boldsymbol{\theta}^{(0)}$ for the optimization algorithm, the method allows to estimate one or more parameters values $\hat{\boldsymbol{\theta}}$ which minimize the difference between the force $P(t; \boldsymbol{\theta})$ resulting from the FE simulation and the experimental data $P^{exp}(t)$. The inverse problem is formulated by the following equation:

$$\hat{\boldsymbol{\theta}} = \underset{\boldsymbol{\theta} \in \Theta}{\operatorname{argmin}} \omega [P(t; \boldsymbol{\theta}), P^{exp}(t)] \quad (3.1)$$

where ω is the objective function.

Once they lead to a good agreement between the numerical results and the experimental data, the procedure is stopped. In order to identify the material parameters for different behavior laws from nanoindentation response $y(t)$, the updating process of the numerical model based on the experimental (or pseudo-experimental) data is used. The computation time for an updating process depends on the starting point $\boldsymbol{\theta}^{(0)}$ and the number of parameters in the behavior law.

3.3.1. Objective function

The objective function ω is defined to quantify the difference between the numerical model and the experimental (or pseudo-experimental) data. When the nanoindentation test is displacement-controlled mode, the objective function is defined as (Qasmi et al., 2004):

$$\omega(\boldsymbol{\theta}) = \frac{1}{2T} \sum_{k=1}^T \left[\frac{P_k(\boldsymbol{\theta}) - P_k^{exp}}{P_{max}^{exp}} \right]^2 = \frac{1}{2} \mathbf{r}^T \mathbf{r} \quad (3.2)$$

$T = 1000$ is the number of data points for each nanoindentation test, i.e. number of measured force values $P_k(\boldsymbol{\theta}) = P(t_k; \boldsymbol{\theta})$ and $P_k^{exp} = P^{exp}(t_k)$, P_{max}^{exp} is the maximum of the experimental nanoindentation force and \mathbf{r} is the residues vector which represent the difference between the numerical and experimental responses. T is sufficiently large so that it does not influence the reported results. The period $\Delta t = t_{k+1} - t_k$ depends on the nanoindentation rate.

Note that if the nanoindentation test is force-controlled, the objective function is formulated using the displacement response $h(t; \boldsymbol{\theta})$, instead of $P(t; \boldsymbol{\theta})$.

As mentioned in chapter 1, many authors showed that using single nanoindentation $P-h$ curve does not lead to a unique solution of the inverse problem (Alkorta et al., 2005b; Kang et al., 2012; K.K. Tho et al., 2004) and that additional information is required (Bolzon et al., 2011, 2004; Kang et al., 2018). Consequently, combination of several nanoindentation tests performed at several nanoindentation rates with the same indenter tip and dual nanoindentation tests from the five indenter tips is used during this work, the total objective function is given by the sum of the objective functions of all tests.

$$\omega(\boldsymbol{\theta}) = \sum_{e=1}^n \left[\frac{1}{2T} \sum_{k=1}^T \left(\frac{P_k^{(e)}(\boldsymbol{\theta}) - P_k^{exp(e)}}{P_{max}^{exp(e)}} \right)^2 \right] = \frac{1}{2} \mathbf{r}^T \mathbf{r} \quad \mathbf{r}: T \times n \quad (3.3)$$

where n is the number of nanoindentation tests.

3.3.2. Minimization algorithm

The objective function (Equation 3.2 and 3.3) is minimized by a local numerical optimization technique based on the Levenberg-Marquardt algorithm (Levenberg, 1944; Marquardt, 1963) implemented in MIC2M software (Modélisation et Identification du Comportement Mécanique non

linéaire des Matériaux) (F. Richard, 2000). This algorithm is widely used in the identification of material properties using nanoindentation technique (Qasmi et al., 2004; Gamonpilas et al., 2010; Clément et al., 2013; Stan and Fetecau, 2013). It is an improvement of the classic Gauss-Newton method for solving nonlinear least-squares regression problems. The main advantage of this technique is the robustness and the rapid convergence (Richard, 2017).

Levenberg-Marquardt is an iterative nonlinear minimization method. Initiated at the starting point $\boldsymbol{\theta}^{(k)} = \boldsymbol{\theta}^{(0)}$, it is desired to find the vector $\boldsymbol{\theta}^{(k+1)} = \boldsymbol{\theta}^{(k)} + \mathbf{d}\boldsymbol{\theta}$ that best satisfies the estimated solution. Hence, at each step, it is required to determine the increment $\mathbf{h} = \mathbf{d}\boldsymbol{\theta}$ to approach the solution. A function $\tilde{\omega}$ is iteratively minimized, which approaches ω in the neighborhood of $\boldsymbol{\theta} = \boldsymbol{\theta}^{(k)}$:

$$\tilde{\omega} = \omega(\boldsymbol{\theta}) + \mathbf{T}\mathbf{g}\mathbf{h} + \frac{1}{2} \mathbf{T}\mathbf{h}\mathbf{H}\mathbf{h} \quad (3.4)$$

where $\mathbf{T}\mathbf{g}$ is the transpose of the gradient of ω defined as:

$$g_i = \frac{\partial \omega}{\partial \theta_i} \quad i = 1, \dots, n_\theta \quad (3.5)$$

where n_θ is the number of the parameters and \mathbf{H} is the hessian of the objective function ω in $\boldsymbol{\theta}$:

$$H_{ij} = \left. \frac{\partial^2 \omega}{\partial \theta_i \partial \theta_j} \right|_{\boldsymbol{\theta}} \quad i = 1, \dots, n_\theta \quad (3.6)$$

The quadratic approximation (Equation. 3.4) is minimized when its gradient is zero. This gives the expression of the increment \mathbf{h} :

$$\mathbf{h} = -\mathbf{H}^{-1}\mathbf{g} \quad (3.7)$$

The Gauss-Newton method facilitates the resolution and accelerates the descent to the optimized value of the objective function ω . Using single test, the coefficients of the jacobian matrix \mathbf{J} of the objective function ω are given by:

$$J_{kj} = \frac{\partial r_k}{\partial \theta_j} = \frac{1}{sc_k} \frac{\partial P_k}{\partial \theta_j} \quad k = 1, \dots, T; j = 1, \dots, n_\theta \quad (3.8)$$

where sc_k is a scale factor associated to the force $P_k(\boldsymbol{\theta})$. If an absolute uncertainty is considered on each force increment $P(t_k)$, this factor can be written as (Richard, 2017):

$$sc_k = \sqrt{T} \left| \max_k P(t_k) \right| \quad (3.9)$$

The gradient can be defined as follows:

$$\mathbf{g} = {}^T \mathbf{J} \mathbf{r} \quad (3.10)$$

and the components are:

$$g_i = \sum_{k=1}^T \frac{\partial r_k}{\partial \theta_i} r_k = \sum_{k=1}^T \frac{1}{sc_k} \frac{\partial P_k}{\partial \theta_i} r_k \quad i = 1, \dots, n_\theta \quad (3.11)$$

For several nanoindentation tests, the equation 3.11 becomes:

$$g_i = \sum_{e=1}^n \sum_{k=1}^T \frac{\partial r_k^{(e)}}{\partial \theta_i} r_k^{(e)} = \sum_{e=1}^n \sum_{k=1}^T \frac{1}{sc_k^{(e)}} \frac{\partial P_k^{(e)}}{\partial \theta_i} r_k^{(e)} \quad i = 1, \dots, n_\theta \quad (3.12)$$

The approximation of the gradient \mathbf{g} and the hessian matrix \mathbf{H} can be obtained from the Gauss-Newton matrix \mathbf{G} :

$$\mathbf{H} \approx \mathbf{G} = {}^T \mathbf{J} \mathbf{J} \quad (3.13)$$

Using the finite difference scheme, the components of the matrix \mathbf{H} can be formulated as:

$$H_{ij} \approx \sum_{e=1}^n \sum_{k=1}^T \left[\frac{1}{sc_k^{(e)}} \frac{\partial P_k^{(e)}}{\partial \theta_i} \frac{\partial P_k^{(e)}}{\partial \theta_j} \right] \quad (3.14)$$

If the nanoindentation test (e) is force-controlled, the components of the matrix \mathbf{H} are formulated using the displacement vector $h_k^{(e)}$ instead of $P_k^{(e)}$.

This approximation is valid in the following cases:

- ω is low in the neighborhood of convergence, because the Gauss-Newton matrix becomes close to the Hessian.
- ω is inhomogeneous, which amounts to assuming that the Gauss-Newton matrix depends on the point $\boldsymbol{\theta}$.

In the case where these conditions are not satisfied, badly conditioned matrices can be obtained. In order to improve the convergence, Marquardt (Marquardt, 1963) used a damping parameter λ proposed by Levenberg (Levenberg, 1944) for the least squares problems. Their strategy is based on the division of the value of λ by 10 in each iteration and increase it by successive multiplication by 10 when the objective function does not decrease.

$$\underline{\mathbf{h}} = -[\underline{\mathbf{H}} + \lambda \mathbf{I}]^{-1} \underline{\mathbf{g}} \quad (3.15)$$

$$\underline{H}_{ij} = \frac{H_{ij}}{\sqrt{H_{ii}H_{jj}}}; \underline{g}_i = \frac{g_i}{\sqrt{H_{ii}}} \quad i, j = 1, \dots, n_\theta$$

Therefore, the increment \mathbf{h} is obtained as follows:

$$\underline{h}_i = \frac{h_i}{\sqrt{H_{ii}}} \quad (3.16)$$

In order to avoid that the vector $\boldsymbol{\theta} + \mathbf{h}$ leaves the imposed domain Θ , an additional condition is taken into account. It consists to multiply λ by 10 when $(\boldsymbol{\theta} + \mathbf{h}) \notin \Theta$. The implementation of the algorithm consists of iteratively repeating the following steps:

- Choose a starting point $\boldsymbol{\theta}$;
- Calculate the objective function $\omega = \omega(\boldsymbol{\theta})$;
- Let $\lambda = 10^{-3}$, $\|\mathbf{d}\boldsymbol{\theta}\| = d\omega = 0$, $\sigma = 10^{-3}$ (data uncertainty);
- Repeat the computation as long as $\|\mathbf{d}\boldsymbol{\theta}/\boldsymbol{\theta}\| > 10^{-3}$ and $|d\omega|/\omega > 10^{-3}$ or $\omega > \sigma^2 N_v/2$;
 - I. Update the jacobian matrix $\mathbf{J}(\boldsymbol{\theta})$;
 - II. Update the hessian \mathbf{h} and the parameter λ ;
 - III. Calculate the objective function $\omega = \omega(\boldsymbol{\theta} + \mathbf{h})$;
 - IV. Evaluate ω , If $\omega(\boldsymbol{\theta} + \mathbf{h}) > \omega(\boldsymbol{\theta})$ or $(\boldsymbol{\theta} + \mathbf{h}) \notin \Theta$: $\lambda = 10\lambda$, return to II;
 - V. $\lambda = \lambda/10$, $\mathbf{d}\boldsymbol{\theta} = \mathbf{h}$, $d\omega = \omega(\boldsymbol{\theta} + \mathbf{h}) - \omega(\boldsymbol{\theta})$;
 - VI. $\boldsymbol{\theta} = \boldsymbol{\theta} + \mathbf{d}\boldsymbol{\theta}$, $\omega = \omega(\boldsymbol{\theta})$;
- Stop if the algorithm leads $\hat{\boldsymbol{\theta}} = \boldsymbol{\theta}$.

The principal advantage of this algorithm is the convergence speed. It is very important to start from an initial point, which is close to the solution to identify because the algorithm may converge to a local minimum if it begins far. The uniqueness of this solution is one of the major issues in nanoindentation field.

3.3.3. Parameters uncertainties

The uncertainty $\Delta\theta_j$ on the estimated value of the parameter θ_j after the updating process using single nanoindentation test can be obtained from the following equation in $\theta_j = \hat{\theta}_j$:

$$\frac{\Delta\theta_j}{\theta_j} = \sqrt{2\omega[\bar{\mathbf{H}}^{-1}]_{jj}} \quad (3.17)$$

where $\bar{\mathbf{H}}$ is a dimensionless pseudo-hessian matrix computed by forward finite difference method (Pac et al., 2014; Richard et al., 2013). For single test, the components of $\bar{\mathbf{H}}$ are given as:

$$\bar{H}_{ij} = \frac{1}{T} \frac{\theta_i \theta_j}{P_{max}^2} \sum_{k=1}^T \frac{\partial P_k(\boldsymbol{\theta})}{\partial \theta_i} \frac{\partial P_k(\boldsymbol{\theta})}{\partial \theta_j} \quad i, j = 1, \dots, n_\theta \quad (3.18)$$

where P_{max} is the maximum of the numerical nanoindentation force.

In the case of an updating process using several nanoindentation tests, the uncertainty becomes:

$$\frac{\Delta\theta_j}{\theta_j} = \sqrt{\frac{2}{n} \omega[\mathbf{H}^{-1}]_{jj}} \quad (3.19)$$

and the pseudo-hessian matrix \mathbf{H} is calculated from the following equation:

$$\bar{H}_{ij} = \sum_{e=1}^n \left[\frac{1}{T} \frac{\theta_i \theta_j}{(P_{max}^{(e)})^2} \sum_{k=1}^T \frac{\partial P_k^{(e)}(\boldsymbol{\theta})}{\partial \theta_i} \frac{\partial P_k^{(e)}(\boldsymbol{\theta})}{\partial \theta_j} \right] \quad i, j = 1, \dots, n_\theta \quad (3.20)$$

In order to illustrate the updating process, experimental data from the nanoindentation test realized on PP at 1000 nm/min with Berkovich indenter tip using the triangular loading are used in Equation 3.1 for the viscoelastic behavior law (E, c_1, ν, η) . A starting point $\boldsymbol{\theta}^{(01)}$ is chosen to initialize the minimization algorithm (Table 3.2) and to solve the minimization problem. This procedure requires about 40 FE simulations (height iterations and five simulations for each one). Figure 3.9 illustrates the convergence of the objective function. The evolution of the four parameters during the minimization process is shown in Figure 3.10. The $P-h$ curves obtained using the starting point and the estimated solution are plotted in Figure 3.11. The curve obtained with the estimated solution is in good agreement with the experimental one.

Table 3.2. Estimated parameters set $\hat{\boldsymbol{\theta}}$ (Equation 3.1) and uncertainties (Equation 3.17).

	Parameter	Starting value	Estimated value	Uncertainty
j	θ_j	$\theta_j^{(01)}$	$\hat{\theta}_j$	$\Delta\theta_j/\theta_j$ (%)
1	E (GPa)	1.50	1.63	7.0
2	c_1 (GPa)	12.25	1.05	6.0
3	ν	0.4	0.13	90
4	η (GPa.s)	65	18.56	15
		4.59×10^{-2}	1.24×10^{-5}	

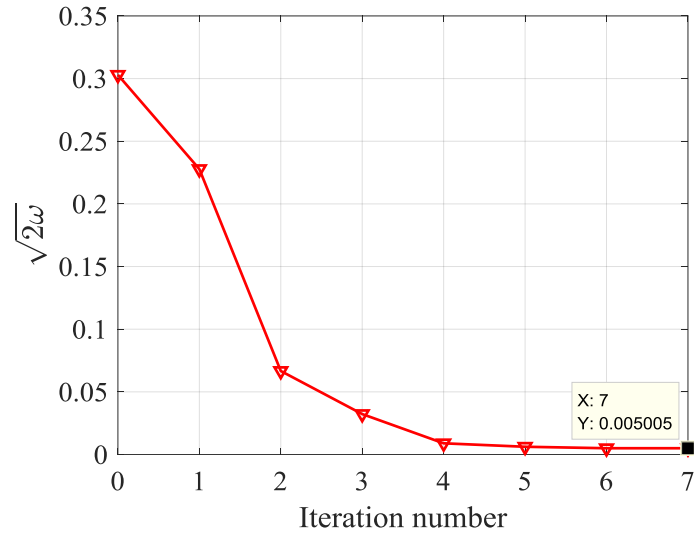


Figure 3.9. Convergence of the objective function $\sqrt{2\omega}$ during the updating process.

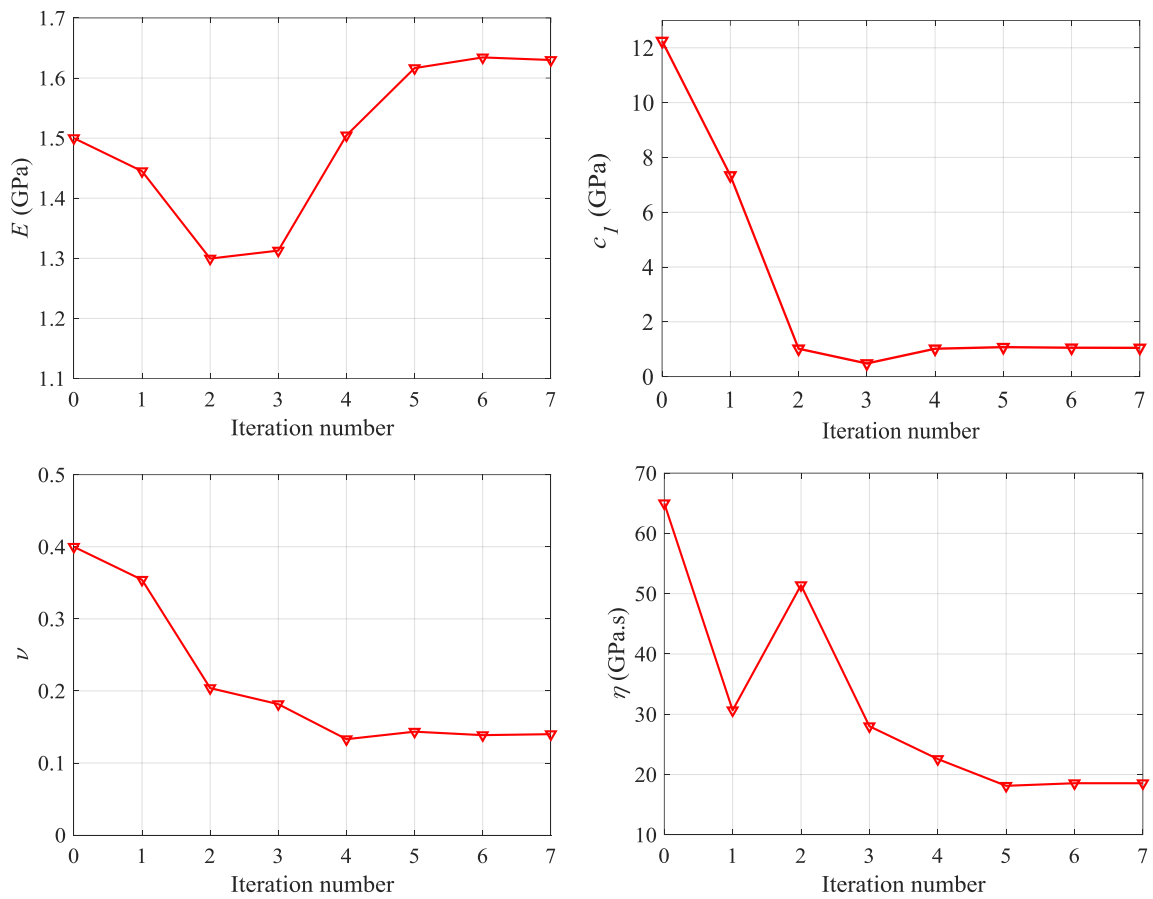


Figure 3.10. Evolution of the four parameters (E , c_1 , ν , η) during the updating process using starting point

$$\boldsymbol{\theta}^{(01)} = (E = 1.5 \text{ GPa}, c_1 = 12.25 \text{ GPa}, \nu = 0.4, \eta = 65 \text{ GPa.s}).$$

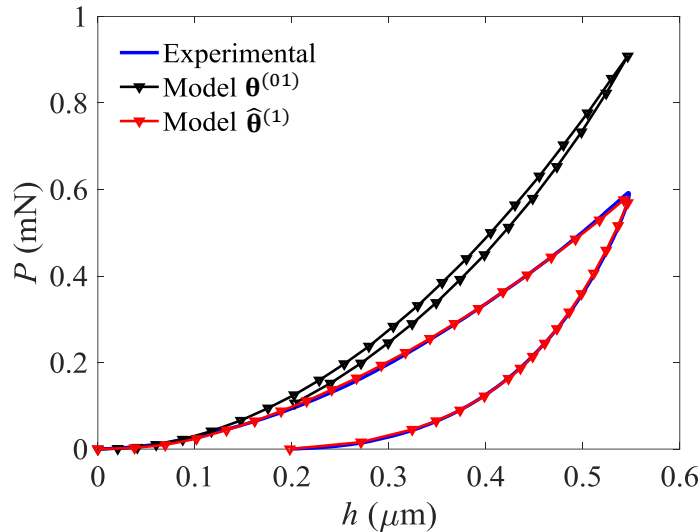


Figure 3.11. Experimental ($\dot{h} = 1000$ nm/min) and simulated nanoindentation curves for the starting point $\theta^{(01)} = (E = 1.5$ GPa, $c_1 = 12.25$ GPa, $\nu = 0.4$, $\eta = 65$ GPa.s) and the estimated solution $\hat{\theta}^{(1)} = (E = 1.63$ GPa, $c_1 = 1.05$ GPa, $\nu = 0.13$, $\eta = 18.56$ GPa.s).

Several updating process are also performed using VE, VEVP and VEP behavior laws and the results will be presented in Chapter 4 and 5. The present study pretends to investigate the stability of the material properties obtained by using the updating process of the FEM on the nanoindentation response. The uniqueness of the parameters of VE, VEVP and VEP behaviors laws will be studied (Chapter 4 and 5). The parameters uncertainties for different behavior laws will be also quantified. These uncertainties are an important indicator of the parametric identifiability after the updating process. Indeed, the results can be disappointing despite the very good agreement between estimated solution and the experimental data. The completeness of data contained in the nanoindentation force will be quantified by an identifiability index that allows to know a priori the better identifiability of the material properties. In the next section, sensitivity analysis which allows to quantify the effect of the behavior law parameters on the nanoindentation response $y(t)$ is presented.

3.4. Sensitivity analysis

The sensitivity analysis plays an important role in the identification procedures. It is usually performed to evaluate how, and to which extent, variations of the behavior law input data (material parameters values for example) influence the output data (in our case the force or displacement response as a function of time). It also assesses the parameters identifiability and provides a basis for the design of the experiments. In nanoindentation field, Bolzon et al. and Bocciarelli et al. used the sensitivity analysis to show the accuracy of the approach proposed for the identification of the material parameters from the nanoindentation curves and the imprint mapping (Bolzon et al., 2004; Bocciarelli et al., 2005;

Bocciarelli and Bolzon, 2007). Magnenet et al. studied the sensitivity of the Drucker–Prager elasto-plastic behavior using nanoindentation load-displacement curves performed with five indenter shapes: spherical, conical, cylindrical, tetrahedral and pyramidal (Magnenet et al., 2008). Three sensitivity analysis methods are generally used in mechanical problems namely, the Direct Differentiation Method (DDM) (Huang and Lu, 2007), the Adjoint State Method (ASM) (Zhang et al., 2007) and the Finite Difference Method (FDM) (Bolzon et al., 2004; Magnenet et al., 2008) which is employed in this work.

In the case of single nanoindentation test, the sensitivity matrix \mathbf{S} whose coefficients S_{kj} describe the sensitivity of the nanoindentation force P_k to the parameter θ_j . This matrix has dimension of $T \times n_\theta$ and is obtained by considering n_θ sensitivity vectors \mathbf{S}_j :

$$\mathbf{S} = [\mathbf{S}_1 \ \mathbf{S}_2 \ \mathbf{S}_3 \ \dots \ \mathbf{S}_{n_\theta}] \quad (3.21)$$

Using a finite difference scheme, the components of sensitivity vectors \mathbf{S}_j are given by (for a single nanoindentation test):

$$S_{kj} = \frac{\theta_j}{P_{max}} \frac{\partial P_k}{\partial \theta_j} \approx \frac{(1 + \varepsilon)\theta_j}{P_{max}} \frac{\partial P_k}{\partial \theta_j} \quad (3.22)$$

where P_k is the nanoindentation force at time t_k , $\theta_j (j = 1, \dots, n_\theta)$ are the number of the material parameters which depends on the behavior law, ε is the perturbation and P_{max} is the maximal nanoindentation force.

The sensitivity δ_j of the nanoindentation force to the parameter θ_j can be computed as:

$$\delta_j = \frac{\theta_j}{P_{max}} \sqrt{\frac{1}{T} \sum_{k=1}^T \left(\frac{\partial P_k}{\partial \theta_j} \right)^2} \quad (3.23)$$

When the nanoindentation test is force-controlled, the same analysis is performed using the displacement response $h(t; \boldsymbol{\theta})$, instead of $P(t; \boldsymbol{\theta})$.

In the case of combination of several nanoindentation tests, the Equation 3.22 and 3.23 become:

$$S_{kj} = \sum_{e=1}^n \frac{\theta_j}{P_{max}^{(e)}} \frac{\partial P_k^{(e)}}{\partial \theta_j} \approx \sum_{e=1}^n \frac{(1 + \varepsilon)\theta_j}{P_{max}^{(e)}} \frac{\partial P_k^{(e)}}{\partial \theta_j} \quad (3.24)$$

$$\delta_j = \sum_{e=1}^n \frac{\theta_j}{P_{max}^{(e)}} \sqrt{\frac{1}{T} \sum_{k=1}^T \left(\frac{\partial P_k^{(e)}}{\partial \theta_j} \right)^2} \quad (3.25)$$

As mentioned in the section 3.2.2, the convergence is obtained using mesh size with a factor $d = 10$ for the cube corner indenter and $d = 5$ for Berkovich indenter tip. In order to investigate the effect of the relative perturbation ε , a sensitivity analysis to the four parameters of the VE behavior law (E, c_1, ν, η) using the pseudo-experimental triangular test realized at 500 nm/min in displacement-controlled mode for cube corner and Berkovich indenter tips with several values of $\varepsilon \in [10^{-1}, 10^{-3}]$ is performed. The value of each parameter is changed by a relative perturbation ε with respect to its initial value. The computation time of this analysis is 7.5 hours for the cube corner indenter tip and 2.5 hours for the Berkovich one. In Figure 3.12 and Figure 3.13, the sensitivity vectors of the nanoindentation force to the behavior law parameters calculated by finite difference (Equation 3.22) using the solution ($E = 1.47$ GPa, $c_1 = 0.94$ GPa, $\nu = 0.4$, $\eta = 17.08$ GPa.s) and four perturbation values are presented. It can be observed that the noise amplitude decreases when the ε value increases and there is gaps between the vectors. For example, the difference between the maximum values of the sensitivity vectors is about 0.035 for c_1 and 0.011 for η for both indenter tips. It is essential to investigate if these differences and the noise amplitude will affect or no the identifiability results.

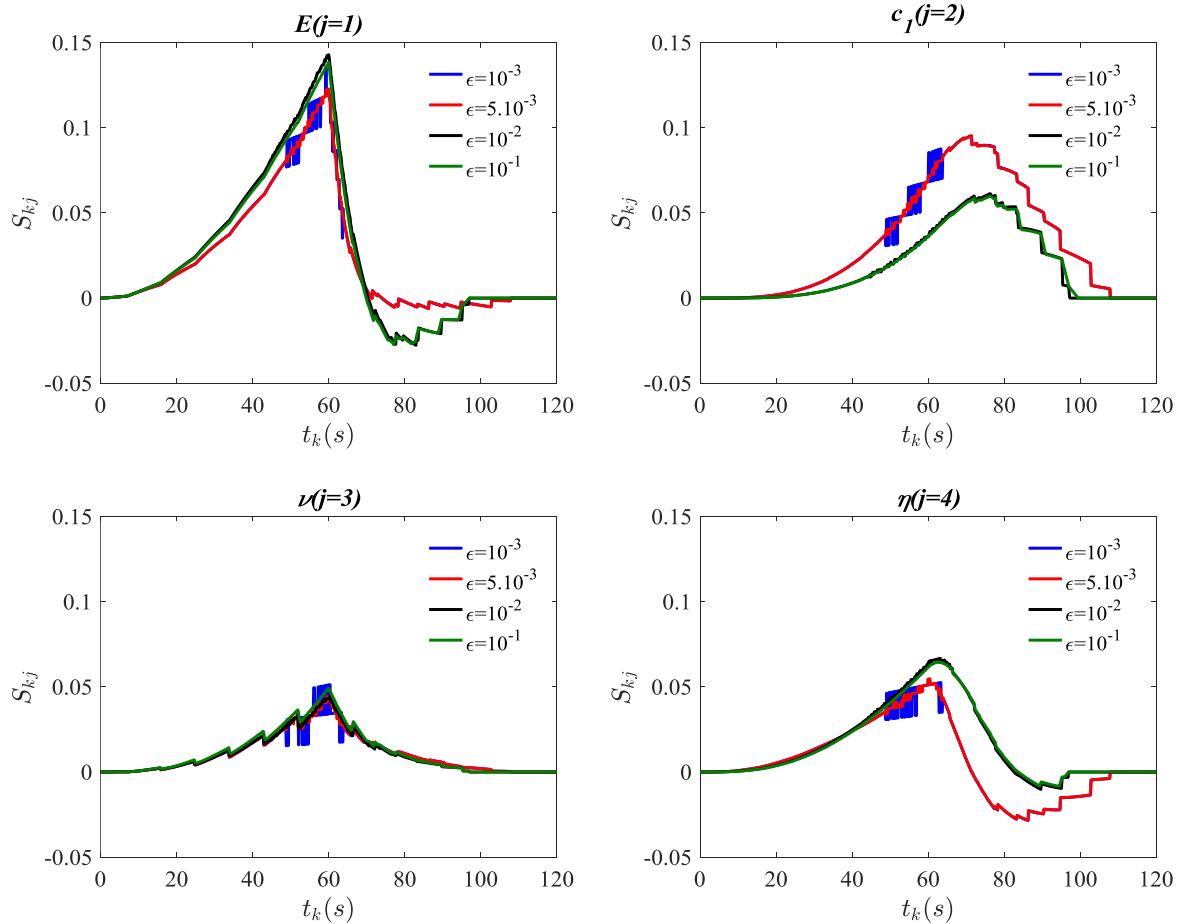


Figure 3.12. Effect of the relative perturbation ε on the sensitivity results using the solution ($E = 1.47$ GPa, $c_1 = 0.94$ GPa, $\nu = 0.4$, $\eta = 17.08$ GPa.s) with cube corner indenter tip.

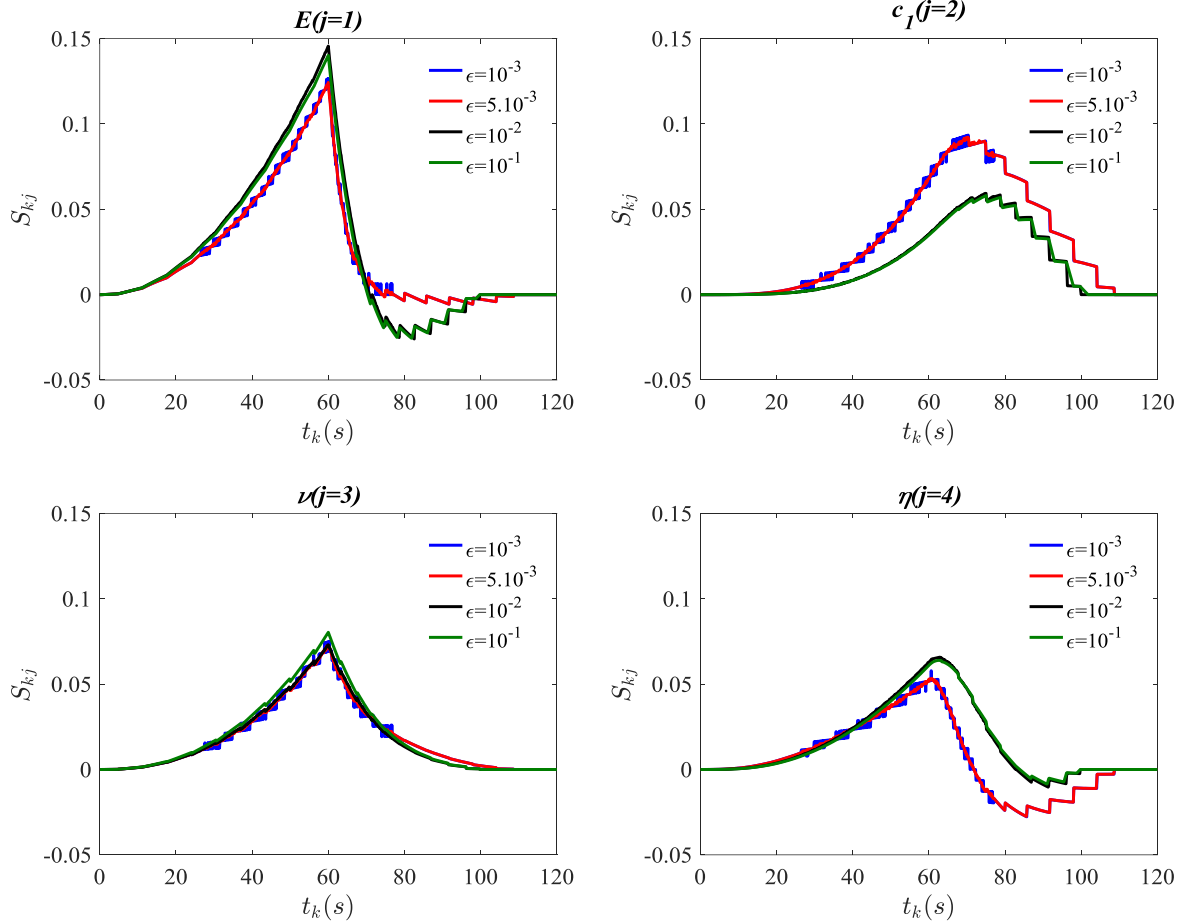


Figure 3.13. Effect of the relative perturbation ϵ on the sensitivity results using the solution ($E = 1.47$ GPa, $c_1 = 0.94$ GPa, $\nu = 0.4$, $\eta = 17.08$ GPa.s) with Berkovich indenter tip.

In this paragraph, the smoothing procedure used to examine the effect of the noise amplitude on the identifiability results is described. The local regression method (loess) based on the weighted linear least squares and second-degree polynomial model is employed. This method requires a smoothing parameter which defines a window of neighboring points to include in the smoothing computation for each data point, less than or equal to 1. A large smoothing parameter increases the smoothness but decreases the resolution of the smoothed data set, while a small smoothing parameter decreases the smoothness but increases the resolution of the smoothed data set. In Figure 3.14, the sensitivity vectors computed using nanoindentation test performed at 1000 nm/min with Berkovich indenter tip for the solution ($E = 1.47$ GPa, $c_1 = 0.94$ GPa, $\nu = 0.4$, $\eta = 17.08$ GPa.s) with relative perturbation $\epsilon = 10^{-3}$ are plotted. The smoothing parameter used in this case is 0.08. As we can see, these vectors are disturbed during the two last third of the loading segment and the two first third of the unloading segment. These noises are mainly caused by numerical problems due to the contact between the indenter tip and the sample.

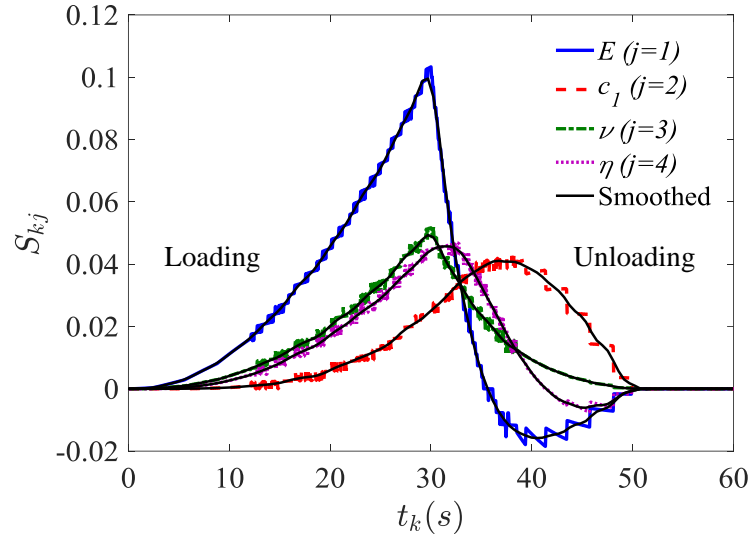


Figure 3.14. Sensitivity vectors of nanoindentation force to the material parameters θ_j during loading and unloading segments before and after smoothing using nanoindentation test performed at 1000 nm/min with Berkovich indenter tip for the solution ($E = 1.47$ GPa, $c_1 = 0.94$ GPa, $\nu = 0.4$, $\eta = 17.08$ GPa.s).

In Figure 3.15, we display the sensitivity vectors of the nanoindentation force to the four parameters calculated using the nanoindentation tests carried out at 500 nm/min with equivalent cube corner and Berkovich indenter tips for the same solution. In this analysis, a relative perturbation $\varepsilon = 10^{-3}$ is considered. The local regression method (loess) is then used to smooth the vectors. The smoothing parameters used in this case are 0.16 for the cube corner indenter and 0.1 for the Berkovich indenter. It is observed that the noise amplitude is more important for cube corner indenter tip than Berkovich one.

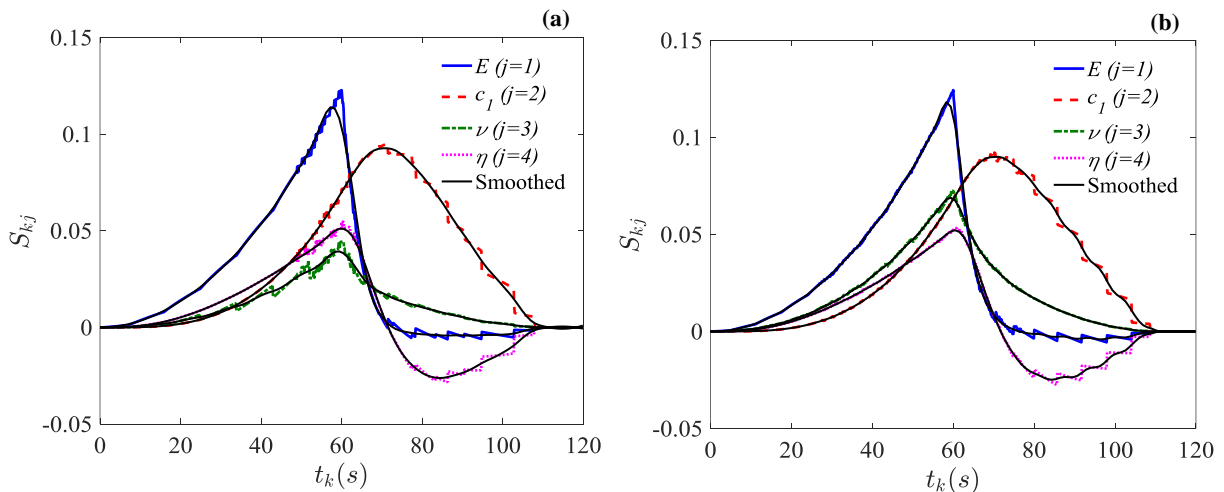


Figure 3.15. Sensitivity vectors of the nanoindentation force to the material parameters θ_j during loading and unloading after and before smoothing using nanoindentation test performed at 500 nm/min for the solution ($E = 1.47$ GPa, $c_1 = 0.94$ GPa, $\nu = 0.4$, $\eta = 17.08$ GPa.s). (a) cube corner indenter tip. (b) Berkovich indenter tip.

In this work, the sensitivity analysis is firstly performed using the VE behavior law (Chapter 4) in order to evaluate the effect of the parameters on the nanoindentation data from several loading types such as triangular, trapezoidal, exponential and sinusoidal with the five conical indenter tips. Then the effect of the parameters of the V EVP and VEP behavior laws is also examined (Chapter 5). The identifiability index based on the sensitivity matrix is presented in the next section.

3.5. Identifiability index

Herein, an identifiability index proposed to quantify the reliability of the behavior law parameters after or before the updating process of the nanoindentation test is presented. In this context, it is clear that an ill-posed inverse problem can hardly provide a unique solution. This problem was previously studied in plastic and elasto-plastic behaviors (Cao and Lu, 2004b; Phadikar et al., 2013). In this thesis, an identifiability index called *I*-index, developed by Richard et al (Richard et al., 2013) will be used to quantify the completeness of data contained in the nanoindentation data by conditioning the matrix $\bar{\mathbf{H}}$ (Equation 3.17 and 3.19). This *I*-index appears to be convenient to explore and investigate what are the optimal loading conditions to determine the parameters of the material whatever the constitutive law. The analysis can be carried out before and after the updating process and therefore does not necessarily require the experimental measurements (only pseudo-experimental loading). The *I*-index is a measure of the conditioning of the inverse problem and is defined as (Richard et al., 2013; Pac et al., 2014):

$$I = \log_{10} \left(\frac{\lambda_{max}}{\lambda_{min}} \right) > 0 \quad (3.26)$$

where λ_{max} and λ_{min} are the maximum and minimum eigenvalue of the matrix $\bar{\mathbf{H}}$ at the considered calculation point θ , respectively.

The lower the *I*-index, the better conditioned is the matrix, which means its inverse can be calculated with great accuracy. Contrarily, if the *I*-index is large, the matrix is considered as ill-conditioned. Some *I*-index values defining practical limits can be found in the literature (Gujarati, D.N, 1988). This procedure allows to distinguish the potentially identifiable combinations ($I \leq 2$) of material parameters from those which are not ($I > 3$).

In Figure 3.16, we graphically display these limits through an example with two parameters (θ_1, θ_2). The red ellipse (Figure 3.16b) represents the identification zone described by the following equation (Renner, 2016):

$$\lambda_1 x_1^2 + \lambda_2 x_2^2 = 2\omega(\hat{\theta}) \quad (3.27)$$

where λ_1 and λ_2 are the eigenvalues of the matrix $\bar{\mathbf{H}}(\lambda_1 \leq \lambda_2)$. The length of long half-axis *a* and the length of short half-axis *b* of the ellipse are defined as:

$$\begin{cases} a = \sqrt{\frac{2\omega(\hat{\theta})}{\lambda_1}} \\ b = \sqrt{\frac{2\omega(\hat{\theta})}{\lambda_2}} \end{cases} \quad (3.28)$$

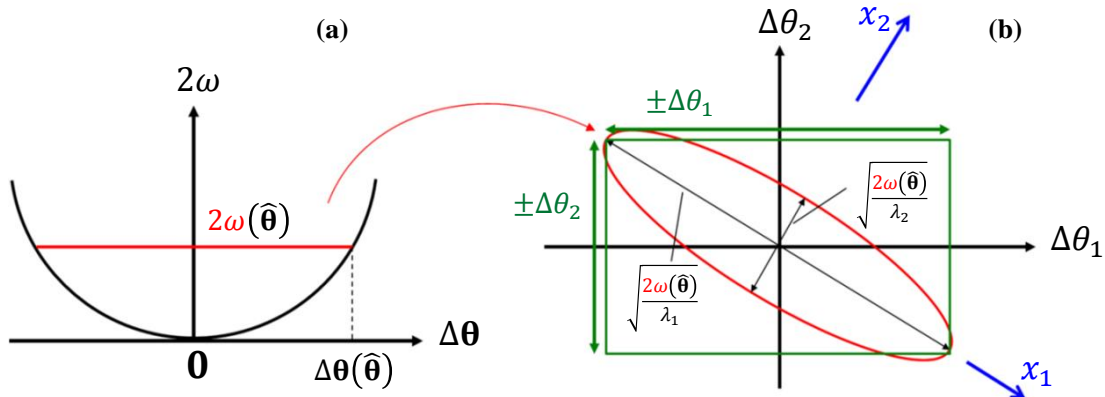


Figure 3.16. (a) Evolution of the function 2ω as function of $\Delta\theta$. (b) Projection function in the space $(\Delta\theta_1, \Delta\theta_2)$ (Renner, 2016).

The limits of the I -index depend on the shape of the projection function $2\omega(\hat{\theta})$ in the space $(\Delta\theta_1, \Delta\theta_2)$. In the case where $a = b$, the projection function correspond to a circle and better identifiability is obtained (Figure 3.17a). It can be observed that the longer the ellipse, the identification of the parameter becomes difficult (Figure 3.17b) or impossible (Figure 3.17c). These I -index values correspond to the ratio between relative uncertainties over two estimated parameters up to 10 ($I = 2$) and 30 ($I = 3$) if an updating process was performed.

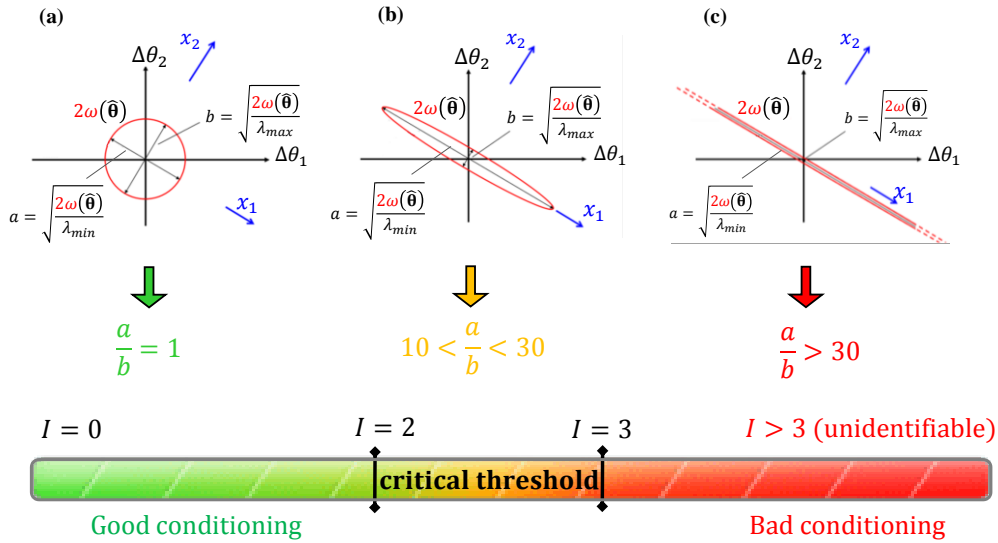


Figure 3.17. Projection function $2\omega(\hat{\theta})$ in the space $(\Delta\theta_1, \Delta\theta_2)$ for different values of the I -index (Richard, 2017).

For the VE behavior law, the I -index is calculated using the nanoindentation pseudo-experimental triangular test performed at 500 nm/min with cube corner and Berkovich indenter tips to investigate the effect of the relative perturbation ε . Figure 3.18 presents the results for three combinations of parameters calculated using the solution ($E = 1.47$ GPa, $c_1 = 0.94$ GPa, $\nu = 0.4$, $\eta = 17.08$ GPa.s) with both indenter tips. It can be observed that in the interest zone ($I < 3$) the relative perturbation ε does not have significant influence on the I -index values. The same study is performed for the V EVP and VEP behavior laws to determine an acceptable perturbation value.

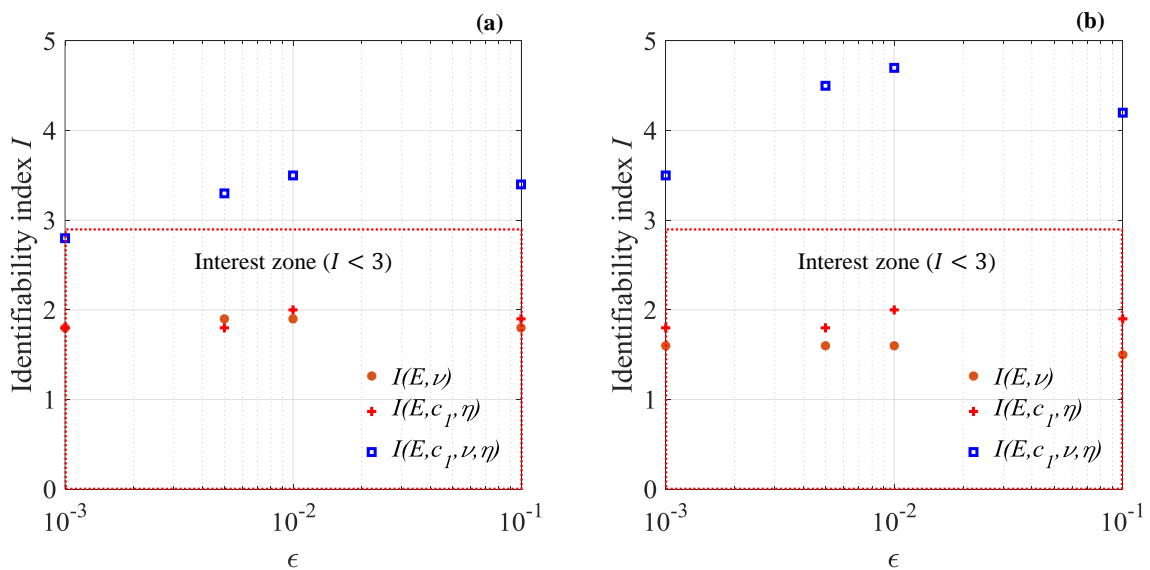


Figure 3.18. I -index versus the relative perturbation ε using the solution ($E = 1.47$ GPa, $c_1 = 0.94$ GPa, $\nu = 0.4$, $\eta = 17.08$ GPa.s) for three combinations of parameters, (a) Cube corner indenter tip. (b) Berkovich indenter tip.

In Figure 3.19, the I -index of three combination of VE parameters using the numerical test performed at 1000 nm/min with Berkovich indenter tip are displayed. In this study, a relative perturbation $\varepsilon = 10^{-3}$ is considered. The impact of smoothing procedure on the I -index results is studied. It can be seen that in the interest zone ($I < 3$), the smoothing procedure increase I -index values when only the loading segment is used. The same I -index is obtained with or without smoothing procedure when both loading and unloading segments are considered. It can be concluded that this procedure does not change the I -index results in the case of VE behavior. The same study is performed for the VEP and VEP behavior laws.

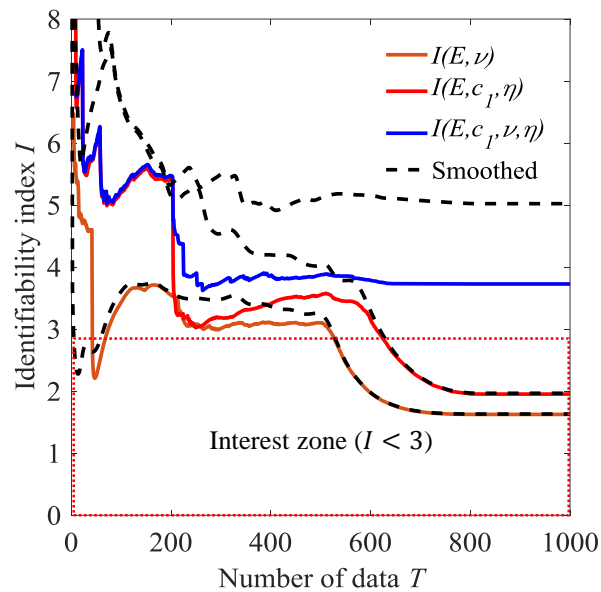


Figure 3.19. Evolution of the I -index for the nanoindentation test performed at 1000 nm/min for the solution ($E = 1.47$ GPa, $c_1 = 0.94$ GPa, $\nu = 0.4$, $\eta = 17.08$ GPa.s) with $\varepsilon = 10^{-3}$.

The stability of the obtained solutions will be studied for each behavior through this I -index. It can be used to design the nanoindentation experimental tests to be performed in order to ensure a better significance to the parameters estimated from the updating process. A parametric identifiability analysis will be presented in Chapter 4 and 5 to quantify the reliability of the estimated parameters using the VE, VEP and VEPV behavior laws.

3.6. Conclusion

In this chapter, the 2D-axisymmetric and 3D FEM, which have been used for the modeling of the nanoindentation test, are described. The convergence study of the 2D-axisymmetric FEM is performed for the VE behavior in order to ensure the convergence of the numerical solution for all indenter geometries which are equivalent half angles $\alpha = 42.28^\circ$ (cube corner), 57° , 60° , 65° and 70.3° (Berkovich).

The finite element model updating method (FEMU) used in the identification procedure of the material properties from the nanoindentation load-displacement curves is detailed. The sensitivity of the nanoindentation data to the VE behavior law parameters and the effect of the relative perturbation are studied.

The identifiability index allows to measure the richness of the information contained in the nanoindentation curves and it also allows to examine the stability of the identified parameters. Despite it has been shown in literature that additional information may yield more reliable identification results, this solution has not been fully investigated for different material behavior, motivating the study of the identifiability of the parameters using different nanoindentation responses. Besides, in spite of the considered information, the identifiability seems to have a close relationship with the nanoindentation rate and the indenter tip geometry. Moreover, different loading type (i.e., triangular, trapezoidal, exponential or sinusoidal) need to be compared to better understand the issue, since the parameters identifiability may be influenced not only by the measured experimental response, but also by the way the numerical simulation is performed. In conclusion, the identifiability analysis carried out in this work will answer the following questions:

- What is the effect of the nanoindentation rate on the identifiability result ?
- Does the loading type and indenter equivalent half angle has an influence on the identifiability of the behavior law parameters ?
- How does the identifiability of parameters differ if several nanoindentation tests are taken into account ?
- Finally, does the dual or plural indenter approach allows to determine unique solution of the inverse problem ?

This chapter summarizes all the main factors that need consideration in order to accurately extract the mechanical properties of materials using the nanoindentation technique. In the next chapter, we will employ the FEMU method together with identifiability index to estimate and study the stability of the viscoelastic properties determined from nanoindentation data.

Estimation of the viscoelastic properties of materials from nanoindentation curves

4.1.	Introduction	85
4.2.	Viscoelastic behavior law	85
4.3.	Non-uniqueness of the solutions	86
4.3.1.	Updating process from experimental data of single test	87
4.3.2.	Sensitivity analysis	93
4.3.3.	A posteriori identifiability analysis.....	95
4.3.4.	Comparison between 2D and 3D FEM.....	96
4.4.	A priori identifiability analysis using a single nanoindentation test.....	98
4.4.1.	Effect of depth rate	98
4.4.2.	Effect of loading type	99
4.4.3.	Effect of the tip angle	100
4.4.4.	Effect of measurement noise.....	101
4.4.5.	Link between dissipation and identifiability	106
4.5.	Combination of nanoindentation tests for well-posed the inverse problem	109
4.5.1.	Several nanoindentation triangular tests	109
4.5.2.	Dual nanoindentation.....	110
4.6.	Estimation of the VE behavior parameters from dual nanoindentation experimental data	118
4.7.	Assessment of the VE behavior.....	119
4.8.	Conclusion.....	122

4.1. Introduction

In this chapter, the stability of the viscoelastic properties of polypropylene (PP) extracted by the Finite Element Model Updating (FEMU) of the nanoindentation test described in the previous chapter is investigated. A four-parameter viscoelastic (VE) behavior law, which has been implemented in the 2D axisymmetric and 3D FEM is described. The updating process using a nanoindentation experimental triangular test conducted at depth rate 1000 nm/min with several starting points of the minimization algorithm is presented. The effect of the nanoindentation rate, apex angles of the indenter and the measurement noise on the identifiability are numerically studied. Thus, the link between the identifiability index (*I*-index) presented in Chapter 3.5 and the dissipation energy is shown. In order to design an experimental procedure that leads to a unique solution for the inverse problem, combinations of nanoindentation tests and apex angles are carried out through the *I*-index. Finally, an updating process using two nanoindentation experimental tests carried out at 500 nm/min with cube corner and Berkovich indenter tips is performed.

4.2. Viscoelastic behavior law

In this section, an isotropic linear VE law with constant Poisson's ratio ν to model the behavior of PP is considered. This behavior law is provided in ANSYS FE software. The Helmholtz free energy ψ (Lemaitre and Chaboche, 1994) can be written as:

$$\psi = \frac{1}{2\rho} (\boldsymbol{\varepsilon}^e : \mathbf{C} : \boldsymbol{\varepsilon}^e + \boldsymbol{\alpha}_1 : \mathbf{C}_1 : \boldsymbol{\alpha}_1) \quad (4.1)$$

where $\boldsymbol{\varepsilon}^e$ is the elastic strains tensor, $\boldsymbol{\alpha}_1$ is the internal variables tensor representing the anelastic phenomena, ρ is the density, $\mathbf{C}(E, \nu)$ and $\mathbf{C}_1(c_1, \nu)$ are the elastic and anelastic fourth-order stiffness tensors. E and c_1 are the instantaneous modulus, and the anelastic modulus, respectively; the symbol “:” stands for the tensor inner product. The state laws derive from this energy:

$$\boldsymbol{\sigma} = \rho \frac{\partial \psi}{\partial \boldsymbol{\varepsilon}^e} \quad \text{and} \quad \mathbf{X}_1 = \rho \frac{\partial \psi}{\partial \boldsymbol{\alpha}_1} \quad (4.2)$$

where $\boldsymbol{\sigma}$ is the Cauchy stress tensor and \mathbf{X}_1 is the anelastic stress tensor. The dissipation potential Ω is defined as:

$$\Omega = \frac{E}{2\eta} (\boldsymbol{\sigma} - \mathbf{X}_1) : \mathbf{S} : (\boldsymbol{\sigma} - \mathbf{X}_1) \quad (4.3)$$

where η is the viscosity coefficient in the elastic domain and \mathbf{S} the elastic compliance (fourth-order) tensor such as $\mathbf{S} : \mathbf{C} = \mathbf{I}$ (identity tensor). The derivatives of this potential Ω give the internal variables evolutions:

$$\dot{\boldsymbol{\varepsilon}}^{an} = \frac{\partial \Omega}{\partial \boldsymbol{\sigma}} \quad \text{and} \quad \dot{\boldsymbol{\alpha}}_1 = -\frac{\partial \Omega}{\partial \mathbf{X}_1} \quad (4.4)$$

where $\boldsymbol{\varepsilon}^{an}$ is the anelastic strain which is defined as the difference between the total $\boldsymbol{\varepsilon}$ and elastic $\boldsymbol{\varepsilon}^e$ strains.

$$\boldsymbol{\varepsilon}^{an} = \boldsymbol{\varepsilon} - \boldsymbol{\varepsilon}^e \quad (4.5)$$

This linear viscoelastic behavior law with constant Poisson's ratio is controlled by four material parameters, which define the parameter set $\boldsymbol{\theta} = (\theta_1, \theta_2, \theta_3, \theta_4) = (E, c_1, \nu, \eta)$.

From a rheological point of view, the behavior chosen here is, for elastic contribution, a linear spring whose stiffness is E and Poisson's ratio ν , and for anelastic contribution (delayed elasticity), a classical Kelvin-Voigt model which consists of a linear viscous damper of viscosity η and a linear spring of stiffness c_1 with internal stress X_1 placed in parallel (Figure 4.1).

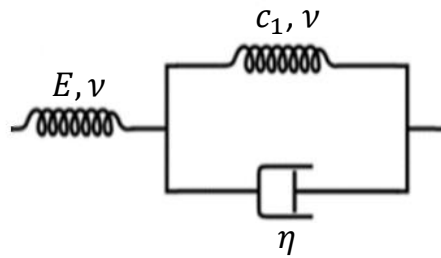


Figure 4.1. VE rheological model.

4.3. Non-uniqueness of the solutions

The problem of non-uniqueness of the inverse problem solution of the viscoelastic properties of PP estimated from a single nanoindentation experimental triangular load-unload test is investigated using FEMU. For that, the 2D-axisymmetric FEM of nanoindentation test presented in Chapter 3 is used. The obtained $P-h$ curves are compared with experimental results and the parameters uncertainties are computed for each starting point of the updating process. In addition, the sensitivities of the parameters to the nanoindentation force are calculated as well as the I -index described in Chapter 3. A comparison between the identifiability results from 2D-axisymmetric and 3D FEM is also performed.

4.3.1. Updating process from experimental data of single test

Herein, experimental data from the nanoindentation test realized on PP at 1000 nm/min using the triangular loading presented in Chapter 2 are used in Equation 3.1. Three starting points $\boldsymbol{\theta}^{(01)}$, $\boldsymbol{\theta}^{(02)}$ and $\boldsymbol{\theta}^{(03)}$ are chosen to initialize the minimization algorithm (Table 4.1). The evolutions of the four parameters during the minimization process are shown in Figure 4.2. The parameters E , c_1 and η tend towards the same values whatever the starting point with acceptable uncertainties (Equation 3.17) (about 15% for the viscosity η). However the obtained values for Poisson's ratio ν are multiple with a high uncertainty (about 140%). The value of the objective function ω is almost identical for all three cases and remains very low. Therefore, there is non-uniqueness of the solution of the inverse problem. The evolution of the parameter $E/(1 - \nu^2)$ for the three starting points is shown in Figure 4.3. The estimated solutions tend to the same value. It indicates that this parameter can be determined from single nanoindentation test. Figure 4.4 illustrates that the obtained solutions generate almost the same $P-h$ curve as the one obtained experimentally.

Table 4.1. Estimated parameters set $\hat{\boldsymbol{\theta}}$ (Equation 3.1) using three starting points and uncertainties (Equation 3.17).

		Parameter	Starting value	Estimated value	Uncertainty
j	θ_j		$\theta_j^{(0)}$	$\hat{\theta}_j$	$\Delta\theta_j/\theta_j$ (%)
Starting point 1: $\boldsymbol{\theta}^{(01)}$	1	E (GPa)	1.50	1.63	7.0
	2	c_1 (GPa)	12.25	1.05	6.0
	3	ν	0.4	0.13	90
	4	η (GPa. s)	65	18.56	15
Objective function $\omega^{(1)}$			4.59×10^{-2}	1.24×10^{-5}	
Starting point 2: $\boldsymbol{\theta}^{(02)}$	1	E (GPa)	1.40	1.63	6.0
	2	c_1 (GPa)	8.0	1.05	6.0
	3	ν	0.3	0.03	137
	4	η (GPa. s)	45	18.48	15
Objective function $\omega^{(2)}$			2.18×10^{-2}	1.24×10^{-5}	
Starting point 3: $\boldsymbol{\theta}^{(03)}$	1	E (GPa)	1.20	1.63	7.0
	2	c_1 (GPa)	4.0	1.06	6.0
	3	ν	0.2	0.03	138
	4	η (GPa. s)	30	18.50	15
Objective function $\omega^{(3)}$			5.18×10^{-3}	1.24×10^{-5}	

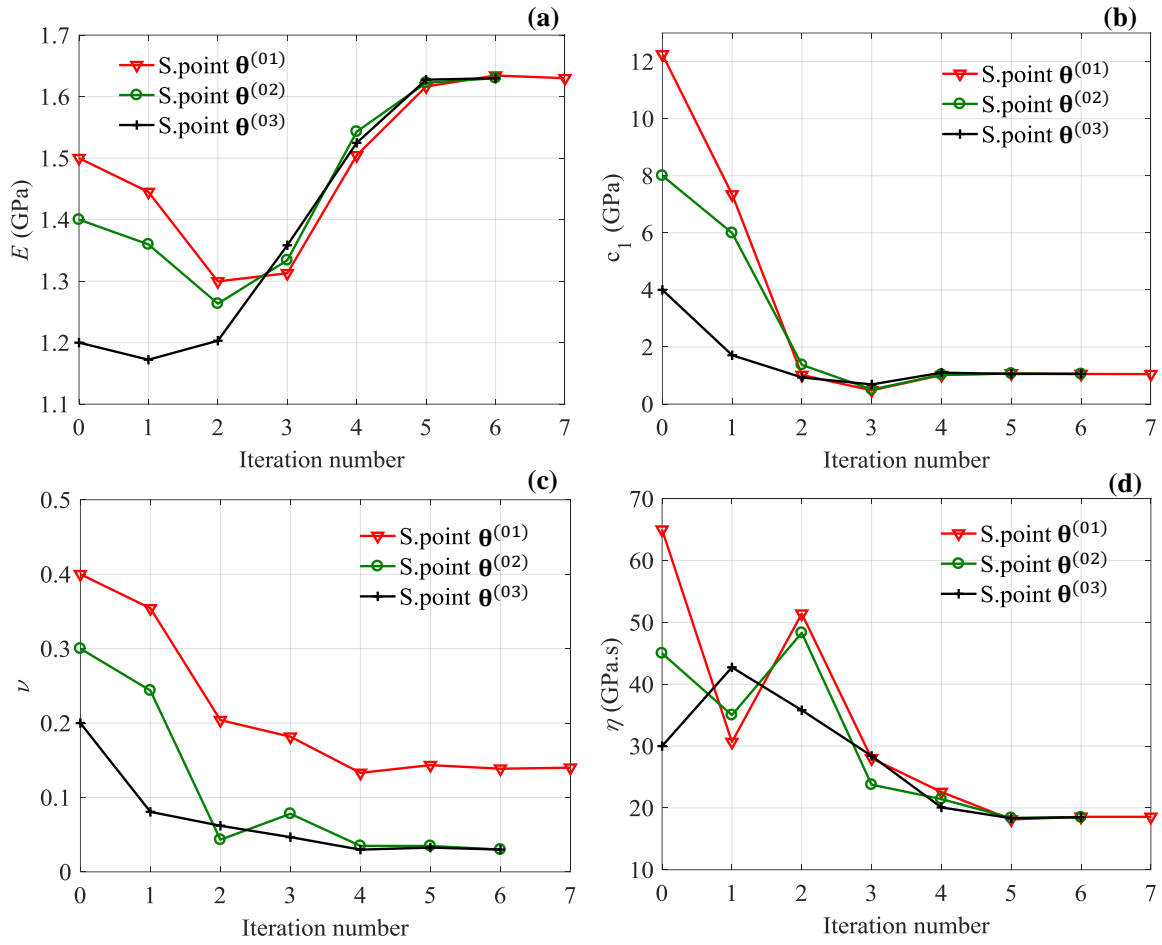


Figure 4.2. Evolution of the four parameters (E , c_1 , ν , η) during the updating process using three starting points $\theta^{(01)}$, $\theta^{(02)}$ and $\theta^{(03)}$.

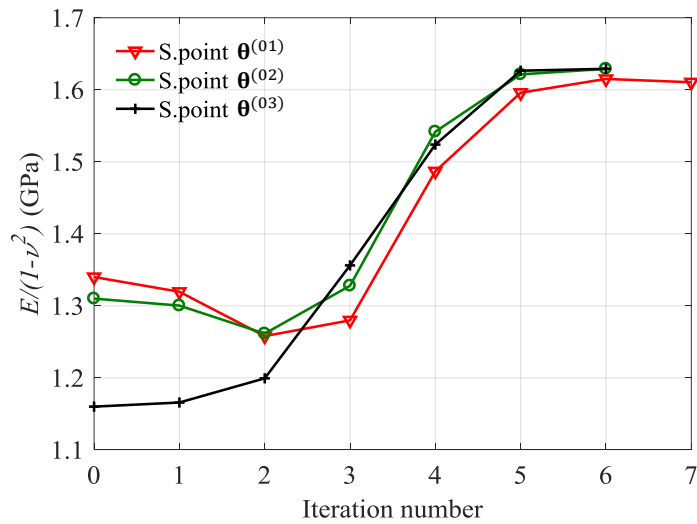


Figure 4.3. Evolution of the parameter ($E/(1-\nu^2)$) during the updating process using three starting points $\theta^{(01)}$, $\theta^{(02)}$ and $\theta^{(03)}$.

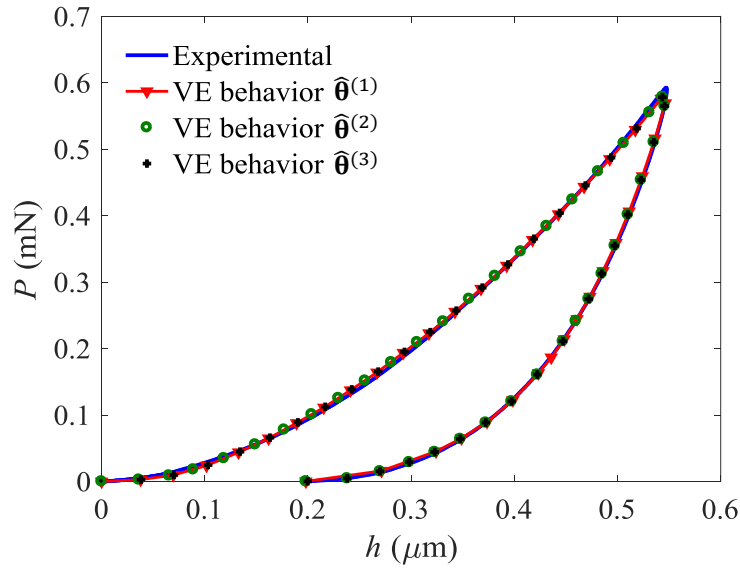


Figure 4.4. Experimental ($\dot{h} = 1000$ nm/min) and simulated nanoindentation curves for the three solutions $\hat{\theta}^{(1)} = (E = 1.63$ GPa, $c_1 = 1.05$ GPa, $\nu = 0.13$, $\eta = 18.56$ GPa.s), $\hat{\theta}^{(2)} = (E = 1.63$ GPa, $c_1 = 1.05$ GPa, $\nu = 0.03$, $\eta = 18.48$ GPa.s) and $\hat{\theta}^{(3)} = (E = 1.63$ GPa, $c_1 = 1.06$ GPa, $\nu = 0.03$, $\eta = 18.50$ GPa.s).

Furthermore, the Poisson's ratio is badly estimated comparing the obtained value with those given in the literature for PP ($\nu \sim 0.3$ to 0.42) (Gao and Mäder, 2002; Jakes et al., 2008). Updating processes can also be performed by imposing one of the four material parameters. Two particular cases are considered. In the first case A, the Young's modulus E is set to 1.50 GPa and the three parameters ν , c_1 and η are estimated (starting point: $\theta^{(04)} = (E = 1.50$ GPa (imposed), $c_1 = 12.25$ GPa, $\nu = 0.4$, $\eta = 65$ GP.s)). In the second case B, the value of the Poisson's ratio ν is set to 0.4 and E , c_1 and η are estimated (starting point: $\theta^{(05)} = (E = 1.50$ GPa, $c_1 = 12.25$ GPa, $\nu = 0.4$ (imposed), $\eta = 65$ GP.s)). Figure 4.5 shows the evolution of the four parameters during the minimization process. The obtained values are multiple except for the parameter c_1 . The parameters estimated resulting from the updating process are presented in Table 4.2. It can be noted that imposing a parameter increases considerably the uncertainties of the estimated parameters even on E and c_1 . The objective function values are not identical for the two solutions but they are the same order in magnitude. The five solutions $\hat{\theta}^{(1)}$, $\hat{\theta}^{(2)}$, $\hat{\theta}^{(3)}$, $\hat{\theta}^{(4)}$ and $\hat{\theta}^{(5)}$ are summarized in Table 4.3. All of the obtained load-displacement curves are in good agreement with the experimental data (Figure 4.6).

Table 4.2. Estimated parameters for the two particular cases A and B.

	Parameter		Starting value	Estimated value	Uncertainty
	j	θ_j	$\theta_j^{(0)}$	$\hat{\theta}_j$	$\Delta\theta_j/\theta_j$ (%)
Starting point 4: $\theta^{(04)}$ (Case A)	1	E (GPa)	1.50 (imposed)	1.50 (imposed)	10
	2	c_1 (GPa)	12.25	0.96	24
	3	ν	0.4	0.02	291
	4	η (GPa.s)	65	22.87	29
Objective function $\omega^{(4)}$			4.59×10^{-2}	3.27×10^{-5}	
Starting point 5: $\theta^{(05)}$ (Case B)	1	E (GPa)	1.50	1.47	44
	2	c_1 (GPa)	12.25	0.94	48
	3	ν	0.4 (imposed)	0.4 (imposed)	145
	4	η (GPa.s)	65	17.08	41
Objective function $\omega^{(5)}$			4.59×10^{-2}	1.31×10^{-5}	

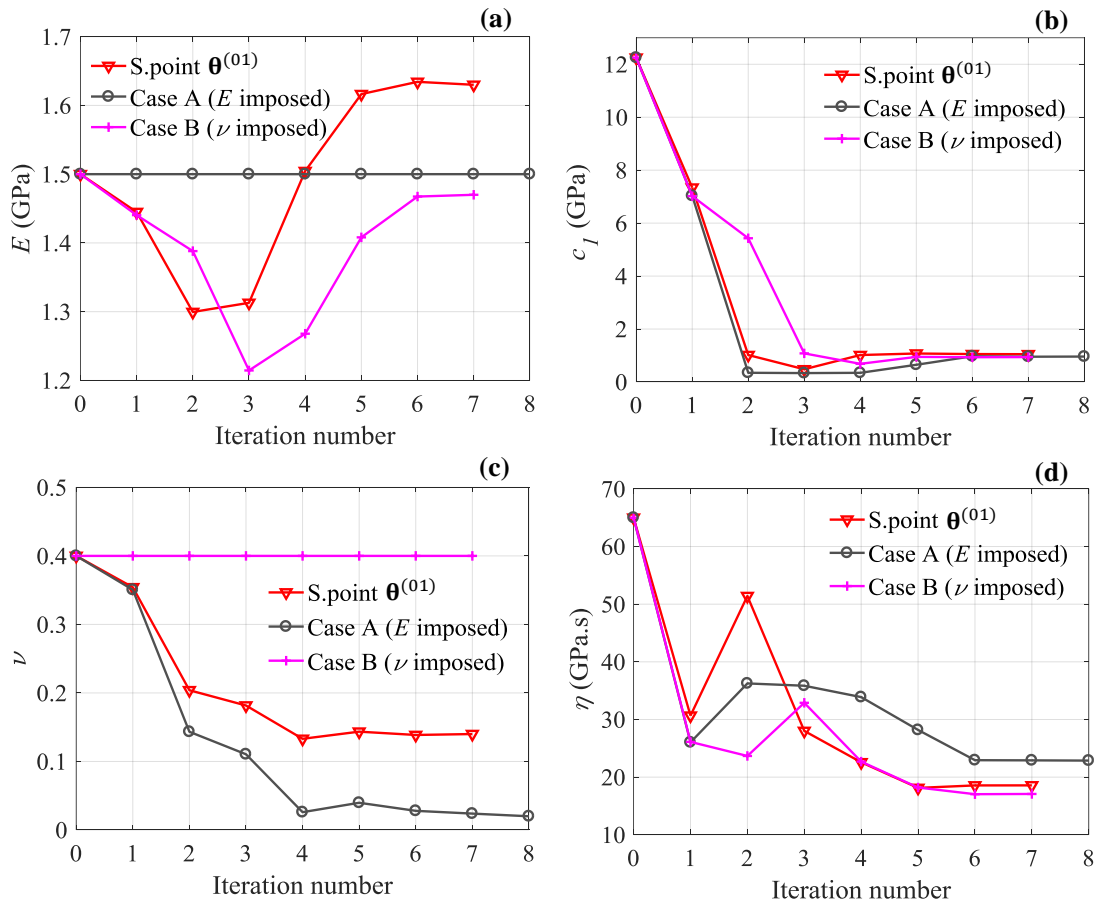


Figure 4.5. Evolution of the four parameters (E , c_1 , ν , η) during the updating process for the two particular cases A and B. Comparison with a case with 4 free parameters for the starting point ($\theta^{(01)} = E = 1.5$ GPa, $c_1 = 12.25$ GPa, $\nu = 0.4$, $\eta = 65$ GPa.s).

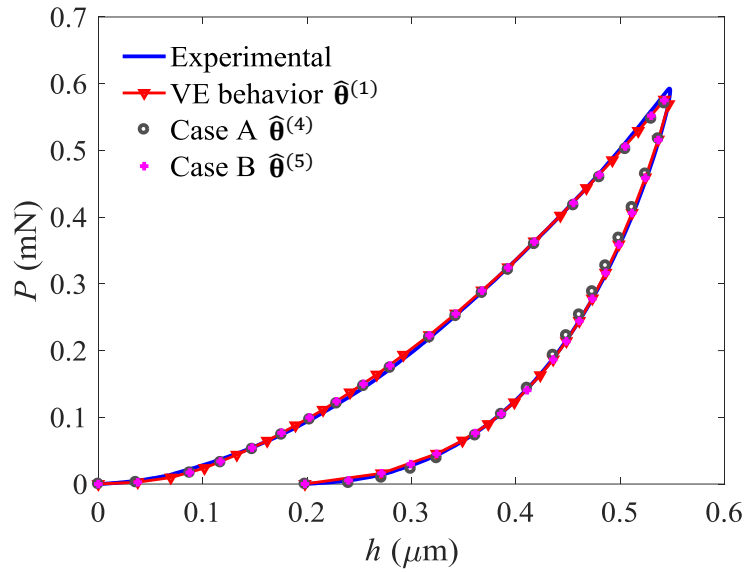


Figure 4.6. Experimental ($\dot{h} = 1000$ nm/min) and simulated nanoindentation curves for the three solutions $\hat{\theta}^{(1)} = (E = 1.63$ GPa, $c_1 = 1.05$ GPa, $\nu = 0.13$, $\eta = 18.56$ GPa.s), $\hat{\theta}^{(4)} = (E = 1.50$ GPa, $c_1 = 0.96$ GPa, $\nu = 0.02$, $\eta = 22.87$ GPa.s) and $\hat{\theta}^{(5)} = (E = 1.47$ GPa, $c_1 = 0.94$ GPa, $\nu = 0.4$, $\eta = 17.08$ GPa.s).

Table 4.3. Five solutions of the inverse problem.

j	1	2	3	4	
Solution	E (GPa)	c_1 (GPa)	ν	η (GPa.s)	ω
$\hat{\theta}^{(1)}$	1.63	1.05	0.13	18.56	1.24×10^{-5}
$\hat{\theta}^{(2)}$	1.63	1.05	0.03	18.48	1.24×10^{-5}
$\hat{\theta}^{(3)}$	1.63	1.06	0.03	18.50	1.24×10^{-5}
$\hat{\theta}^{(4)}$	1.50 (imposed)	0.96	0.02	22.87	3.27×10^{-5}
$\hat{\theta}^{(5)}$	1.47	0.94	0.4 (imposed)	17.08	1.31×10^{-5}

Considering that the five sets of parameters give almost the same P - h curve at depth rate of 1000 nm/min. Simulations have been carried out using nanoindentation tests simulated at depth rates of 50, 500 and 5000 nm/min for the five solutions ($\hat{\theta}^{(1)}$, $\hat{\theta}^{(2)}$, $\hat{\theta}^{(3)}$, $\hat{\theta}^{(4)}$, $\hat{\theta}^{(5)}$). Figure 4.7, Figure 4.8 and Figure 4.9 display the comparison between five numerical results. It can be seen that for these nanoindentation depth rates, these solutions do not lead to the same P - h curve. Particularly, the results obtained for the solution $\hat{\theta}^{(4)}$ (with a Poisson's ratio $\nu \sim 0$) differs from the others. It means that there is non-uniqueness of the solution of the inverse problem. It suggests that an identification procedure based on the data obtained at different nanoindentation depth rates could be more robust. However, this procedure is expensive and time consuming to execute (24h for one VE simulation using the experimental test (Figure 2.8) presented in Chapter 2).

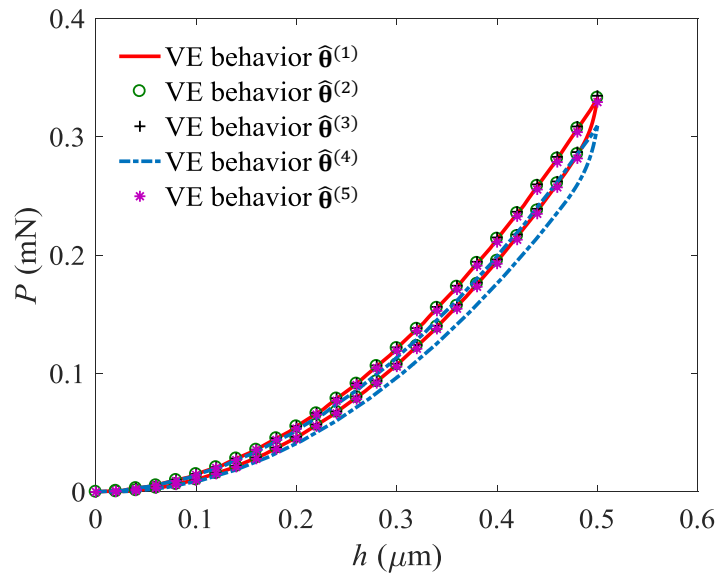


Figure 4.7. Nanoindentation (P - h) curves for the five solutions at nanoindentation depth rate of 50 nm/min.

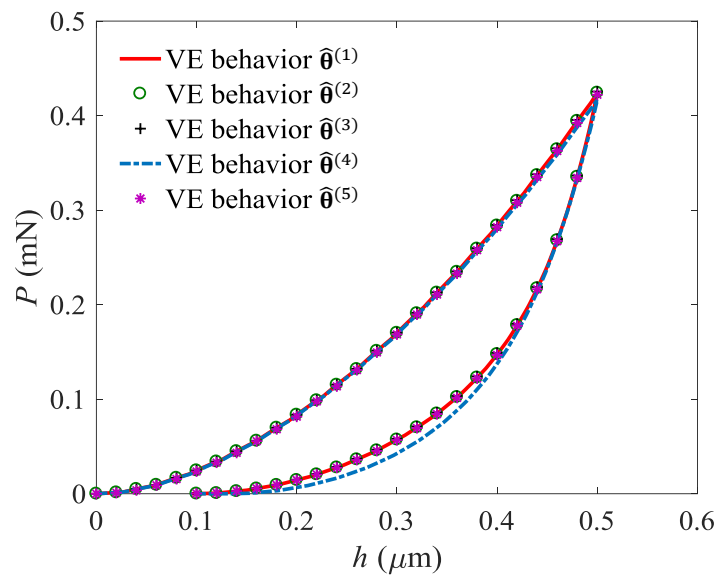


Figure 4.8. Nanoindentation (P - h) curves for the five solutions at nanoindentation depth rate of 500 nm/min.

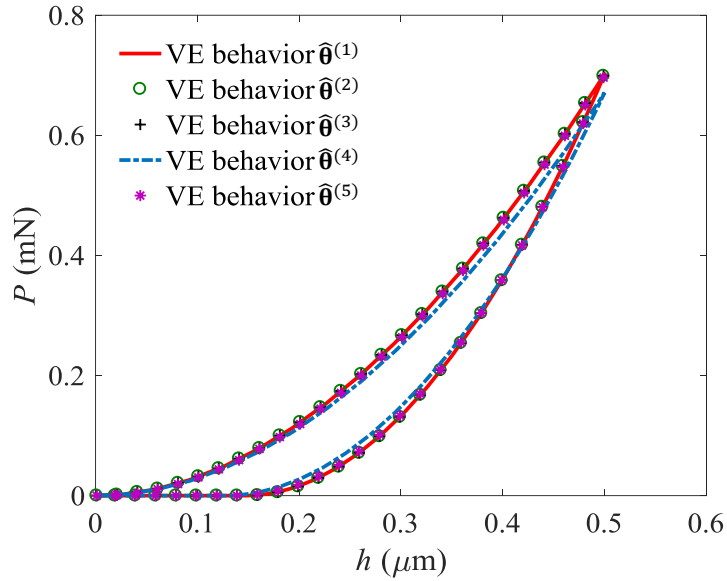


Figure 4.9. Nanoindentation (P - h) curves for the five solutions at nanoindentation depth rate 5000 nm/min.

4.3.2. Sensitivity analysis

To probe the uniqueness of a solution resulting from an updating process may appear to be very time consuming. In fact, an updating process for four parameters requires about 40 FE simulations (5 simulations by 8 iterations) with Berkovich indenter tip for each starting point and for each nanoindentation test. Another way is to investigate, a priori, the identifiability of the parameters. In this way, it is needed to estimate the sensitivity of the nanoindentation force to the material parameters. A sensitivity analysis is performed for the five solutions $\hat{\theta}^{(1)}$, $\hat{\theta}^{(2)}$, $\hat{\theta}^{(3)}$, $\hat{\theta}^{(4)}$ and $\hat{\theta}^{(5)}$ (2.5 hours for each sensitivity study) using the nanoindentation triangular test realized at 1000 nm/min in displacement-controlled mode. The norms of sensitivity vectors δ_j calculated using Equation 3.23 are displayed in Figure 4.10. The Young's modulus E is the most sensitive parameter, which means that it is the most influential to the nanoindentation curve. Then the anelastic modulus c_1 and the viscosity coefficient in the elastic domain η have almost the same effect expect for the solution $\hat{\theta}^{(4)}$ (with $\nu \sim 0$). The sensitivities appear to be well balanced for each solution. An exception can be noted for the Poisson's ratio. In fact, there is a lack of sensitivity to ν for the solutions $\hat{\theta}^{(1)}$, $\hat{\theta}^{(2)}$, $\hat{\theta}^{(3)}$ and $\hat{\theta}^{(4)}$ where the sensitivity to this coefficient is close to zero (Figure 4.10).

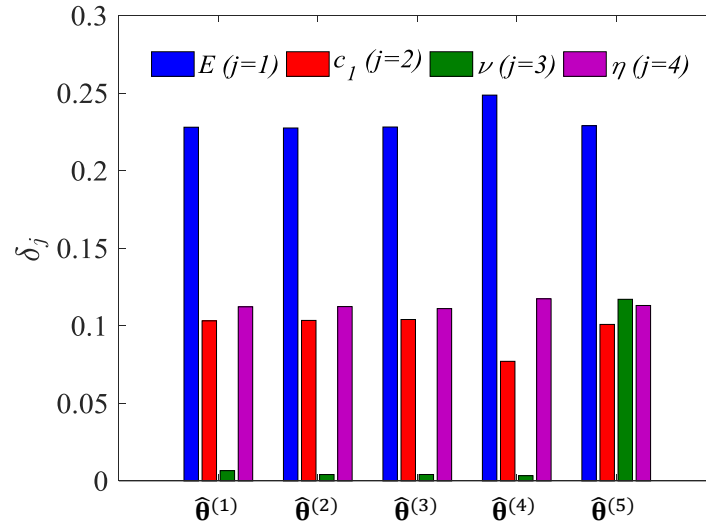


Figure 4.10. Sensitivity of the nanoindentation force P to θ_j for the five solutions $\hat{\theta}^{(1)}$, $\hat{\theta}^{(2)}$, $\hat{\theta}^{(3)}$, $\hat{\theta}^{(4)}$ and $\hat{\theta}^{(5)}$ (Table 4.3) using triangular test at 1000 nm/min.

The sensitivity vectors S_{kj} of the nanoindentation force have thus been calculated using Equation 3.22. Figure 4.11 a shows that the sensitivity vectors are very similar (up to a multiplicative factor) during the loading phase. Because of this collinearity between the sensitivity vectors, the identification of the four VE parameters from the sole loading phase is thus expected to be very difficult. Focusing on the sensitivity to E , we note that during the unloading part the proportionality with c_1 and η is lost. It seems to indicate that the unloading segment is more suitable to distinguish solution parameters and so to identify them. It also appears that the sensitivity vectors to E and ν are almost collinear during the loading segment (OA) and even during the first tier of the unloading segment (AB) in Figure 4.11 b, thus their identification using a single nanoindentation loading data is impossible. This is understood as a consequence of the sensitivity of the Boussinesq's problem to the sole $E/(1 - \nu^2)$ parameter (Boussinesq, 1885).

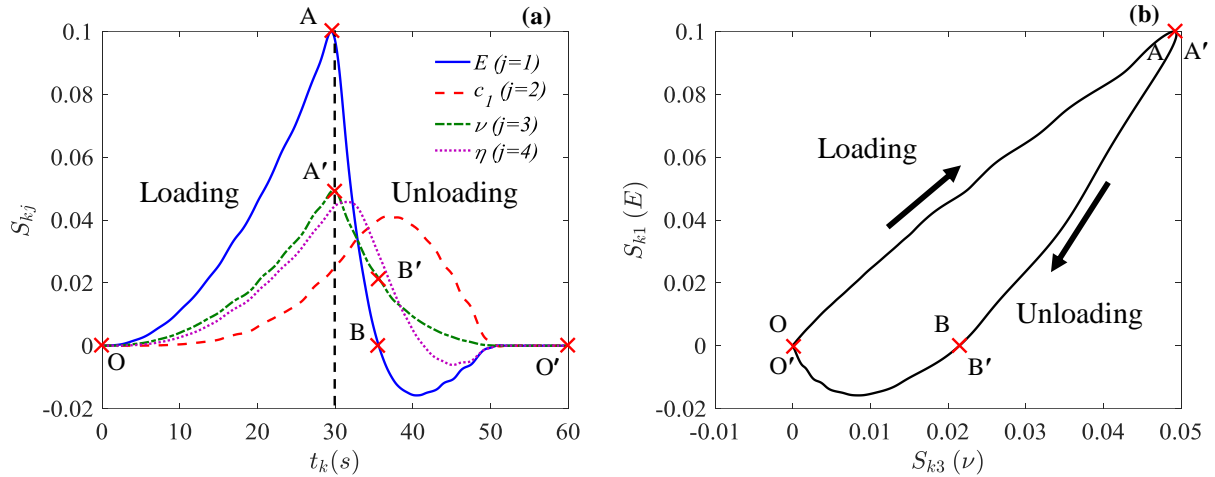


Figure 4.11. (a) Sensitivity vectors of the nanoindentation force to the material parameters θ_j during loading and unloading after smoothing using triangular test at 1000 nm/min. (b) Collinearity between sensitivity vectors S_{k1} and S_{k3} (sensitivities to E and ν , respectively).

4.3.3. A posteriori identifiability analysis

In order to quantify the completeness of the data used in the updating process, the I -index is determined from Equation 3.26 using the solution $\hat{\theta}^{(5)}$ with the nanoindentation test realized at 1000 nm/min for all combinations of parameters (6 couples, 4 triplets and 1 quadruplet) as a function of the considered data subsets (load-unload, only load and only unload). These results are summarized in Table 4.4 (without smoothing the sensitivity vectors). The identification of all combinations of two parameters is possible from load-unload test and only unloading segment ($I < 2$). It seems possible to identify three parameters (E, c_1, η) when the Poisson's ratio is known. The value of the index $I(E, c_1, \eta)$ is greater than 3 only when the sole loading segment is considered and less than 2 as soon as the unloading phase is taken into account. For this combination of parameters, the identifiability is better if only unload is considered ($I = 1.5$) than if both load and unload are considered ($I = 1.9$). It can be observed that the relevant information is therefore contained in the unloading part, confirming the conclusions drawn from the sensitivity vectors analysis. The I -index is higher than 3 for the combination of four parameters from single nanoindentation load-unload test. The identification of the full set of parameters is considered to be impossible because of the inverse problem is too ill-posed ($I > 3$).

Table 4.4. I -index for all combinations of parameters using triangular test at 1000 nm/min with the solution $\hat{\theta}^{(5)}$. $I \leq 2$ (green, potentially identifiable), $I < 2 \leq 3$ (difficult to identify), $I > 3$ (red, not identifiable).

Combination	Load-unload	Load	Unload
E, c_1	0.8	2.5	0.2
c_1, η	0.8	2.1	0.8
c_1, ν	0.8	2.1	1.0
E, η	1.4	2.8	0.8
E, ν	1.6	3.1	0.9
ν, η	1.9	3.0	1.8
E, c_1, η	1.9	3.5	1.5
c_1, ν, η	2.1	3.2	2.2
E, ν, η	2.5	3.8	2.1
E, c_1, ν	3.0	3.7	2.6
E, c_1, ν, η	3.7	3.9	3.5

4.3.4. Comparison between 2D and 3D FEM

Herein, the identifiability results using the 2D-axisymmetric and 3D FEM are compared. For that, a sensitivity analysis is performed using nanoindentation test of 1000 nm/min with 3D conical and Berkovich indenter tips. The 2D model has about 5000 elements. The conical and Berkovich 3D model are modelled by 39000 and 33500 elements. In Figure 4.12, the P - h curves obtained using both indenter tips are plotted. It can be seen that 2D and 3D conical indenter tips generate the same P - h curve. For the Berkovich indenter tip, there is small difference in the simulation results that will may be affect the identifiability results. Concerning the I -index, the obtained results are almost the same for the two conical indenter tips and do not agree with Berkovich indenter tip (Figure 4.13). It can be seen that using 3D Berkovich indenter tip, the four VE parameters are identifiable ($I = 2$) which is not the case using the 2D or 3D conical indenter tips ($I = 3.7$). The 3D Berkovich indenter tip considerably improves the identifiability results. Consequently, an identification procedure using single nanoindentation test and the 3D FEM may allow to uniquely extract the four VE properties. This results is in good agreement with that proposed by Kang et al. (Kang et al., 2012).

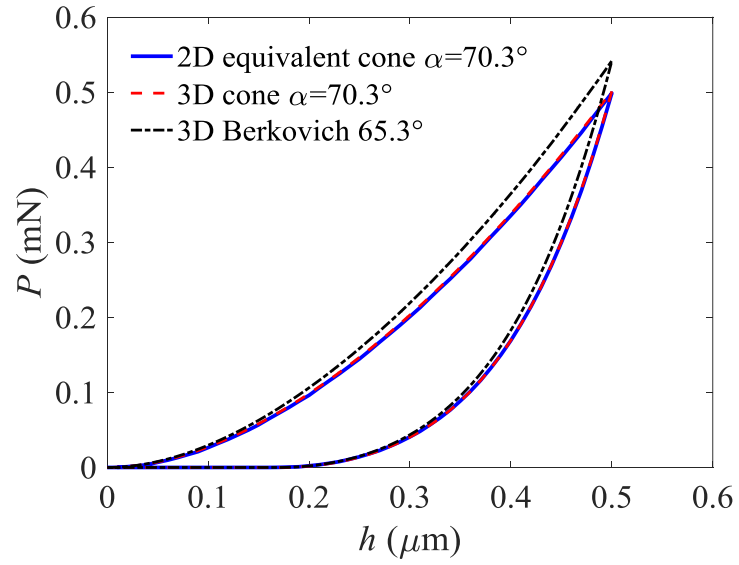


Figure 4.12. Comparison of the nanoindentation P - h curves at 1000 nm/min using 2D and 3D FEM.

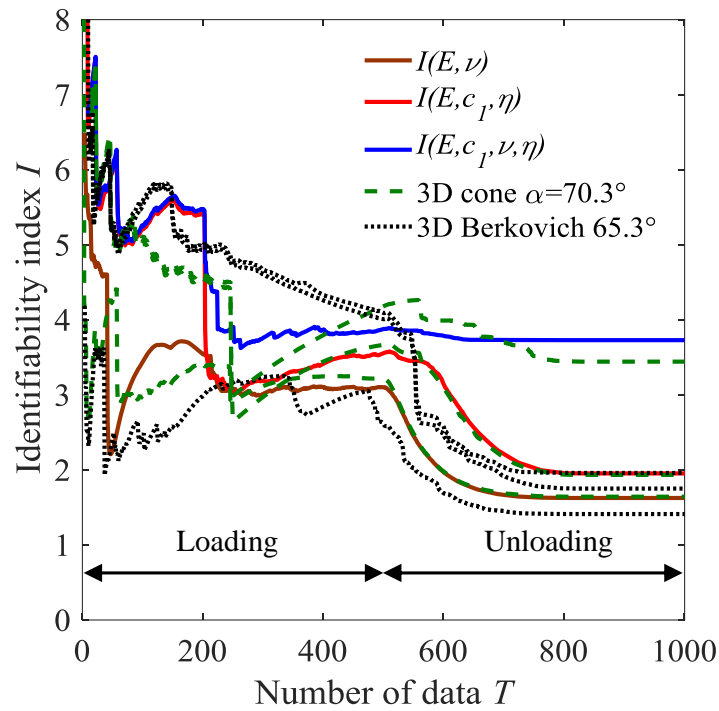


Figure 4.13. Comparison of the I -index for three combinations of parameters using nanoindentation test at 1000 nm/min with 2D, 3D conical and 3D Berkovich indenter tips.

4.4. A priori identifiability analysis using a single nanoindentation test

In this section, we focus on the possibility to identify the viscoelastic parameters from a single nanoindentation test. The effects of nanoindentation depth rate, loading type (triangular, trapezoidal, exponential and sinusoidal), the noise on the nanoindentation force and the indenter tip angle are investigated.

4.4.1. Effect of depth rate

The I -index is calculated for the nanoindentation triangular load-unload tests (50, 100, 500, 2500, 5000, 10000, 20000 nm/min) which are displayed in Chapter 2, with the solution $\hat{\theta}^{(5)} = (E = 1.47 \text{ GPa}, c_1 = 0.94 \text{ GPa}, \nu = 0.4, \eta = 17.08 \text{ GPa.s})$ using Berkovich indenter tip. In Figure 4.14, the load-displacement curves for all nanoindentation depth rates are presented. Table 4.5 shows that it is possible to identify two parameters using any nanoindentation depth rate and three parameters when using a rate between 500 and 1000 nm/min ($I \leq 2$). The depth rate does not improve the four material parameter I -index ($I > 3$). It can be concluded that whatever the depth rate, in the considered range the identification of the four material parameter from single nanoindentation triangular test is impossible.

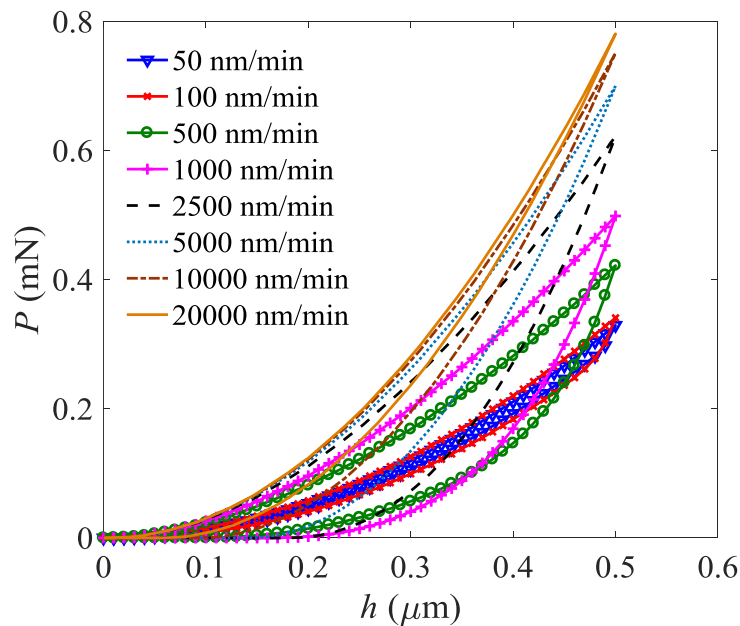


Figure 4.14. P - h simulated curves for all depth rates using the solutions $\hat{\theta}^{(5)}$ and Berkovich indenter tip.

Table 4.5. I -index for all combinations of parameters for all nanoindentation triangular load-unload tests using the solution $\hat{\theta}^{(5)}$. $I \leq 2$ (green, potentially identifiable), $I < 2 \leq 3$ (difficult to identify), $I > 3$ (red, not identifiable).

Combination	50 nm/min	100 nm/min	500 nm/min	1000 nm/min	2500 nm/min	5000 nm/min	10000 nm/min	20000 nm/min
E, c_1	2.3	1.7	0.6	0.8	1.9	2.8	3.7	4.2
c_1, η	2.2	1.7	0.6	0.8	1.7	2.3	2.3	2.2
c_1, ν	2.7	2.2	1.1	0.8	1.3	2.0	2.8	3.2
E, η	1.8	1.4	1.6	1.4	1.3	1.5	2.0	2.5
E, ν	2.8	2.5	1.6	1.6	2.0	2.4	2.9	3.4
ν, η	1.6	1.1	1.1	1.9	1.3	1.1	1.2	1.6
E, c_1, η	3.3	3.1	1.8	1.9	3.0	3.7	4.0	4.3
c_1, ν, η	3.4	3.3	2.3	2.1	2.5	3.0	3.1	3.3
E, ν, η	3.0	2.9	1.8	2.6	3.7	4.0	4.2	4.3
E, c_1, ν	3.5	3.5	2.9	3.0	3.6	4.0	4.2	4.4
E, c_1, ν, η	3.5	3.5	3.6	3.7	4.0	4.1	4.3	4.4

4.4.2. Effect of loading type

Herein, the identifiability analysis is performed using the trapezoidal, exponential and sinusoidal nanoindentation tests, which are displayed in Chapter 2. The results are summarized in Table 4.6. Like for the triangular loading, all combinations of two parameters are identifiable from trapezoidal and exponential tests. Three parameters (E, c_1, η) are potentially identifiable ($I \leq 2$) when the Poisson's ratio is known using trapezoidal loading. Comparing the results from single nanoindentation test in terms of I -index, the addition of a plateau just after the loading phase does not appear very helpful. It is observed that the better identifiability of the three parameters (E, c_1, η) is obtained using the exponential loading. Finally, the addition of a sinusoidal signal at the chosen frequency to the triangular loading phase is no more interesting for this material and all combinations of parameters are in the best case difficult to identify. The identification of the four parameters still impossible.

Table 4.6. Minima and maxima I -index values ($[I_{min}; I_{max}]$) for different loading types: triangular, trapezoidal, exponential and a sinusoidal loading with max rate (1000 nm/min), and $f = 4$ Hz for the solution $\hat{\theta}^{(5)}$. $I \leq 2$ (green, potentially identifiable), $I < 2 \leq 3$ (difficult to identify), $I > 3$ (red, not identifiable).

Combination	Triangular load-unload	Trapezoidal load-unload	Exponential load-unload	Triangular load	Sinusoidal load
E, c_1	[0.6; 4.2]	[0.6; 4.2]	[0.6; 5.7]	2.5	2.5
c_1, η	[0.6; 2.3]	[0.7; 2.5]	[0.7; 2.6]	2.1	2.1
c_1, ν	[0.8; 3.2]	[0.9; 3.2]	[1.1; 4.6]	2.1	2.1
E, η	[1.3; 2.5]	[1.2; 2.3]	[1.1; 3.8]	2.8	2.7
E, ν	[1.6; 3.4]	[1.6; 3.3]	[1.6; 4.1]	3.1	3.1
ν, η	[1.1; 1.9]	[0.9; 1.9]	[0.7; 2.3]	3.0	2.9
E, c_1, η	[1.8; 4.3]	[2.0; 4.4]	[1.6; 5.7]	3.5	3.4
c_1, ν, η	[2.0; 3.4]	[2.3; 3.6]	[2.1; 4.7]	3.2	3.1
E, ν, η	[1.8; 4.3]	[2.3; 4.4]	[1.8; 4.5]	3.8	3.7
E, c_1, ν	[2.9; 4.4]	[3.1; 4.5]	[2.7; 5.7]	3.7	3.7
E, c_1, ν, η	[3.5; 4.4]	[3.6; 4.5]	[3.7; 5.7]	3.9	3.8

4.4.3. Effect of the tip angle

A study has also been conducted to investigate the influence of the indenter half angle α on the I -index. Five indenter tips with equivalent half angle of $\alpha = 42.28^\circ$ (cube corner), 57° , 60° , 65° and 70.3° (Berkovich) are considered. The P - h curves for these indenter tips using depth rate of 500 nm/min with the solution $\hat{\theta}^{(5)}$ are shown in Figure 4.15. The obtained I -index results are given in Table 4.7. Comparing the values of the I -index, it is found that the indenter tip angle does not have a great influence on the identifiability. The I -index values are almost the same and the four material parameters are, in the best case difficult to identify.

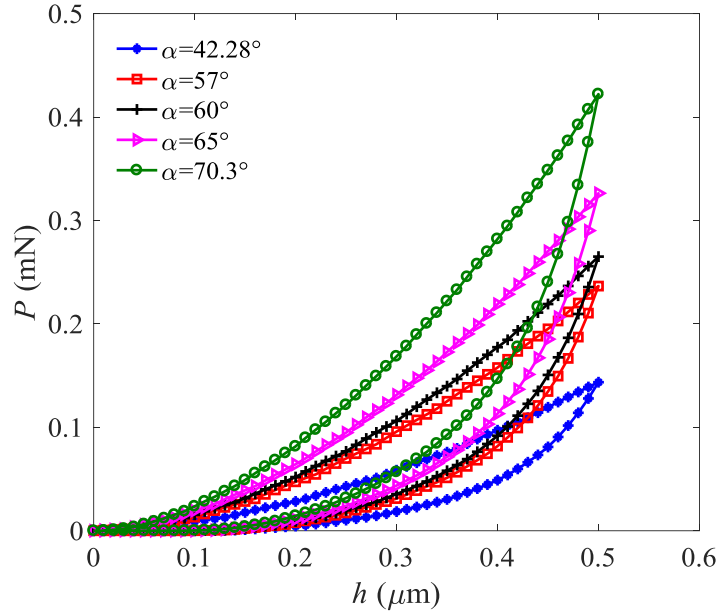


Figure 4.15. P - h simulated curves for all indenter tips using nanoindentation depth rate of 500 nm/min and the solution $\hat{\theta}^{(5)}$.

Table 4.7. I -index for all combinations of parameters using the nanoindentation load-unload test of 500 nm/min with five indenter tip angles for the solution $\hat{\theta}^{(5)}$. $I \leq 2$ (green, potentially identifiable), $I < 2 \leq 3$ (difficult to identify), $I > 3$ (red, not identifiable).

Combination	Cube corner ($\alpha = 42.28^\circ$)	$\alpha = 57^\circ$	$\alpha = 60^\circ$	$\alpha = 65^\circ$	Berkovich ($\alpha = 70.3^\circ$)
E, c_1	0.5	0.6	0.6	0.6	0.6
c_1, η	0.6	0.6	0.6	0.6	0.6
c_1, ν	1.4	1.1	1.1	1.1	1.1
E, η	1.5	1.6	1.6	1.6	1.6
E, ν	1.8	1.6	1.6	1.6	1.6
ν, η	1.0	1.0	1.0	1.1	1.1
E, c_1, η	1.7	1.8	1.8	1.8	1.8
c_1, ν, η	2.2	2.3	2.3	2.3	2.3
E, ν, η	1.9	1.8	1.8	1.8	1.8
E, c_1, ν	2.7	2.8	2.8	2.8	2.9
E, c_1, ν, η	2.8	3.2	3.1	3.4	3.6

4.4.4. Effect of measurement noise

The I -index results using the nanoindentation test performed at nanoindentation depth rate of 1000 nm/min show that it is possible to identify E, c_1 and η by assuming that the Poisson's ratio is known

$\nu = 0.4$ ($I(E, c_1, \eta) = 1.9$) (Table 4.4). In order to explore the effect of noise on the updating process results, a white Gaussian noise is used to disrupt the nanoindentation force P from the test at nanoindentation depth rate of 1000 nm/min.

$$\tilde{P}(t) = P(t) + \mathcal{N}(0, s)P_{max} \quad (4.6)$$

where $\mathcal{N}(0, s)$ is a normal (Gaussian) distribution with zero mean and standard deviation s . P_{max} is the maximum value of nanoindentation force $P(t)$.

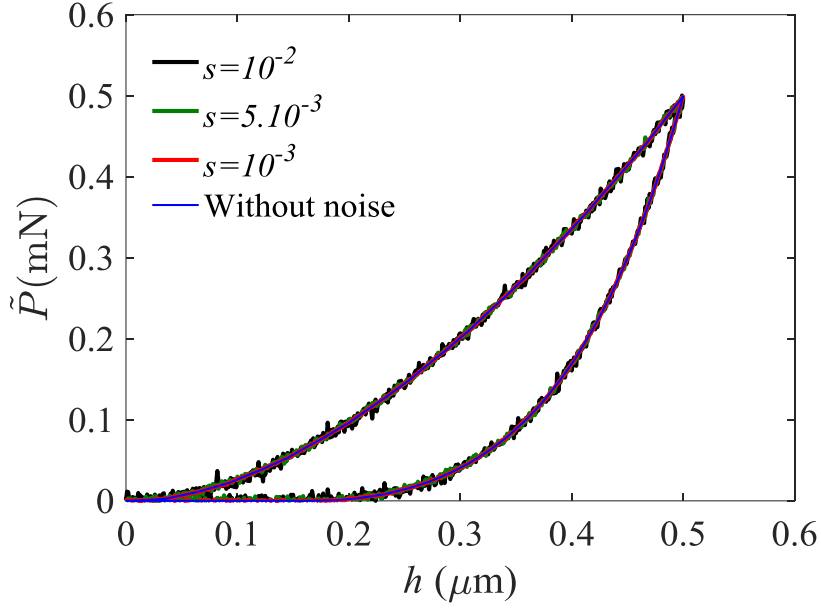


Figure 4.16. Nanoindentation P - h curves for three levels of measurement noise of nanoindentation triangular test at 1000 nm/min.

In Figure 4.16, we show the nanoindentation P - h curves for noise levels used in the updating process calculations with the starting points $\boldsymbol{\theta}^{(05)} = (E = 1.50 \text{ GPa}, c_1 = 12.25 \text{ GPa}, \nu = 0.4 \text{ (imposed)}, \eta = 65 \text{ GPa.s})$, $\boldsymbol{\theta}^{(06)} = (E = 1.40 \text{ GPa}, c_1 = 8.0 \text{ GPa}, \nu = 0.4 \text{ (imposed)}, \eta = 45 \text{ GPa.s})$ and $\boldsymbol{\theta}^{(07)} = (E = 1.20 \text{ GPa}, c_1 = 4.0 \text{ GPa}, \nu = 0.4 \text{ (imposed)}, \eta = 30 \text{ GPa.s})$. The solutions obtained for the starting point $\boldsymbol{\theta}^{(05)}$ and various noise levels are presented in Table 4.8. It can be clearly observed that the uncertainties values increase when increasing the noise level and vice versa. From a noise level $s = 10^{-2}$, large uncertainties are obtained for all parameters (about 213% for the Poisson's ratio). Figure 4.17 presents the evolution of the parameters E , c_1 and η during the updating process. The obtained solution is not very sensitive to this type of noise.

Table 4.8. Estimated solutions for the four levels of measurement noise using load-unload test with the starting point $\theta^{(05)}$.

Noise		Parameter	Starting value	Estimated value	Uncertainty
s	j	θ_j	$\theta_j^{(0)}$	$\hat{\theta}_j$	$\Delta\theta_j/\theta_j$ (%)
10^{-2}	1	E (GPa)	1.50	1.446	64
	2	c_1 (GPa)	12.25	0.933	73
	3	ν	0.4 (imposed)	0.4 (imposed)	213
	4	η (GPa.s)	65	17.27	66
ω			4.90×10^{-2}	4.70×10^{-5}	
5×10^{-3}	1	E (GPa)	1.50	1.454	32
	2	c_1 (GPa)	12.25	0.939	37
	3	ν	0.4 (imposed)	0.4 (imposed)	106
	4	η (GPa.s)	65	17.00	32
ω			4.96×10^{-2}	1.18×10^{-5}	
10^{-3}	1	E (GPa)	1.50	1.449	11
	2	c_1 (GPa)	12.25	0.935	12
	3	ν	0.4 (imposed)	0.4 (imposed)	35
	4	η (GPa.s)	65	17.15	11
ω			4.94×10^{-2}	1.32×10^{-6}	
0	1	E (GPa)	1.50	1.449	9.0
	2	c_1 (GPa)	12.25	0.935	10
	3	ν	0.4 (imposed)	0.4 (imposed)	30
	4	η (GPa.s)	65	17.18	10
ω			4.93×10^{-2}	8.30×10^{-7}	

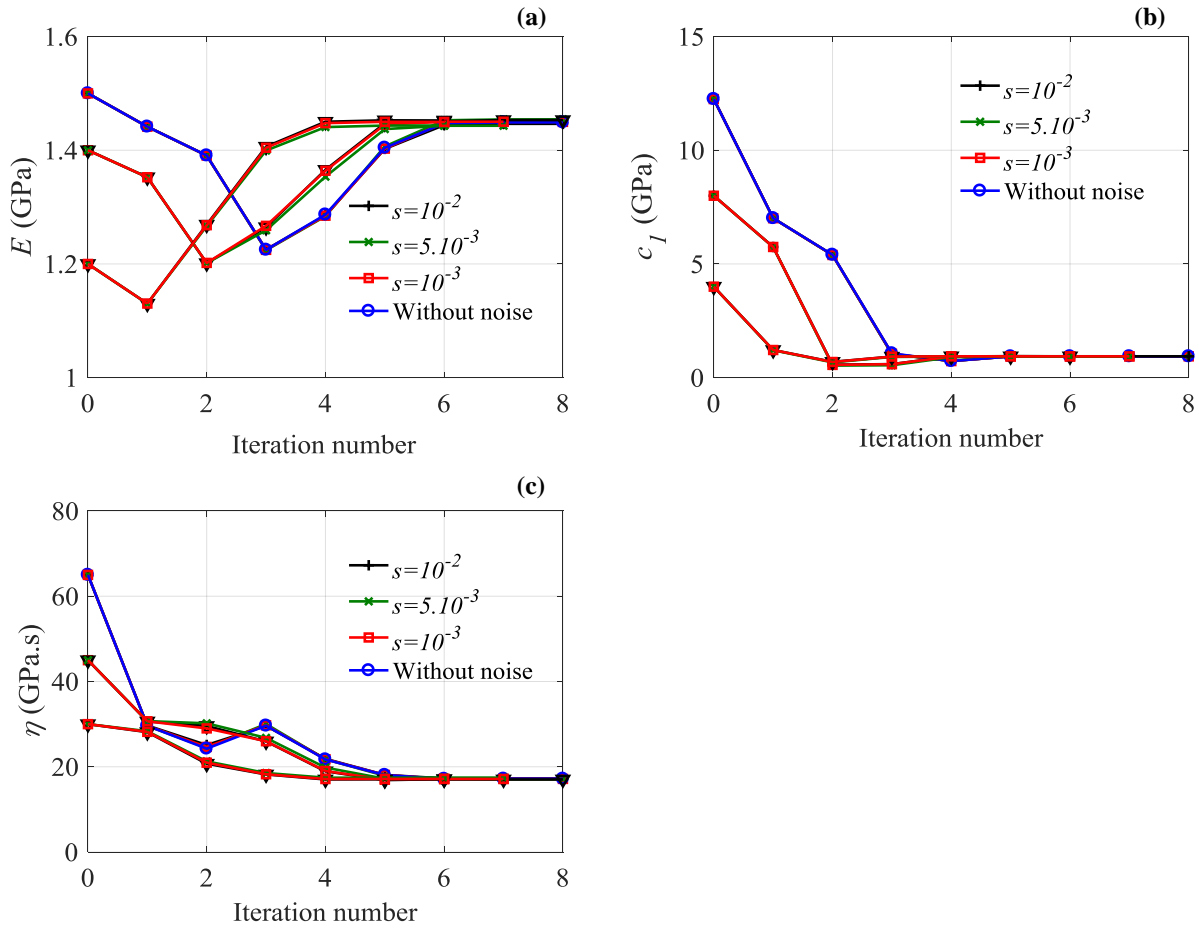


Figure 4.17. Evolution of the 3 parameters (E , c_1 , η) during the updating process for the three starting points of the minimization algorithm $\theta^{(05)}$, $\theta^{(06)}$ and $\theta^{(07)}$ using noisy force values.

The meaning of the I -index results is illustrated by reproducing this analysis only using the loading segments. The identifiability results show that the identification of the parameters E , c_1 and η is not possible in that case $I(E, c_1, \eta) = 3.5$ (Table 4.4). Despite very small values of the objective function, the relative uncertainties between the obtained and imposed solutions are very large as shown in Table 4.9. The obtained solution is very sensitive to the noise during the loading segment (Figure 4.18). It is also observed that the convergence of the minimization algorithm is longer.

Table 4.9. Estimated solutions for the three levels of measurement noise using loading segments with the starting point $\theta^{(0)}$.

Noise		Parameter	Starting value	Estimated value	Uncertainty
s	j	θ_j	$\theta_j^{(0)}$	$\hat{\theta}_j$	$\Delta\theta_j/\theta_j$ (%)
10^{-2}	1	E (GPa)	1.40	1.345	92
	2	c_1 (GPa)	8.0	0.829	191
	3	ν	0.4 (imposed)	0.4 (imposed)	277
	4	η (GPa.s)	45	21.88	242
ω			1.26×10^{-2}	5.14×10^{-5}	
5×10^{-3}	1	E (GPa)	1.40	1.396	43
	2	c_1 (GPa)	8.0	0.883	83
	3	ν	0.4 (imposed)	0.4 (imposed)	132
	4	η (GPa.s)	45	19.37	109
ω			1.27×10^{-2}	1.18×10^{-5}	
10^{-3}	1	E (GPa)	1.40	1.363	13
	2	c_1 (GPa)	8.0	0.817	25
	3	ν	0.4 (imposed)	0.4 (imposed)	40
	4	η (GPa.s)	45	21.17	34
ω			1.26×10^{-2}	1.05×10^{-6}	

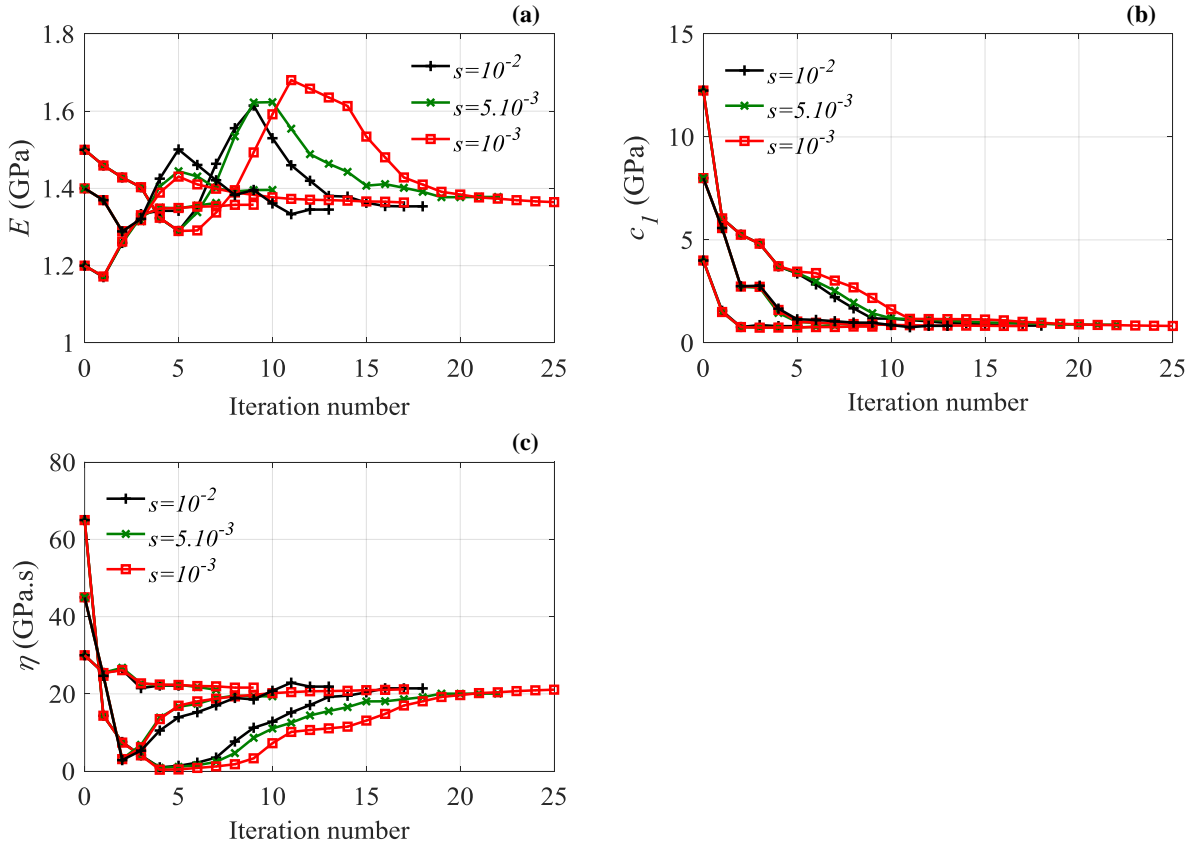


Figure 4.18. Evolution of the 3 parameters (E , c_1 , η) during the updating process for the three starting points of the minimization algorithm $\theta^{(05)}$, $\theta^{(06)}$ and $\theta^{(07)}$ using loading segments of noisy force.

4.4.5. Link between dissipation and identifiability

The loss factor (intrinsic damping) $\tan(\delta)$, which is used to measure a viscoelastic material property in the case of tensile and harmonic loading can be approached for any of the considered loading signals considered herein, by discarding any signal harmonic so that:

$$\tan(\delta) = \frac{2\pi f E \eta}{c_1(E + c_1) + (2\pi f)^2 \eta^2} \quad (4.7)$$

where f is the fundamental frequency. In the case of the nanoindentation test: $f = 1/t_{max}$.

The I -index is calculated for the numerical nanoindentation triangular tests presented in Chapter 2 with equivalent cube corner and Berkovich indenter tips using displacement-controlled and force-controlled modes to investigate the effect of nanoindentation rate.

In Figure 4.19, the results for three combinations of parameters calculated using the solution $\hat{\theta}^{(5)}$ with the equivalent cube corner indenter tip are presented. Using the force-controlled mode, it can be

observed that the I -index values of the four parameters fall for the three slowest rates (60, 120 and 600 $\mu\text{N}/\text{min}$) (Figure 4.19b). This problem disappears if the Poisson's ratio is known. The better identifiability of the material parameters is obtained with a depth rate between 500 nm/min ($t_{max} = 120$ s) and 1000 nm/min ($t_{max} = 60$ s) in displacement-controlled mode and a load rate 600 $\mu\text{N}/\text{min}$ ($t_{max} = 120$ s) and 1200 $\mu\text{N}/\text{min}$ ($t_{max} = 60$ s) in force-controlled mode. It also shows that the I -index is well correlated to the loss factor (Figure 4.19). In particular, we note that when the loss factor is maximum, (i.e when the dissipation is maximum) the I -index is minimum, (i.e the identifiability is the maximum).

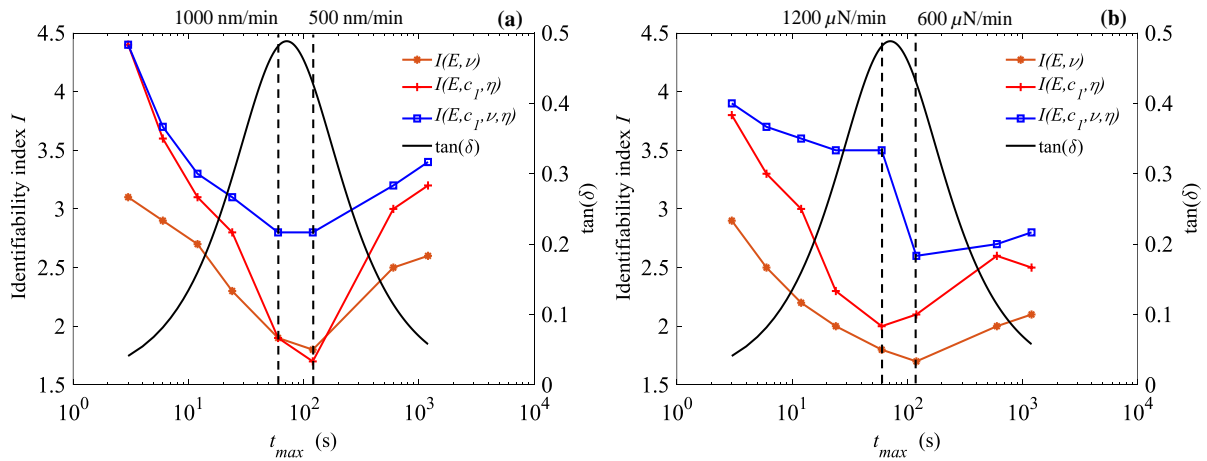


Figure 4.19. I -index for the nanoindentation triangular tests and the loss factor using the solution $\hat{\theta}^{(5)}$ with equivalent cube corner indenter tip, (a) displacement-controlled mode. (b) force-controlled mode.

For the equivalent Berkovich tip (Figure 4.20), it can be seen that the better identifiability of the four material parameters is obtained using a nanoindentation depth rate between 500 nm/min ($t_{max} = 120$ s) and 1000 nm/min ($t_{max} = 60$ s) in displacement-controlled mode and a nanoindentation load rate about 1200 $\mu\text{N}/\text{min}$ ($t_{max} = 60$ s) in force-controlled mode. It also shows that the I -index is well correlated to the loss factor (Figure 4.20), similarly to equivalent cube corner tip.

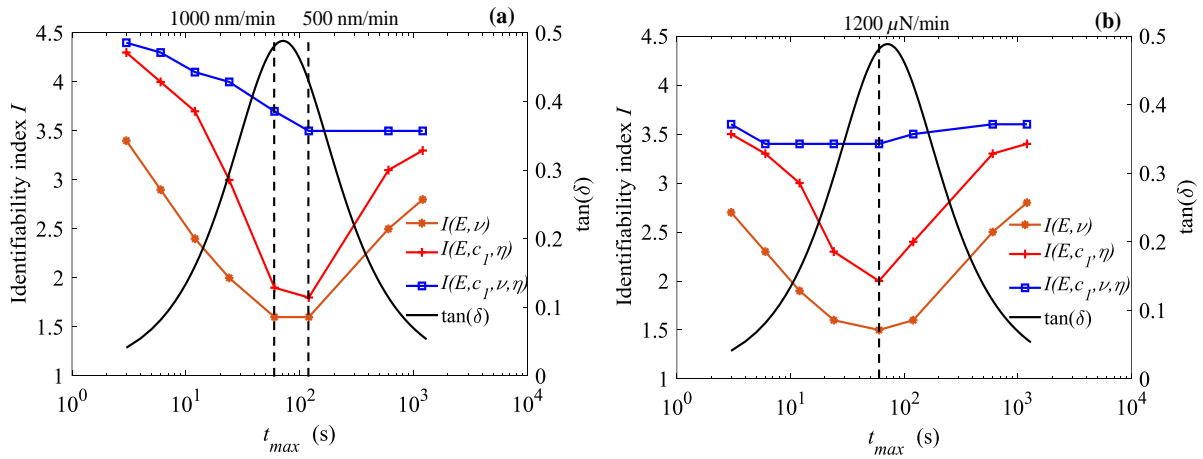


Figure 4.20. I -index for the nanoindentation triangular tests and the loss factor using the solution $\widehat{\theta}^{(5)}$ with equivalent Berkovich indenter tip, (a) displacement-controlled mode. (b) force-controlled mode.

The link between $\tan(\delta)$ and the I -index is also investigated for trapezoidal and exponential loading types using Equation 4.7. Figure 4.21 shows the I -index results for 3 combinations of material parameters with equivalent Berkovich indenter tip as function of the loss factor using the solution $\widehat{\theta}^{(5)}$. It can be seen that, whatever the loading type, the better identifiability corresponds to conditions, which maximize the loss factor. The link between $\tan(\delta)$ and the I -index depends on the nanoindentation rate to solicit the dissipative phenomena, which is different from a loading to the other.

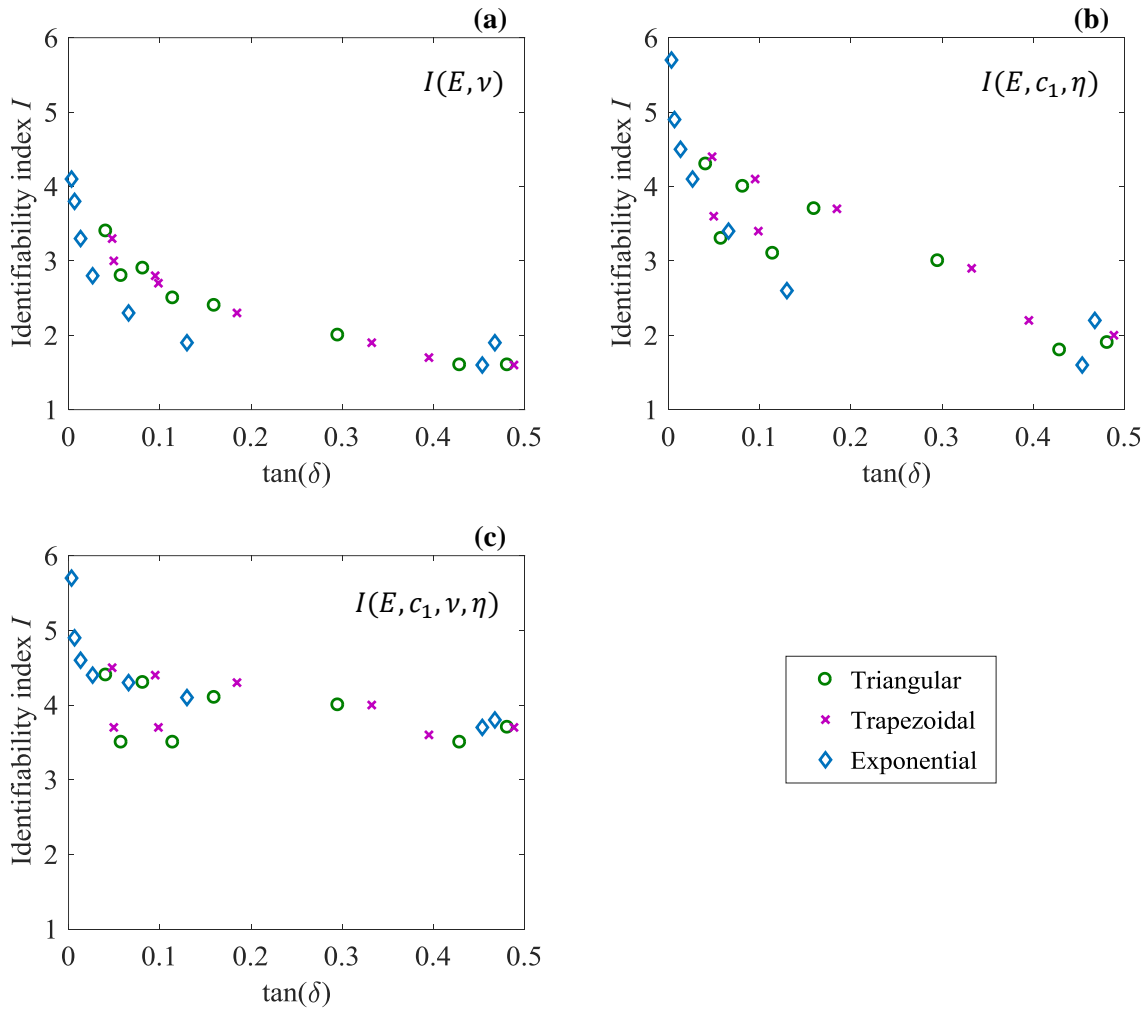


Figure 4.21. I -index versus $\tan(\delta)$ using three loading types with the solution $\hat{\theta}^{(5)}$ for three combinations of parameters, (a) $I(E, \nu)$. (b) $I(E, c_1, \eta)$. (c) $I(E, c_1, \nu, \eta)$.

4.5. Combination of nanoindentation tests for well-posed the inverse problem

In order to determine the better identifiability of the four material parameters, the subset of nanoindentation triangular tests simulated in displacement-controlled mode with Berkovich indenter tip is investigated. Then, all combinations of dual indenter tips from the five indenter tip angles (42.2° , 57° , 60° , 65° , 70.3°) using nanoindentation test simulated at 500 nm/min is examined.

4.5.1. Several nanoindentation triangular tests

In this section, the identifiability analysis is carried out using a set of 2 to 8 nanoindentation triangular tests (50, 100, 500, 1000, 2500, 5000, 10000, 20000 nm/min) for the solution $\hat{\theta}^{(5)}$. Table 4.10 summarizes the I -index values for all subsets of nanoindentation tests. The combination of nanoindentation triangular tests decreases the maximum I -index values, and therefore improves the identification robustness. All combinations of two parameters can be identified from the subset of two

nanoindentation tests. The subset of multiple nanoindentation tests allows to identify the first 9 combinations of parameters. For example, the combination of three parameter (E, c_1, η) is identifiable whatever the subset if six nanoindentation tests are considered. The identification of the four material parameters (E, c_1, ν, η) is still impossible despite the additional information. The value of the I -index for the four material parameters is never less than 3.5. Comparing the I -index results from single nanoindentation test (Table 4.4) and the subset of several tests (Table 4.10), it is observed that the set of eight nanoindentation rates does not necessarily lead to better I -index compared to a single but properly chosen one.

Table 4.10. Minima and maxima I -index values ($[I_{min}; I_{max}]$) of all combinations of parameters for all subsets of nanoindentation triangular load-unload tests using the solution $\hat{\Theta}^{(5)}$. $I \leq 2$ (green, potentially identifiable), $I < 2 \leq 3$ (difficult to identify), $I > 3$ (red, not identifiable).

Combination	2 tests	3 tests	4 tests	5 tests	6 tests	7 tests	8 tests
E, c_1	[0.5; 3.9]	[0.5; 3.3]	[0.5; 2.6]	[0.5; 1.7]	[0.6; 1.2]	[0.6; 0.8]	0.7
c_1, η	[0.4; 2.3]	[0.3; 2.2]	[0.3; 1.7]	[0.3; 1.0]	[0.4; 0.9]	[0.4; 0.7]	0.6
c_1, ν	[0.5; 2.9]	[0.5; 2.4]	[0.5; 1.7]	[0.5; 1.1]	[0.5; 0.9]	[0.5; 0.8]	0.7
E, η	[1.2; 2.3]	[1.1; 2.1]	[1.2; 2.0]	[1.2; 1.8]	[1.3; 1.6]	[1.3; 1.5]	1.4
E, ν	[1.6; 3.1]	[1.6; 2.8]	[1.5; 2.5]	[1.6; 2.2]	[1.6; 2.0]	[1.7; 1.8]	1.7
ν, η	[0.7; 1.5]	[0.7; 1.3]	[0.8; 1.2]	[0.8; 1.1]	[0.8; 1.0]	[0.9; 0.9]	0.9
E, c_1, η	[1.3; 4.2]	[1.3; 3.8]	[1.3; 3.2]	[1.3; 2.1]	[1.3; 1.6]	[1.3; 1.5]	1.4
c_1, ν, η	[1.1; 3.4]	[1.1; 3.0]	[1.0; 2.3]	[1.0; 1.9]	[1.1; 1.6]	[1.2; 1.4]	1.3
E, ν, η	[1.7; 4.3]	[1.6; 4.1]	[1.6; 3.9]	[1.6; 3.1]	[1.7; 2.5]	[1.8; 2.0]	1.9
E, c_1, ν	[2.5; 4.2]	[2.4; 4.0]	[2.4; 3.6]	[2.4; 2.9]	[2.5; 2.7]	[2.5; 2.6]	2.6
E, c_1, ν, η	[3.5; 4.3]	[3.5; 4.3]	[3.5; 4.2]	[3.5; 4.1]	[3.6; 3.9]	[3.7; 3.8]	3.7

4.5.2. Dual nanoindentation

Herein, the combination of the tip angles is numerically investigated in order to determine the better approach to identify the four material properties. Table 4.11 presents the I -index values for all dual nanoindentation using triangular test at 500 nm/min in displacement-controlled mode with the solution $\hat{\Theta}^{(5)}$. Whatever the combination, it is possible to identify two parameters, however, for three parameters, the tips have to be carefully chosen. The value of the I -index for the combination of four parameters from the combination of equivalent cube corner ($\alpha = 42.28^\circ$) and Berkovich ($\alpha = 70.3^\circ$) tips is equal to 2. Contrary to the single nanoindentation, both loading and unloading phases should be used. The identification of all combinations of parameters using loading and unloading phases with these particular tip angles may thus provide a unique solution. The identifiability is difficult from unloading phases and impossible if only loading phases are considered. Figure 4.22 displays the simulated load-displacement

curves for the two indenter tips at 500 nm/min for the solution $\hat{\theta}^{(5)}$. This figure will be employed in an updating process to verify the uniqueness of the solution.

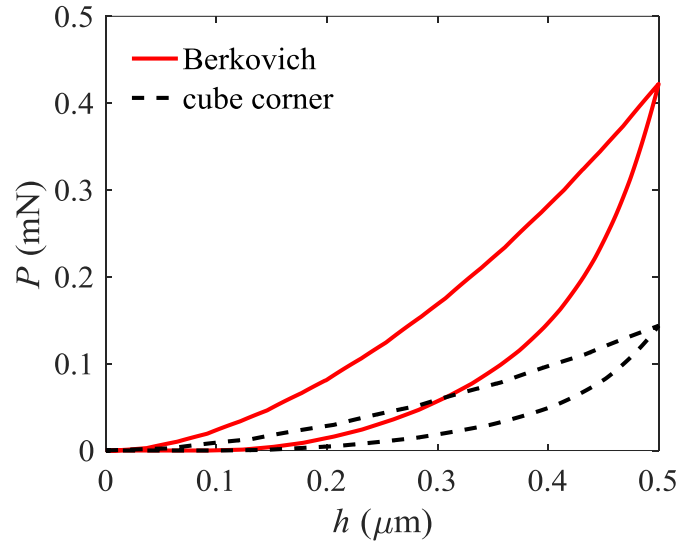


Figure 4.22. Nanoindentation pseudo-experimental (P - h) curves for equivalent cube corner and Berkovich indenter tips at 500 nm/min obtained using the solution $\hat{\theta}^{(5)} = (E = 1.47 \text{ GPa}, c_1 = 0.94 \text{ GPa}, \nu = 0.4, \eta = 17.08 \text{ GPa}\cdot\text{s})$.

Table 4.11. I -index for all combinations of parameters for all dual nanoindentation data at 500 nm/min with the solution $\hat{\theta}^{(5)}$. $I \leq 2$ (green, potentially identifiable), $I < 2 \leq 3$ (difficult to identify), $I > 3$ (red, not identifiable).

Combination	Dual nanoindentation Loads-unloads [$I_{min}; I_{max}$]	Loads-unloads ($\alpha_1 = 42.28^\circ, \alpha_2 = 70.3^\circ$)	Loads	Unloads
E, c_1	[0.6; 0.6]	0.6	2.1	0.8
c_1, η	[0.6; 0.6]	0.6	1.8	0.8
c_1, ν	[1.1; 1.2]	1.1	1.5	1.5
E, η	[1.6; 1.6]	1.6	2.9	0.9
E, ν	[1.5; 1.6]	1.5	1.9	0.9
ν, η	[1.0; 1.1]	1.0	1.6	0.4
E, c_1, η	[1.8; 1.8]	1.8	3.0	1.7
c_1, ν, η	[1.7; 2.3]	1.7	2.1	2.0
E, ν, η	[1.7; 1.8]	1.7	3.0	1.3
E, c_1, ν	[1.9; 2.8]	1.9	2.2	2.1
E, c_1, ν, η	[2.0; 3.3]	2.0	3.1	2.1

After determining the better dual nanoindentation that will probably provide a unique solution of the inverse problem, the norms of sensitivity vectors calculated for the five solutions with cube corner

and Berkovich indenter tips at nanoindentation rate of 500 nm/min using Equation 3.23 are displayed in Figure 4.23 and Figure 4.24. For both indenter tips, the nanoindentation force is sensitive to all parameters. The Young's modulus E and the anelastic modulus c_1 are the most influential. Then the viscosity coefficient in the elastic domain η has almost the same effect expect for all solutions. As for the nanoindentation test at 1000 nm/min, the Poisson's ratio is the least influential parameter for the solutions $\hat{\theta}^{(1)}, \hat{\theta}^{(2)}, \hat{\theta}^{(3)}$ and $\hat{\theta}^{(4)}$.

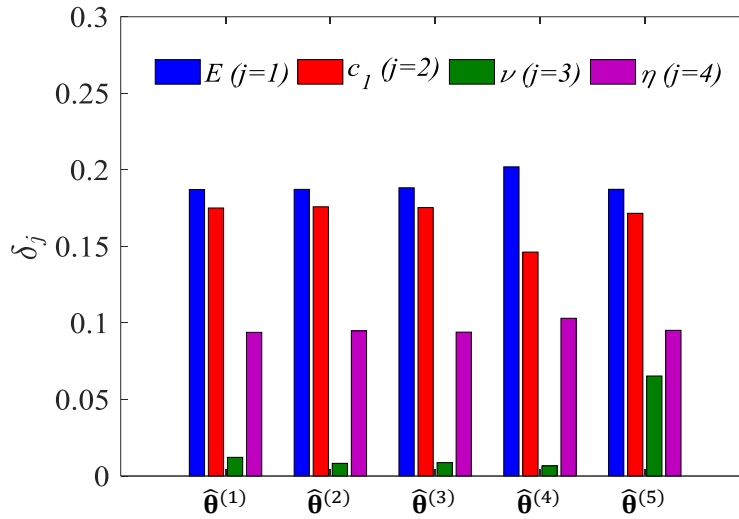


Figure 4.23. Sensitivity of the nanoindentation force P to θ_j for the five solutions $\hat{\theta}^{(1)}, \hat{\theta}^{(2)}, \hat{\theta}^{(3)}, \hat{\theta}^{(4)}$ and $\hat{\theta}^{(5)}$ (Table 4.3) using triangular test with cube corner tip at 500 nm/min.

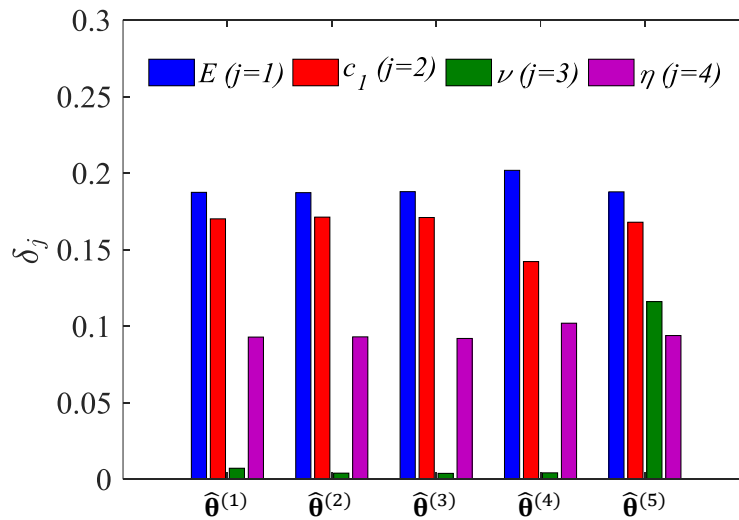


Figure 4.24. Sensitivity of the nanoindentation force P to θ_j for the five solutions $\hat{\theta}^{(1)}, \hat{\theta}^{(2)}, \hat{\theta}^{(3)}, \hat{\theta}^{(4)}$ and $\hat{\theta}^{(5)}$ (Table 4.3) using triangular with Berkovich tip at 500 nm/min.

Figure 4.25 Figure 4.26 show that the vectors are identical during the loading part for the both indenter tips. The identification of these four parameters from the loading phases is thus impossible as

shown by the I -index results. We can note that the sensitivity vectors to E and ν are almost collinear during the loading part (OA) and the first tier of the unloading part (AB) in (Figure 4.25b, Figure 4.26b), thus their identification using a single nanoindentation loading data is impossible with cube corner or Berkovich indenter tip.

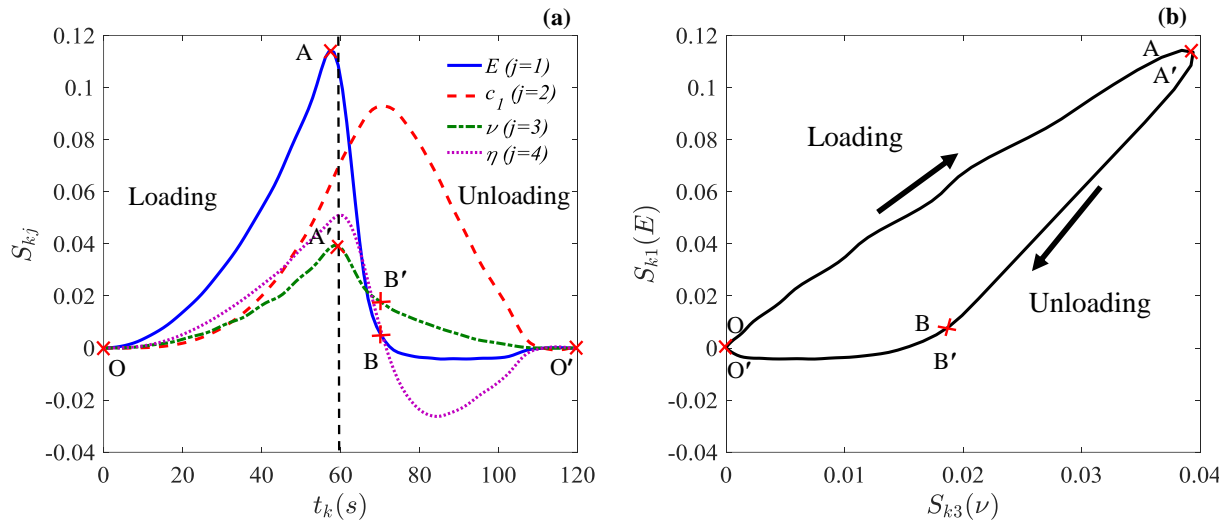


Figure 4.25. (a) Sensitivity vectors of the nanoindentation force to the material parameters θ_j during loading and unloading after smoothing using triangular test at 500 nm/min with cube corner indenter tip. (b) collinearity between sensitivity vectors S_{k1} and S_{k3} (sensitivities to E and ν , respectively).

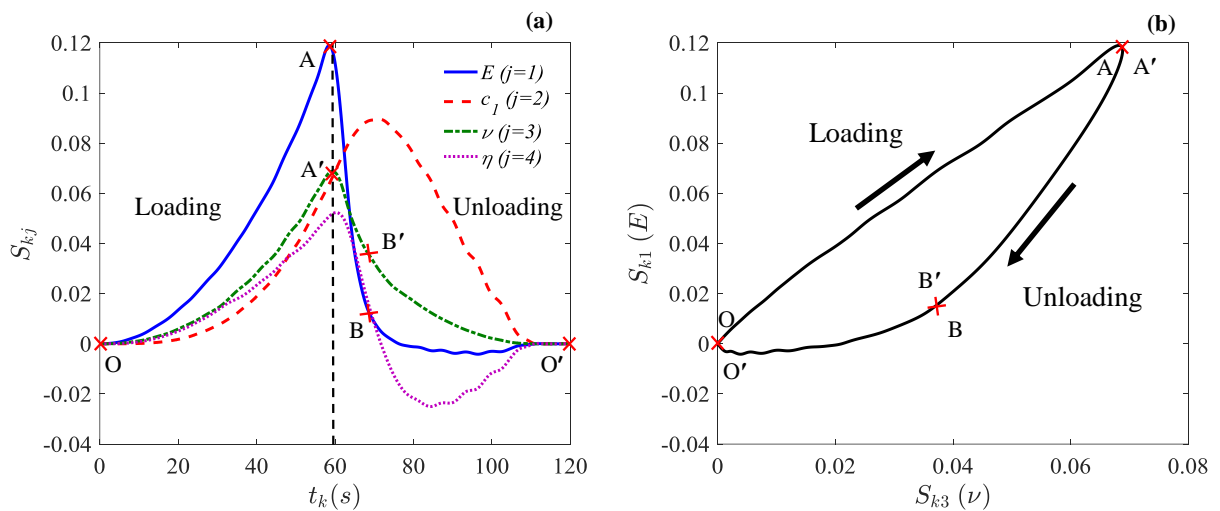


Figure 4.26. (a) Sensitivity vectors of the nanoindentation force to the material parameters θ_j during loading and unloading after smoothing using triangular test at 500 nm/min with Berkovich indenter tip. (b) collinearity between sensitivity vectors S_{k1} and S_{k3} (sensitivities to E and ν , respectively).

As shown above, the results of the identifiability analysis suggest that dual nanoindentation (cube corner and Berkovich) may provide a unique solution for the full set of four unknown parameters.

Herein, three updating processes are thus performed using equivalent cube corner and Berkovich indenter tips with the pseudo-experimental tests at 500 nm/min (Figure 4.22). These updating processes make use of the three starting points $\theta^{(01)}$, $\theta^{(02)}$ and $\theta^{(03)}$. In addition, other starting point $\theta^{(08)}$, which is far from the reference solution is also considered. As expected from I -index results, the obtained solutions are the same for the four starting points (Table 4.12) and almost equal to the solution $\hat{\theta}^{(5)}$. The evolution of the four parameters during the algorithm iterations is illustrated in Figure 4.27. The obtained P - h curves are compared with the pseudo-experimental data (Figure 4.28).

Table 4.12. Estimated solutions for the three starting points using dual nanoindentation.

	Parameter		Starting value	Estimated value
	j	θ_j	$\theta_j^{(0)}$	$\hat{\theta}_j$
Starting point 5: $\theta^{(05)}$	1	E (GPa)	1.50	1.47
	2	c_1 (GPa)	12.25	0.94
	3	ν	0.4 (imposed)	0.4 (imposed)
	4	η (GPa.s)	65	17.08
Objective function $\omega^{(5)}$			4.59×10^{-2}	1.31×10^{-5}
Starting point 1: $\theta^{(01)}$	1	E (GPa)	1.50	1.45
	2	c_1 (GPa)	12.25	0.95
	3	ν	0.4	0.39
	4	η (GPa.s)	65	17.40
Objective function $\omega^{(1)}$			8.56×10^{-1}	2.79×10^{-5}
Starting point 2: $\theta^{(02)}$	1	E (GPa)	1.40	1.45
	2	c_1 (GPa)	8.0	0.95
	3	ν	0.3	0.39
	4	η (GPa.s)	45	17.40
Objective function $\omega^{(2)}$			4.40×10^{-1}	2.79×10^{-5}
Starting point 3: $\theta^{(03)}$	1	E (GPa)	1.20	1.45
	2	c_1 (GPa)	4.0	0.95
	3	ν	0.2	0.39
	4	η (GPa.s)	30	17.40
Objective function $\omega^{(3)}$			1.17×10^{-1}	2.79×10^{-5}
Starting point 8: $\theta^{(08)}$	1	E (GPa)	5.0	1.45
	2	c_1 (GPa)	10	0.95
	3	ν	0.25	0.39
	4	η (GPa.s)	2.0	17.40
Objective function $\omega^{(8)}$			$1.01 \times 10^{+1}$	2.89×10^{-5}

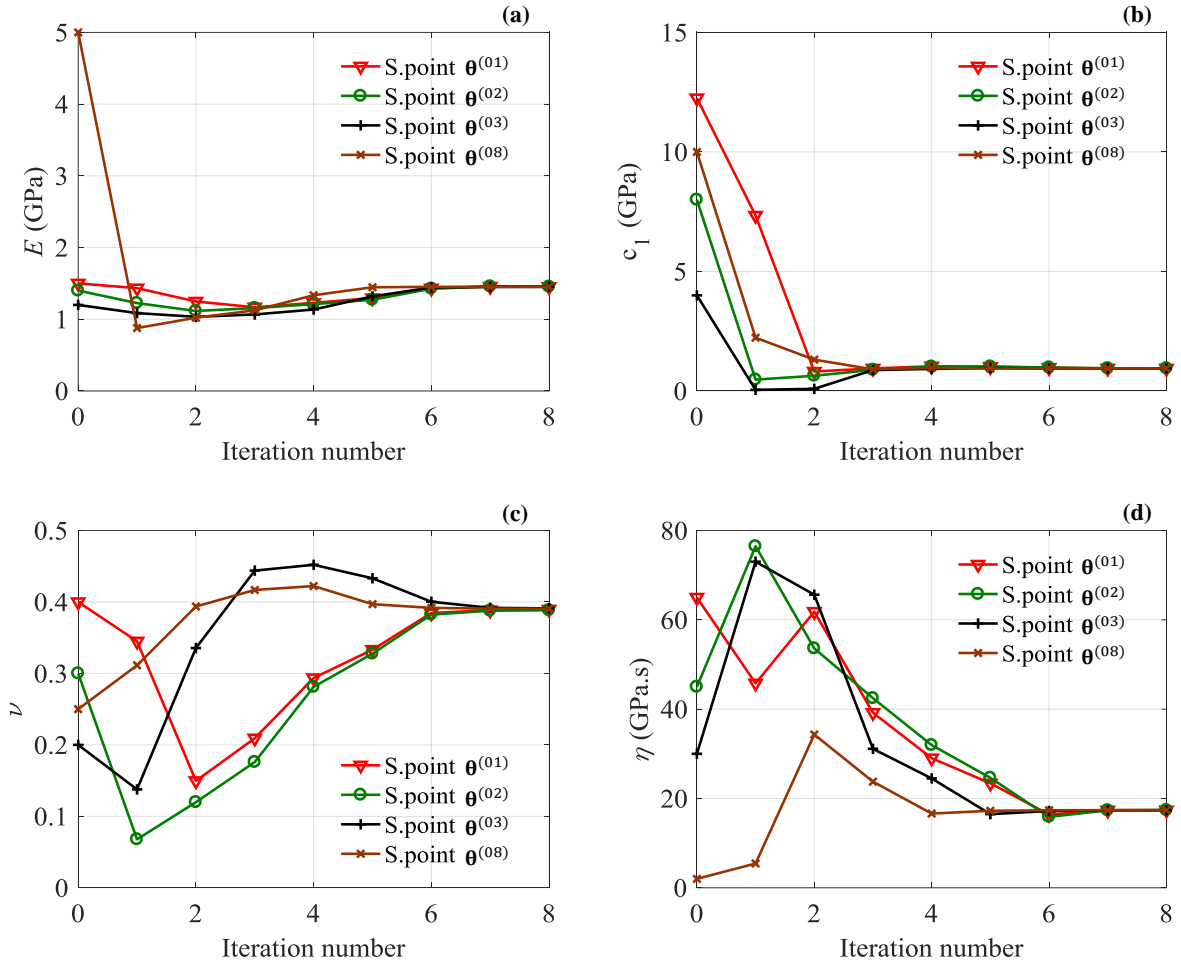


Figure 4.27. Evolution of the 4 parameters (E , c_1 , ν , η) during the updating process using the three starting points $\theta^{(01)}$, $\theta^{(02)}$, $\theta^{(03)}$ and $\theta^{(08)}$ with dual nanoindentation technique.

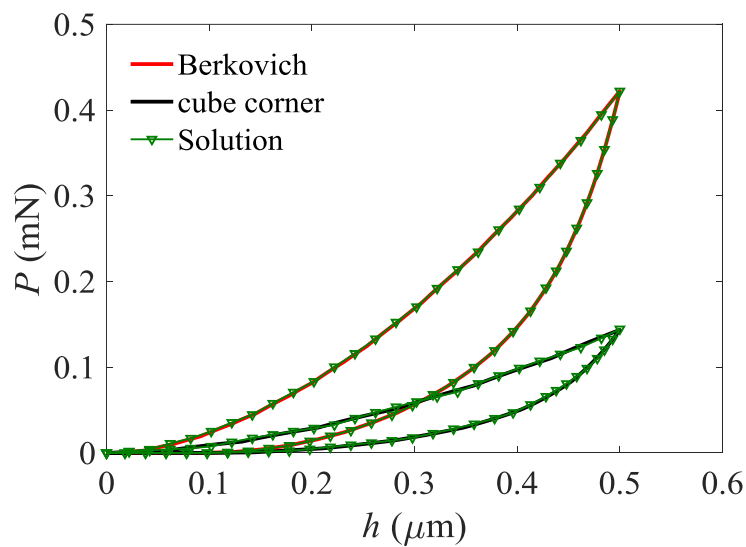


Figure 4.28. Nanoindentation (P - h) pseudo-experimental and simulated curves of the obtained solution.

It is demonstrated that dual nanoindentation test with cube corner and Berkovich indenter tips at 500 nm/min allows to uniquely identify the four VE parameter. In the following section, the effect of the measurement noise on the estimated solution is examined.

4.5.2.1. Effect of measurement noise

The I -index results using two nanoindentation tests performed at nanoindentation depth rate of 500 nm/min with equivalent cube corner and Berkovich indenter tips indicate that it is possible to identify the four parameters ($I(E, c_1, \nu, \eta) = 2$) (Table 4.11). The effect of measurement noise on the obtained solution is investigated. Both the nanoindentation forces obtained with 500 nm/min using equivalent cube corner and Berkovich indenter tips are corrupted by noise according to Equation 4.6 (Figure 4.29).

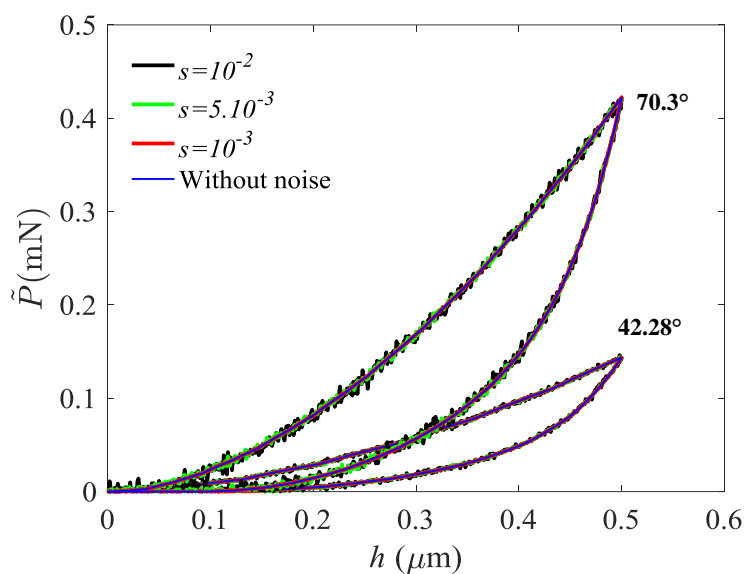


Figure 4.29. Disrupted pseudo-experimental nanoindentation P - h curves ($\dot{h} = 500$ nm/min) for three levels of noise with equivalent cube corner and Berkovich indenter tips obtained using $\hat{\theta}^{(5)}$.

The estimated solutions using Equation 3.1 and the uncertainties (Equation 3.11) for three noise standard deviations are presented in Table 4.13. The four material parameters tend towards the same values whatever the starting point (Figure 4.30) and these values are close to the reference solution (lower than 5%). Comparing with the case of single nanoindentation, the Poisson's ratio uncertainty decreased but still considerable (about 66% for the level 10^{-2}). The solution is not very sensitive to this type of noise, thereby proving the proposed procedure is adequate to retrieve a unique set of viscoelastic parameters.

Table 4.13. Estimated solutions for the three levels of measurement noise using dual nanoindentation with the starting point $\theta^{(02)}$. Reference $\hat{\theta}^{(5)} = (E = 1.47 \text{ GPa}, c_1 = 0.94 \text{ GPa}, \nu = 0.4, \eta = 17.08 \text{ GPa.s})$.

Noise	Parameter	Starting value	Estimated value	Uncertainty
s	j θ_j	$\theta_j^{(0)}$	$\hat{\theta}_j$	$\Delta\theta_j/\theta_j$ (%)
10^{-2}	1 E (GPa)	1.40	1.454	28
	2 c_1 (GPa)	8.0	0.954	18
	3 ν	0.3	0.381	66
	4 η (GPa.s)	45	17.58	47
ω		4.90×10^{-2}	4.89×10^{-4}	
5×10^{-3}	1 E (GPa)	1.40	1.461	16
	2 c_1 (GPa)	8.0	0.945	10
	3 ν	0.3	0.388	34
	4 η (GPa.s)	45	17.28	26
ω		4.96×10^{-2}	1.47×10^{-4}	
10^{-3}	1 E (GPa)	1.40	1.453	7.0
	2 c_1 (GPa)	8.0	0.947	5.0
	3 ν	0.3	0.388	16
	4 η (GPa.s)	45	17.41	12
ω		4.94×10^{-2}	3.26×10^{-5}	
0	1 E (GPa)	1.40	1.454	7.0
	2 c_1 (GPa)	8.0	0.947	4.0
	3 ν	0.3	0.388	15
	4 η (GPa.s)	45	17.40	11
ω		4.40×10^{-1}	2.79×10^{-5}	

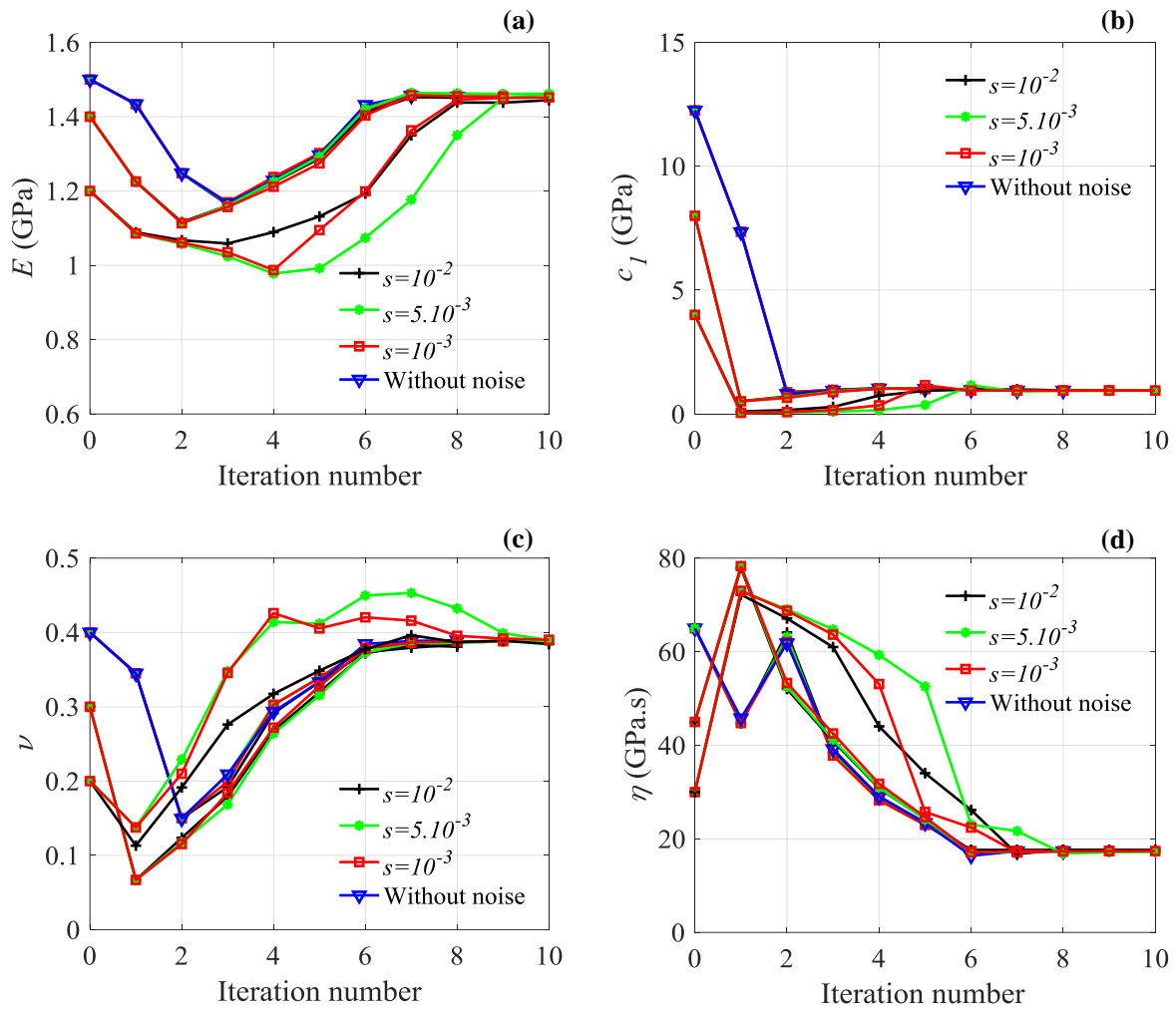


Figure 4.30. Evolution of the 4 parameters (E , c_1 , ν , η) during the updating process for the three starting points of the minimization algorithm $\theta^{(01)}$, $\theta^{(02)}$ and $\theta^{(03)}$ using noisy force values of dual nanoindentation data.

4.6. Estimation of the VE behavior parameters from dual nanoindentation experimental data

In this section, two experimental nanoindentation tests ($n = 2$) carried out using the cube corner and Berkovich indenter tips at depth rate of 500 nm/min are considered (see Chapter 2). For the updating process, the starting point $\theta^{(01)}$ is chosen to initialize the minimization algorithm. The identified parameters are summarized in Table 4.14. Unlike the updating process using single test for the VE behavior (Table 4.3), the Poisson's ratio tends to the limit value ($\nu = 0.5$). The nanoindentation experimental P - h curves and the numerical results are plotted in Figure 4.31. The results show a poor agreement between the experimental data and the updating process results. This may be due to the plastic

deformation in the material behavior. It can be concluded that under nanoindentation, the PP is probably not only deformed in the viscoelastic domain.

Table 4.14. Estimated parameters of the viscoelastic behavior using the dual nanoindentation (cube corner and Berkovich tips).

	Parameter		Starting value	Estimated value
	j	θ_j	$\theta_j^{(0)}$	$\hat{\theta}_j$
Starting point: $\theta^{(01)}$	1	E (GPa)	1.50	1.03
	2	c_1 (GPa)	12.25	0.17
	3	ν	0.4	0.5
	4	η (GPa.s)	65	49.17
Objective function ω			2.24	6.71×10^{-2}

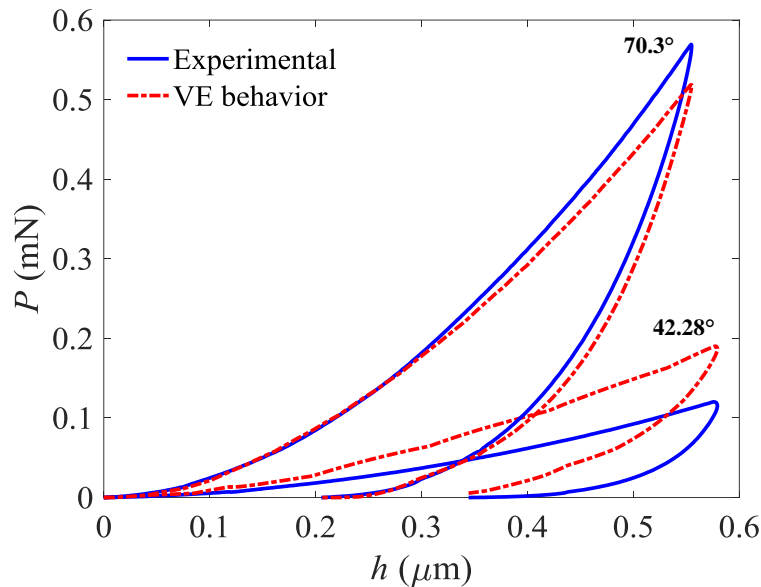


Figure 4.31. Nanoindentation (P - h) experimental and simulated curves for the viscoelastic behavior from dual nanoindentation with cube corner and Berkovich indenter tips at 500 nm/min.

4.7. Assessment of the VE behavior

In order to examine the validity of the VE behavior, FE simulations are carried out using all experimental tests performed at single nanoindentation rate with cube corner and Berkovich indenter tips (Chapter 2) for the solution $\hat{\theta}^{(5)} = (E = 1.47 \text{ GPa}, c_1 = 0.94 \text{ GPa}, \nu = 0.4, \eta = 17.08 \text{ GPa.s})$. The P - h curves are presented in Figure 4.32 and Figure 4.33. For both indenter tips, it can be observed that the shape of the numerical curves changes by increasing the indentation rate. The comparison of the experimental and numerical curves enables us to deduce that this viscoelastic behavior law is not capable to completely describe the material behavior. The same conclusion is obtained from the comparison

between the numerical simulation using the solution $\hat{\theta}^{(5)}$ and the tensile test (Figure 4.34). It is suggested that using another behavior law, indenter tip geometry or FEM may provide better description of the mechanical behavior of PP. For that, two behavior laws will be studied in the next chapter:

- Viscoelastic-viscoplastic behavior law (VEVP)
- Viscoelastic-plastic behavior law (VEP)

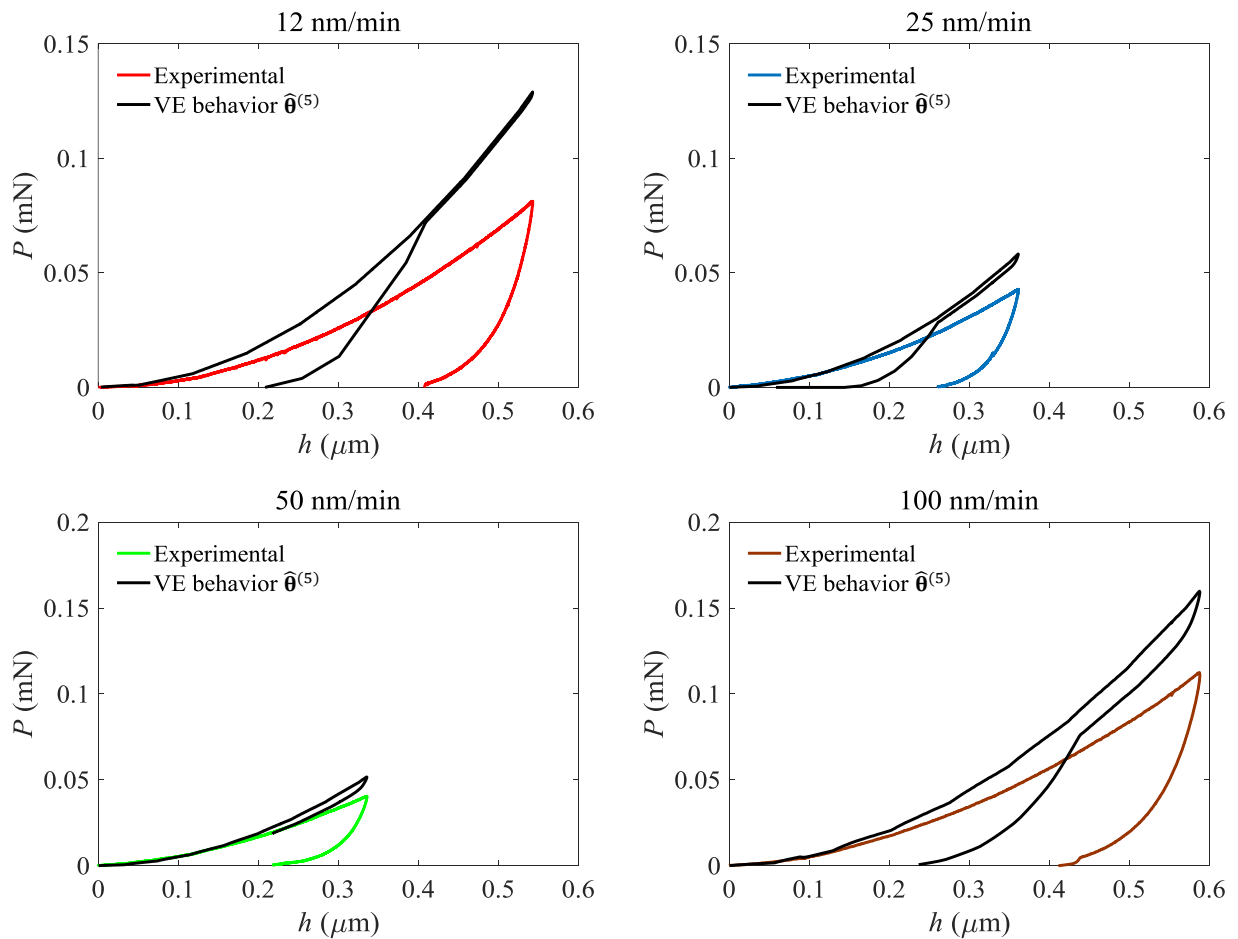


(Figure 4.32 following) →

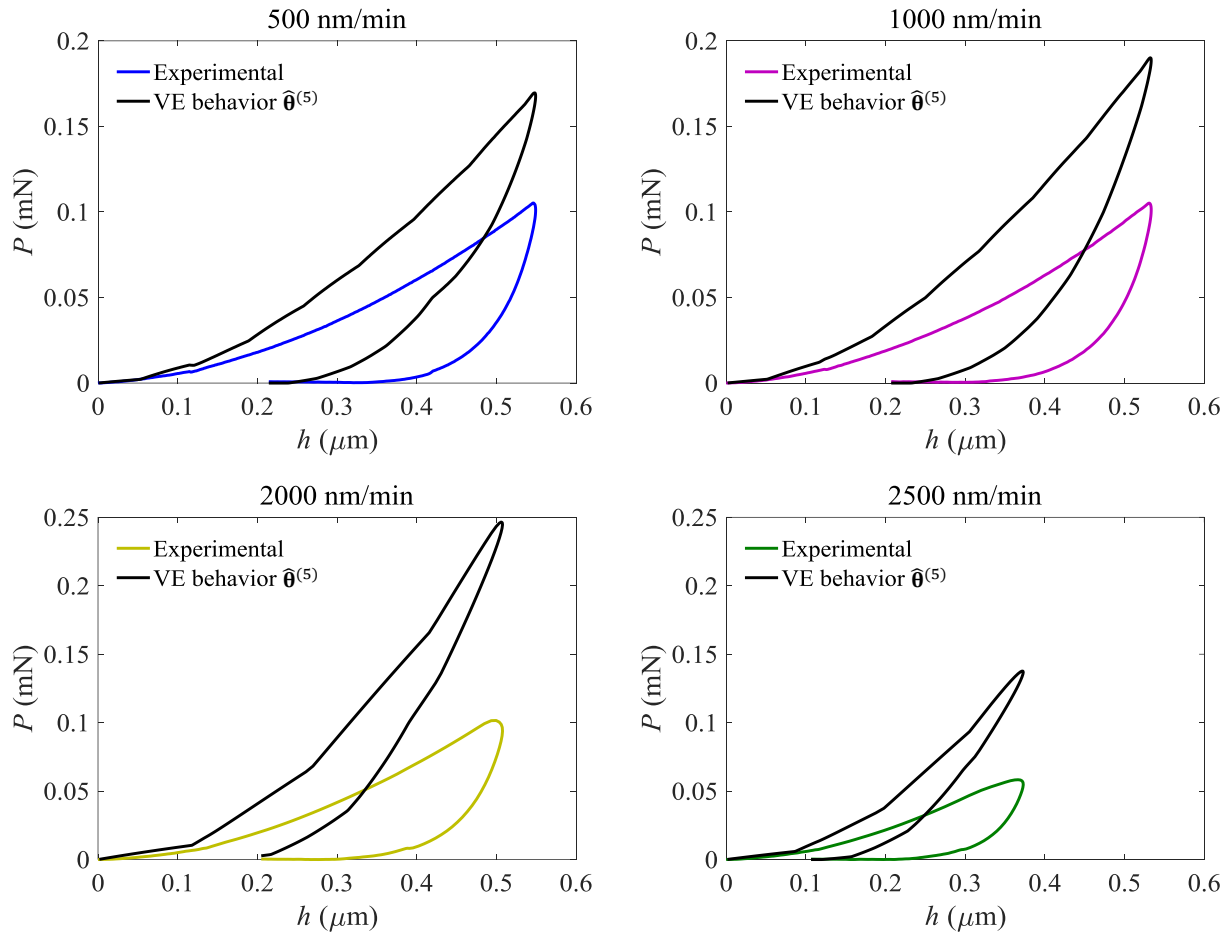
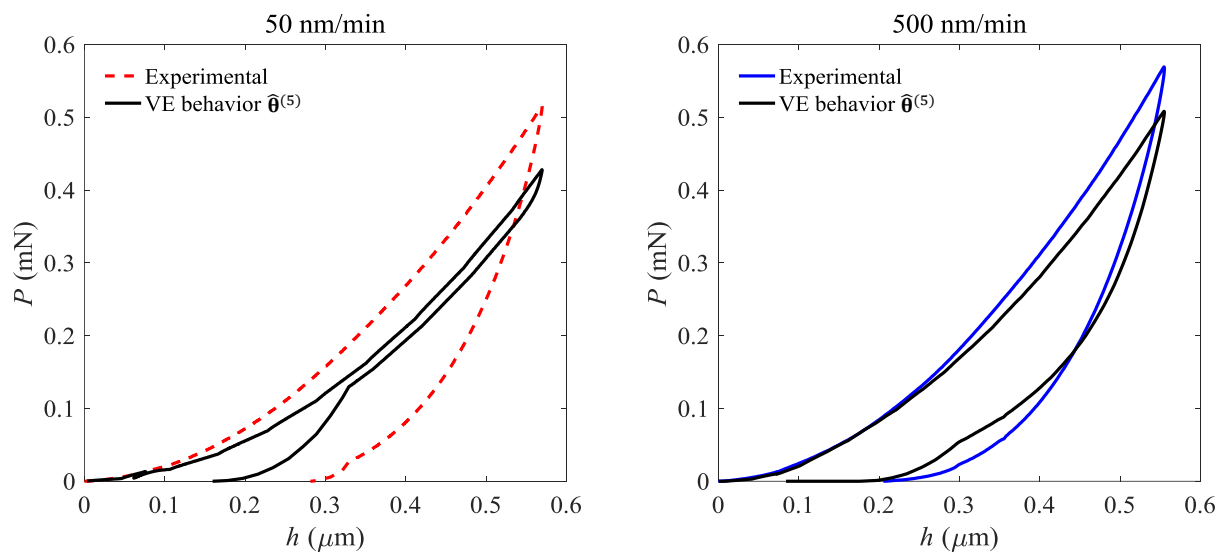


Figure 4.32. Experimental and simulated nanoindentation curves of PP at rates of 12, 25, 50, 100, 500, 1000, 2000, and 2500 nm/min using cube corner tip for the VE behavior with the solution $\hat{\theta}^{(5)}$



(Figure 4.33 following) \rightarrow

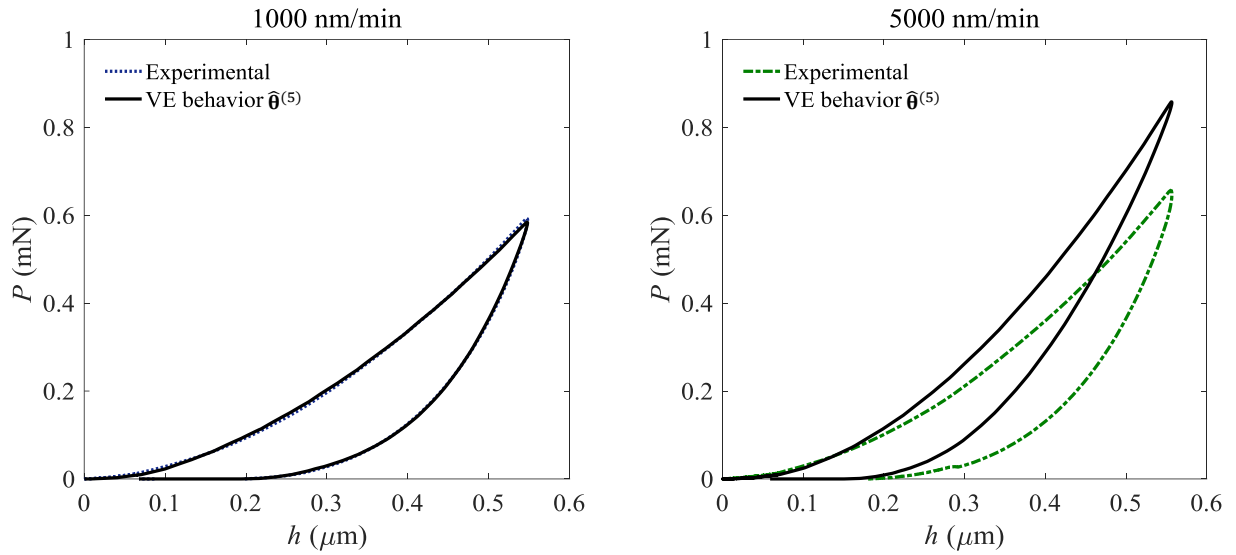


Figure 4.33. Experimental and simulated nanoindentation curves of PP at rates of 50, 500, 1000, and 5000 nm/min using Berkovich indenter tip for the VE behavior with the solution $\hat{\theta}^{(5)}$.

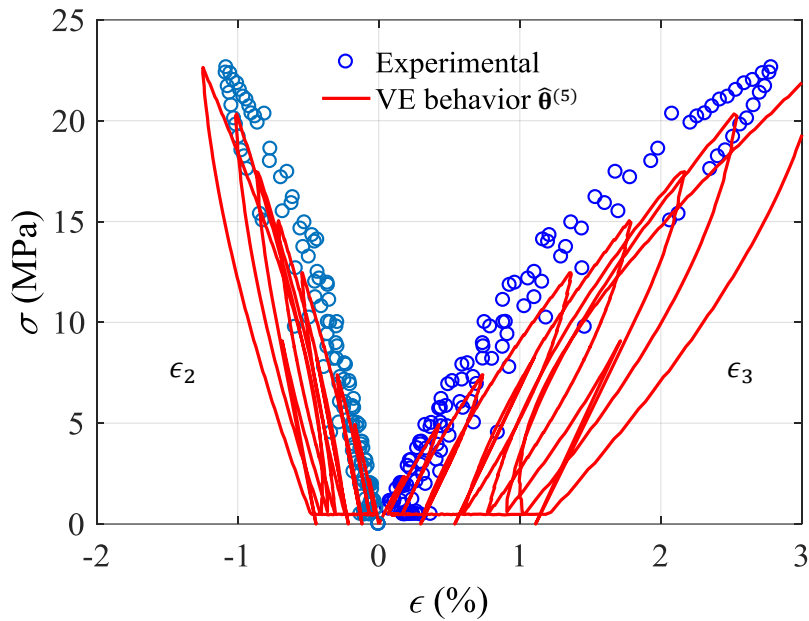


Figure 4.34. Experimental data of the tensile test and simulation response using the VE behavior for the estimated solution $\hat{\theta}^{(5)}$.

4.8. Conclusion

In this chapter, the stability of the viscoelastic properties of polypropylene determined by the FEMU of the nanoindentation test has been studied. A four-parameter viscoelastic behavior law has been implemented in a 2D-axisymmetric FEM. The FEMU method illustrates that a single nanoindentation experimental triangular load-unload test conducted at constant nanoindentation depth rate (~ 1000 nm/min) is not sufficient to uniquely determine the four viscoelastic properties of the material. The updating

process leads to multiple solutions for the values of the four parameters (E, c_1, ν, η) of the viscoelastic behavior law. The identification of the four parameters from a single nanoindentation triangular test is thus considered as impossible. The identifiability analysis allows the quantification of the ill-posed character of the inverse problem by a scalar I -index and shows that it is possible to identify three parameters (E, c_1, η) even if only the unloading phase is taken into account, which proves that the relevant information is in the unloading phase.

The effect of nanoindentation depth rate, loading type (triangular, trapezoidal, exponential, sinusoidal) and tip angle on the identifiability has been numerically investigated. The comparison between the results from the different loading types shows that the identification of the four material parameters is not possible. The included half angle α of the indenter tip does not have a significant influence on the identifiability results. It is also found that the updating process solutions are not very sensitive to the measurement noise.

The comparison between the loss factor and the I -index results from the nanoindentation triangular tests indicates that the better identifiability of the material parameters is obtained at the maximum loss factor, which corresponds to the maximum of the dissipated energy. It is also observed that, whatever the loading type, the best identifiability is obtained if the loss factor is maximum.

The combination of several triangular load-unload tests improves the identification robustness and does not lead to better I -index for the four material parameters compared to a single but properly chosen one. We numerically show that the combination of two nanoindentation triangular tests carried out at a constant nanoindentation depth rate using equivalent cone apex angles of cube corner (42.28°) and Berkovich (70.3°) indenter tips allows for the retrieval of a unique solution of the inverse problem, which is robust with respect to the noise. The four material parameters are potentially identifiable using this experimental protocol if the material behavior is viscoelastic.

The I -index can be used to numerically design the nanoindentation tests which allow to activate the dissipative phenomena as much as possible, thus to identify intrinsic and reliable properties. In order to identify the material behavior, the plasticity phenomena will be taken into account in the behavior law in the next chapter.

Estimation of the viscoelastic-viscoplastic properties of materials from dual nanoindentation

5.1.	Introduction	125
5.2.	Viscoelastic-viscoplastic behavior law.....	125
5.2.1.	Results of the updating procedure for the V EVP behavior law	128
5.2.2.	Assessment of the V EVP behavior	131
5.2.3.	Sensitivity analysis	134
5.2.4.	Identifiability analysis	138
5.3.	Viscoelastic-plastic behavior law	140
5.3.1.	Results of the updating procedure for the V EP behavior law	140
5.3.2.	Assessment of the V EP behavior.....	143
5.3.3.	Sensitivity analysis	146
5.3.4.	Identifiability analysis	150
5.4.	Conclusion.....	152

5.1. Introduction

In the previous chapter, it has been shown that during the nanoindentation test, the polypropylene (PP) does not only exhibit a viscoelastic behavior. The optical images of the imprint show that the indented material does not return to initial state after unloading, which indicates that there is a residual plastic deformation (Figure 5.1). For a complete description of the material behavior, plasticity should be taken into account in the behavior law. In order to identify the mechanical behavior of PP, viscoelastic-viscoplastic (VEVP) and viscoelastic-plastic (VEP) behaviors have been considered. From the literature, the yield strength of PP is about 60 MPa (Ashby, 1994). The sensitivities of the nanoindentation force to the VEVP and VEP behaviors parameters is assessed. The identifiability analysis is carried out in order to extract accurate mechanical properties of the material.

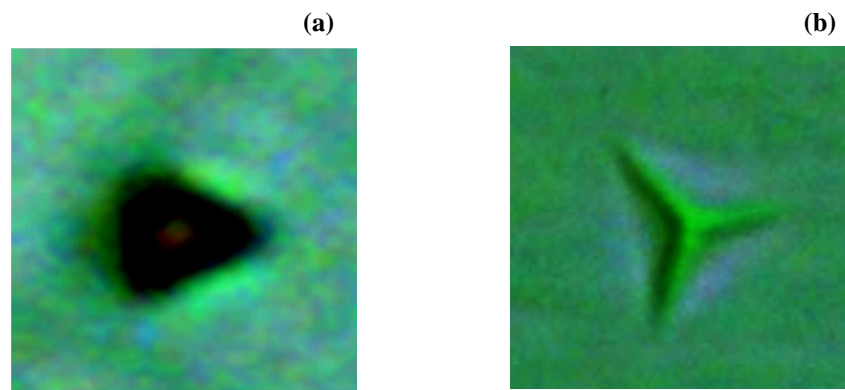


Figure 5.1. Optical images of imprints on PP samples. (a) cube corner indenter tip ($2.48 \times 2.48 \mu\text{m}^2$).
(b) Berkovich indenter tip ($6.55 \times 6.55 \mu\text{m}^2$).

5.2. Viscoelastic-viscoplastic behavior law

As mentioned in the Chapter 1, behavior laws, which combine viscoelasticity and viscoplasticity have been proposed to investigate the mechanical behavior of polymers (Kermouche et al., 2013; Chen et al., 2015). For example, the behavior law developed by Chen et al, which is controlled by ten parameters, is fully capable to reproduce the mechanical behavior of UHMWPE (Figure 1.19). In this section, the viscoelastic-viscoplastic (VEVP) behavior law established by Poilâne et al. (Poilâne et al., 2014) and implemented in ANSYS FE software through UMAT subroutine is used for the investigation of the material behavior. The rheological model consists in the connection in series of the VE model presented in Chapter 4.2 and a VP model, which is composed of a linear spring of hardening coefficient c_2 , a linear viscous damper of viscosity K which is associated with a plastic slider of yield strength σ_y in parallel (Figure 5.2). This VEVP behavior involves seven parameters as follows:

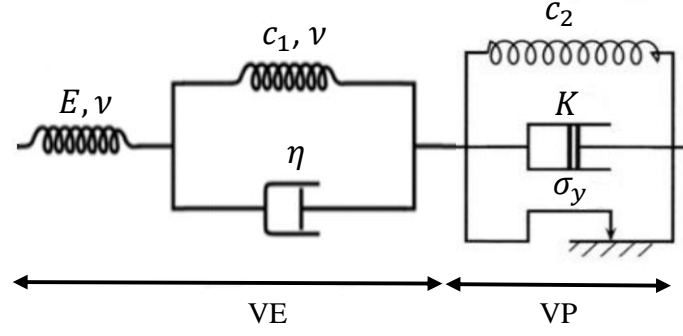


Figure 5.2. V EVP rheological model.

The total strain tensor $\boldsymbol{\varepsilon}$ is defined as the sum of the elastic $\boldsymbol{\varepsilon}^e$, anelastic $\boldsymbol{\varepsilon}^{an}$ and viscoplastic $\boldsymbol{\varepsilon}^{vp}$ strains:

$$\boldsymbol{\varepsilon} = \boldsymbol{\varepsilon}^e + \boldsymbol{\varepsilon}^{an} + \boldsymbol{\varepsilon}^{vp} \quad (5.1)$$

The viscoelastic strain $\boldsymbol{\varepsilon}^{ve}$ is given by the sum of the elastic and anelastic strains:

$$\boldsymbol{\varepsilon}^{ve} = \boldsymbol{\varepsilon}^e + \boldsymbol{\varepsilon}^{an} \quad (5.2)$$

The inelastic strain $\boldsymbol{\varepsilon}^{in}$ is defined as the sum of the anelastic $\boldsymbol{\varepsilon}^{an}$ and viscoplastic $\boldsymbol{\varepsilon}^{vp}$ strains:

$$\boldsymbol{\varepsilon}^{in} = \boldsymbol{\varepsilon}^{an} + \boldsymbol{\varepsilon}^{vp} \quad (5.3)$$

Based on the framework of irreversible thermodynamics, the Helmholtz free energy is given by (Lemaitre and Chaboche, 1994):

$$\psi = \frac{1}{2\rho} \left(\boldsymbol{\varepsilon}^e : \mathbf{C} : \boldsymbol{\varepsilon}^e + \boldsymbol{\alpha}_1 : \mathbf{C}_1 : \boldsymbol{\alpha}_1 + \frac{2}{3} \boldsymbol{\alpha}_2 : \mathbf{C}_2 : \boldsymbol{\alpha}_2 \right) \quad (5.4)$$

where $\boldsymbol{\varepsilon}^e$ is the elastic strains tensor, $\boldsymbol{\alpha}_i$ is the internal variables tensors representing the inelastic phenomena, ρ is the density, $\mathbf{C}(E, \nu)$, $\mathbf{C}_1(c_1, \nu)$ and $\mathbf{C}_2(c_2)$ are the elastic, anelastic and viscoplastic stiffness tensors which are defined by:

$$\boldsymbol{\sigma} = \mathbf{C}(E, \nu) : \boldsymbol{\varepsilon} \quad \text{with the Hooke's law } \sigma_{ij} = \frac{E}{1+\nu} \left[\varepsilon_{ij} + \frac{\nu}{1-2\nu} \varepsilon_{kk} \delta_{ij} \right] \quad (5.5)$$

$$\mathbf{C}_1(c_1, \nu) = \frac{c_1}{E} \mathbf{C} \quad (5.6)$$

$$\mathbf{C}_2(c_2) = c_2 \mathbf{I}_4 \quad (5.7)$$

where E , ν , c_1 and c_2 are the instantaneous modulus, the Poisson's ratio, the anelastic modulus and the coefficient of the linear kinematic hardening, respectively; the symbol “:” stands for the tensor inner product, \mathbf{I}_4 is a fourth-order identity tensor. The state laws derive from this energy:

$$\boldsymbol{\sigma} = \rho \frac{\partial \psi}{\partial \boldsymbol{\varepsilon}^e}, \quad \mathbf{X}_1 = \rho \frac{\partial \psi}{\partial \boldsymbol{\alpha}_1} \quad \text{and} \quad \mathbf{X}_2 = \rho \frac{\partial \psi}{\partial \boldsymbol{\alpha}_2} \quad (5.8)$$

where $\boldsymbol{\sigma}$ is the Cauchy stress tensor, \mathbf{X}_1 and \mathbf{X}_2 are the tensors representing the inelastic phenomena.

The dissipation potential Ω is defined as follows:

$$\Omega = \frac{E}{2\eta} (\boldsymbol{\sigma} - \mathbf{X}_1) : \mathbf{S} : (\boldsymbol{\sigma} - \mathbf{X}_1) + \frac{1}{2K} \langle f \rangle^2 \quad (5.9)$$

where η and K are the viscosity coefficients in the viscoelastic and viscoplastic domains, \mathbf{S} the elastic compliance (fourth-order) tensor such as $\mathbf{S} : \mathbf{C} = \mathbf{I}$ (identity tensor).

The function f is given by:

$$f(\boldsymbol{\sigma}, \mathbf{X}_2) = \overline{\boldsymbol{\sigma} - \mathbf{X}_2} - \sigma_y \quad (5.10)$$

where σ_y is the yield strength.

The Von Mises stress is expressed as follows:

$$\overline{\boldsymbol{\sigma} - \mathbf{X}_2} = \sqrt{\frac{3}{2} \text{dev}(\boldsymbol{\sigma} - \mathbf{X}_2) : \text{dev}(\boldsymbol{\sigma} - \mathbf{X}_2)} \quad (5.11)$$

where $\text{dev}(\boldsymbol{\sigma} - \mathbf{X}_2)$ is expressed as:

$$\text{dev}(\boldsymbol{\sigma} - \mathbf{X}_2) = (\boldsymbol{\sigma} - \mathbf{X}_2) - \frac{1}{3} \text{Tr}(\boldsymbol{\sigma} - \mathbf{X}_2) \mathbf{I} \quad (5.12)$$

The Macaulay brackets correspond to:

$$\langle f \rangle = \begin{cases} 0, & \text{if } f < 0 \\ f, & \text{if } f \geq 0 \end{cases} \quad (5.13)$$

By deriving the Helmholtz free energy ψ according to the Equation 5.8, we obtain the state laws:

$$\boldsymbol{\sigma} = \mathbf{C} : \boldsymbol{\varepsilon}^e \quad (5.14)$$

$$\mathbf{X}_1 = \frac{c_1}{E} \mathbf{C} : \boldsymbol{\alpha}_1 \quad (5.15)$$

$$\mathbf{X}_2 = \frac{2}{3} c_2 \boldsymbol{\alpha}_2 \quad (5.16)$$

The derivatives of the potential Ω give the internal variables evolutions:

$$\dot{\boldsymbol{\epsilon}}^{in} = \dot{\boldsymbol{\alpha}}_1 + \dot{\boldsymbol{\alpha}}_2 \quad (5.17)$$

$$\dot{\boldsymbol{\alpha}}_1 = \frac{E}{\eta} \mathbf{S} : (\boldsymbol{\sigma} - \mathbf{X}_1) \quad (5.18)$$

$$\dot{\boldsymbol{\alpha}}_2 = \frac{1}{K} \langle f \rangle \frac{\text{dev}(\boldsymbol{\sigma} - \mathbf{X}_2)}{\boldsymbol{\sigma} - \mathbf{X}_2} \quad (5.19)$$

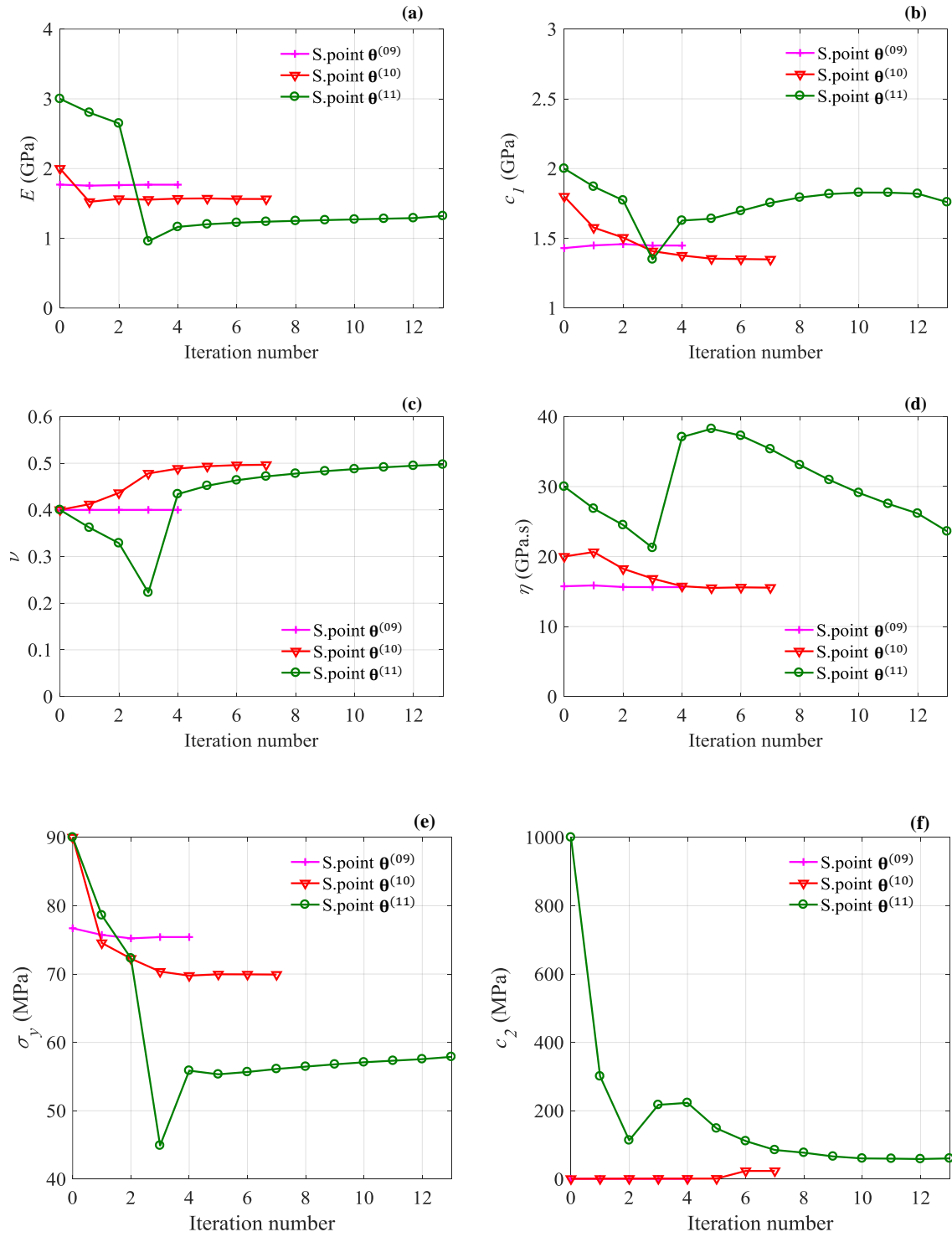
This V EVP behavior law is controlled by seven material parameters, which define the parameter set $\boldsymbol{\theta} = (\theta_1, \theta_2, \theta_3, \theta_4, \theta_5, \theta_6, \theta_7) = (E, c_1, \nu, \eta, \sigma_y, c_2, K)$. In order to determine these parameters from nanoindentation responses, the FEMU method is employed. The identifiability index (*I*-index) introduced in Chapter 3.5 is then used to examine the parameters identifiability.

5.2.1. Results of the updating procedure for the V EVP behavior law

Herein, two experimental triangular tests realized at nanoindentation depth rate of 500 nm/min with cube corner and Berkovich indenter tips in displacement-controlled mode are used for the updating process of the 2D-axisymmetric FEM to identify the V EVP properties of material (Equation 3.1). Three starting points $\boldsymbol{\theta}^{(09)}$, $\boldsymbol{\theta}^{(10)}$, and $\boldsymbol{\theta}^{(11)}$ are considered for the minimization algorithm (Table 5.1). The computation time for each identification is about 30 days. The evolution of the seven parameters during the minimization process are displayed in Figure 5.3. It can be seen that the estimated parameters are not the same for the three starting points. In the case the Poisson's ratio is imposed, the algorithm converges faster with less iterations. Comparing with the VE behavior results (Chapter 4.6), the objective function value decreases, which indicates that the V EVP behavior is more adapted to the description of the material behavior. Despite the difference observed between the estimated parameters, Figure 5.4 shows that the numerical and experimental *P-h* curves are nearly the same.

Table 5.1. Estimated parameters set $\hat{\theta}$ (Equation 3.1) for the V EVP behavior law using three starting points.

	Parameter	Starting value	Estimated value
j	θ_j	$\theta_j^{(0)}$	$\hat{\theta}_j$
Starting point 09: $\theta^{(09)}$	1 E (GPa)	1.77	1.77
	2 c_1 (GPa)	1.43	1.45
	3 ν	0.4 (imposed)	0.4 (imposed)
	4 η (GPa. s)	15.75	15.63
	5 σ_y (MPa)	76.60	75.40
	6 c_2 (GPa)	10^{-3}	9.7×10^{-4}
	7 K (GPa. s)	10^{-4}	1.03×10^{-4}
Objective function $\omega^{(9)}$		1.90×10^{-2}	2.30×10^{-3}
Starting point 10: $\theta^{(10)}$	1 E (GPa)	2.0	1.56
	2 c_1 (GPa)	1.8	1.35
	3 ν	0.4	0.5
	4 η (GPa. s)	20	15.55
	5 σ_y (MPa)	90	69.92
	6 c_2 (GPa)	10^{-3}	2.4×10^{-2}
	7 K (GPa. s)	10^{-4}	2.5×10^{-3}
Objective function $\omega^{(10)}$		7.43×10^{-2}	1.93×10^{-3}
Starting point 11: $\theta^{(11)}$	1 E (GPa)	3.0	1.32
	2 c_1 (GPa)	2.0	1.76
	3 ν	0.4	0.5
	4 η (GPa. s)	30	23.60
	5 σ_y (MPa)	90	57.88
	6 c_2 (GPa)	1.0	6.06×10^{-2}
	7 K (GPa. s)	0.1	7.80×10^{-3}
Objective function $\omega^{(11)}$		1.03	4.28×10^{-3}



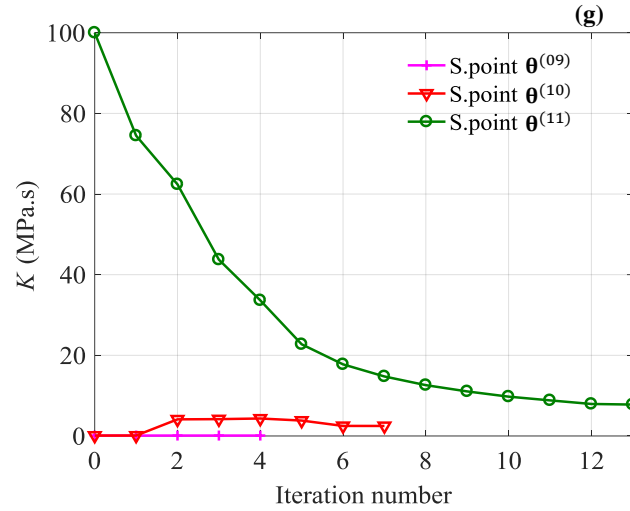


Figure 5.3. Evolution of the seven parameters ($E, c_1, \nu, \eta, \sigma_y, c_2, K$) of the V EVP behavior during the updating process using the three starting points $\theta^{(09)}$, $\theta^{(10)}$ and $\theta^{(11)}$ with dual nanoindentation technique.

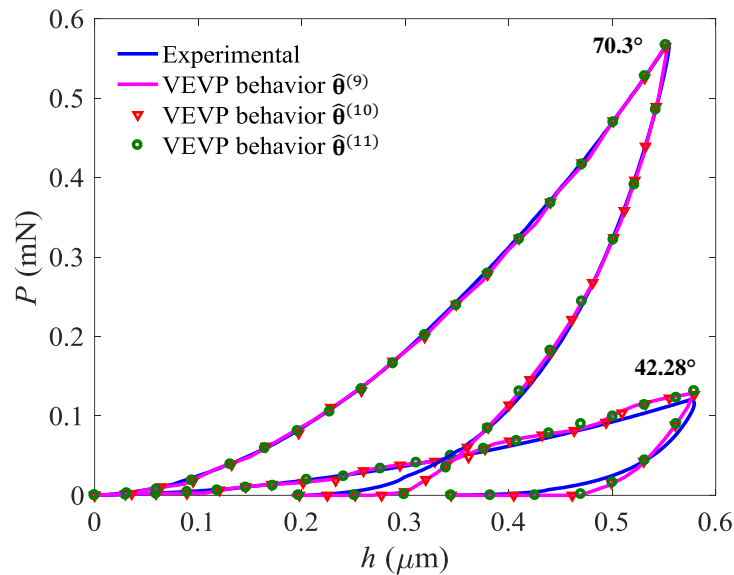
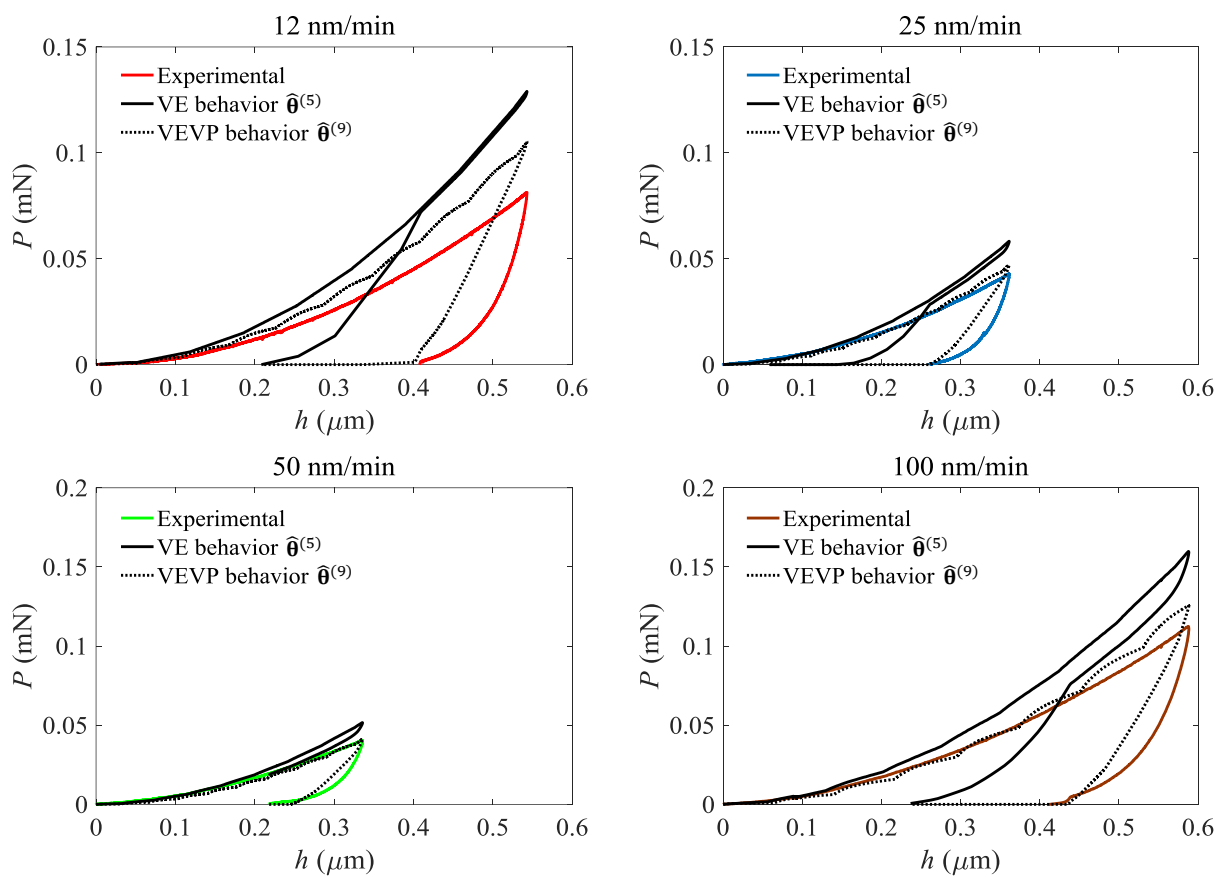


Figure 5.4. Experimental ($\dot{h} = 500$ nm/min) and simulated nanoindentation (P - h) curves using cube corner and Berkovich indenter tips for the three V EVP solutions (Table 5.1).

5.2.2. Assessment of the V EVP behavior

In this section, 2D-axisymmetric FEM is used to evaluate the V EVP behavior prediction. The solution $\hat{\theta}^{(9)} = (E = 1.77$ GPa, $c_1 = 1.45$ GPa, $\nu = 0.4$ (imposed), $\eta = 15.63$ GPa.s, $\sigma_y = 75.40$ MPa, $c_2 = 9.7 \times 10^{-4}$ GPa, $K = 1.03 \times 10^{-4}$ GPa.s) is considered for the numerical simulations using all experimental tests carried out with cube corner and Berkovich indenter tips (Chapter 2.3). The experimental and numerical P - h curves are plotted in Figure 5.5 and Figure 5.6. For both indenter tips, the numerical results are improved comparing with those obtained using the VE behavior (Chapter 4.7).

It is obvious that for the test performed at 500 nm/min, the P - h curves are in a good agreement with the experimental data. It also can be seen that increasing the depth rate, the behavior law does not predict the material behavior and particularly the elastic return. Concerning the Berkovich indenter tip (Figure 5.6), the behavior prediction agrees nearly with the loading segment of the nanoindentation tests performed at 50 nm/min, 500 nm/min and 1000 nm/min. The difference between the numerical and experimental P - h curves may be due to the rounded indenter tip effect or the geometry of the FEM. The numerical simulations using the 3D FEM may be useful to improve the results. A comparison between a tensile test and the V EVP behavior using the solution $\hat{\theta}^{(9)}$ is given in Figure 5.7. The numerical result and experimental data are almost in good agreement. These results show that the V EVP law is better for describing the material behavior than the VE one.



(Figure 5.5 following) →

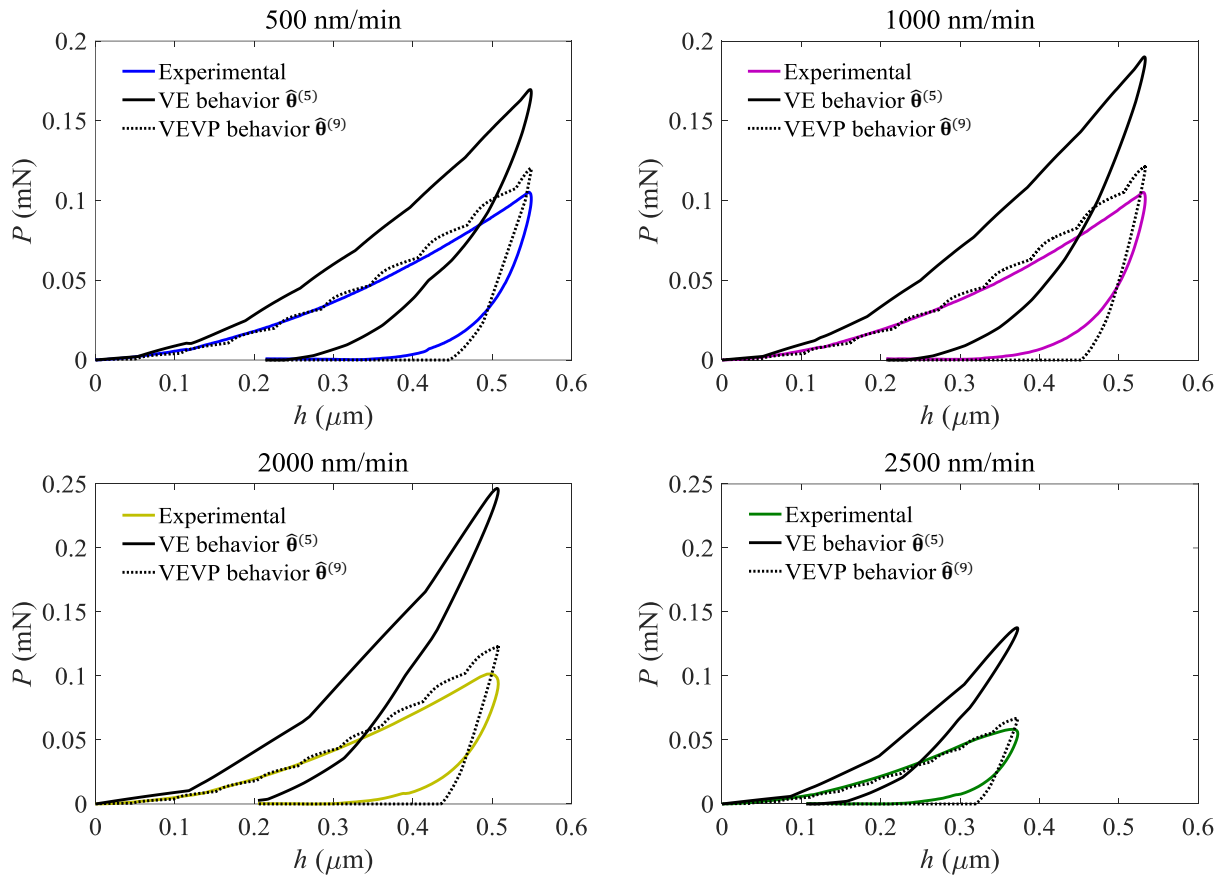
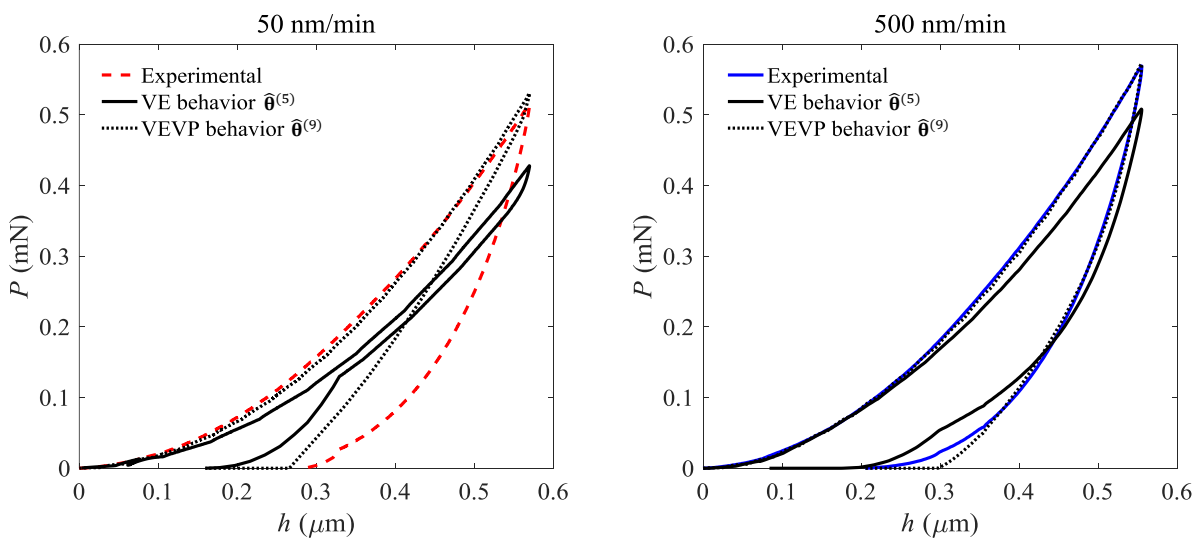


Figure 5.5. Experimental and simulated nanoindentation ($P-h$) curves of PP at rates of 12, 25, 50, 100, 500, 1000, 2000, and 2500 nm/min using cube corner indenter tip for the V EVP behavior with the solution $\hat{\theta}^{(9)}$.



(Figure 5.6 following) \rightarrow

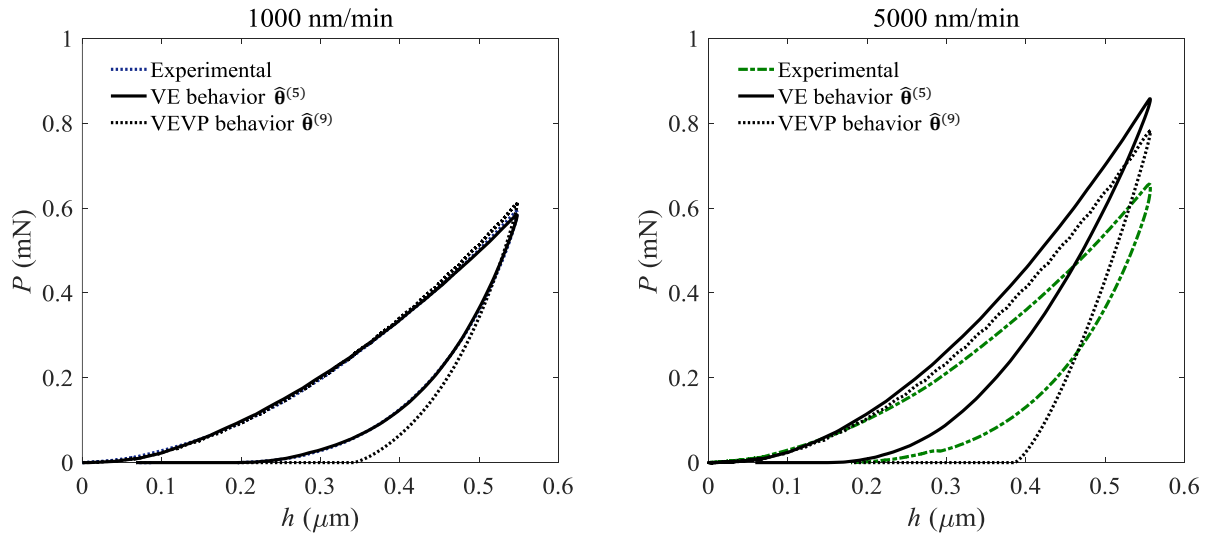


Figure 5.6. Experimental and simulated nanoindentation (P - h) curves of PP at rates of 50, 500, 1000, and 5000 nm/min using Berkovich indenter tip for the VE behavior with the solution $\hat{\theta}^{(5)}$ and V EVP behavior with $\hat{\theta}^{(9)}$.

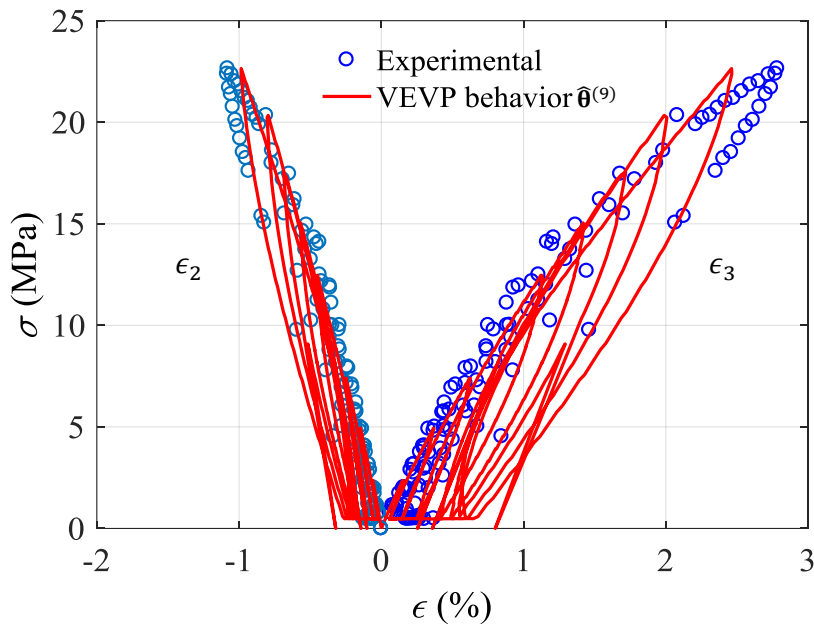


Figure 5.7. Experimental data of the tensile test and simulation response using the V EVP behavior for the estimated solution $\hat{\theta}^{(9)}$.

5.2.3. Sensitivity analysis

In this section, a sensitivity analysis is performed for the solution $\hat{\theta}^{(9)}$ (with imposed Poisson's ratio) using nanoindentation tests conducted at 500 nm/min with cube corner and Berkovich indenter tips. The tests are discretized in $T_1 = 940$ points for cube corner indenter tip and $T_2 = 1000$ points for

the Berkovich indenter tip. The relative perturbation ε is set to 5×10^{-3} . The norms of the sensitivity vectors δ_j are defined as:

$$\delta_j = \sum_{e=1}^2 \frac{\hat{\theta}_j^{(9)}}{P_{max}^{(e)}} \sqrt{\frac{1}{T_e} \sum_{k=1}^{T_e} \left(\frac{\partial P_k^{(e)}}{\partial \theta_j} \Big|_{\hat{\theta}^{(9)}} \right)^2} \quad (5.20)$$

Figure 5.8 shows that the nanoindentation force is sensitive to the seven V EVP parameters ($E, c_1, \nu, \eta, \sigma_y, c_2, K$). The yield strength σ_y is the most influential one. Then, the sensitivities to the VE parameters E, c_1, ν and η are of almost similar magnitudes. The hardening coefficient c_2 and the viscosity coefficient K are the least sensitive parameters, which can be due to their low values. The ratio between the norms of the sensitivities of σ_y (most sensitive) and c_2 (least sensitive) is about 28.8. It also appears that for both indenter tips, the sensitivity to (c_2, K) are close to zero. This may affect the identifiability of the behavior law parameters.

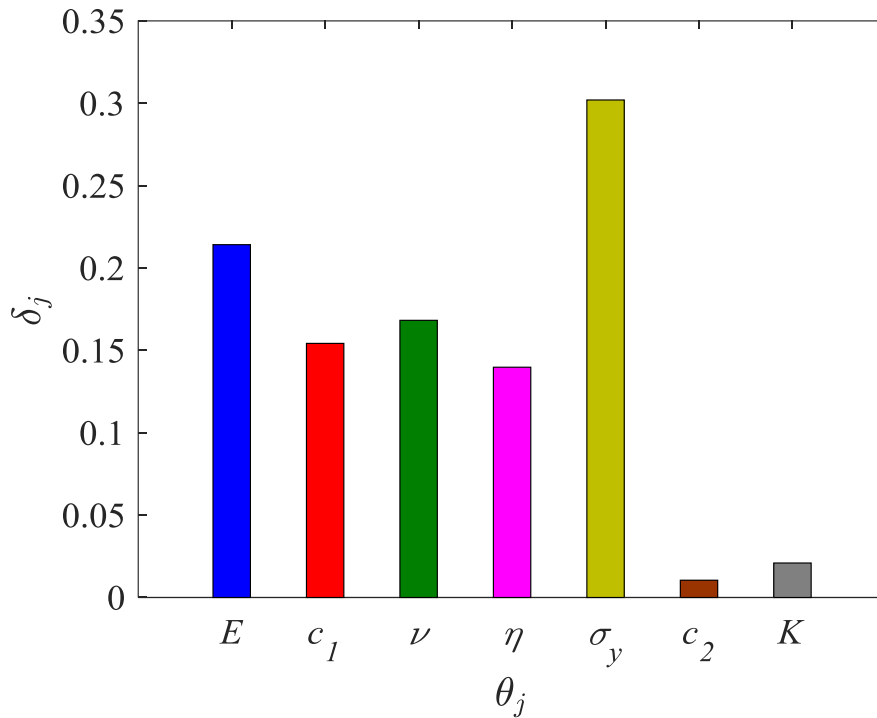
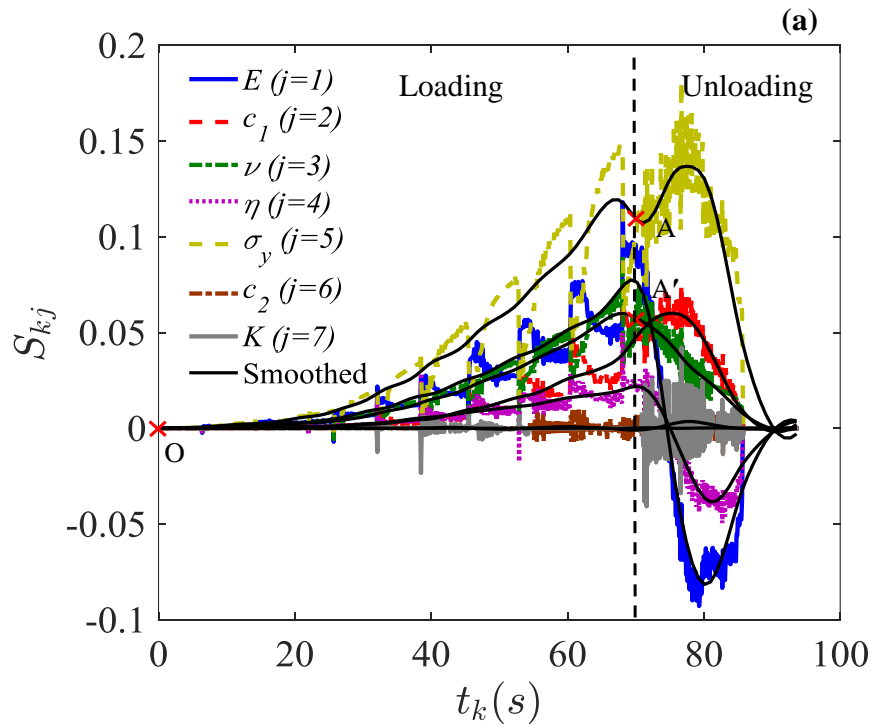


Figure 5.8. Sensitivity of the nanoindentation force P to θ_j for the solution $\hat{\theta}^{(9)}$ using nanoindentation tests performed with cube corner and Berkovich indenter tips for the V EVP behavior.

The sensitivity vectors of the nanoindentation force to the behavior law parameters are calculated using the following equation:

$$S_{kj} = \sum_{e=1}^2 \frac{\hat{\theta}_j^{(9)}}{P_{max}^{(e)}} \frac{\partial P_k^{(e)}}{\partial \theta_j} \bigg|_{\hat{\theta}^{(9)}} \approx \sum_{e=1}^2 \frac{(1 + \varepsilon) \hat{\theta}_j^{(9)}}{P_{max}^{(e)}} \frac{\partial P_k^{(e)}}{\partial \theta_j} \quad (5.21)$$

The same smoothing procedure presented in Chapter 3.4 is employed with smoothing parameter equal 0.2 for the cube corner indenter tip and 0.06 for the Berkovich indenter tip (Figure 5.9a and Figure 5.10a). For both indenter tips the sensitivity vectors to the parameters E , c_1 , ν , η and σ_y are almost similar during the loading segment. For example, Figure 5.9b and Figure 5.10b illustrate the collinearity between the sensitivity vectors (ν, σ_y) , which means that their identification from the sole loading phase is thus expected to be impossible. For the cube corner indenter tip, the sensitivity vectors to (E, η) and (c_1, σ_y) remain almost proportional during the unloading segment. Concerning the Berkovich indenter tip, the sensitivity vectors to (E, ν) are almost collinear during the unloading segment.



(Figure 5.9 following) →

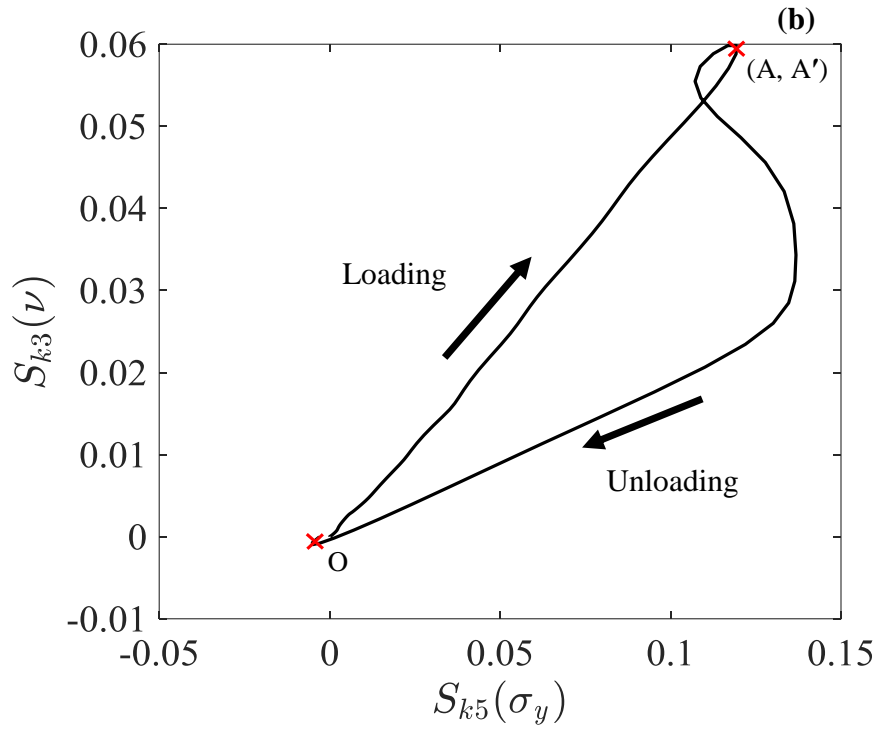
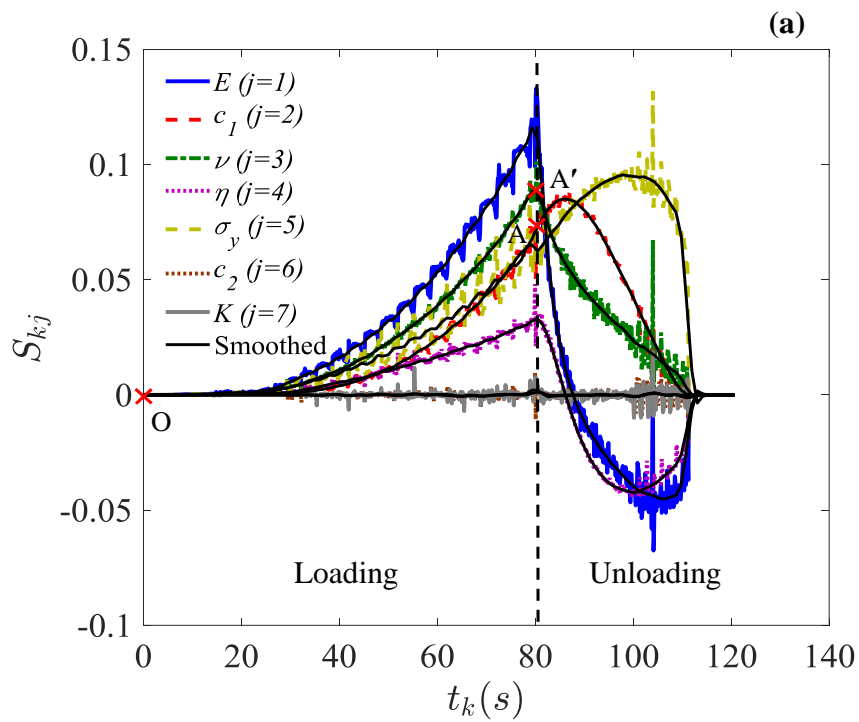


Figure 5.9. (a) Sensitivity vectors of the nanoindentation force to the material parameters θ_j during loading and unloading using cube corner indenter tip for the VEPV behavior. (b) Collinearity between sensitivity vectors S_{k3} and S_{k5} (sensitivities to ν and σ_y , respectively).



(Figure 5.10 following) →

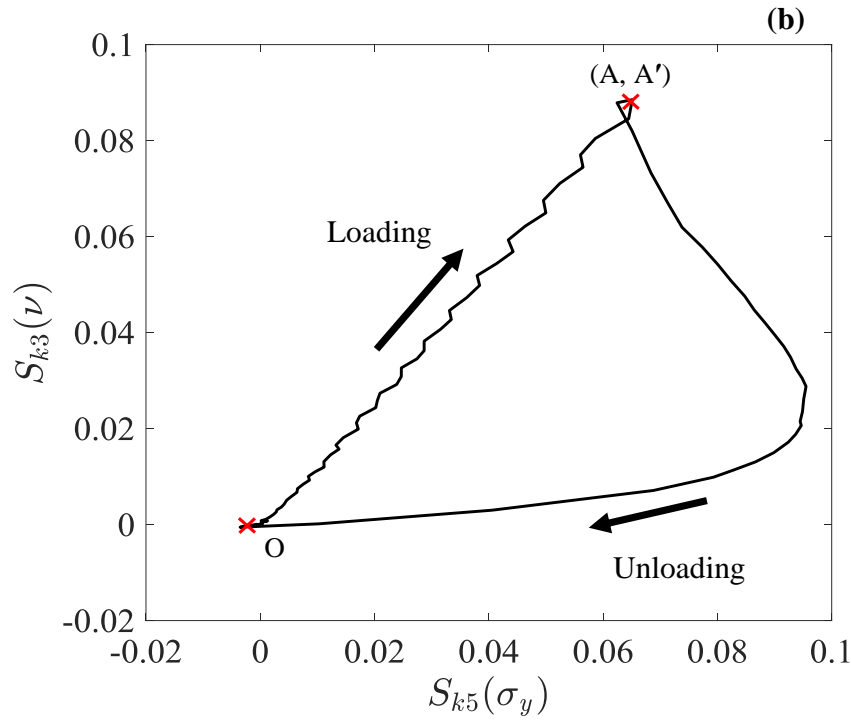


Figure 5.10. (a) Sensitivity vectors of the nanoindentation force to the material parameters θ_j during loading and unloading using Berkovich indenter tip for the VEV behavior. (b) Collinearity between sensitivity vectors S_{k3} and S_{k5} (sensitivities to ν and σ_y , respectively).

5.2.4. Identifiability analysis

This I -index is calculated from Equation 3.26 for the 120 parameters combinations (21 couples, 35 triplets, 35 quadruplets, 21 quintuplets, 7 sextuplets and 1 septuplet) and for various time subsets (loads-unloads, loads only, unloads only) using the smoothed vectors for the solution $\hat{\theta}^{(9)}$. In Figure 5.11, the evolution of the I -index for five combinations of parameters using dual nanoindentation data is shown. The I -index is disturbed during loading segment, which can be due to the contact problems between the cube corner indenter tip and the specimen. Subsequently, these perturbations disappear for the Berkovich indenter tip. When considering that the anelastic and viscoplastic parameters ($c_1, \eta, \sigma_y, c_2, K$) are known, the elastic parameters are identifiable $I(E, \nu) = 0.9$. It is also observed that the identification of the three parameters (E, c_1, η) from the cube corner test is difficult ($I = 2.2$) and becomes possible when the Berkovich test is considered ($I = 1.4$). This identifiability is better than that obtained with the VE behavior presented in Chapter 4.3 ($I = 1.9$). In the case when the viscoplastic parameters (σ_y, c_2, K) are known, the identifiability of the viscoelastic parameters is difficult $I(E, c_1, \nu, \eta) = 2.2$. This result is better than that obtained using single nanoindentation test ($I(E, \nu, c_1, \eta) = 3.7$). Also, the identification of the five parameters ($E, \nu, c_1, \eta, \sigma_y$) from cube corner test is impossible ($I = 4.1$) and becomes difficult when adding the Berkovich test ($I = 2.9$). The additional information improves the

identifiability results. This result agrees with that obtained for the elasto-plastic behavior (Le, 2008; Heinrich et al., 2009). The identification of the seven V EVP parameters from the dual nanoindentation (cube corner, Berkovich) is impossible ($I = 4.9$). The I -index results obtained without smoothing procedure shows that this procedure increases the I -index values (about 12 %). In addition, considering the combination (Berkovich, cube corner), the identifiability results lead to the same conclusions.

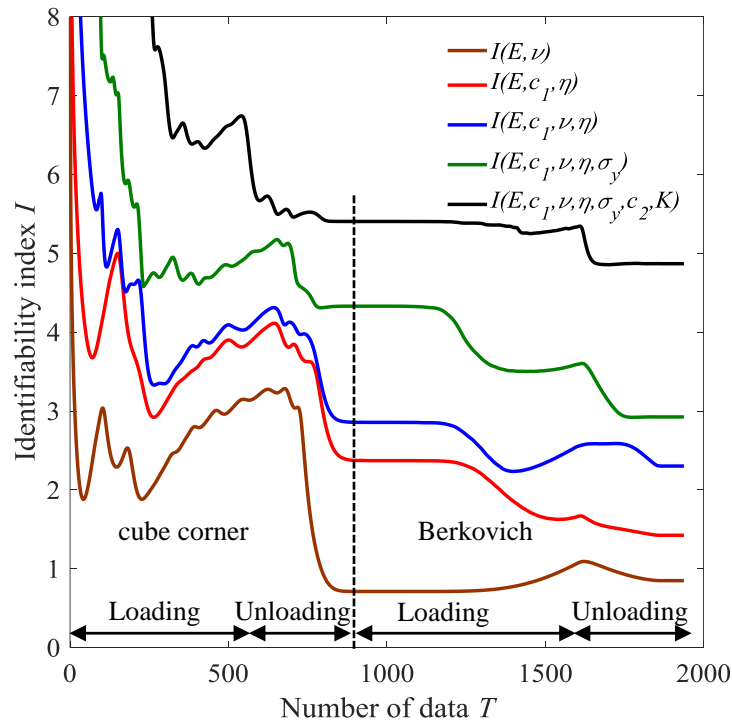


Figure 5.11. Evolution of the I -index for five combinations of parameters using nanoindentation experimental tests of cube corner and Berkovich indenter tips at 500 nm/min with the V EVP behavior law.

The minima and maxima values of the I -index of all combinations of V EVP behavior parameters are presented in Table 5.2. It can be seen that it is possible to identify some combination of two and three parameters ($I \leq 2$) from these dual nanoindentation data and only using the loading or unloading segments. In the case where the VE parameters (E, c_1, ν, η) are imposed, the identification of the viscoplastic parameters (σ_y, c_2, K) remains impossible ($I = 4.5$). The identification of four parameters (E, ν, η, σ_y) from the two load-unload tests is difficult ($I = 2.1$) and becomes possible when only the unloading segments are taken into account ($I = 2.0$). All combinations of five parameters are in the best case difficult to be identify. The identification of six and seven parameters is impossible whatever the considered nanoindentation data (loads-unloads, loads only, unloads only) ($I > 3$).

Table 5.2. Minima and maxima I -index values ($[I_{min}; I_{max}]$) for different combinations of parameters with the solution $\hat{\boldsymbol{\theta}}^{(9)}$. $I \leq 2$ (green, potentially identifiable), $I < 2 \leq 3$ (difficult to identify), $I > 3$ (red, not identifiable).

Combination	Loads-unloads	Loads	Unloads
2 parameters	[0.5; 4.3]	[0.7; 4.3]	[0.1; 4.4]
3 parameters	[1.3; 4.5]	[2.3; 4.9]	[1.0; 4.5]
4 parameters	[2.1; 4.6]	[3.5; 5.1]	[2.0; 4.6]
5 parameters	[2.9; 4.7]	[4.5; 5.2]	[2.9; 4.7]
6 parameters	[4.4; 4.8]	[4.7; 5.4]	[4.3; 4.7]
$E, c_1, \nu, \eta, \sigma_y, c_2, K$	4.9	5.4	4.8

5.3. Viscoelastic-plastic behavior law

Herein, a viscoelastic-plastic (VEP) behavior law is used to characterize the mechanical behavior of PP. The rheological model consists in the VE part of the VEP one presented in section 5.2 connected in series with a plastic slider of yield strength σ_y as seen in Figure 5.12. In this case, the viscosity K is set to 1 MPa.s and the coefficient of the linear kinematic hardening to $c_2 = 0$ to enable the plastic deformation.

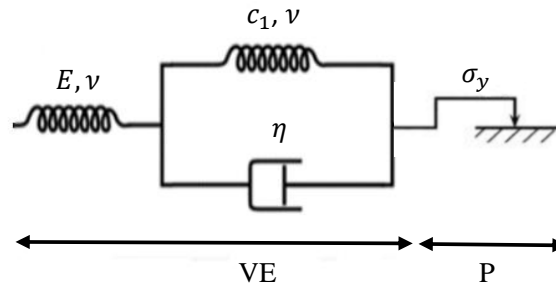


Figure 5.12. VEP rheological model.

This VEP behavior law is controlled by five material parameters, which define the parameter set $\boldsymbol{\theta} = (\theta_1, \theta_2, \theta_3, \theta_4, \theta_5) = (E, c_1, \nu, \eta, \sigma_y)$. The updating process and identifiability analysis are presented in the following paragraphs.

5.3.1. Results of the updating procedure for the VEP behavior law

In this case, the same dual nanoindentation tests (cube corner, Berkovich) are used and four starting points ($\boldsymbol{\theta}^{(12)}, \boldsymbol{\theta}^{(13)}, \boldsymbol{\theta}^{(14)}, \boldsymbol{\theta}^{(15)}$) are considered (Table 5.3). The starting point $\boldsymbol{\theta}^{(12)}$ is chosen by adding a yield strength to the estimated solution of the VE behavior $\hat{\boldsymbol{\theta}}^{(5)}$ ($\hat{\boldsymbol{\theta}}^{(12)} = (E = 1.47 \text{ GPa}, c_1 = 0.94$

GPa, $\nu = 0.4$ (imposed), $\eta = 17.08$ GPa.s, $\sigma_y = 60$ MPa). The updating process lasts about 23 days of computation for each starting point. The evolution of the five parameters during the minimization process are illustrated in Figure 5.13. As for the VEP behavior, the Poisson's ratio tends to the value $\nu = 0.5$. When ν is free, the parameters E , c_1 , η and σ_y tend towards the same values whatever the starting point. The value of the objective function ω is almost identical for all four cases. Comparing its value with those obtained for the VEP behavior, one can conclude that the VEP behavior law is more adequate to the description of the material behavior. Then, it is obvious that the numerical and experimental P - h curves are very close for both indenter tips (Figure 5.14).

Table 5.3. Estimated parameters set $\hat{\theta}$ (Equation 3.1) for the VEP behavior law using four starting points.

	Parameter		Starting value	Estimated value
	j	θ_j	$\theta_j^{(0)}$	$\hat{\theta}_j$
Starting point 12: $\theta^{(12)}$	1	E (GPa)	1.47	1.77
	2	c_1 (GPa)	0.94	1.43
	3	ν	0.4 (imposed)	0.4 (imposed)
	4	η (GPa.s)	17.08	15.75
	5	σ_y (MPa)	60	76.70
Objective function $\omega^{(12)}$			9.78×10^{-2}	2.07×10^{-3}
Starting point 13: $\theta^{(13)}$	1	E (GPa)	4.0	1.61
	2	c_1 (GPa)	3.0	1.31
	3	ν	0.4	0.5
	4	η (GPa.s)	60	14.41
	5	σ_y (MPa)	90	69.96
Objective function $\omega^{(13)}$			1.44	1.86×10^{-3}
Starting point 14: $\theta^{(14)}$	1	E (GPa)	2.0	1.57
	2	c_1 (GPa)	1.5	1.32
	3	ν	0.3	0.5
	4	η (GPa.s)	40	15.25
	5	σ_y (MPa)	70	70.28
Objective function $\omega^{(14)}$			5.39×10^{-2}	1.88×10^{-3}
Starting point 15: $\theta^{(15)}$	1	E (GPa)	1.5	1.63
	2	c_1 (GPa)	1.0	1.31
	3	ν	0.25	0.5
	4	η (GPa.s)	20	14.48
	5	σ_y (MPa)	60	69.56
Objective function $\omega^{(15)}$			1.41×10^{-1}	1.86×10^{-3}

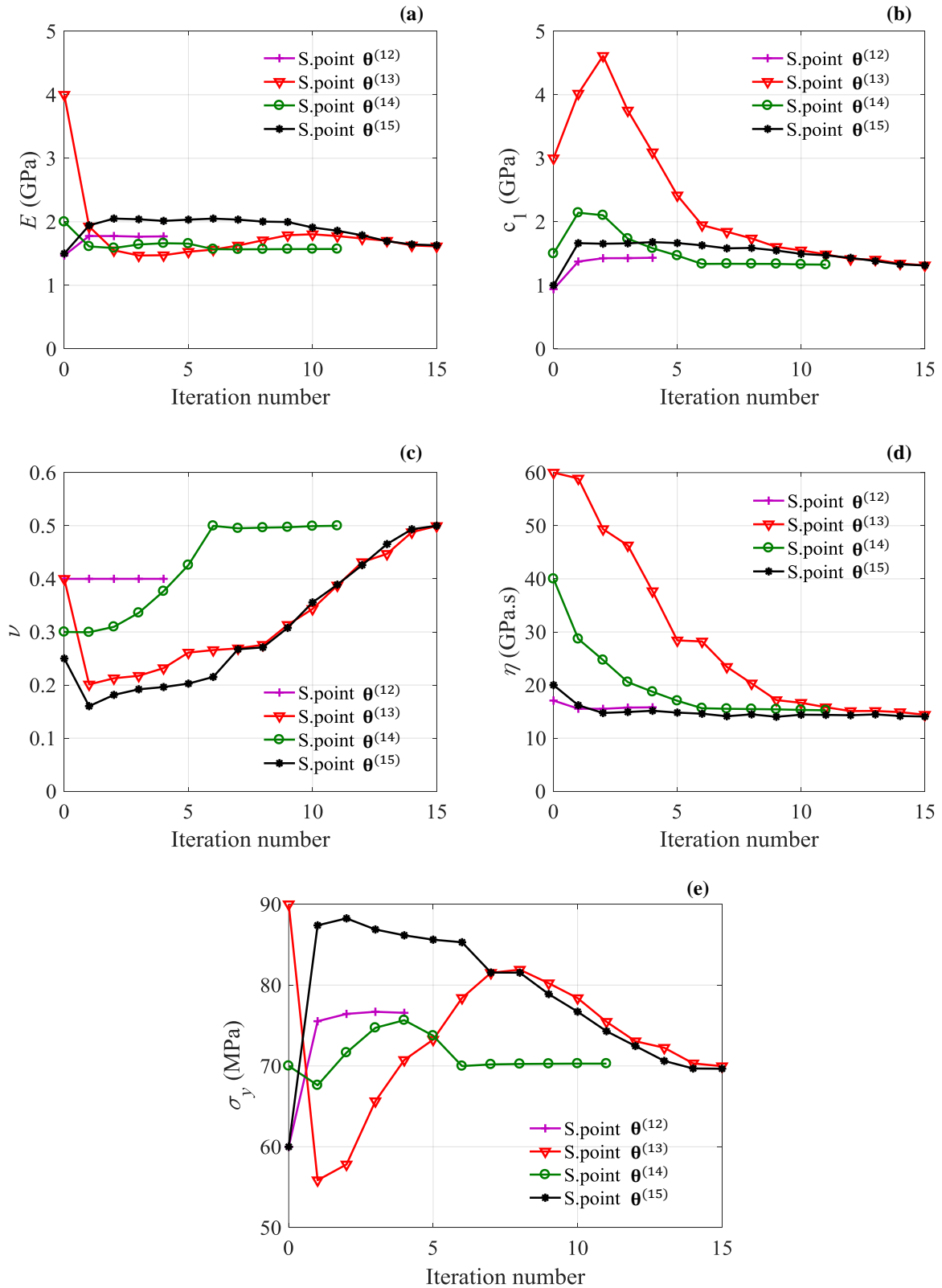


Figure 5.13. Evolution of the 5 parameters (E , c_1 , ν , η , σ_y) of the VEP behavior during the updating process using the four starting points $\theta^{(12)}$, $\theta^{(13)}$, $\theta^{(14)}$ and $\theta^{(15)}$ with dual nanoindentation technique.

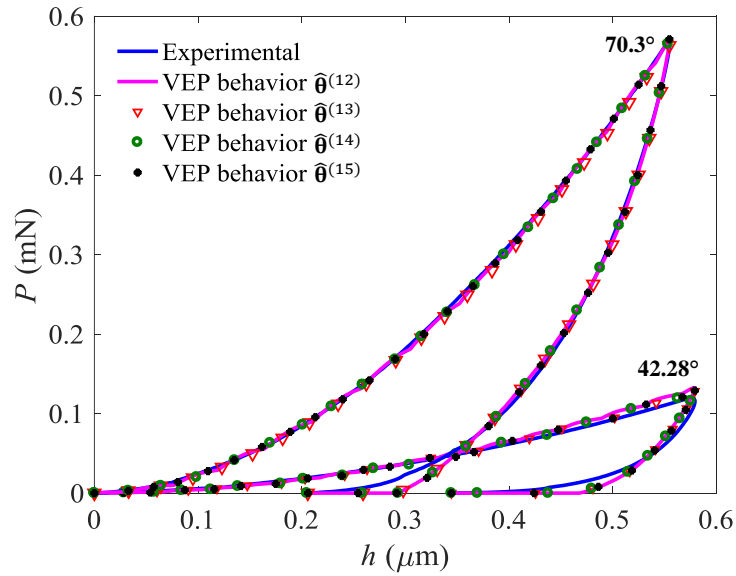
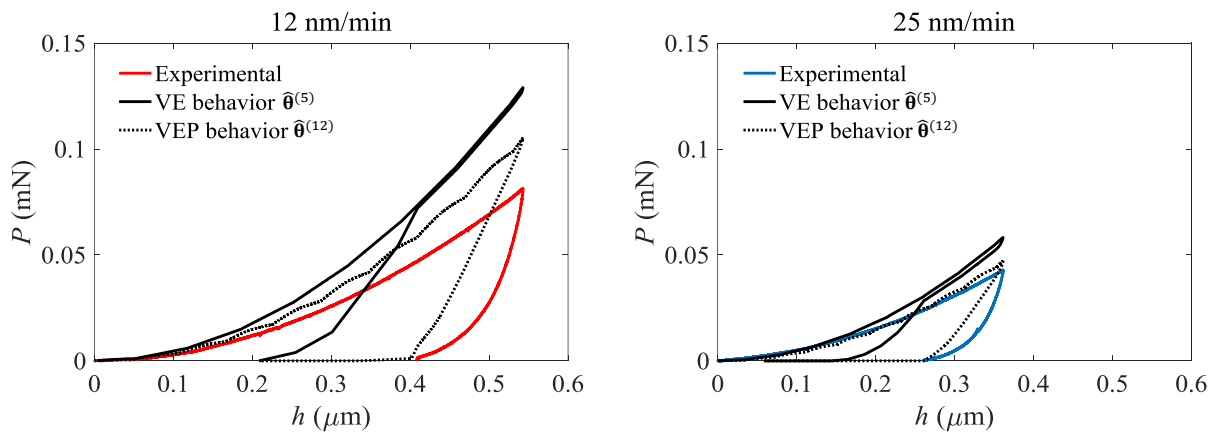


Figure 5.14. Experimental ($\dot{h} = 500 \text{ nm/min}$) and simulated nanoindentation P - h curves using cube corner and Berkovich indenter tips for the four VEP solutions (Table 5.3).

5.3.2. Assessment of the VEP behavior

To validate the behavior law, numerical simulations have been carried out using experimental tests performed at single nanoindentation rate with cube corner and Berkovich indenter tips (Chapter 2.3) for the solution $\hat{\theta}^{(12)} = (E = 1.77 \text{ GPa}, c_1 = 1.43 \text{ GPa}, \nu = 0.4 \text{ (imposed)}, \eta = 15.75 \text{ GPa}\cdot\text{s}, \sigma_y = 76.70 \text{ MPa})$. Figure 5.15 and Figure 5.16 present the experimental and numerical P - h curves for both indenter tips. The numerical results are nearly the same as those obtained with the VEP behavior (Figure 5.5 and Figure 5.6). It indicates that the VEP behavior law does not exactly predict the PP behavior. The comparison between the simulation results and the tensile test data shows that the VEP law predicts the PP behavior better than the VEPV one (Figure 5.17).



(Figure 5.15 following) \rightarrow

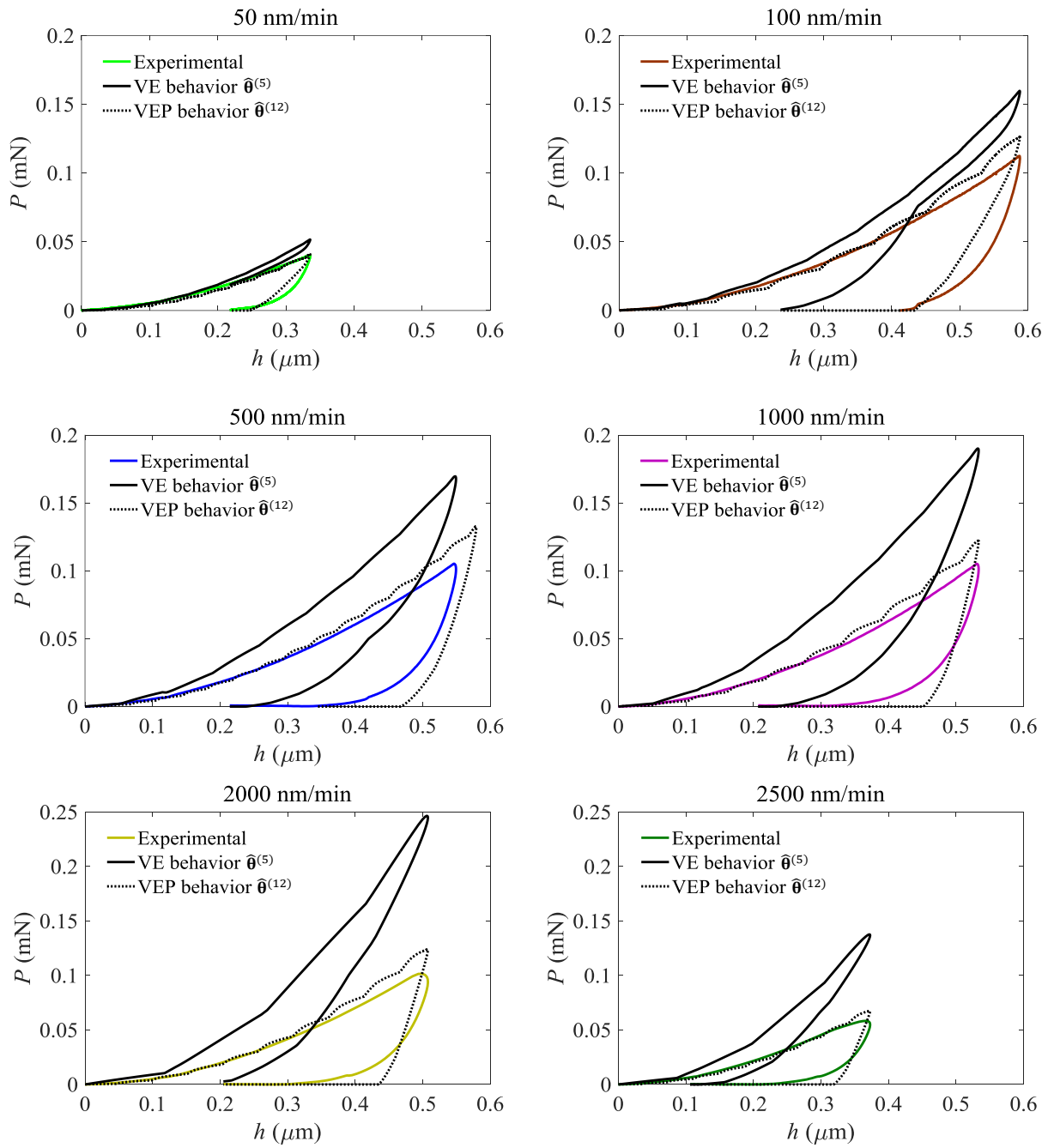


Figure 5.15. Experimental and simulated nanoindentation (P - h) curves of PP at rates of 12, 25, 50, 100, 500, 1000, 2000, and 2500 nm/min using cube corner tip for the VEP behavior with the solution $\hat{\theta}^{(12)}$.

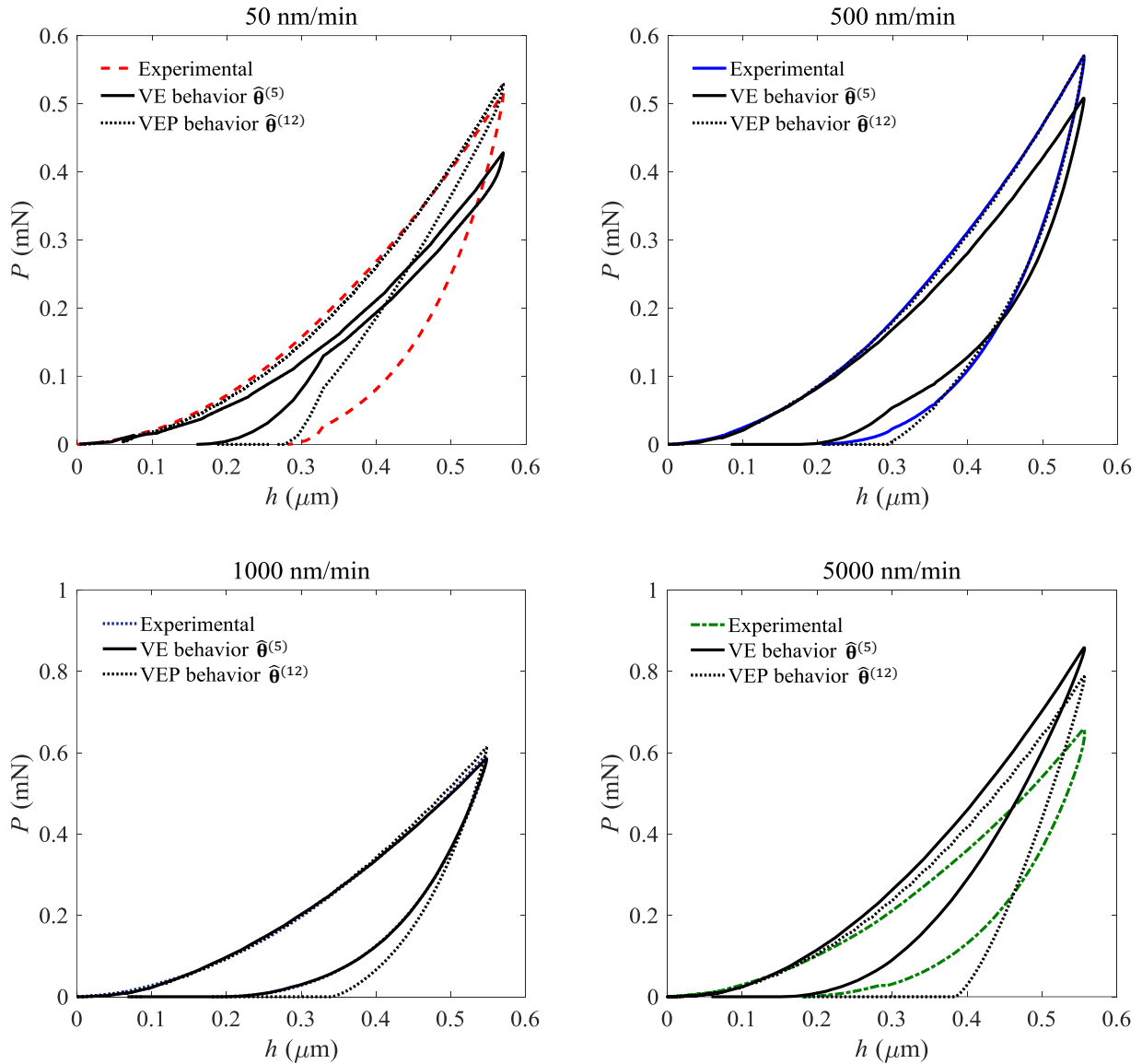


Figure 5.16. Experimental and simulated nanoindentation (P - h) curves of PP at rates of 50, 500, 1000, and 5000 nm/min using Berkovich indenter tip for the VEP behavior with the solution $\hat{\theta}^{(12)}$.

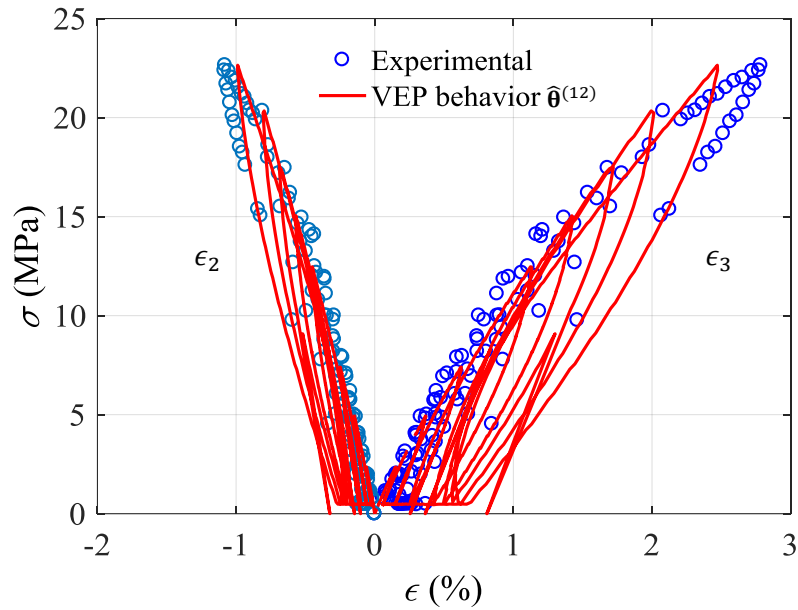


Figure 5.17. Experimental data of the tensile test and simulation response using the VEP behavior for the estimated solution $\hat{\theta}^{(12)}$.

5.3.3. Sensitivity analysis

In order to investigate the identification the VEP properties of PP, the sensitivity of the nanoindentation force to the parameters estimated from the updating process $\theta = (E, c_1, \nu, \eta, \sigma_y)$ is studied using the dual nanoindentation tests (cube corner, Berkovich). The norm of sensitivity vectors calculated using Equation 5.20 for the solution $\hat{\theta}^{(12)}$. For this analysis, the computation time is about 15 days. Figure 5.18 shows that the nanoindentation force is sensitive to the five VEP parameters. The yield strength σ_y is the most sensitive parameter. The norms of the sensitivities to the parameters E, c_1 and ν have almost the same magnitude. The viscosity coefficient η is the least influential parameter. The ratio between the norms of the sensitivities of σ_y and η about 3.5.

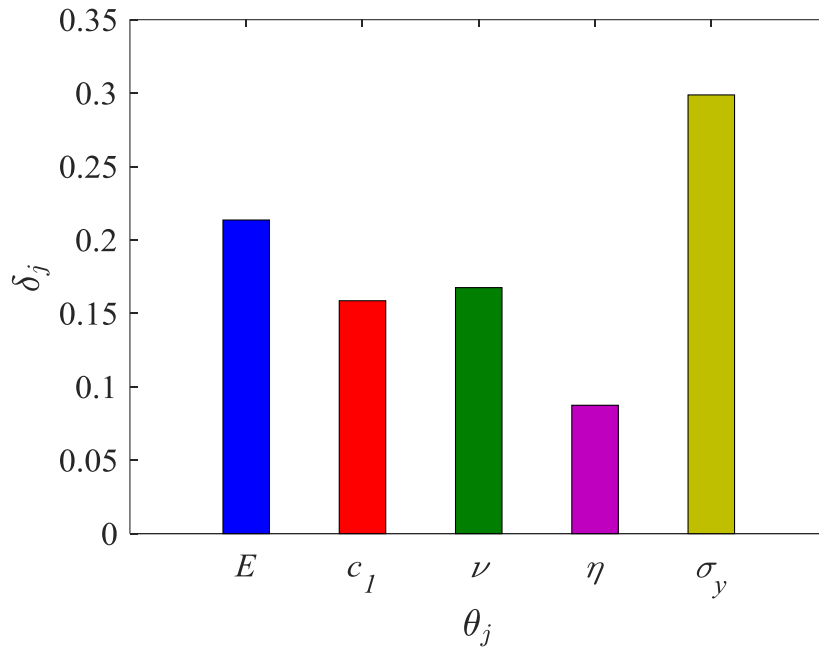


Figure 5.18. Sensitivity of the nanoindentation force P to θ_j for the solution $\hat{\theta}^{(12)}$ using nanoindentation experimental tests performed using cube corner and Berkovich indenter tips for the VEP behavior.

The sensitivity vectors of the nanoindentation force have been computed using Equation 5.21 for the solution $\hat{\theta}^{(12)}$. The same smoothing procedure presented in Chapter 3.4 is used with smoothing parameter 0.2 for the cube corner indenter tip and 0.1 for the Berkovich indenter tip. As for the VEP behavior, the sensitivity vectors are very similar during the loading segments, which indicates that the identification of the five VEP parameters from the loading segments is expected to be difficult (Figure 5.19 and Figure 5.20). The proportionality between the sensitivity to ν and σ_y during the loading segment and the last half of unloading is illustrated in Figure 5.19b and Figure 5.20b. It means that their identification using single loading phase is impossible. Focusing on the cube corner indenter tip, it is observed that the sensitivity vectors to (E, η) and (c_1, σ_y) remains almost proportional during the unloading segment. This proportionality indicates that the identification of these parameters from this test will be impossible. For the Berkovich indenter tip, the proportionality remains for (E, ν) and it is lost for (c_1, σ_y) during the unloading segment.

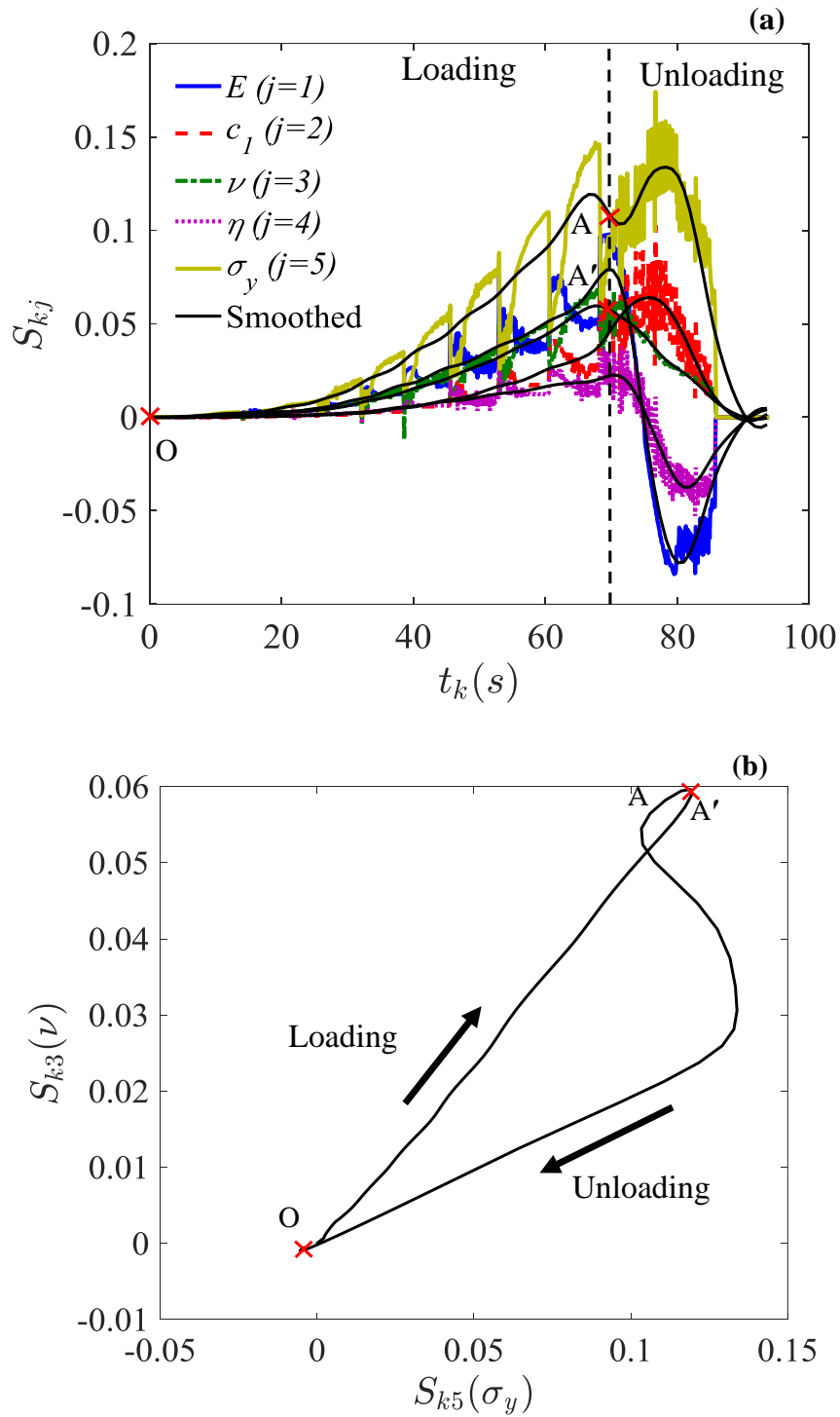


Figure 5.19. (a) Sensitivity vectors of the nanoindentation force to the material parameters θ_j during loading and unloading using cube corner indenter tip for the VEP behavior. (b) Collinearity between sensitivity vectors S_{k3} and S_{k5} (sensitivities to ν and σ_y , respectively).

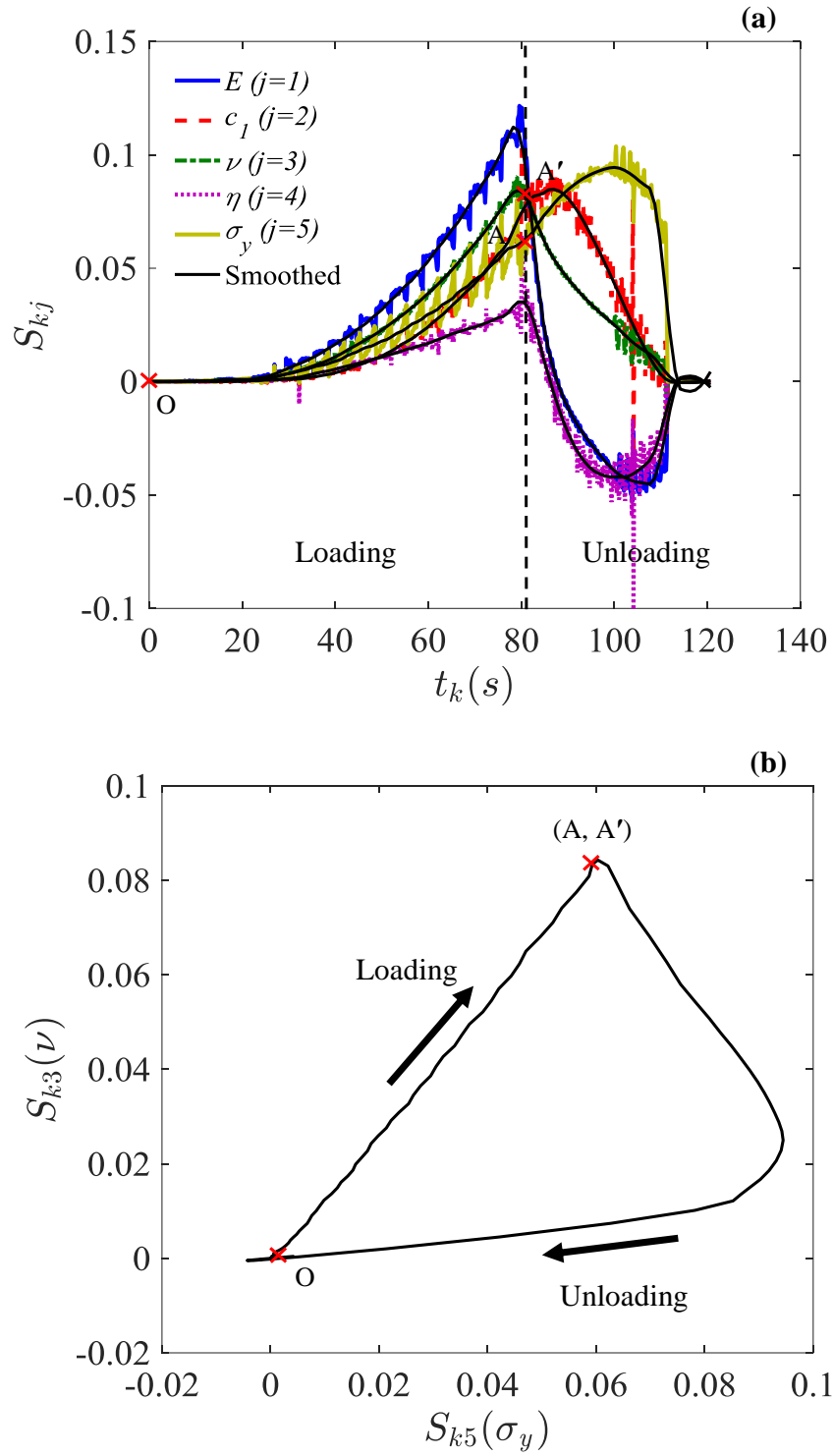


Figure 5.20. (a) Sensitivity vectors of the nanoindentation force to the material parameters θ_j during loading and unloading using Berkovich indenter tip for the VEP behavior. (b) Collinearity between sensitivity vectors S_{k3} and S_{k5} (sensitivities to ν and σ_y , respectively).

5.3.4. Identifiability analysis

In this section, the identifiability of the VEP parameters $\theta = (E, c_1, \nu, \eta, \sigma_y)$ is studied using the dual nanoindentation experimental tests performed at 500 nm/min with cube corner and Berkovich indenter tips. This I -index is calculated for the 26 parameters combinations (10 couples, 10 triplets, 5 quadruplets and 1 quintuplet) and for various time subsets (loads-unloads, loads only, unloads only) using the smoothed vectors for the solution $\hat{\theta}^{(12)}$ (with imposed Poisson's ratio). In Figure 5.21, the evolution of the I -index for four combinations of parameters using dual nanoindentation data is plotted. For all combinations, the I -index value decreases once the unloading segment is considered. For example, the value of the index $I(E, c_1, \eta) = 2.2$ only when the cube corner test is considered and equal 2 as soon as the Berkovich test is taken into account. In case the yield strength σ_y is known, the identifiability of the VE parameters is difficult $I(E, c_1, \nu, \eta) = 2.2$. The identification of the five VEP parameters from this dual nanoindentation remains difficult ($I = 2.8$).

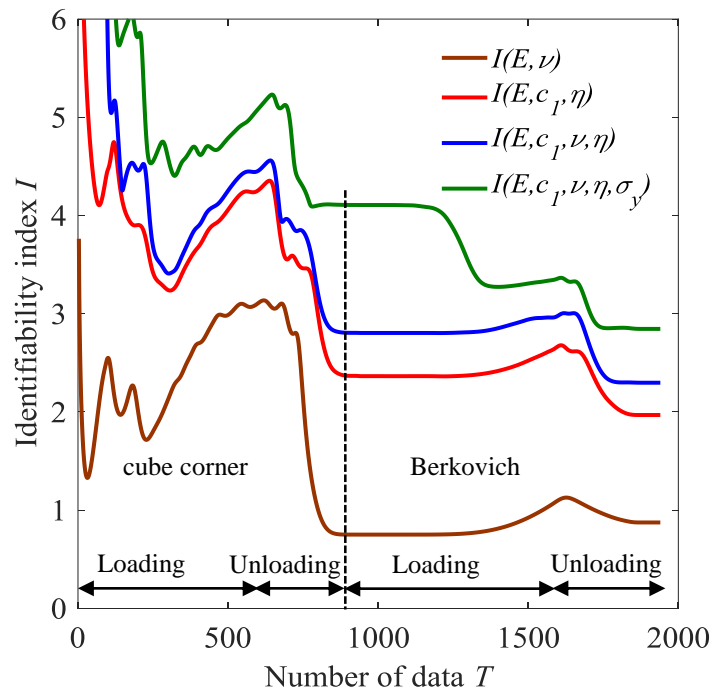


Figure 5.21. Evolution of the I -index for four combinations of parameters using nanoindentation experimental tests of cube corner and Berkovich indenter tips at 500 nm/min with the VEP behavior.

The values of the I -index of all combinations of VEP parameters calculated using dual nanoindentation (cube corner, Berkovich) are summarized in Table 5.4. It can be seen that all combinations of two parameters present an I -index < 2 , which means that they are identifiable using the dual nanoindentation tests and only unloading segments. The identifiability of the parameters (E, c_1, η) is better from the sole unloading segments ($I = 1.6$) than both nanoindentation tests ($I = 2.0$).

For the triplets (E, ν, η) and (E, η, σ_y) , the I -index is $I > 2$ when using the two tests and becomes possible when only the unloading segments are considered $I < 2$. In the case where we assume that the elastic parameters (E, ν) are known, the viscous and plastic parameters are identifiable ($I(c_1, \eta, \sigma_y) = 1.3$). It is also observed that when the yield strength σ_y is imposed, the identifiability of the VE parameters (E, c_1, ν, η) from these dual nanoindentation data is difficult ($I = 2.2$). The identification of the five VEP parameters $(E, c_1, \nu, \eta, \sigma_y)$ from this dual nanoindentation tests as well as the unloading segments is also difficult ($I = 2.8$).

Table 5.4. I -index for all combinations of VEP parameters using nanoindentation experimental tests of cube corner and Berkovich indenter tips at 500 nm/min with the solution $\widehat{\theta}^{(12)}$. $I \leq 2$ (green, potentially identifiable), $I < 2 \leq 3$ (difficult to identify), $I > 3$ (red, not identifiable).

Combination	Loads-unloads	Loads	Unloads
E, c_1	0.5	2.3	0.2
E, ν	0.9	2.8	0.2
E, η	1.6	3.5	1.3
E, σ_y	0.5	1.1	0.8
c_1, ν	1.3	2.1	1.9
c_1, η	0.6	2.0	0.7
c_1, σ_y	1.3	1.3	1.4
ν, η	0.8	3.0	0.3
ν, σ_y	1.3	1.3	1.4
η, σ_y	1.1	1.8	1.3
E, c_1, ν	2.1	2.9	2.2
E, c_1, η	2.0	3.7	1.6
E, c_1, σ_y	1.4	2.6	1.8
E, ν, η	2.1	3.7	1.5
E, ν, σ_y	2.0	3.5	2.2
E, η, σ_y	2.2	3.8	2.0
c_1, ν, η	1.8	3.1	2.2
c_1, ν, σ_y	1.7	2.7	2.4
c_1, η, σ_y	1.3	2.7	1.7
ν, η, σ_y	1.9	3.6	1.9
E, c_1, ν, η	2.2	3.9	2.2
E, c_1, ν, σ_y	2.8	3.5	2.9
E, c_1, η, σ_y	2.3	4.0	2.2
E, ν, η, σ_y	2.4	3.9	2.3
c_1, ν, η, σ_y	2.4	3.8	2.7
$E, c_1, \nu, \eta, \sigma_y$	2.8	4.1	2.9

5.4. Conclusion

In this chapter, the mechanical behavior of the PP under nanoindentation is studied using the FEMU method with two behavior laws, which are V EVP, and V EP.

Firstly, the updating process of the 2D-axisymmetric FEM has been performed using the dual nanoindentation experimental tests conducted at 500 nm/min with cube corner and Berkovich indenter tips for the V EVP behavior with seven parameters ($E, c_1, \nu, \eta, \sigma_y, c_2, K$). This procedure illustrates that this dual nanoindentation is not sufficient to uniquely estimate the V EVP properties of material. The identifiability analysis is performed using several nanoindentation data (loads-unloads tests, only loads and only unloads). It indicates that the addition of the information improves the identifiability results. The I -index results show that the identification of the V EVP properties from this dual nanoindentation is however impossible ($I = 4.9$). It suggests that an identification procedure using several nanoindentation tests carried out at different rates may allow to extract a unique V EVP properties.

Secondly, updating process of the 2D-axisymmetric FEM on the same dual nanoindentation tests leads to multiple solutions for the values of the five parameters ($E, c_1, \nu, \eta, \sigma_y$) of the V EP behavior law. The identifiability of the V EP parameters is then calculated. It shows that the identification of the five V EP parameters is considered as difficult ($I = 2.8$). The better description of the PP behavior under nanoindentation is obtained with the V EP behavior law.

Conclusions and future work

The identification of the viscoelastic-viscoplastic (VEVP) properties of materials from nanoindentation data is the main focus of this work. Three approaches can be employed to determine mechanical properties of materials from nanoindentation data. The first one uses analytical methods based on the contact theory, the second uses the contact theory and the finite element (FE) method and the third method is based on the combination of the FE method and an optimization process (the finite element model updating (FEMU)) which is used in this thesis. A constitutive VEP behavior law is implemented in the ANSYS FE software through a subroutine UMAT with a viscoelastic-plastic (VEP) particular case.

Series of experimental nanoindentation triangular tests are performed on PP samples in displacement-controlled mode using Berkovich and cube corner indenter tips at constant and multiple depth rates. Also, pseudo-experimental nanoindentation tests are numerically simulated with triangular, trapezoidal, exponential and sinusoidal loading types. These nanoindentation tests are used in the identification of the mechanical properties and the identifiability investigation.

Two parametric two-dimensional (2D) axisymmetric and three-dimensional (3D) FEM are constructed using the ANSYS FE software. The 2D-axisymmetric FEM allows the simulation of the nanoindentation of material using different behavior laws. The results obtained using the two FEM models are compared in the viscoelastic (VE) case. It is shown that the 3D model improves greatly the identifiability results. The mechanical properties of the material are determined using the FEMU method for different behavior laws.

In the first case, the four parameters VE behavior law available in ANSYS FE software has been used in the 2D-axisymmetric FEM, for time consuming reason. The FEMU process of nanoindentation test illustrates that a single nanoindentation experimental triangular load-unload test conducted at constant nanoindentation depth rate (~ 1000 nm/min) is not sufficient to uniquely determine the four

VE properties of the PP. The updating process of the 2D-axisymmetric FEM on these experimental data leads to multiple solutions for the values of the four parameters (E, c_1, ν, η) of the VE behavior law. In order to extract a unique solution of the VE parameters from the FEMU method, an identifiability analysis is performed. It allows the quantification of the ill-posed character of the inverse problem by a scalar identifiability index (I -index) and shows that the identification of the four VE parameters from a single nanoindentation triangular load-unload test is impossible ($I = 3.7$). However, it is possible to identify three parameters (E, c_1, η) even if only the unloading phase is taken in account ($I = 1.5$), which proves that the relevant information is in the unloading phase.

The effect of nanoindentation depth rate, loading type (triangular, trapezoidal, exponential, sinusoidal) and indenter tip angle on the identifiability has been numerically investigated. The comparison between the results from the different loading types shows that the identification of the four material parameters from single test is not possible. The included half angle α of the indenter tip does not have a significant influence on the identifiability results. It is also found that the updating process solutions are not very sensitive to the measurement noise.

The comparison between the loss factor and the I -index results from the nanoindentation triangular tests indicates that the better identifiability of the material parameters is obtained at the maximum loss factor, which corresponds to the maximum of the dissipated energy. It is also observed that, whatever the loading type, the best identifiability is obtained if the loss factor is maximum.

The combination of several triangular load-unload tests improves the identification robustness and does not lead to better I -index for the four material parameters compared to a single but properly chosen one. We show that the combination of two numerical nanoindentation triangular tests carried out at a constant nanoindentation depth rate using equivalent cone apex angles of cube corner (42.28°) and Berkovich (70.3°) indenter tips allows for the retrieval of a unique solution of the inverse problem, which is robust with respect to the noise. The four material parameters are potentially identifiable using this experimental protocol if the material behavior is viscoelastic.

In the last part of the thesis, the mechanical behavior of the PP under nanoindentation is studied using the FEMU method with two behavior laws, which are V EVP and VEP behaviors.

The updating process of the 2D-axisymmetric FEM is conducted using the dual nanoindentation experimental tests performed at 500 nm/min with cube corner and Berkovich indenter tips for the V EVP behavior law ($E, c_1, \nu, \eta, \sigma_y, c_2, K$). The values of the obtained objective function indicate that the V EVP behavior improves the capability to describe the experimental data compared with the VE one but the obtained solution is not unique. The identifiability analysis illustrates that the addition of the information enhances the identifiability results. It is shown that the identification of four parameters (E, ν, η, σ_y)

from these dual nanoindentation data is difficult ($I = 2.1$) and becomes possible when only the unloading segments are considered ($I = 2.0$). The identification of the seven V EVP parameters from these data is impossible ($I = 4.9$).

The FEMU method using the same dual nanoindentation tests leads to multiple solutions for the values of the five VEP parameters ($E, c_1, \nu, \eta, \sigma_y$). It is observed that if the Poisson's ratio is known, the identification of the four parameters (E, c_1, η, σ_y) from these data is difficult ($I = 2.2$). The I -index value of the five VEP parameters is $I = 2.8$. This result informs us about the difficulty of the identification procedure but indicates that a certain richness of these nanoindentation data may help to yield an I -index ≤ 2 .

According to the investigations of the different behavior laws, it is suggested that the PP behavior under nanoindentation is better described using the VEP behavior law.

It is interesting to note that the I -index can be used to numerically design the nanoindentation tests which allow to activate the dissipative phenomena as much as possible, thus to identify intrinsic and reliable properties. The results obtained for the VE behavior give a quite good reference for the future investigations.

- For the identification of the V EVP properties, it is suggested that an identification procedure using several nanoindentation tests performed at different rates may allow to determine a unique and intrinsic properties. However, this study is expensive and time consuming to carry out.
- Concerning the 3D FEM, it could be important to perform a convergence study in order to optimize the contact between the indenter tip and the specimen.
- The identifiability analysis has been shown that the four VE properties can be identified using single Berkovich nanoindentation test with the 3D FEM (the computational time is about 40 hours). Along this way, it is interesting to perform the same analysis for the V EVP behavior law using dual (or plural) nanoindentation tests. In addition, considering the true indenter tip geometry may improve the identifiability of material parameters.

Bibliography

- Alkorta, J., Martínez-Esnaola, J.M., Sevillano, J.G., 2005a. Absence of one-to-one correspondence between elastoplastic properties and sharp-indentation load–penetration data. *J. Mater. Res.* 20, 432–437.
- Alkorta, J., Martínez-Esnaola, J.M., Sevillano, J.G., 2005b. Absence of one-to-one correspondence between elastoplastic properties and sharp-indentation load–penetration data. *J. Mater. Res.* 20, 432–437.
- Ansys 16.0, 2016.
- Arizzi, F., Rizzi, E., 2014. Elastoplastic parameter identification by simulation of static and dynamic indentation tests. *Model. Simul. Mater. Sci. Eng.* 22, 035017.
- Ashby, M.F., 1994. Materials selection in mechanical design. *Metall. Ital.* 86, 475–475.
- Berkovich, E.S., 1950. Three-faceted diamond pyramid for studying microhardness by indentation. *Zavod. Lab.* 13, 345–347.
- Bhattacharya, A.K., Nix, W.D., 1988. Analysis of elastic and plastic deformation associated with indentation testing of thin films on substrates. *Int. J. Solids Struct.* 24, 1287–1298.
- Bocciarelli, M., Bolzon, G., 2009. Indentation and imprint mapping for the identification of interface properties in film-substrate systems. *Int. J. Fract.* 155, 1–17.
- Bocciarelli, M., Bolzon, G., 2007. Indentation and imprint mapping for the identification of constitutive parameters of thin layers on substrate: Perfectly bonded interfaces. *Mater. Sci. Eng. A* 448, 303–314.
- Bocciarelli, M., Bolzon, G., Maier, G., 2005. Parameter identification in anisotropic elastoplasticity by indentation and imprint mapping. *Mech. Mater.* 37, 855–868.
- Bolzon, G., Bocciarelli, M., Chiarullo, E.J., 2009. Mechanical characterization of materials by micro-indentation and AFM scanning, in: *Applied Scanning Probe Methods XII*. Springer, pp. 85–120.
- Bolzon, G., Buljak, V., Maier, G., Miller, B., 2011. Assessment of elastic–plastic material parameters comparatively by three procedures based on indentation test and inverse analysis. *Inverse Probl. Sci. Eng.* 19, 815–837.
- Bolzon, G., Maier, G., Panico, M., 2004. Material model calibration by indentation, imprint mapping and inverse analysis. *Int. J. Solids Struct.* 41, 2957–2975.
- Bolzon, G., Talassi, M., 2013. An effective inverse analysis tool for parameter identification of anisotropic material models. *Int. J. Mech. Sci.* 77, 130–144.
- Boussinesq, J., 1885. Application des potentiels à l'étude de l'équilibre et du mouvement des solides élastiques: principalement au calcul des déformations et des pressions que produisent, dans ces solides, des efforts quelconques exercés sur une petite partie de leur surface ou de leur intérieur: mémoire suivi de notes étendues sur divers points de physique, mathématique et d'analyse. Gauthier-Villars.
- Brun, C., Delobelle, P., Fromm, M., Berger, F., Chambaudet, A., Jaffiol, F., 2001. Mechanical properties determined by nanoindentation tests of polypropylene modified by He⁺ particle implantation. *Mater. Sci. Eng. A* 315, 63–69.
- Bucaille, J.L., Felder, E., Hochstetter, G., 2002. Identification of the viscoplastic behavior of a polycarbonate based on experiments and numerical modeling of the nano-indentation test. *J. Mater. Sci.* 37, 3999–4011.

- Bucaille, J.-L., Stauss, S., Felder, E., Michler, J., 2003. Determination of plastic properties of metals by instrumented indentation using different sharp indenters. *Acta Mater.* 51, 1663–1678.
- Bulychev, S.I., Alekhin, V.P., Shorshorov, M.H., Ternovskii, A.P., Shnyrev, G.D., 1975. Determining Young's modulus from the indenter penetration diagram. *Ind Lab* 41, 1409–1412.
- Cao, Y., Huber, N., 2006. Further investigation on the definition of the representative strain in conical indentation. *J. Mater. Res.* 21, 1810–1821.
- Cao, Y.P., Lu, J., 2004a. A new method to extract the plastic properties of metal materials from an instrumented spherical indentation loading curve. *Acta Mater.* 52, 4023–4032.
- Cao, Y.P., Lu, J., 2004b. Depth-sensing instrumented indentation with dual sharp indenters: stability analysis and corresponding regularization schemes. *Acta Mater.* 52, 1143–1153.
- Cao, Y.P., Qian, X.Q., Lu, J., Yao, Z.H., 2005. An energy-based method to extract plastic properties of metal materials from conical indentation tests. *J. Mater. Res.* 20, 1194–1206.
- Capehart, T.W., Cheng, Y.T., 2003. Determining constitutive models from conical indentation: Sensitivity analysis. *J. Mater. Res.* 18, 827–832.
- Casals, O., Alcalá, J., 2005. The duality in mechanical property extractions from Vickers and Berkovich instrumented indentation experiments. *Acta Mater.* 53, 3545–3561.
- Chen, X., Ashcroft, I.A., Wildman, R.D., Tuck, C.J., 2015. An inverse method for determining the spatially resolved properties of viscoelastic–viscoplastic three-dimensional printed materials. *Proc. R. Soc. Math. Phys. Eng. Sci.* 471, 20150477.
- Chen, X., Ogasawara, N., Zhao, M., Chiba, N., 2007. On the uniqueness of measuring elastoplastic properties from indentation: the indistinguishable mystical materials. *J. Mech. Phys. Solids* 55, 1618–1660.
- Chen, Z., Diebels, S., 2013. Parameter re-identification in nanoindentation problems of viscoelastic polymer layers: small deformation. *ZAMM-J. Appl. Math. Mech. Für Angew. Math. Mech.* 93, 88–101.
- Chen, Z., Diebels, S., Peter, N.J., Schneider, A.S., 2013. Identification of finite viscoelasticity and adhesion effects in nanoindentation of a soft polymer by inverse method. *Comput. Mater. Sci.* 72, 127–139.
- Cheng, L., Xia, X., Scriven, L.E., Gerberich, W.W., 2005. Spherical-tip indentation of viscoelastic material. *Mech. Mater.* 37, 213–226.
- Cheng, L., Xia, X., Yu, W., Scriven, L.E., Gerberich, W.W., 2000. Flat-punch indentation of viscoelastic material. *J. Polym. Sci. Part B Polym. Phys.* 38, 10–22.
- Cheng, Y.-T., Cheng, C.-M., 2004. Scaling, dimensional analysis, and indentation measurements. *Mater. Sci. Eng. R Rep.* 44, 91–149.
- Cheng, Y.-T., Cheng, C.-M., 1999. Can stress–strain relationships be obtained from indentation curves using conical and pyramidal indenters? *J. Mater. Res.* 14, 3493–3496.
- Cheng, Y.-T., Cheng, C.-M., 1998a. Scaling approach to conical indentation in elastic-plastic solids with work hardening. *J. Appl. Phys.* 84, 1284–1291.
- Cheng, Y.-T., Cheng, C.-M., 1998b. Analysis of indentation loading curves obtained using conical indenters. *Philos. Mag. Lett.* 77, 39–47.
- Chollacoop, N., Dao, M., Suresh, S., 2003. Depth-sensing instrumented indentation with dual sharp indenters. *Acta Mater.* 51, 3713–3729.
- Clément, P., Meille, S., Chevalier, J., Olagnon, C., 2013. Mechanical characterization of highly porous inorganic solids materials by instrumented micro-indentation. *Acta Mater.* 61, 6649–6660.
- Collin, J.-M., Mauvoisin, G., Pilvin, P., El Abdi, R., 2007. Identification des paramètres d'une loi de comportement élastoplastique par indentation continue sphérique, in: *Congrès Français de Mécanique*. AFM, Maison de la Mécanique, 39/41 rue Louis Blanc-92400 Courbevoie.
- Constantinescu, A., Tardieu, N., 2001. On the identification of elastoviscoplastic constitutive laws from indentation tests. *Inverse Probl. Eng.* 9, 19–44.
- Cook, R.F., 2018. A flexible model for instrumented indentation of viscoelastic–plastic materials. *MRS Commun.* 8, 586–590.
- Cook, R.F., Oyen, M.L., 2007. Nanoindentation behavior and mechanical properties measurement of polymeric materials. *Int. J. Mater. Res.* 98, 370–378.
- Dao, M., Chollacoop, N., Van Vliet, K.J., Venkatesh, T.A., Suresh, S., 2001. Computational modeling of the forward and reverse problems in instrumented sharp indentation. *Acta Mater.* 49, 3899–3918.

- Daphalapurkar, N.P., Dai, C., Gan, R.Z., Lu, H., 2009. Characterization of the linearly viscoelastic behavior of human tympanic membrane by nanoindentation. *J. Mech. Behav. Biomed. Mater.* 2, 82–92.
- Doerner, M.F., Nix, W.D., 1986. A method for interpreting the data from depth-sensing indentation instruments. *J. Mater. Res.* 1, 601–609.
- Dumas, G., Baronet, C.N., 1971. Elastoplastic indentation of a half-space by an infinitely long rigid circular cylinder. *Int. J. Mech. Sci.* 13, 519–530.
- F. Richard, 2000. MIC2M Software: Modélisation et Identification du Comportement Mécanique des Matériaux/Modeling and Identification of the Mechanical Behavior of Materials,.
- Fischer, A.C., 2002. Cripps, Nanoindentation. *Mech. Eng. Ser.* Springer-Verlag N. Y.
- Fischer-Cripps, A.C., 2006. Critical review of analysis and interpretation of nanoindentation test data. *Surf. Coat. Technol.* 200, 4153–4165.
- Fischer-Cripps, A.C., 2004. A simple phenomenological approach to nanoindentation creep. *Mater. Sci. Eng. A* 385, 74–82.
- Fizi, Y., 2015. Object-oriented finite element and inverse analysis to determine elastic-plastic properties of an arc-sprayed composite coating, in: *Congrès Français de Mécanique. AFM, Association Française de Mécanique.*
- Follansbee, P.S., Sinclair, G.B., 1984. Quasi-static normal indentation of an elasto-plastic half-space by a rigid sphere—I: Analysis. *Int. J. Solids Struct.* 20, 81–91.
- Gamonpilas, C., Charalambides, M.N., Williams, J.G., Dooling, P.J., Gibbon, S.R., 2010. Predicting the mechanical behaviour of starch gels through inverse analysis of indentation data. *Appl Rheol* 20, 33283.
- Gao, S.-L., Mäder, E., 2002. Characterisation of interphase nanoscale property variations in glass fibre reinforced polypropylene and epoxy resin composites. *Compos. Part Appl. Sci. Manuf.* 33, 559–576.
- Giannakopoulos, A.E., Larsson, P.-L., 1997. Analysis of pyramid indentation of pressure-sensitive hard metals and ceramics. *Mech. Mater.* 25, 1–35.
- Giannakopoulos, A.E., Larsson, P.-L., Vestergaard, R., 1994. Analysis of Vickers indentation. *Int. J. Solids Struct.* 31, 2679–2708.
- Giannakopoulos, A.E., Suresh, S., 1999. Determination of elastoplastic properties by instrumented sharp indentation. *Scr. Mater.* 40, 1191–1198.
- Graham, G.A., 1965. The contact problem in the linear theory of viscoelasticity. *Int. J. Eng. Sci.* 3, 27–46.
- Gu, Y., Nakamura, T., Prchlik, L., Sampath, S., Wallace, J., 2003. Micro-indentation and inverse analysis to characterize elastic-plastic graded materials. *Mater. Sci. Eng. A* 345, 223–233.
- Guessasma, S., Sehaki, M., Lourdin, D., Bourmaud, A., 2008. Viscoelasticity properties of biopolymer composite materials determined using finite element calculation and nanoindentation. *Comput. Mater. Sci.* 44, 371–377.
- Gujarati, D.N., 1988. *Basic econometrics*, 2 nd. ed. McGraw-Hill, New York.
- Harding, J.W., Sneddon, I.N., 1945. The elastic stresses produced by the indentation of the plane surface of a semi-infinite elastic solid by a rigid punch, in: *Mathematical Proceedings of the Cambridge Philosophical Society.* Cambridge University Press, pp. 16–26.
- Hardy, C., Baronet, C.N., Tordion, G.V., 1971. The elasto-plastic indentation of a half-space by a rigid sphere. *Int. J. Numer. Methods Eng.* 3, 451–462.
- Heinrich, C., Waas, A.M., Wineman, A.S., 2009. Determination of material properties using nanoindentation and multiple indenter tips. *Int. J. Solids Struct.* 46, 364–376.
- Hertz, H., 1881. *Über die berührung fester elastischer Körper.* *J. Reineu Angew Mathem* 92 156.
- Hill, R., Storakers, B., Zdunek, A.B., 1989. A theoretical study of the Brinell hardness test. *Proc R Soc Lond A* 423, 301–330.
- Huang, G., Daphalapurkar, N.P., Gan, R.Z., Lu, H., 2008. A method for measuring linearly viscoelastic properties of human tympanic membrane using nanoindentation. *J. Biomech. Eng.* 130, 014501.
- Huang, G., Lu, H., 2007. Measurements of two independent viscoelastic functions by nanoindentation. *Exp. Mech.* 47, 87–98.
- Huang, X., Pelegri, A.A., 2007. Finite element analysis on nanoindentation with friction contact at the film/substrate interface. *Compos. Sci. Technol.* 67, 1311–1319.
- Hunter, S.C., 1960. The Hertz problem for a rigid spherical indenter and a viscoelastic half-space. *J. Mech. Phys. Solids* 8, 219–234.

- Jäger, A., Lackner, R., Eberhardsteiner, J., 2007. Identification of viscoelastic properties by means of nanoindentation taking the real tip geometry into account. *Meccanica* 42, 293–306.
- Jakes, J.E., Frihart, C.R., Beecher, J.F., Moon, R.J., Stone, D.S., 2008. Experimental method to account for structural compliance in nanoindentation measurements. *J. Mater. Res.* 23, 1113–1127.
- Jang, J., Lance, M.J., Wen, S., Pharr, G.M., 2005. Evidence for nanoindentation-induced phase transformations in germanium. *Appl. Phys. Lett.* 86, 131907.
- Johnson, K.L., 1985. *Contact mechanics*. Cambridge university press.
- Kang, J.J., Becker, A.A., Sun, W., 2012. Determining elastic–plastic properties from indentation data obtained from finite element simulations and experimental results. *Int. J. Mech. Sci.* 62, 34–46.
- Kang, J.J., Becker, A.A., Sun, W., 2011. A combined dimensional analysis and optimization approach for determining elastic–plastic properties from indentation tests. *J. Strain Anal. Eng. Des.* 46, 749–759.
- Kang, J.J., Becker, A.A., Wen, W., Sun, W., 2018. Extracting elastic-plastic properties from experimental loading-unloading indentation curves using different optimization techniques. *Int. J. Mech. Sci.* 144, 102–109.
- Kavanagh, K.T., Clough, R.W., 1971. Finite element applications in the characterization of elastic solids. *Int. J. Solids Struct.* 7, 11–23.
- Kermouche, G., Aleksy, N., Bergheau, J.-M., 2013. Viscoelastic-viscoplastic modelling of the scratch response of PMMA. *Adv. Mater. Sci. Eng.* 2013.
- Kermouche, G., Loubet, J.L., Bergheau, J.M., 2008. Extraction of stress–strain curves of elastic–viscoplastic solids using conical/pyramidal indentation testing with application to polymers. *Mech. Mater.* 40, 271–283.
- Kim, B.R., 1999. *Modeling of particle interaction with polymer multi-layered structures* (Ph.D. Thesis). The Pennsylvania State University, Pennsylvania.
- King, R.B., 1987. Elastic analysis of some punch problems for a layered medium. *Int. J. Solids Struct.* 23, 1657–1664.
- Knapp, J.A., Follstaedt, D.M., Myers, S.M., Barbour, J.C., Friedmann, T.A., 1999. Finite-element modeling of nanoindentation. *J. Appl. Phys.* 85, 1460–1474.
- Kruzic, J.J., Kim, D.K., Koester, K.J., Ritchie, R.O., 2009. Indentation techniques for evaluating the fracture toughness of biomaterials and hard tissues. *J. Mech. Behav. Biomed. Mater.* 2, 384–395.
- Kucharski, S., Mroz, Z., 2001. Identification of plastic hardening parameters of metals from spherical indentation tests. *Mater. Sci. Eng. A* 318, 65–76.
- Kucuk, Y., Mollamahmutoglu, C., Wang, Y., Lu, H., 2013. Nonlinearly viscoelastic nanoindentation of PMMA under a spherical tip. *Exp. Mech.* 53, 731–742.
- Lan, H., Venkatesh, T.A., 2007. Determination of the elastic and plastic properties of materials through instrumented indentation with reduced sensitivity. *Acta Mater.* 55, 2025–2041.
- Laursen, T.A., Simo, J.C., 1992. A study of the mechanics of microindentation using finite elements. *J. Mater. Res.* 7, 618–626.
- Le, M.-Q., 2011. Improved reverse analysis for material characterization with dual sharp indenters. *Int. J. Solids Struct.* 48, 1600–1609.
- Le, M.-Q., 2009. Material characterization by dual sharp indenters. *Int. J. Solids Struct.* 46, 2988–2998.
- Le, M.-Q., 2008. A computational study on the instrumented sharp indentations with dual indenters. *Int. J. Solids Struct.* 45, 2818–2835.
- Lee, C.H., Kobayashi, S., 1970. Elastoplastic analysis of plane-strain and axisymmetric flat punch indentation by the finite-element method. *Int. J. Mech. Sci.* 12, 349–370.
- Lee, C.H., Masaki, S., Kobayashi, S., 1972. Analysis of ball indentation. *Int. J. Mech. Sci.* 14, 417IN1421–420IN2426.
- Lee, E.H., 1955. Stress analysis in visco-elastic bodies. *Q. Appl. Math.* 183–190.
- Lee, E.H., Radok, J.R.M., 1960. The contact problem for viscoelastic bodies. *J. Appl. Mech.* 27, 438–444.
- Lemaitre, J., Chaboche, J.L., 1994. *Mechanics of solid materials*. Cambridge university press.
- Levenberg, K., 1944. A method for the solution of certain non-linear problems in least squares. *Q. Appl. Math.* 2, 164–168.
- Liao, Y., Zhou, Y., Huang, Y., Jiang, L., 2009. Measuring elastic–plastic properties of thin films on elastic–plastic substrates by sharp indentation. *Mech. Mater.* 41, 308–318.
- Lichinchi, M., Lenardi, C., Haupt, J., Vitali, R., 1998. Simulation of Berkovich nanoindentation experiments on thin films using finite element method. *Thin Solid Films* 312, 240–248.

- Liu, K., VanLandingham, M.R., Ovaert, T.C., 2009. Mechanical characterization of soft viscoelastic gels via indentation and optimization-based inverse finite element analysis. *J. Mech. Behav. Biomed. Mater.* 2, 355–363.
- Love, A.E.H., 1939. Boussinesq's problem for a rigid cone. *Q. J. Math.* 161–175.
- Love, A.E.H., 1929. The stress produced in a semi-infinite solid by pressure on part of the boundary. *Philos. Trans. R. Soc. Lond. Ser. Contain. Pap. Math. Phys. Character* 228, 377–420.
- Lu, H., Wang, B., Ma, J., Huang, G., Viswanathan, H., 2003. Measurement of creep compliance of solid polymers by nanoindentation. *Mech. Time-Depend. Mater.* 7, 189–207.
- Luo, J., Lin, J., 2007. A study on the determination of plastic properties of metals by instrumented indentation using two sharp indenters. *Int. J. Solids Struct.* 44, 5803–5817.
- Magenet, V., Giraud, A., Homand, F., 2008. Parameter sensitivity analysis for a Drücker–Prager model following from numerical simulations of indentation tests. *Comput. Mater. Sci.* 44, 385–391.
- Maier, C., Calafut, T., 1998. Polypropylene: the definitive user's guide and databook. William Andrew.
- Marquardt, D.W., 1963. An algorithm for least-squares estimation of nonlinear parameters. *J. Soc. Ind. Appl. Math.* 11, 431–441.
- Martynova, E., 2016. Determination of the properties of viscoelastic materials using spherical nanoindentation. *Mech. Time-Depend. Mater.* 20, 85–93.
- Marx, D.T., Riester, L., 1999. Mechanical properties of carbon–carbon composite components determined using nanoindentation. *Carbon* 37, 1679–1684.
- Mata, M., Alcalá, J., 2004. The role of friction on sharp indentation. *J. Mech. Phys. Solids* 52, 145–165.
- Menčík, J., He, L.H., Němeček, J., 2011. Characterization of viscoelastic-plastic properties of solid polymers by instrumented indentation. *Polym. Test.* 30, 101–109.
- Menčík, J., He, L.H., Swain, M.V., 2009. Determination of viscoelastic–plastic material parameters of biomaterials by instrumented indentation. *J. Mech. Behav. Biomed. Mater.* 2, 318–325.
- Mendenhall, H.V., Roth, J.H., Kennedy, J.C., Winter, G.D., Lumb, W.V., 1987. Evaluation of the polypropylene braid as a prosthetic anterior cruciate ligament replacement in the dog. *Am. J. Sports Med.* 15, 543–546.
- Moy, C.K., Bocciarelli, M., Ringer, S.P., Ranzi, G., 2011. Identification of the material properties of Al 2024 alloy by means of inverse analysis and indentation tests. *Mater. Sci. Eng. A* 529, 119–130.
- Nakamura, T., Gu, Y., 2007. Identification of elastic–plastic anisotropic parameters using instrumented indentation and inverse analysis. *Mech. Mater.* 39, 340–356.
- Nakamura, T., Wang, T., Sampath, S., 2000. Determination of properties of graded materials by inverse analysis and instrumented indentation. *Acta Mater.* 48, 4293–4306.
- Olaf, J.M., Scheer, C., 1993. Finite element analysis of indentation experiments in surfaces and surface coated materials. *Comput. Mater. Sci.* 1, 276–282.
- Oliver, W.C., Pharr, G.M., 2004. Measurement of hardness and elastic modulus by instrumented indentation: Advances in understanding and refinements to methodology. *J. Mater. Res.* 19, 3–20.
- Oliver, W.C., Pharr, G.M., 1992. An improved technique for determining hardness and elastic modulus using load and displacement sensing indentation experiments. *J. Mater. Res.* 7, 1564–1583.
- Ovaert, T.C., Kim, B.R., Wang, J., 2003. Multi-parameter models of the viscoelastic/plastic mechanical properties of coatings via combined nanoindentation and non-linear finite element modeling. *Prog. Org. Coat.* 47, 312–323.
- Oyen, M.L., 2006. Analytical techniques for indentation of viscoelastic materials. *Philos. Mag.* 86, 5625–5641.
- Oyen, M.L., Cook, R.F., 2003. Load–displacement behavior during sharp indentation of viscous–elastic–plastic materials. *J. Mater. Res.* 18, 139–150.
- Pac, M.-J., Giljean, S., Rousselot, C., Richard, F., Delobelle, P., 2014. Microstructural and elasto-plastic material parameters identification by inverse finite elements method of Ti (1- x) AlxN (0 < x < 1) sputtered thin films from Berkovich nano-indentation experiments. *Thin Solid Films* 569, 81–92.
- Peng, G., Feng, Y., Huan, Y., Zhang, T., 2013. Characterization of the viscoelastic-plastic properties of UPVC by instrumented sharp indentation. *Polym. Test.* 32, 1358–1367.
- Peng, G., Zhang, T., Feng, Y., Huan, Y., 2012. Determination of shear creep compliance of linear viscoelastic-plastic solids by instrumented indentation. *Polym. Test.* 31, 1038–1044.
- Phadikar, J.K., Bogetti, T.A., Karlsson, A.M., 2013. On the uniqueness and sensitivity of indentation testing of isotropic materials. *Int. J. Solids Struct.* 50, 3242–3253.

- Poilâne, C., Cherif, Z.E., Richard, F., Vivet, A., Doudou, B.B., Chen, J., 2014. Polymer reinforced by flax fibres as a viscoelastoplastic material. *Compos. Struct.* 112, 100–112.
- Qasmi, M., Delobelle, P., Richard, F., Brun, C., Fromm, M., 2004. Viscoelastic mechanical properties determined by nanoindentation tests and its numerical modelling of polypropylene modified by He⁺ particle implantation and e- irradiation. *Prog. Org. Coat.* 51, 195–204.
- Radok, J.R.M., 1957. Visco-elastic stress analysis. *Q. Appl. Math.* 15, 198–202.
- Rauchs, G., 2006. Optimization-based material parameter identification in indentation testing for finite strain elasto-plasticity. *ZAMM-Journal Appl. Math. Mech.* 539–562.
- Rauchs, G., Bardon, J., Georges, D., 2010. Identification of the material parameters of a viscous hyperelastic constitutive law from spherical indentation tests of rubber and validation by tensile tests. *Mech. Mater.* 42, 961–973.
- Renner, E., 2016. Vers l'identification d'une loi de plasticité monocristalline par analyse topographique d'empreintes de nanoindentation Berkovich (PhD Thesis). Université de Franche Comté.
- Resapu, R.R., Nagendran, K.B., Bradshaw, R.D., 2008. A finite element method for the determination of optimal viscoelastic material properties from indentation tests of polymer film and wire with polymer insulation. *Exp. Mech.* 48, 713–729.
- Rho, J.-Y., Tsui, T.Y., Pharr, G.M., 1997. Elastic properties of human cortical and trabecular lamellar bone measured by nanoindentation. *Biomaterials* 18, 1325–1330.
- Richard, F., 2017. Vers une détermination guidée par l'identifiabilité du comportement mécanique des matériaux par nanoindentation (PhD Thesis). COMUE Université Bourgogne Franche-Comté.
- Richard, F., Villars, M., Thibaud, S., 2013. Viscoelastic modeling and quantitative experimental characterization of normal and osteoarthritic human articular cartilage using indentation. *J. Mech. Behav. Biomed. Mater.* 24, 41–52.
- Samadi-Dooki, A., Voyiadjis, G.Z., Stout, R.W., 2018. A combined experimental, modeling, and computational approach to interpret the viscoelastic response of the white matter brain tissue during indentation. *J. Mech. Behav. Biomed. Mater.* 77, 24–33.
- Schiffmann, K.I., 2006. Nanoindentation creep and stress relaxation tests of polycarbonate: Analysis of viscoelastic properties by different rheological models. *Z. Für Met.* 97, 1199–1211.
- Seltzer, R., Cisilino, A.P., Frontini, P.M., Mai, Y.-W., 2011. Determination of the Drucker–Prager parameters of polymers exhibiting pressure-sensitive plastic behaviour by depth-sensing indentation. *Int. J. Mech. Sci.* 53, 471–478.
- Shimamoto, A., Tanaka, K., Akiyama, Y., Yoshizaki, H., 1996. Nanoindentation of glass with a tip-truncated Berkovich indenter. *Philos. Mag. A* 74, 1097–1105.
- Shimizu, S., Yanagimoto, T., Sakai, M., 1999. Pyramidal indentation load–depth curve of viscoelastic materials. *J. Mater. Res.* 14, 4075–4086.
- Sinclair, G.B., Follansbee, P.S., Johnson, K.L., 1985. Quasi-static normal indentation of an elasto-plastic half-space by a rigid sphere—II. Results. *Int. J. Solids Struct.* 21, 865–888.
- Sneddon, I.N., 1965. The relation between load and penetration in the axisymmetric Boussinesq problem for a punch of arbitrary profile. *Int. J. Eng. Sci.* 3, 47–57.
- Sneddon, I.N., 1946. The elastic stresses produced in a thick plate by the application of pressure to its free surfaces, in: *Mathematical Proceedings of the Cambridge Philosophical Society*. Cambridge University Press, pp. 260–271.
- Stan, F., Fetecau, C., 2013. Characterization of viscoelastic properties of molybdenum disulphide filled polyamide by indentation. *Mech. Time-Depend. Mater.* 17, 205–221.
- Stan, F., Munteanu, A.V., Fetecau, C., 2011. Analysis of visco-elastic-plastic behaviour of short glass fiber-reinforced polyamide 66 composite (PA66 GF30). *Mater. Plast.* 48, 1–6.
- Storåkers, B., Larsson, P.-L., 1994. On Brinell and Boussinesq indentation of creeping solids. *J. Mech. Phys. Solids* 42, 307–332.
- Sun, G., Xu, F., Li, G., Huang, X., Li, Q., 2014. Determination of mechanical properties of the weld line by combining micro-indentation with inverse modeling. *Comput. Mater. Sci.* 85, 347–362.
- Swaddiwudhipong, S., Tho, K.K., Liu, Z.S., Zeng, K., 2005. Material characterization based on dual indenters. *Int. J. Solids Struct.* 42, 69–83.
- Tang, B., Ngan, A.H.W., 2003. Accurate measurement of tip-sample contact size during nanoindentation of viscoelastic materials. *J. Mater. Res.* 18, 1141–1148.
- Tho, K. K., Swaddiwudhipong, S., Liu, Z.S., Zeng, K., Hua, J., 2004. Uniqueness of reverse analysis from conical indentation tests. *J. Mater. Res.* 19, 2498–2502.
- Tho, K.K., Swaddiwudhipong, S., Liu, Z.S., Zeng, K., Hua, J., 2004. Uniqueness of reverse analysis from conical indentation tests. *J. Mater. Res.* 19, 2498–2502.

- Ting, T.C.T., 1966. The contact stresses between a rigid indenter and a viscoelastic half-space. *J. Appl. Mech.* 33, 845–854.
- Troyon, M., Huang, L., 2005. Correction factor for contact area in nanoindentation measurements. *J. Mater. Res.* 20, 610–617.
- Tunvisut, K., Busso, E.P., O’ Dowd, N.P., Brantner, H.P., 2002. Determination of the mechanical properties of metallic thin films and substrates from indentation tests. *Philos. Mag. A* 82, 2013–2029.
- Vandamme, M., Ulm, F.-J., 2006. Viscoelastic solutions for conical indentation. *Int. J. Solids Struct.* 43, 3142–3165.
- VanLandingham, M.R., Chang, N.-K., Drzal, P.L., White, C.C., Chang, S.-H., 2005. Viscoelastic characterization of polymers using instrumented indentation. I. Quasi-static testing. *J. Polym. Sci. Part B Polym. Phys.* 43, 1794–1811.
- Vasile, C., 2000. *Handbook of polyolefins*. CRC Press.
- Venkatesh, T.A., Van Vliet, K.J., Giannakopoulos, A.E., Suresh, S., 2000. Determination of elasto-plastic properties by instrumented sharp indentation: guidelines for property extraction. *Scr. Mater.* 42, 833–839.
- Vlassak, J.J., Nix, W.D., 1994. Measuring the elastic properties of anisotropic materials by means of indentation experiments. *J. Mech. Phys. Solids* 42, 1223–1245.
- Wang, H.F., Bangert, H., 1993. Three-dimensional finite element simulation of Vickers indentation on coated systems. *Mater. Sci. Eng. A* 163, 43–50.
- Wang, J., 2001. Material property identification of polymer thin films under the indentation test (PhD Thesis). The Pennsylvania State University.
- Wang, J., Ovaert, T.C., 2009. Computational mechanical property determination of viscoelastic/plastic materials from nanoindentation creep test data. *J. Mater. Res.* 24, 1245–1257.
- Wang, M., Wu, J., Hui, Y., Zhang, Z., Zhan, X., Guo, R., 2017. Identification of elastic-plastic properties of metal materials by using the residual imprint of spherical indentation. *Mater. Sci. Eng. A* 679, 143–154.
- Woigard, J., 2006. Some results on the indentation of an elastic half space. *Philos. Mag.* 86, 5199–5217.
- Yan, J., Karlsson, A.M., Chen, X., 2007. Determining plastic properties of a material with residual stress by using conical indentation. *Int. J. Solids Struct.* 44, 3720–3737.
- Yang, W.H., 1966. The contact problem for viscoelastic bodies. *J. Appl. Mech.* 33, 395–401.
- Yao, W., Yoshida, K., Fernandez, M., Vink, J., Wapner, R.J., Ananth, C.V., Oyen, M.L., Myers, K.M., 2014. Measuring the compressive viscoelastic mechanical properties of human cervical tissue using indentation. *J. Mech. Behav. Biomed. Mater.* 18–26.
- Zeng, K., Giannakopoulos, A.E., Rowcliffe, D.J., 1995. Vickers indentations in glass—II. Comparison of finite element analysis and experiments. *Acta Metall. Mater.* 43, 1945–1954.
- Zhang, C.Y., Zhang, Y.W., Zeng, K.Y., 2004. Extracting the mechanical properties of a viscoelastic polymeric film on a hard elastic substrate. *J. Mater. Res.* 19, 3053–3061.
- Zhang, M.-G., Cao, Y.-P., Li, G.-Y., Feng, X.-Q., 2014. Spherical indentation method for determining the constitutive parameters of hyperelastic soft materials. *Biomech. Model. Mechanobiol.* 13, 1–11.
- Zhang, Z.L., Kristiansen, H., Liu, J., 2007. A method for determining elastic properties of micron-sized polymer particles by using flat punch test. *Comput. Mater. Sci.* 39, 305–314.
- Zhao, M., Ogasawara, N., Chiba, N., Chen, X., 2006. A new approach to measure the elastic-plastic properties of bulk materials using spherical indentation. *Acta Mater.* 54, 23–32.

Titre : Identification des propriétés viscoélastique-viscoplastique des matériaux par nanoindentation instrumentée

Mots clés : viscoélasticité, viscoplasticité, nanoindentation, identifiabilité, unicité, FEMU

Résumé : La nanoindentation est une technique très utilisée pour extraire les propriétés mécaniques des matériaux à partir de courbes force-déplacement. Cependant, l'unicité et le caractère intrinsèque des valeurs estimées restent des problèmes ouverts, particulièrement lorsque des phénomènes visqueux sont exhibés. Dans ce travail, une loi de comportement viscoélastique-viscoplastique (VEVP) a été implémentée dans le code éléments finis (EF) ANSYS par l'intermédiaire une subroutine UMAT avec un cas particulier: viscoélastique-plastique (VEP). Le cas viscoélastique (VE) a été traité en utilisant la loi disponible sur ANSYS. L'objectif principal est d'extraire des propriétés intrinsèques et fiables par nanoindentation. Dans ce contexte, une série d'essais expérimentaux de nanoindentation a été réalisée sur du polypropylène (PP) en déplacement contrôlé avec les indenteurs cube corner et Berkovich. La méthode du recalage de modèle EF montre que l'identification des propriétés VE intrinsèques au PP à partir d'un essai expérimental triangulaire effectué à 1000 nm/min est impossible. Afin de quantifier la richesse de l'information contenue dans l'essai de nanoindentation, un indice d'identifiabilité (*I*-index) basé sur le conditionnement numérique du problème inverse est utilisé. Les effets de la vitesse de déplacement, de type de chargement (triangulaire, trapézoïdal, exponentiel et sinusoïdal) et de l'angle de la pointe de l'indenteur sont étudiés dans le cas VE. On montre qu'il existe une corrélation entre les résultats d'identifiabilité et l'énergie dissipée par le matériau. Quelques combinaisons d'essais triangulaires de nanoindentation et d'angles de pointe sont aussi investiguées.

On montre que la méthode de nanoindentation à double pointes (cube corner et Berkovich) avec des essais triangulaires charge-décharge s'avère robuste pour extraire tous les paramètres VE. Le recalage de modèle utilisant deux essais expérimentaux de nanoindentation réalisés à 500 nm/min avec les indenteurs cube corner et Berkovich montre que durant l'essai de nanoindentation, le PP ne se déforme pas seulement dans le domaine VE.

L'investigation du comportement du PP est étendue en ajoutant la viscoplasticité dans la loi de comportement. Le recalage de modèle VEVP conduit à des solutions multiples des paramètres. L'analyse d'identifiabilité réalisée avec ce modèle illustre que l'identification des paramètres est impossible. On montre aussi que l'identification des paramètres VEP à partir de cette double nanoindentation est difficile.

Ces résultats ouvrent la voie à l'utilisation de cet *I*-index pour concevoir une combinaison d'essais de nanoindentation capable de garantir l'unicité et le caractère intrinsèque au matériau des propriétés extraites.

Title : Identification of the viscoelastic-viscoplastic properties of materials by instrumented nanoindentation

Keywords : viscoelasticity, viscoplasticity, nanoindentation, identifiability, uniqueness, FEMU

Abstract : Instrumented nanoindentation is a popular technique to extract the material properties from the measured load-displacement curves. However, the uniqueness and the intrinsic character of the estimated material parameters remain open issues, particularly when viscous phenomena are exhibited. In this thesis, a constitutive viscoelastic-viscoplastic (VEVP) behavior law is implemented in the finite element software ANSYS through a subroutine UMAT with a viscoelastic-plastic (VEP) particular case. The viscoelastic (VE) was treated using the behavior law available in ANSYS. The goal is to extract reliable and intrinsic properties by nanoindentation. In this context, series of nanoindentation experimental tests are carried out on the polypropylene (PP) in displacement-controlled mode using cube corner and Berkovich indenter tips. The Finite Element Model Updating (FEMU) shows that the identification of intrinsic VE properties of PP from single experimental nanoindentation test performed at 1000 nm/min is not possible. In order to quantify the richness of the information contained in the nanoindentation test, an identifiability index (*I*-index) based on the numerical conditioning of the inverse problem is used. The effect of nanoindentation depth rate, loading type (triangular, trapezoidal, exponential and sinusoidal) and apex angle is numerically investigated using this *I*-index in the VE case. We show a correlation between the identifiability results and the energy dissipated by the material. Several combinations of nanoindentation triangular tests and indenter tip angles are also investigated.

We show that a dual nanoindentation method (cube corner and Berkovich) with triangular load-unload tests is an interesting combination to reliably extract all the VE parameters. The updating process using dual nanoindentation experimental tests conducted at 500 nm/min with cube corner and Berkovich indenter tips shows that under nanoindentation the PP is not only deformed in the VE domain.

The investigation of the PP behavior is extended by including viscoplasticity in the behavior law. The updating process of the VEP behavior law leads to multiple solutions for the values of the behavior parameters. The identifiability analysis carried out using this behavior shows that the identification of the material parameters from this dual nanoindentation data is impossible. We also carried out an updating process and identifiability analysis with the VEP behavior law. The obtained results show that the identification of the VEP parameters is difficult. These results pave the way for the design of a combination of nanoindentation tests based on this *I*-index to guarantee the uniqueness and the intrinsic character of the extracted properties.